

Justus-Liebig-Universität Gießen
I. Physikalisches Institut

Advanced Group III-Nitride Nanowire Heterostructures

Self-Assembly and Position-Controlled Growth

Dissertation

zur Erlangung des

Doktorgrades der Naturwissenschaften

Doctor rerum naturalium

(Dr. rer. nat.)

vorgelegt dem

Fachbereich 07

Mathematik und Informatik, Physik, Geographie

Gießen 2017

von

Master of Science

Pascal Hille

angefertigt bei

Prof. Dr. Martin Eickhoff

Zusammenfassung

Gruppe III-Nitrid Nanodrähte und Nanodrahtheterostrukturen wurden mittels plasmaunterstützter Molekularstrahlepitaxie hergestellt. Rasterelektronen- und Transmissionselektronenmikroskopie sowie Röntgendiffraktometrie dienten zur strukturellen Charakterisierung der Proben. Die optischen Eigenschaften der Nanodrahtstrukturen wurden mit Hilfe von Photolumineszenzspektroskopieverfahren (Dauertstrich und zeitaufgelöst) untersucht.

Sofern nicht auf GaN als Material beschränkt, wurden alle untersuchten Nanodrahtheterostrukturen (AlN/GaN Übergitter sowie $\text{In}_x\text{Ga}_{1-x}\text{N}/\text{GaN}$ Heterostrukturen) auf GaN Nanodrahttemplaten hergestellt. Für letztere wurden zwei unterschiedliche Wachstumsmodi verwendet. Zum Einen das etablierte selbstassemblierte Wachstum auf Si(111) sowie das während dieser Arbeit entwickelte positionskontrollierte Wachstum von GaN Nanodrähten auf Si(111) mittels einer Ti(N) Nanolochmaske.

Das selbstassemblierte Wachstum auf Si(111) ist der Standardprozess zur Herstellung von GaN Nanodrähten durch Molekularstrahlepitaxie. Bisherige Arbeiten beschränkten sich vornehmlich auf die Analyse des Einflusses der Substrattemperatur und des Metallflusses auf das Wachstum und die Eigenschaften von GaN Nanodrähten. Für das Wachstum ist jedoch das Aufspalten/Anregen von molekularem Stickstoff von Nöten, um zur GaN-Bildung beitragen zu können. Dies geschieht im verwendeten Aufbau durch eine Radiofrequenz-Plasmaentladung. Der Einfluss der dazu verwendeten Parameter (Stickstofffluss und eingekoppelte Leistung) auf das Wachstum und die optischen Eigenschaften der GaN Nanodrähte wurde in dieser Arbeit untersucht. Es wurde gezeigt, dass eine erhöhte eingekoppelte Leistung zu dem vermehrten Einbau von Punktdefekten, vermeintlich Stickstoffleerstellen, führt. Bei einer Erhöhung des Stickstoffflusses wurde ein Anstieg der Dichte oberflächennaher Ga-Leerstellen beobachtet.

Die n-Typ Dotierung von GaN mittels Germanium erlaubt das Erreichen sehr hoher Konzentrationen ($\approx 10^{20} \text{ cm}^{-3}$) freier Ladungsträger. Dies wurde ausgenutzt, um die starken internen elektrischen Felder (MV/cm-Bereich) in polaren GaN Nanodisks (ähnlich den 2D Quantentrögen) elektrostatisch abzuschirmen. Die Nanodisks wurden zwischen AlN Barrieren hergestellt. Das Lumineszenzsignal der GaN Nanodisks wurde durch die Abschirmung der internen elektrischen Felder zu höheren Energien verschoben. Zeitaufgelöster Photolumineszenzspektroskopie an den Ge-dotierten GaN Nanodisks zeigte außerdem eine signifikante Erhöhung des Überlapps der Wellenfunktionen von Elektronen und Löchern mit steigender Dotierkonzentration. Eine hohe Oszillatorstärke ist essenziell für die Konstruktion effizienter opto-elektronischer Bauelemente.

Durch einen komplementären Ansatz, basierend auf undotierten AlN/GaN Nanodisküber-

gittern, konnte ebenfalls eine Abschirmung der internen elektrischen Felder erreicht werden. Dazu wurde die Höhe der AlN Barriere bis auf 1 nm verringert, sodass die gegensätzlich geladenen Grenzflächen zu den benachbarten Nanodisks näher zusammenrückten. Das Resultat ist eine Abschwächung (Verstärkung) der elektrischen Felder in den aktiven GaN Nanodisks (AlN Barrieren). Eine Blauverschiebung des Lumineszenzsignals sowie eine Reduzierung der Ladungsträgerlebensdauern konnte analog zu den Ge-dotierten GaN Nanodisks gezeigt werden.

Der Einfluss des Stickstoffflusses und der in das Plasma eingekoppelten Leistung auf das Wachstum und die Eigenschaften von $\text{In}_x\text{Ga}_{1-x}\text{N}/\text{GaN}$ Nanodrähten wurde ebenfalls analysiert. Ein inhomogener Einbau von In konnte mittels Röntgendiffraktometrie und Transmissionselektronenmikroskopie gezeigt werden. Die beobachteten Lumineszenzsignale stammen aus indiumreichen Bereichen in den Nanodrähten. Ein zunehmender Partialdruck des angebotenen Stickstoffs führte zu einem erhöhten lokalen In-Einbau. Bei einer Erhöhung der eingekoppelten Leistung wurde kein Einfluss auf den In-Gehalt beobachtet. Jedoch wurde ein deutlicher Einfluss auf die optischen Eigenschaften beobachtet. Eine höhere eingekoppelte Leistung während des Wachstumsprozesses der Nanodrähte führte zu einer Abnahme der Lumineszenzintensität. Letzteres wurde auf eine erhöhte Dichte nicht-strahlender Rekombinationpfade durch die Bildung von Stickstoffleerstellen zurückgeführt. Des Weiteren wurden $10\times \text{In}_x\text{Ga}_{1-x}\text{N}/\text{GaN}$ Nanodiskübergitter synthetisiert. Ein Ladungsträgereinschluss ähnlich dem von 2D Quantentrögen wurde durch eine Blauverschiebung der zugehörigen Lumineszenz mit kleiner werdender Nanodiskhöhe nachgewiesen. Übersteigt die Nanodisk eine Höhe von 4 nm, kommt es zur Konkurrenz zwischen der Ladungsträgerlokalisierung an Bereichen lokal hoher In-Konzentration und der Besetzung der quantisierten Nanodiskzustände.

Das positionskontrollierte Wachstum von GaN Nanodrähten auf Ti(N) Masken mit einem Lochdurchmesser von 70 nm wurde entwickelt und optimiert. Es konnte eine vollständige Selektivität des Wachstumsprozesses für Lochabstände bis $10 \mu\text{m}$ gezeigt werden. Letzteres macht die Untersuchung einzelner stehender Nanodrähte mittels Mikro-Photolumineszenzspektroskopie möglich. Des Weiteren wurde ein Prozess für das selektive Wachstum von $\text{In}_x\text{Ga}_{1-x}\text{N}$ auf positionskontrolliert gewachsenen GaN Nanodrahttemplaten entwickelt.

Contents

1	Introduction	1
2	Fundamentals of the group III-nitride crystal system	3
3	Experimental methods	11
3.1	Plasma-assisted molecular beam epitaxy	11
3.1.1	Flux and beam equivalent pressure	12
3.2	Atomic force microscopy	14
3.3	Electron microscopy	14
3.3.1	Scanning electron microscopy and electron beam lithography	14
3.3.2	Transmission electron microscopy	14
3.4	Photoluminescence spectroscopy	16
3.5	X-Ray diffraction analysis	20
4	Growth of GaN nanowires on silicon	23
4.1	Fundamentals of the GaN nanowire growth	23
4.2	Substrate preparation and GaN nanowire growth	26
4.3	Variation of the gallium flux	28
4.3.1	Morphology and growth rates	28
4.3.2	Photoluminescence spectroscopy	30
4.4	Impact of the atom source operating parameters	33
4.4.1	Plasma diagnostics	33
4.4.2	Morphology and growth rates	36
4.4.3	Photoluminescence spectroscopy	42
4.4.4	Conclusion	44
5	Analysis of internal electric fields in AlN/GaN nanowire heterostructures	47
5.1	Doping-induced screening of internal electric fields	47
5.1.1	Structural analysis	49
5.1.2	Optical analysis	52
5.2	Influence of the AlN barrier thickness on internal electric fields	57
5.3	Comparison	59
5.4	Conclusion	64

6 In_xGa_{1-x}N/GaN nanowire heterostructures	65
6.1 Influence of the atom source operating parameters	65
6.1.1 Growth and structural analysis	66
6.1.2 Photoluminescence spectroscopy	73
6.2 In _x Ga _{1-x} N/GaN nanodisc superlattices	84
6.2.1 Electron microscopy	84
6.2.2 Photoluminescence spectroscopy	88
6.3 Conclusion	96
7 Position-controlled growth of group III-nitride nanowires	98
7.1 Growth mechanism and mask preparation	98
7.2 Position-controlled growth of GaN nanowires	100
7.2.1 Influence of the mask thickness on the growth selectivity	100
7.2.2 Influence of the nitrogen flux on the growth selectivity	103
7.2.3 Influence of the growth time	106
7.2.4 Large nanohole pitches	109
7.2.5 Conclusion	111
7.3 Selective growth of In _x Ga _{1-x} N/GaN nanowire heterostructures	112
7.3.1 Influence of the substrate temperature	112
7.3.2 Influence of the nitrogen flux	115
7.3.3 Influence of the metal flux ratio	117
7.3.4 Conclusion	119
8 Summary	121
Appendix	123
A.1 Effusion cell calibrations	123
A.2 Patterning of Ti nanohole masks	124
A.3 List of samples	125
A.4 Nextnano ³ input parameters	127
A.5 List of publications	129
Acknowledgments/Danksagung	131
Bibliography	133

Abbreviations

ABF	annular bright field
AFM	atomic force microscopy
<i>BEP</i>	beam equivalent pressure
BF	bright field
BSF	basal plane stacking fault
CB	conduction band
CW	continous-wave
DAP	donor-acceptor pair
DF	dark field
EBL	electron beam lithography
EDX	energy dispersive X-Ray spectroscopy
FWHM	full width at half maximum
HAADF	high angle annular dark field
IFGARD	Internal Field Guarded Active Region Design
HRTEM	high resolution transmission electron microscope
HRXRD	high resolution X-Ray diffraction
<i>IQE</i>	internal quantum efficiency
IR	infrared
LED	light emitting diode
LO	longitudinal optical
MBE	molecular beam epitaxy
MOCVD	metal-organic chemical vapor deposition

MOVPE	metal-organic chemical vapor phase epitaxy
NBE	near band edge
ND	nanodisc
NDSL	nanodisc superlattice
n.i.d.	not-intentionally doped
NW	nanowire
NWH	nanowire heterostructure
PAMBE	plasma-assisted molecular beam epitaxy
PCG	position-controlled growth
PL	photoluminescence
QCSE	quantum-confined Stark effect
QD	quantum dot
QW	quantum well
RF	radio frequency
RHEED	reflection high energy electron diffraction
RSM	reciprocal space map
sccm	standard cubic centimetres per minute
SEM	scanning electron microscopy
SNW	single nanowire
STEM	scanning transmission electron microscopy
TEM	transmission electron microscopy
TES	two electron satellite
TR	time-resolved

UHV	ultra-high vacuum
UV	ultraviolet
VB	valence band
V_{Ga}	gallium vacancy
V_{N}	nitrogen vacancy
VLS	vapour-liquid-solid
XRD	X-Ray diffraction

1 Introduction

Self-assembled growth of group III-nitride nanowires (NWs) by molecular beam epitaxy (MBE) was introduced by Yoshizawa et al. [1] and Calle et al. [2] in 1997. The NW geometry allows for efficient strain relaxation at the lateral surfaces [3] which leads to the growth of strain-free single crystals with a low density of structural defects [4–6]. Additionally, the MBE growth technique enables the precise control of the layer thickness in the sub-nanometer range. This enables the integration of axially grown nanodiscs (NDs) in nanowire heterostructures (NWHs) [7–9], similar to the growth of quantum well (QW) and quantum dot (QD) structures in layer systems using, *exempli gratia*, group III-nitride alloys with different band gaps. These heterostructures are, however, significantly strained due to the pseudomorphic growth mechanism which affects carrier-confinement [9–11]. In the case of the group III-nitrides, the optical properties of these NWHs are also affected by strong internal electric fields [12, 13]. The latter are in the MV/cm range and affect the optical properties due to a reduction of the electron-hole wavefunction overlap as a result of the quantum-confined Stark effect (QCSE). Consequently, screening or reduction of these electric fields is mandatory to improve the efficiency of (nano)-opto-electronic devices such as NW light emitting diodes (LEDs) [14] as well as intersubband devices for telecommunication applications [15].

A large conduction band (CB) offset up to 1.8 eV [16, 17] in $\text{Al}_x\text{Ga}_{1-x}\text{N}/\text{GaN}$ heterostructures renders this material composition suitable for the latter application. Due to the tunability of the band gap from the ultraviolet (UV) (3.4 eV GaN [18]) to the infrared (IR) (0.7 eV, InN [19]), $\text{In}_x\text{Ga}_{1-x}\text{N}$ is a promising candidate for the realization of opto-electronic devices operating in the visible spectral range. Fabrication of LEDs in the visible spectral range is the most prominent example for $\text{In}_x\text{Ga}_{1-x}\text{N}$ based devices since the introduction of the blue light-emitting diodes [20–22]. The work by Isamu Akasaki, Hiroshi Amano and Shuji Nakamura on this topic has recently been awarded with the Nobel Prize in Physics 2014 "[...] for the invention of efficient blue light-emitting diodes which has enabled bright and energy-saving white light sources"¹. However, the additional exploitation of the large surface-area-to-volume ratio of $\text{In}_x\text{Ga}_{1-x}\text{N}/\text{GaN}$ NWHs extends the field of possible applications. Optical detection of pH changes [23] in electrolytes and the sensitivity of the photoluminescence (PL) intensity to various gas species [24, 25] were demonstrated using $\text{In}_x\text{Ga}_{1-x}\text{N}/\text{GaN}$ NWHs. However, the growth of high quality $\text{In}_x\text{Ga}_{1-x}\text{N}$ NWs is challenging due to the low InN decomposition temperature of 565 °C [26] and strong fluctuations of

¹https://www.nobelprize.org/nobel_prizes/physics/laureates/2014/ (last visited on Jan. 30th, 2017).

the In content due to spinodal decomposition of the grown material at the applied growth conditions [27].

Control of the NW density and the suppression of the coalescence of neighbouring NWs is desirable to increase reproducibility of the grown samples and to meet required specifications. Though, self-assembled growth leads to thin NWs with a diameter < 100 nm, coalescence of neighbouring NWs introduces structural defects as well as an inhomogeneous diameter distribution. The position-controlled growth (PCG) of GaN NWs by plasma-assisted molecular beam epitaxy (PAMBE) was developed recently [28–34] and allows to define the density and diameter of the NWs by using a nanohole growth mask. The reported diameters of these selectively grown NWs, however, are well above 100 nm due to the relatively large openings of the used nanohole masks.

This work is dedicated to fill gaps in the knowledge about the self-assembled growth of GaN NWs and group III-nitride NWs by PAMBE. Additionally, a PCG process that allows the fabrication of GaN NW templates with a diameter ≤ 100 nm is introduced. Both growth techniques are used to fabricate GaN NW templates for the subsequent overgrowth with group III-nitride NWs. The manipulation of the internal electric fields in AlN/GaN nanodisc superlattices (NDSLs) was studied by following two complementary approaches. Free carrier screening was investigated in Ge doped GaN NDs while the recently proposed Internal Field Guarded Active Region Design (IFGARD) [35] was applied to nominally undoped GaN NDs embedded in AlN barriers. The influence of the atom source operating parameters on the structural and optical properties of GaN NWs and $\text{In}_x\text{Ga}_{1-x}\text{N}/\text{GaN}$ NWs was studied in depth. In the case of $\text{In}_x\text{Ga}_{1-x}\text{N}$, the gathered information was transferred to the growth of $\text{In}_x\text{Ga}_{1-x}\text{N}/\text{GaN}$ NDSLs. Additionally, a PCG process for the selective growth of $\text{In}_x\text{Ga}_{1-x}\text{N}/\text{GaN}$ NWs was developed.

2 Fundamentals of the group III-nitride crystal system

The NWs fabricated in the scope of this work consist of the group III-nitrides AlN, GaN and InN as well as their ternary alloys. Basic properties of the material system and their consequences for NWHs are discussed in this chapter.

Crystal structure and band gap

The group III-nitrides AlN, GaN and InN are a subgroup of the group III-V compound semiconductors and can be synthesized in a hexagonal (wurtzite in figure 2.1) or a cubic (zincblende figure 2.1) crystal structure, depending on the growth conditions. Cubic inclu-

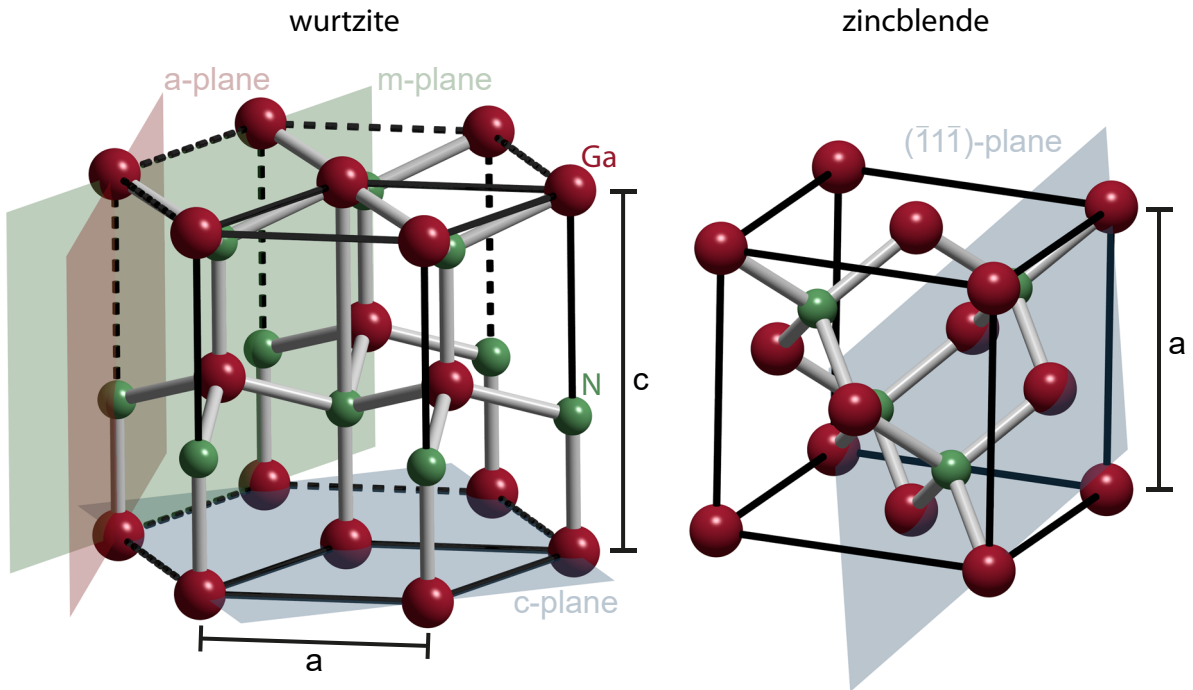


Figure 2.1: *Illustrations of the wurtzite and zincblende crystal structure.*

sions are a common intrinsic defect in hexagonal group III-nitrides because the two phases (wurtzite and zincblende) only differ in their respective stacking sequence. A wurtzite crystal exhibits an A-B stacking sequence, while zincblende features an A-B-C stacking (figure 2.2). Of those two crystal structures, wurtzite is the thermodynamically stable one [36]. Zincblende inclusions in a wurtzite crystal are, therefore, called basal plane stacking faults (BSFs). Within GaN NWs grown on Si substrates, stacking faults are typically observed at the NW/substrate interface [37]. Several monolayers of zincblende GaN that are encapsulated by a hexagonal GaN matrix can introduce regions of carrier confinement

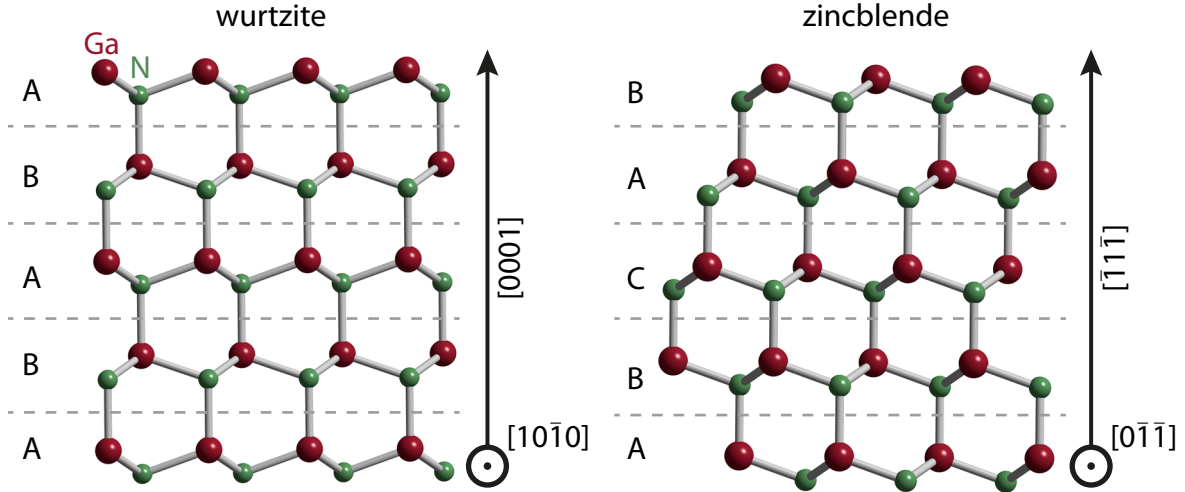


Figure 2.2: Illustrations of the wurtzite and zincblende stacking sequences.

which was demonstrated by Jacopin et al. [38].

The suitability of group III-nitrides for opto-electronic applications is due to their direct band gap. With the latter, the spectral range from the UV to the IR is covered. Band gaps and lattice parameters of the three binaries (AlN, GaN and InN) are listed in table 2.1. The u parameter represents the anion-cation bond length along the (0001)-direction

Material	E_{gap} [eV]	c [Å]	a [Å]	u
GaN	3,438	5,185	3,189	0.376
AlN	6,158	4,982	3,112	0.380
InN	0,756	5,703	3,545	0.377

Table 2.1: Band gaps and lattice parameters of AlN, GaN and InN at 300 K [18]. The u parameter (300 K) is listed according to Ref. [36].

divided by the c parameter. Growth of ternary compounds such as $\text{Al}_x\text{Ga}_{1-x}\text{N}$, $\text{Al}_x\text{In}_{1-x}\text{N}$ and $\text{In}_x\text{Ga}_{1-x}\text{N}$ allows for band gap and lattice parameter engineering within the limits of the values of the binary materials. However, while the lattice parameters are typically linearly interpolated according to Vegard's law [39], the composition dependence of the band gap is described by the non-linear relationship in equation 2.1.

$$E_{\text{gap}}^{A_xB_{1-x}N} = x \cdot E_{\text{gap}}^{AN} + (1-x) \cdot E_{\text{gap}}^{BN} - b \cdot x(1-x) \quad (2.1)$$

The bowing parameter b describes the deviation from a linear interpolation between the binary alloys A and B . In this work, the bowing parameters suggested by Vurgaftman and Meyer [18] were used (table 2.2). Graphical representations of equation 2.1 are given in figure 2.3 for the wurtzite and zincblende phases.

Material	b [eV]
$\text{Al}_x\text{Ga}_{1-x}\text{N}$	0,7
$\text{In}_x\text{Ga}_{1-x}\text{N}$	1,4

Table 2.2: *Bowing parameters suggested by Vurgaftman and Meyer [18].*

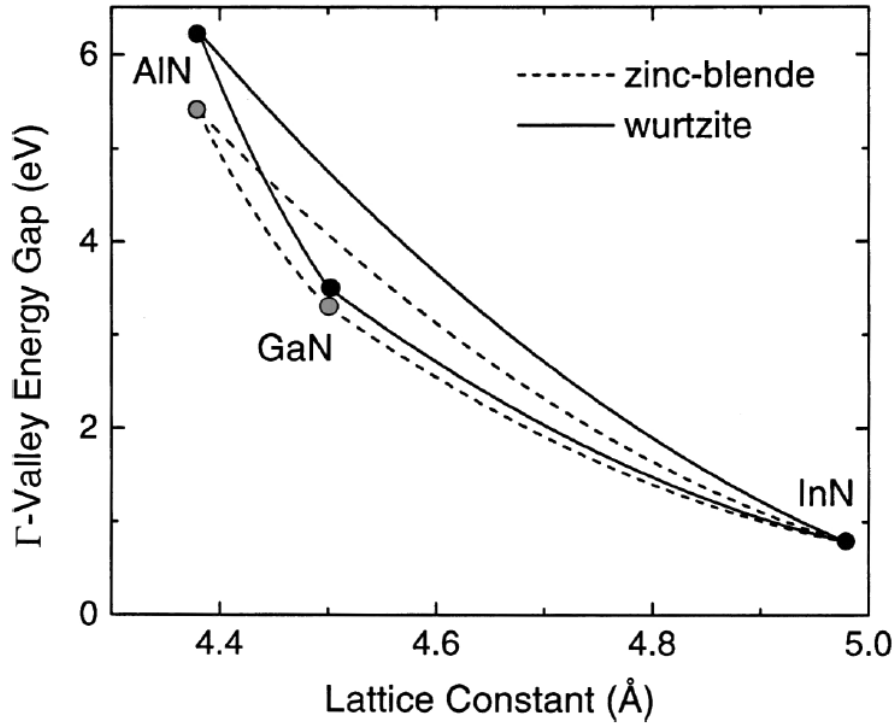


Figure 2.3: *Dependence of the band gaps of hexagonal and cubic group III-nitrides on the a lattice parameter. Reprinted from [I. Vurgaftman and J. R. Meyer, *J. Appl. Phys.*, Vol. 94, No. 6, 15 September 2003], with the permission of AIP Publishing.*

Polarization and heterostructures

Hexagonal group III-nitrides exhibit a permanent dipole moment in $\langle 0001 \rangle$ -direction. This spontaneous polarization of the crystal is due to the deviation of the u parameter from the ideal value of 0.375 in a wurtzite crystal [40]. Along the $\langle 0001 \rangle$ -axis, the

wurtzite crystal consists of two closely stacked hexagonal sublattices. This results in the formation of bilayers, each consisting of one layer of metal atoms and one layer of N atoms (*exempli gratia* bilayer A in figure 2.2). Hence, it is possible to distinguish between two different crystal polarities, depending on whether anions (N-face) or cations (Al-, Ga- or In-face) are on top of these bilayers. By definition, the positive $[0001]$ direction is cation faced. The GaN NWs presented in this work grew along the $[000\bar{1}]$ direction [41, 42]. If

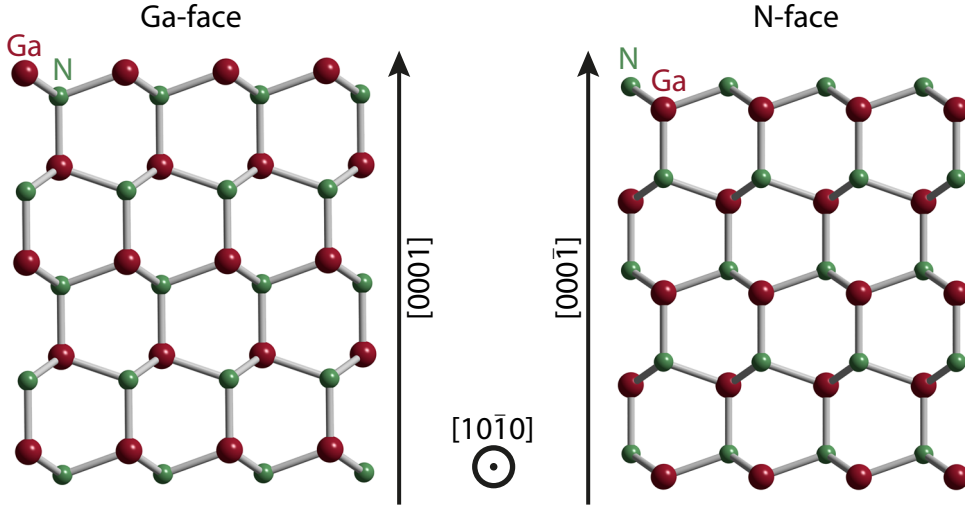


Figure 2.4: Schematics of a Ga and a nitrogen polar GaN crystal.

strained, additional piezoelectric polarization of the crystal occurs, which is superimposed to the spontaneous polarization either enhancing or attenuating the latter. Piezoelectric polarization due to tensile strain increases the resulting polarization and compressive strain consequently reduces the latter.

The polarity of the crystal plays a major role for $\langle 0001 \rangle$ -oriented group III-nitride heterostructures like the $\text{Al}_x\text{Ga}_{1-x}\text{N}/\text{GaN}$ and $\text{In}_x\text{Ga}_{1-x}\text{N}/\text{GaN}$ NWs discussed in chapters 5 and 6, respectively. Regions of carrier confinement are introduced to semiconductor heterostructures to improve thermal stability and to manipulate the energies of their optical transitions. In layer systems, such structures are represented by QWs or QDs, whereas carrier confinement in NWs is achieved by the insertion of NDs. As an example, a high angle annular dark field (HAADF) TEM image of a 40-fold AlN/GaN NDSL is shown in figure 2.5. These NDs exhibit a type I stacking which is schematically shown in figure 2.6a) for two non-polar semiconductors A and B. Confinement of electrons and holes is achieved in the material with the smaller band gap and the electron and hole probability functions are located in the center of the QW in material B. The band structure is significantly altered when the polarization induced internal electric fields of the group III-nitrides are

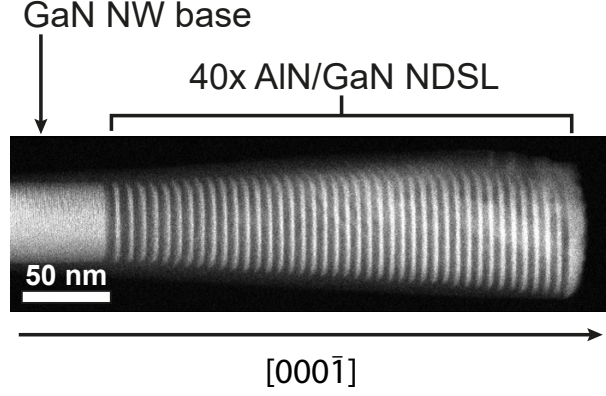


Figure 2.5: HAADF TEM image of an 40-fold AlN/GaN NDSL. The GaN base and NDs appear in bright contrast, whereas the AlN barriers are represented by darker areas in-between the NDs.

considered. Figure 2.6b) schematically shows the influence of internal electric fields on the electron and hole probability density functions and the optical transition energies, using the example of an AlN/GaN heterostructures. Conduction and valence band edges are marked with E_{CB} and E_{VB} , respectively. A sketch of the layer sequence is drawn in figure 2.6c). Due to the difference in lattice parameters, the AlN barriers are under tensile lateral strain and the GaN QW or ND is laterally compressed. The resulting piezoelectric polarization (\mathbf{P}_{PE}) points in the $[000\bar{1}]$ -direction, as does the spontaneous polarization (\mathbf{P}_{SP}), within the AlN and in $[0001]$ -direction in the GaN. The superposition of \mathbf{P}_{SP} and \mathbf{P}_{PE} yields the total polarization of the crystal.

$$\mathbf{P} = \mathbf{P}_{SP} + \mathbf{P}_{PE} \quad (2.2)$$

Quantitatively, $P_{PE,z}$ can be calculated with knowledge of the elastic and piezoelectric constants C_{13} , C_{33} , e_{31} and e_{33} and the in-plane strain $\epsilon_{11} = a - a_0/a_0$ according to equation 2.3 [36, 43].

$$P_{PE,z} = 2\epsilon_{11} \left(e_{31} - e_{33} \frac{C_{13}}{C_{33}} \right) \quad (2.3)$$

Table 2.3 summarizes the values of P_{SP} , e_{13} , e_{33} , C_{31} and C_{33} for the three binaries AlN, GaN and InN. A bound interface charge density is introduced according to equation 2.4 when a gradient of polarization occurs, *exempli gratia*, between the AlN barriers and GaN

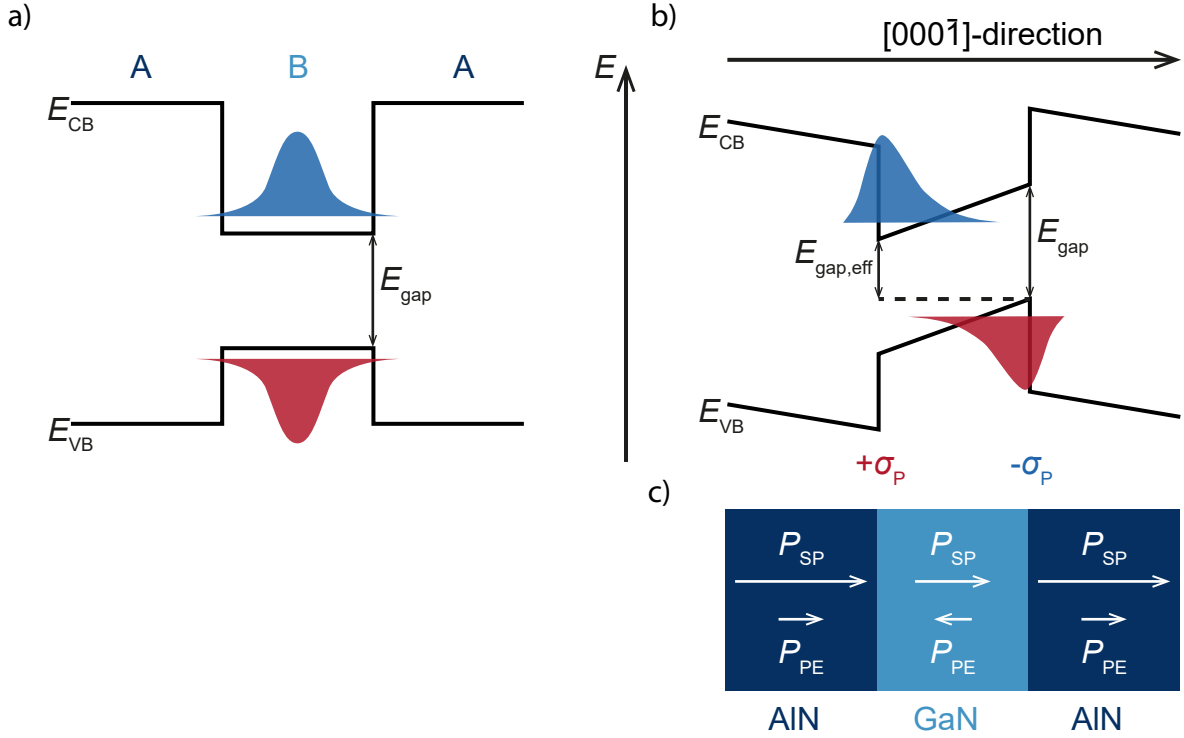


Figure 2.6: a) Schematic of a type I stacking sequence of two non-polar semiconductors A and B. Electron and hole probability density functions are sketched in blue and red, respectively. A schematic of a GaN QW or ND embedded in AlN barriers is shown in b). The layer system of b) is schematically shown in c) where the direction of the spontaneous (P_{SP}) and piezoelectric polarization (P_{PE}) are indicated by arrows.

NDs or at the NW surface.

$$\rho(r) = -\nabla P(r) \quad (2.4)$$

These fixed interface charges ($+\sigma_p$ and $-\sigma_p$ in figure 2.6) give rise to an electric field E_{el} . This electric field affects the potential according to the Poisson equation (equation 2.5) which results in the tilted bands depicted in figure 2.6b).

$$\Delta\Phi = -\frac{\rho(r)}{\epsilon} = -\nabla E_{el}(r) \quad (2.5)$$

Hence, transition energies are red shifted due to the reduction of the intrinsic band gap E_{gap} to an effective band gap $E_{gap,eff}$. Further, the internal electric field separates electrons and holes and reduces their wavefunction overlap. In PL experiments, the latter results in a decrease of the luminescence intensity and an increase of the carrier lifetimes. This

Material	P_{SP} [C m ⁻²]	e_{31} [C m ⁻²]	e_{33} [C m ⁻²]	C_{13} [GPa]	C_{33} [GPa]
AlN	-0,090	-0.6	1.46	108	373
GaN	-0,034	-0.49	0.73	106	398
InN	-0,042	-0.57	0.97	92	224

Table 2.3: *Spontaneous polarization P_{SP} [18], piezoelectric constants e_{ij} [44] and elastic constants C_{ij} [18] of AlN, GaN and InN.*

phenomenon is called the QCSE, in analogy to the Stark effect in atomic physics.

One major aspect of this work is to study the influence of the QCSE on the optical properties of AlN/GaN NDSLs and the effect doping of the NDs or the sophisticated design of not-intentionally doped (n.i.d.) samples have on the internal electric fields. An elaborate investigation is presented in chapter 5.

3 Experimental methods

In this chapter, an overview on the applied experimental characterization techniques and the MBE growth of NWs is given.

3.1 Plasma-assisted molecular beam epitaxy

A *RIBER Compact 12* PAMBE system was used for the fabrication of all investigated samples. The 3D schematic of the growth chamber is shown in figure 3.1. All relevant

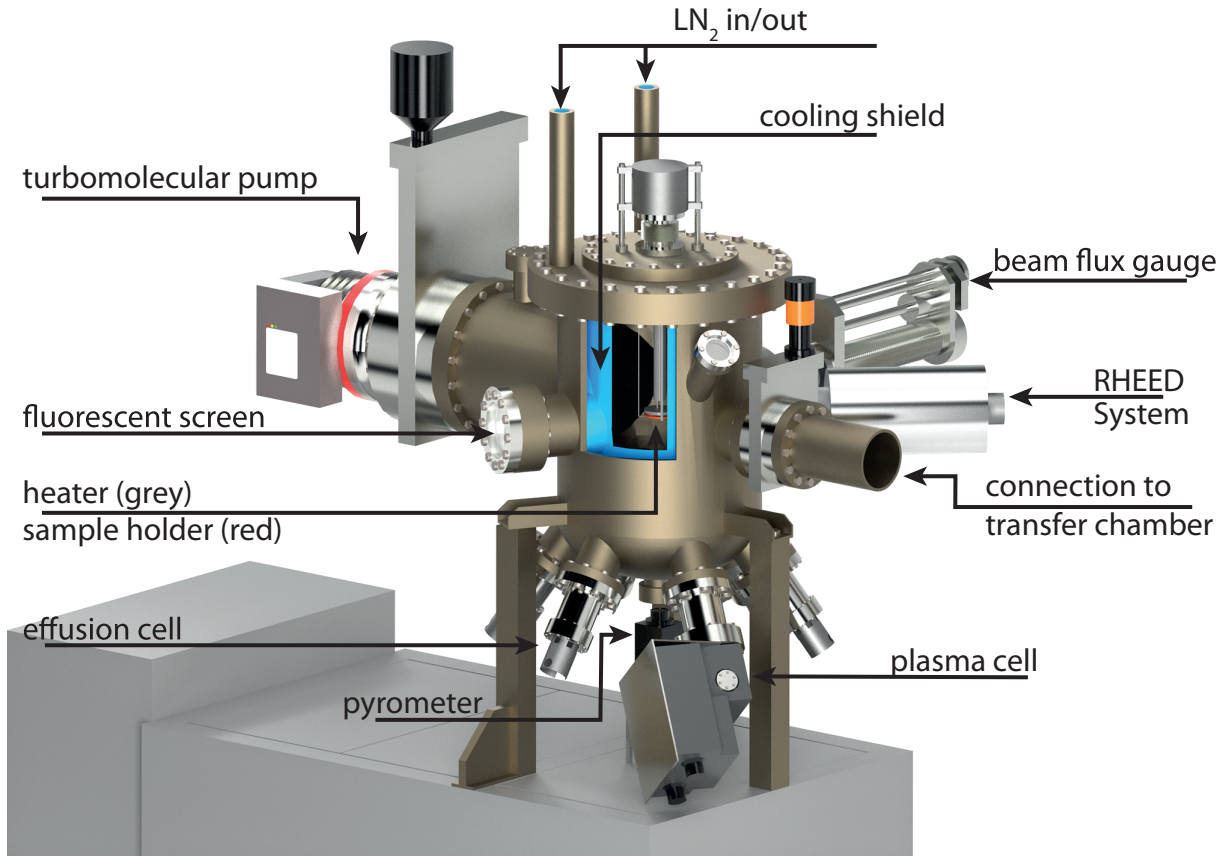


Figure 3.1: Schematic of the *RIBER Compact 12* growth chamber. All relevant components are labeled.

components in figure 3.1 are labeled and will be introduced in the following. The chamber is pumped to ultra-high vacuum (UHV) (10^{-10} mbar to 10^{-11} mbar) by a *HiPace 800 M* turbo molecular pump (*Pfeiffer Vacuum*). *Bayard-Alpert* gauges are used to measure the background pressure as well as the beam equivalent pressure (*BEP*) (beam flux gauge in figure 3.1). The latter is used to calibrate the material fluxes (Al, Ga, In and Ge) at the substrate position. A more detailed discussion of the *BEP* is given in section 3.1.1. While Ga is supplied by a double filament effusion cell, all other materials are evaporated

in single filament effusion cells. The growth chamber is also equipped with a cooling shield filled with liquid nitrogen to thermally decouple the effusion cells and to reduce the background pressure. A *HD25* radio frequency (RF) atom source from *Oxford Applied Research* is used to activate/crack the nitrogen that is needed for the growth of group III-nitrides. Section 4.4.1 gives an in depth analysis of the particular atom source used in the present experiments. The effusion cells are equipped with pneumatic shutters to selectively supply different materials. The temperatures of the cells as well as the substrate are regulated by *Eurotherm 3216* PID controllers. A tantalum heater filament encapsulated in pyrolytic boron nitride is used to heat the substrates by thermal radiation. The substrate temperature is measured through a quartz glass viewport using a pyrometer located in line of sight beneath the substrate. For this purpose, a *SensoTherm Metis MI 16* pyrometer operating at a wavelength of $1.6 \mu\text{m}$ is used. During growth, up to four $1 \times 1 \text{ cm}^2$ substrates can be placed in a tantalum substrate holder which is rotated during the growth process.

In-situ characterization of the sample surface is carried out with a reflection high energy electron diffraction (RHEED) system from *StaiB Instruments*, using an acceleration voltage of 15.5 kV at a filament current of 1.55 A . The electrons are directed onto the sample surface at a small angle and a fluorescence screen is used to visualize the diffraction pattern of the reflected electrons. While this is a versatile technique to study the growth of smooth 2D layers in detail, the application for the 3D growth of GaN NWs is limited. However, the time needed for NW nucleation is accessible by RHEED and can be used to compare the growth conditions of consecutive growth runs. It gives a rough estimation whether or not the applied growth conditions changed compared to previous growth experiments.

3.1.1 Flux and beam equivalent pressure

During his experiments with mercury [45, 46], Martin Knudsen described its evaporation behaviour. An effusion cell that exhibits the same basic evaporation dynamics is therefore called a *Knudsen cell*. In contrast to the effusion cells used here, such a *Knudsen cell* has an aperture plate of negligible thickness and a small opening area A . The material flux (atoms/s) coming out of this type of effusion cell is given by equation 3.1 [47].

$$\Gamma = A(p_{eq} - p_{bg}) \cdot \sqrt{\frac{N_a}{2\pi M k_B T}} \quad (3.1)$$

Besides the vapor pressure p_{eq} (in Torr) of the material to be evaporated at the cell temperature T , its background partial pressure inside the chamber p_{bg} has to be considered. The latter can be neglected in an UHV environment. Further, Avogadro's number N_a as

well as the Boltzmann factor k_B and the molecular mass M of the evaporated material contribute to equation 3.1. The mean free path of the atoms leaving the effusion cell has to be at least ten times larger than the diameter of the aperture opening for equation 3.1 to be valid. The mean free path of Ga atoms at a cell temperature of 950 °C and $p = 10^{-5}$ mbar ($d_{Ga} = 249$ pm [48]) can be estimated to 61 m using equation 3.2 [49].

$$\lambda = \frac{k_B T}{\sqrt{2} \pi d^2 p} \quad (3.2)$$

Therefore, at the applied growth conditions ($p_{N_2} \approx 10^{-5}$ mbar) the large mean free path of the atoms yields a ballistic transport of the evaporated material to the substrate surface. Equation 3.1 requires knowledge of the actual temperature of the evaporated material as well as the vapor pressure inside the effusion cell. However, both is not reliably accessible in a MBE setup. The earlier mentioned BEP is therefore used as a measure for the material fluxes at a given cell temperature. It is determined by putting the beam flux gauge (cf. section 3.1) in the position of the substrate and measuring the pressure produced by an individual effusion cell. As an example, the calibration curve of the Ga cell is given in figure 3.2. The BEP follows the Arrhenius equation $BEP \propto \exp(E_A/k_b T)$ with a thermal

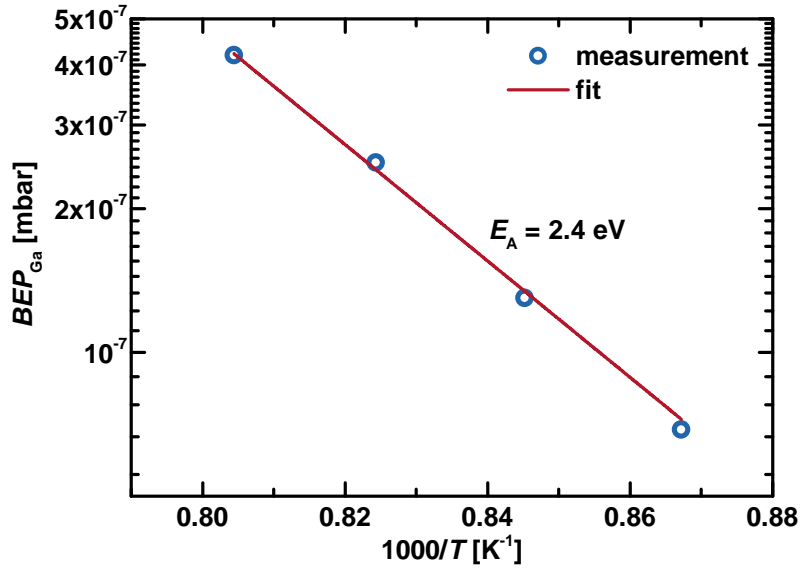


Figure 3.2: Example of a calibration of the Ga effusion cell. Blue symbols represent measurements and the red line is an exponential fit to the data.

activation energy of 2.4 eV extracted from an exponential fit to the data points which only differs slightly from the expected enthalpy of vaporization of Ga (2.65 eV [50]). Frequent calibrations of the effusion cells are necessary to ensure reproducible growth conditions as

the cell characteristics change over time. Exemplary calibrations for all effusion cells used can be found in appendix A.1.

3.2 Atomic force microscopy

An *SmartSPM 1000* from *AIST-NT* was used to determine the surface roughness of the Si(111) substrates and the TiN layers used for the PCG of GaN NWs discussed in chapter 7. The atomic force microscopy (AFM) was operated in tapping mode, where the cantilever is driven to oscillate and the distance between cantilever and sample is adjusted to keep the oscillation amplitude constant yielding the topography of the sample.

3.3 Electron microscopy

In the following, scanning electron microscopy (SEM) and transmission electron microscopy (TEM) techniques that were used to characterize the NW samples will be described. In addition, the SEM setup was used to transfer nanohole patterns to Ti thin films by electron beam lithography (EBL) for the PCG of GaN NWs on Si(111) (cf. chapter 7).

3.3.1 Scanning electron microscopy and electron beam lithography

A *JEOL JSM-7001F* equipped with a secondary electron detector was used to characterize the NW morphology (diameter, density and length). The standard operating parameters were an acceleration voltage of 15kV and an emission current of 50 μ A. Since the NWs as well as the Si(111) substrates were conductive, no special sample preparation was necessary before SEM characterization. Some samples were cleaved to obtain side view images of the NWs.

The SEM is equipped with a *XENOS XeDraw2* upgrade which enables sample patterning by writing the desired structure with the electron beam into an electron sensitive resist. In the present case, the negative resist *ma-N 2401* and the developer *ma-D 331* from *microresist technology* were used. Details on the nanohole mask processing for the PCG of GaN NWs can be found in appendix A.2.

3.3.2 Transmission electron microscopy

Due to the small diameter of the group III-nitride NWs investigated in this work, the preparation for TEM analysis is simplified. The NWs were dispersed onto a TEM grid that consists of a thin carbon film fixed by a copper grid. With TEM, the NWs can be analyzed down to atomic resolution. Therefore, TEM is not only an excellent tool for the analysis of the geometry of NDs but even allows the direct determination of the crystal polarity [41]. A TEM can be operated in diffraction or imaging mode. In the former, the diffraction

pattern of the transmitted electron beam is analyzed, yielding information on the crystal structure of the analyzed sample. In imaging mode, the transmitted electrons are focused by an electron optic to generate the image of the investigated structure. Different imaging modes are available in scanning transmission electron microscopy (STEM), namely bright field (BF) and dark field (DF) imaging. Typically, the detectors are circularly shaped and the imaging modes are accordingly referred to as annular bright field (ABF) and high angle annular dark field (HAADF). The respective detectors are mounted on the optical axis of the microscope (cf. figure 3.3). Transmitted electrons are collected under a high angle on

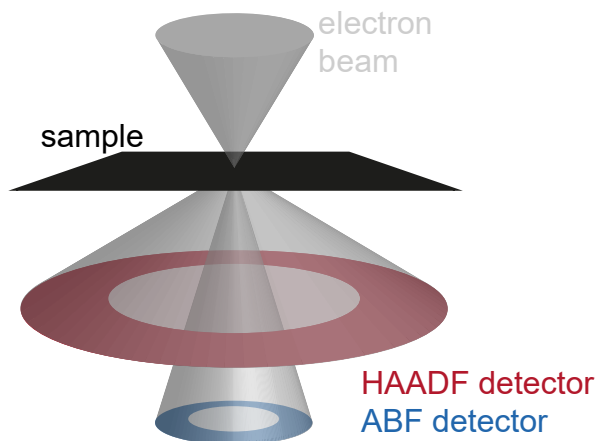


Figure 3.3: *Schematic of a STEM which is equipped with an ABF and a HAADF detector.*

a ringlike detector during HAADF imaging. These electrons are elastically scattered due to interaction with phonons which allows for high Z-contrast (intensity $\propto Z^2$) in HAADF mode and gives excellent information about the chemical composition of the NWs [51]. Therefore, HAADF imaging was used to analyze the structural properties of the AlN/GaN NWs ($\text{In}_x\text{Ga}_{1-x}\text{N}/\text{GaN}$ NWs) presented in chapter 5 (chapter 6). In the case of the $\text{In}_x\text{Ga}_{1-x}\text{N}/\text{GaN}$ NWs, HAADF intensities were compared to calculations, based on the model of Rosenauer and Schowalter [52], to retrieve information about the In content in the $\text{In}_x\text{Ga}_{1-x}\text{N}$ section of the NWs¹. However, HAADF is not suitable to resolve lighter atoms such as the nitrogen in vicinity of heavier atoms like the metal atoms in the group III-nitrides [53]. For this purpose, ABF STEM imaging is used which enables to determine the crystal polarity of group III-nitride NWs directly by resolving the metal-nitrogen bilayers of the crystal [41]. In ABF, the image is the result of the wave interference of the elastically scattered electrons with a negligible contribution from thermal diffuse scattering

¹TEM analysis of the $\text{In}_x\text{Ga}_{1-x}\text{N}/\text{GaN}$ NWs and intensity calculations were performed by Katharina Gries in the group of Prof. Kerstin Volz at the Faculty of Physics and Materials Science Center of the Philipps-Universität Marburg.

by phonons. A STEM can also be equipped with a detector for energy dispersive X-Ray spectroscopy (EDX) measurements. In addition to qualitative information about the incorporated elements, EDX also allows the determination of absolute element concentrations. This was exploited to extract the Ge concentration from highly doped GaN:Ge NWs [54] and to determine the In distribution in $\text{In}_x\text{Ga}_{1-x}\text{N}/\text{GaN}$ NWs. A *Philips EM30* TEM was used for the non-holographic TEM analysis of the $\text{In}_x\text{Ga}_{1-x}\text{N}/\text{GaN}$ NDSLs presented in chapter 6, section 6.2.

3.4 Photoluminescence spectroscopy

Photoluminescence spectroscopy techniques allow to study the optical properties of semiconductors, for example revealing information about impurities, structural defects, excitonic states and details on the electronic band structure. A laser with a photon energy larger than the material band gap is used for excitation. Electron-hole pairs are generated in the semiconductor upon excitation and thermalize to the lowest available energetic states. After thermalization, the carriers either recombine radiatively, contributing to the PL signal, or non-radiatively. In the former case, the energy of the emitted light depends on the recombination path of the carriers, some of which are schematically shown in figure 3.4. One possibility is the direct recombination of electrons and holes (e, h) after thermalization. If the electron is trapped by the potential of a donor and the hole by that of an acceptor, DAP transitions are observed. Also, the carriers can be electrostatically bound to form an exciton with a binding energy E_{bind} . The recombination of a free exciton (FX) is detected at $E = E_{gap} - E_{bind}$. Excitons can also be trapped by the donor and acceptor potentials which further reduces the transition energy by the localization energy of the exciton E_{loc} . Cryogenic temperatures have to be used in PL experiments to observe excitons in GaN, due to their small exciton binding energy of 21 meV. Hence, most of the experiments were conducted in the temperature range of 4 K to 10 K. Three different setups (*Setup A*, *Setup B* and *Setup C*) were used for continuous-wave (CW) PL experiments. A HeCd laser ($\lambda = 325$ nm) was used as an excitation source in all setups if not otherwise mentioned. Time-resolved (TR) PL measurements presented in chapters 5 and 6 were conducted by Nils Rosemann and Vanessa Dahmen in the group of Prof. Dr. Sangam Chatterjee at the Philipps-Universität Marburg² as well as by Dr. Mark Beeler, Dr. Joel Bleuse and Dr. Eva Monroy at the Université Grenoble Alpes³ and CEA-Grenoble⁴. The TR-PL experiments

²Faculty of Physics and Materials Science Center, Philipps-Universität Marburg, Renthof 5, 35032 Marburg, Germany

³Université Grenoble Alpes, 38000 Grenoble, France

⁴CEA-Grenoble, INAC, SP2M / NPSC, 17 av. des Martyrs, 38054 Grenoble, France

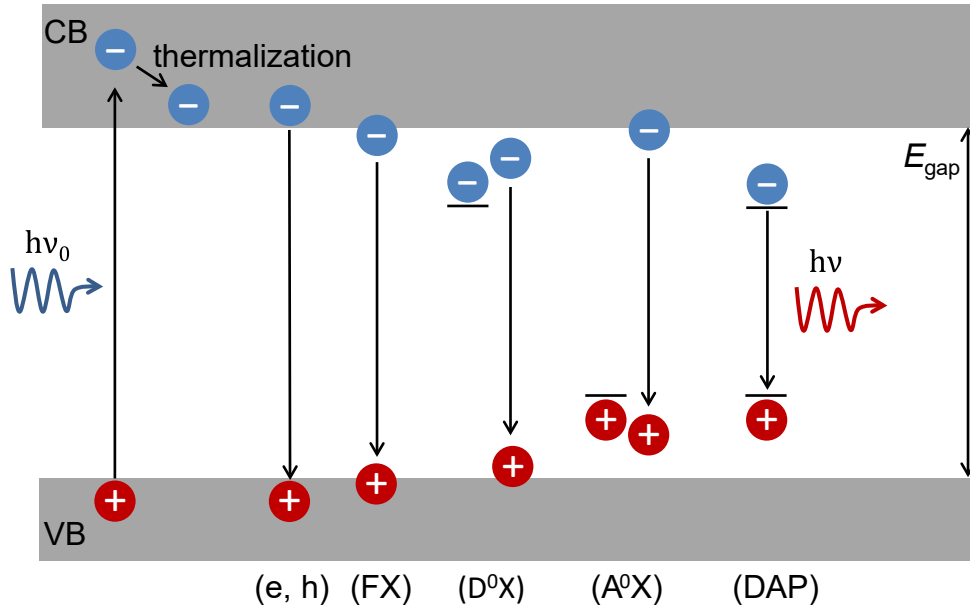


Figure 3.4: *Schematic of radiative PL transition paths. The direct recombination of electrons and holes (e, h) and the transitions of a free exciton (FX), a donor bound exciton (D^0X), an acceptor bound exciton (A^0X) as well as a DAP transitions are sketched.*

presented in chapter 5, section 5.2 were performed by Sarah Kristina Schlichting and Dr. Gordon Callsen in the group of Prof. Dr. Axel Hoffmann at the Technische Universität Berlin⁵

Setup A

Figure 3.5 displays a schematic of PL *Setup A*. The laserlight is modulated by a chopper wheel ($\nu = 77\text{ Hz}$) and focused onto the sample, with a spot diameter of approximately $100\ \mu\text{m}$. The luminescence light is collected by a *Jobin Yvon THR1000* grating spectrometer, equipped with a 2400 lines/mm grating, blazed from 170 to 500 nm. Finally, the measurement signal is generated by a *Hamamatsu R375* photomultiplier and detected with a lock-in technique. A bath cryostat from *Oxford Instruments* is used to perform experiments at 4K using liquid Helium.

Setup B

The second PL setup (*Setup B*) is schematically shown in figure 3.6. Laserlight is coupled into a Y-shaped optical fiber from *Ocean Optics* and collimated ($d_{\text{spot}} \approx 2\text{ mm}$) onto the

⁵Technische Universität Berlin, Institut für Festkörperphysik, Hardenbergstr. 36, 10623 Berlin, Germany

sample. The PL is collected in backscattering geometry with the same fiber and detected by a CCD camera in an *Opto Science QWave VIS* spectrometer. The samples are mounted in a *Microstat HiResII* flow cryostat from *Oxford Instruments* to be cooled down to 4K.

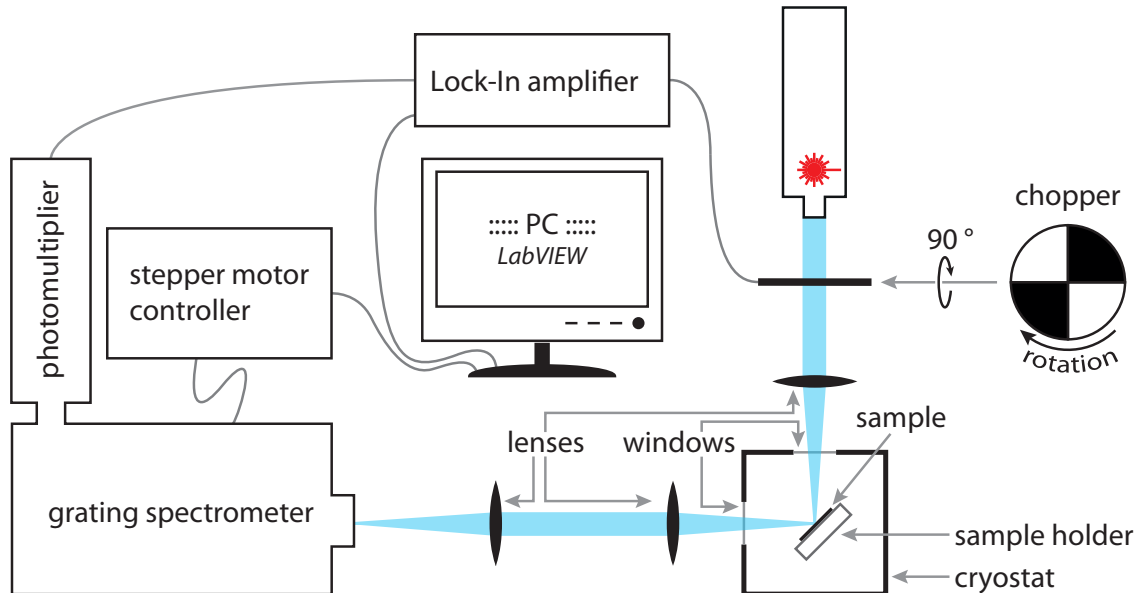


Figure 3.5: Schematic of the PL spectroscopy Setup A.

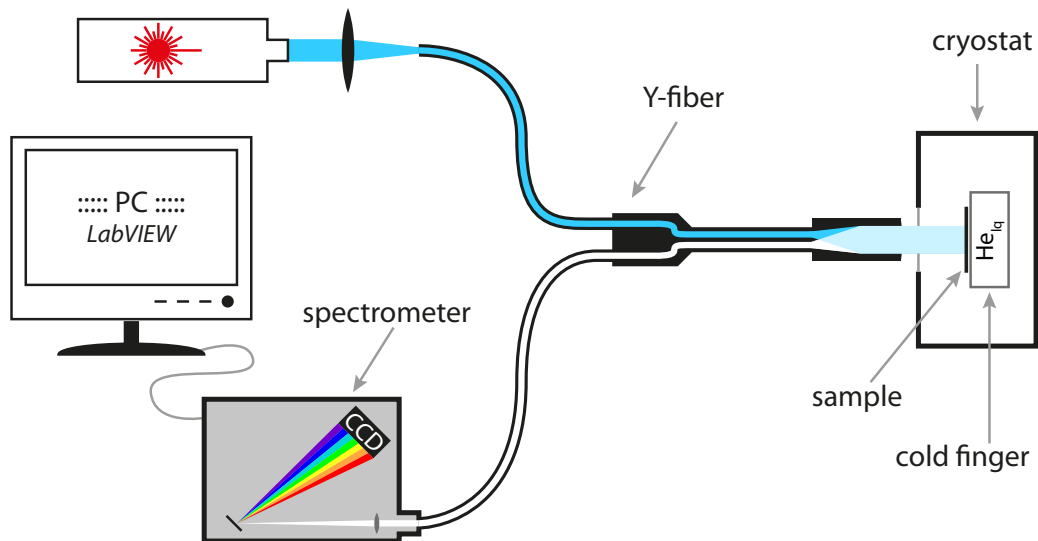


Figure 3.6: Schematic of the PL spectroscopy Setup B.

Setup C

A *Renishaw inVia Raman microscope* connected to a *Leica DM LM/P* optical microscope was used to perform micro-PL measurements. A schematic of *Setup C* is shown in figure 3.7. The spot size of this setup is $5\ \mu\text{m}$ using a 20x UV objective (0.4NA). The latter is also used to collect the PL in backscattering geometry. Afterwards the light is dispersed by a $1800\ \text{lines cm}^{-1}$ grating and detected by a CCD camera.

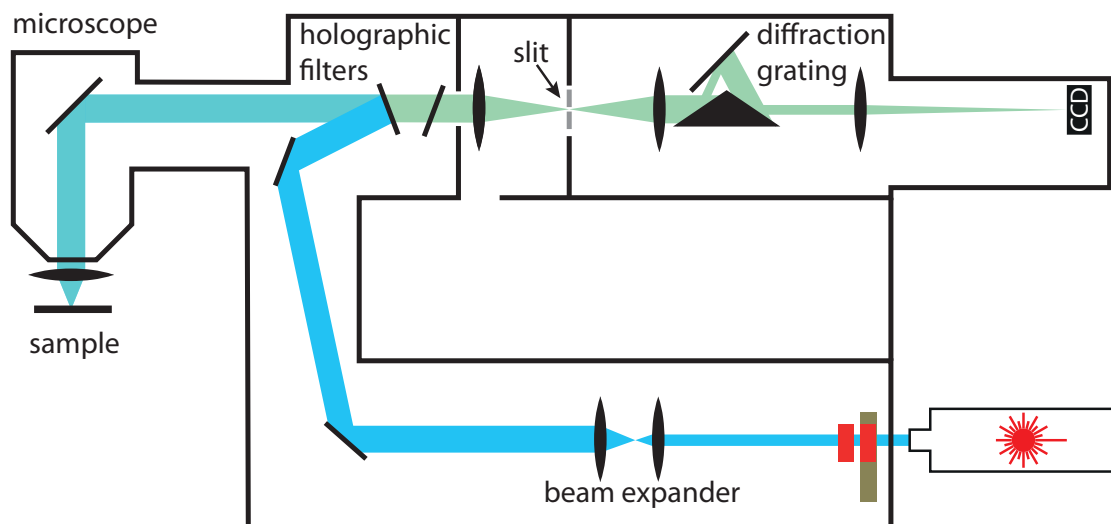


Figure 3.7: Schematic of the μ -PL spectroscopy Setup C.

3.5 X-Ray diffraction analysis

High resolution X-Ray diffraction analysis (HRXRD) analysis of the as grown NW samples was performed to assess the layer periodicity as well as ND and barrier thickness in NDSLs. Additionally, the strain state of heteroepitaxially grown layers and the composition of ternary alloys is accessibly by this non-destructive technique.

A crystal lattice consists of parallel lattice planes which are identified using the Miller indices h , k and l . Constructive interference of X-Rays diffracted by a family of lattice planes with a given h , k , l and a lattice spacing d_{hkl} (cf. figure 3.8) is described by Bragg's law according to

$$\lambda = 2 \cdot d_{hkl} \cdot \sin\theta \quad (3.3)$$

Hence, incident angles θ can be found at a given wavelength λ and lattice plane distance d_{hkl} for which equation 3.3 is fulfilled. This is used in XRD experiments to analyze the structural properties of crystalline samples. A graphical illustration of Bragg's law is given in figure 3.8.

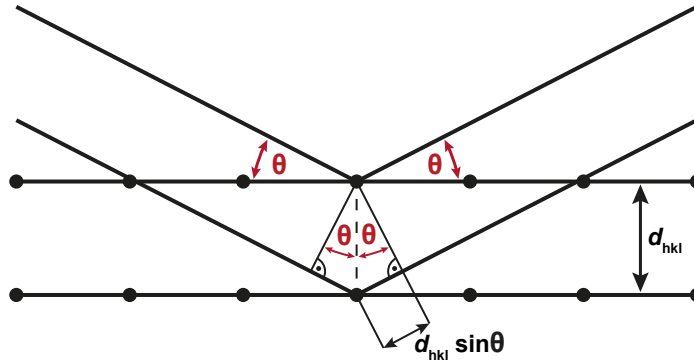


Figure 3.8: *Illustration of Bragg's law.*

For a hexagonal crystal lattice, d_{hkl} can be written as

$$d_{hkl} = \frac{a}{\sqrt{\frac{4}{3}(h^2 + hk + k^2) + \frac{a^2}{c^2}l^2}} \quad (3.4)$$

In equation 3.4, a and c are the lattice parameters. The crystal lattice can be transformed into reciprocal space where each family of planes with distinct values of h , k and l is represented by a point also described by the Miller indices. Analogous to the real space, the reciprocal space is constructed using primitive reciprocal lattice vectors \mathbf{b}_i that can be

linearly combined to a reciprocal lattice vector \mathbf{G} according to

$$\mathbf{G} = h\mathbf{b}_1 + k\mathbf{b}_2 + l\mathbf{b}_3 \quad (3.5)$$

Introducing the wave vectors \mathbf{k}_i , Bragg's law can be expressed by reciprocal lattice vectors according to the Laue conditions using the incident \mathbf{k}_{in} and diffracted \mathbf{k}_{diff} waves:

$$\mathbf{G} = \mathbf{k}_{diff} - \mathbf{k}_{in} = \mathbf{k}_{hkl} = h\mathbf{b}_1 + k\mathbf{b}_2 + l\mathbf{b}_3 \quad (3.6)$$

Here, \mathbf{k}_{hkl} represents the scattering vector. Figure 3.9b) illustrates the diffraction condition for the (102)-reflex. The angle between \mathbf{k}_{in} and \mathbf{k}_{diff} is defined to be 2θ and Ω is the

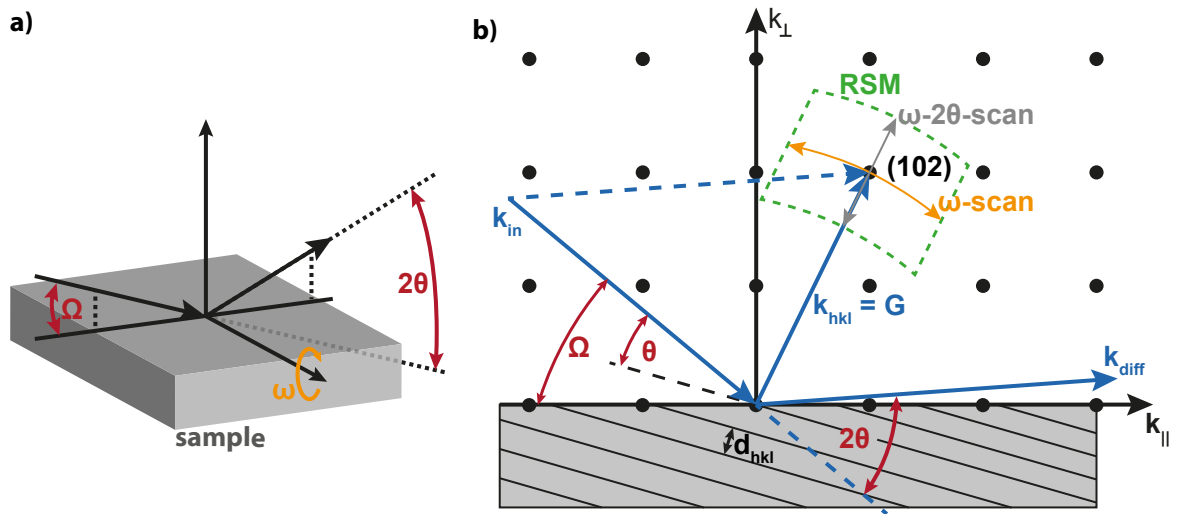


Figure 3.9: a) Schematic of the measured sample and the rotation axis for an ω -scan. Incident and outgoing X-Rays as well as the angles Ω and 2θ are indicated. b) Illustration of the Laue condition in the $(h0l)$ -plane for the (102)-reflex. The upper part of the schematic represents the reciprocal space while the lower part shows the sample including the lattice planes with the distance d for the given hkl . In addition, the scan directions for a ω - and a ω - 2θ -scan are indicated. The area scanned during the measurement of a RSM is framed in green.

angle between the sample surface and \mathbf{k}_{in} . Scattering vectors can be described by a linear combination of a vector parallel \mathbf{k}_{\parallel} and perpendicular \mathbf{k}_{\perp} to the sample surface. Knowing Ω and 2θ , k_{\parallel} and k_{\perp} are calculated according to

$$k_{\parallel} = \frac{2\pi}{\lambda} (\cos(2\theta - \Omega) - \cos(\Omega)) \quad (3.7)$$

$$k_{\perp} = \frac{2\pi}{\lambda} (\sin(2\theta - \Omega) + \sin(\Omega)) \quad (3.8)$$

By definition, symmetrical reflexes ($\Omega = \theta$) are found on the k_{\perp} axis ($h = k = 0$). Knowing k_{\parallel} and k_{\perp} for a given hkl , the lattice parameters c and a of the hexagonal wurtzite lattice are given by

$$c = \frac{2\pi}{k_{\perp}}l \quad \text{and} \quad a = \frac{4\pi}{\sqrt{3}k_{\parallel}}h \quad (3.9)$$

An in depth description of XRD can be found in Ref. [55].

Two type of scan methods were employed during the experiments presented in this work. Only the sample is rotated during an ω -scan (cf. figure 3.9a)), leaving the detector at a fixed position. The sample is rotated around the angle ω and the detector position is adjusted accordingly during a ω - 2θ -scan. This method allows to scan along the direction of the vector k_{hkl} as indicated in figure 3.9b). If a sample contains a superlattice (cf. chapter 5), reflexes corresponding to this superlattice can be observed in symmetrical ω - 2θ -scans. Two neighbouring superlattice reflexes observed at θ_1 and θ_2 can be used to calculate the superlattice periodicity according to

$$d_{\text{period}} = \frac{\lambda}{2(\sin \theta_1 - \sin \theta_2)} \quad (3.10)$$

Equation 3.10 was used to extract the superlattice period of the samples presented in chapter 5. Combining ω - and ω - 2θ -scans allows to record a 2D reciprocal space map (RSM) (cf. figure 3.9b)). For this purpose, ω - 2θ -scans are performed at different ω -offsets. Typically, RSMs are recorded on asymmetrical reflexes to reveal information about the strain state of heterostructures and by that also access reliable information on the chemical composition in, *exempli gratia*, ternary group III-nitrides. In chapter 6, RSMs were used to determine the In concentration in $\text{In}_x\text{Ga}_{1-x}\text{N}/\text{GaN}$ NWHs. A *PANalytical X'Pert PRO MRD* setup with a copper anode was used for the XRD experiments presented in this work. Evaluation of the measurements was carried out using the *X'Pert Epitaxy* software from *PANalytical*.

4 Growth of GaN nanowires on silicon

Since GaN NWs form the base of the more complex NWHs which are presented later in this work, a deep understanding of the underlying growth process is mandatory. The self-assembled growth of GaN NWs is introduced in the following while the PCG will be discussed in chapter 7. Morphological properties of the grown NWs were analyzed by SEM, whereas the optical properties were studied by analysis of the PL spectra recorded on NW ensembles as well as by μ -PL spectroscopy performed on single nanowires (SNWs).

4.1 Fundamentals of the GaN nanowire growth

Semiconductor NWs were introduced by Wagner and Ellis who fabricated Si NWs using a newly developed vapour-liquid-solid (VLS) process in 1964 [56]. For this growth method, metal droplets are required as nucleation sites liquid at the desired growth temperature. These metal droplets absorb the precursors from the gas phase which leads to the formation of a liquid alloy. Nucleation (growth) of the NWs commences at the liquid-solid interface to the substrate (NW) upon supersaturation of the formed alloy droplet. A VLS process can also be applied for the PAMBE growth of compound semiconductors, *exempli gratia*, group III-V NWs. Self-catalytic growth using a liquid Ga-droplet is feasible for the realization of GaAs NWs [57, 58] while GaN NWs can be grown from Ni-droplets [59]. In contrast, GaN NWs can also be grown self-assembled on Si(111) by PAMBE, in absence of any additional catalyst material [4, 5, 60]. The self-assembled growth mode differs from the self-catalytic growth mode as no metal droplets form to initiate growth [61]. A direct comparison of self-assembled and catalytically grown GaN NWs revealed that the use of Ni as a catalyst has a detrimental effect on the optical and structural properties of the NWs [62]. The self-assembled growth has, therefore, been established as the standard process for the fabrication of group III-nitride NWs by PAMBE and has also been used for the NWs presented in the current chapter as well as the NWHs studied in chapters 5 and 6.

At a fixed substrate temperature, different growth windows exist for GaN which result in different sample morphologies. These growth windows depend on the metal-to-nitrogen ratio which is controlled via the metal *BEP* (cf. section 3.1.1) or the atom source operating parameters (cf. section 4.4.1). An increasing GaN growth rate is observed with an increase of the BEP_{Ga} as schematically shown for a constant supply of reactive nitrogen species in figure 4.1 [4]. Three growth regimes can be identified based on figure 4.1. Starting at low BEP_{Ga} , a linear dependence of the GaN growth rate on the BEP_{Ga} is observed (labeled I in figure 4.1) indicating N-rich growth conditions ($\text{III}/\text{V} < 1$). Afterwards, the

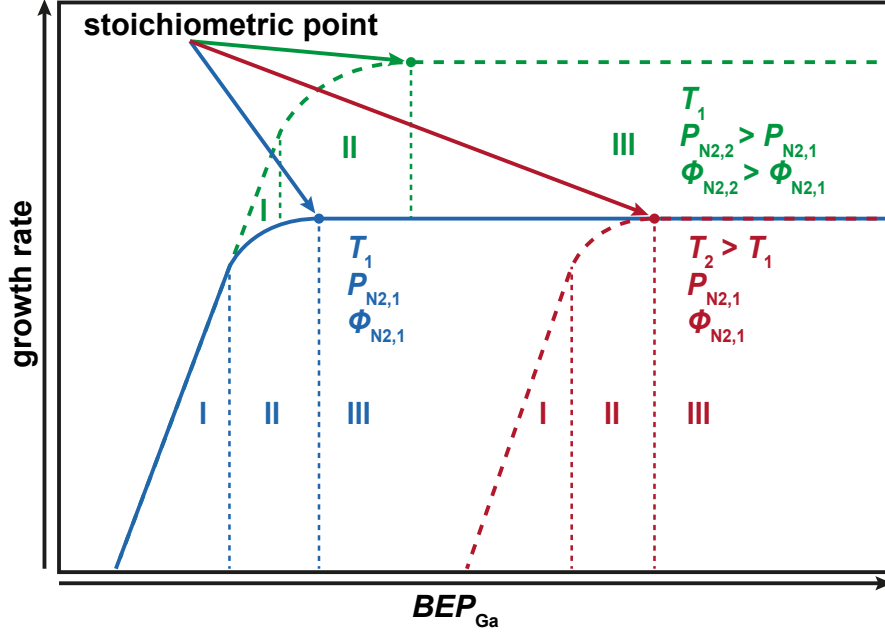


Figure 4.1: Schematic dependence of the GaN growth rate on the BEP_{Ga} . The graph is divided into three growth regimes (I, II and III) and the stoichiometric point ($III/V \approx 1$) is marked by an arrow. The blue line represents growth with the lowest temperature T_1 and the lowest amount of reactive nitrogen species ($P_{N2,1}$, $\Phi_{N2,1}$). An increase of the substrate temperature is assumed for the red line ($T_2 > T_1$) while an increase of the supplied nitrogen is assumed for the green line ($P_{N2,2} > P_{N2,1}$, $\Phi_{N2,2} > \Phi_{N2,1}$).

GaN growth rate depends sublinearly on BEP_{Ga} (labeled II in figure 4.1). This marks the transition region from N-rich to saturated Ga-rich growth. At the stoichiometric point (arrows in figure 4.1), the III/V ratio is close to unity and the growth rate saturates for higher Ga fluxes (labeled III in figure 4.1). In this regime, all the supplied reactive nitrogen is incorporated into the crystal lattice. Layer-by-layer growth of GaN is observed close to the stoichiometric point [63]. However, smooth two dimensional layers without metal accumulation can also be grown at slightly Ga-rich conditions when the GaN surface is covered by a Ga-bilayer which results in the step-flow growth of GaN layers [64]. For higher BEP_{Ga} , Ga droplets are observed in post growth analysis [64, 65] which limits the range of Ga fluxes feasible for the growth of high quality GaN layers. In contrast, N-rich growth conditions lead to the growth of rough layers [64–67]. Gallium nitride NWs are also grown under N-rich growth conditions, however, the substrate temperature is raised to values around 800 °C compared to the growth temperatures around 730 °C used for the layer fabrication. The higher substrate temperatures lead to a further enhancement of Ga adatom diffusion and desorption during the growth of GaN NWs. The diffusion of Ga

adatoms towards the NW tip has been reported to be the driving mechanism of the GaN NW growth [68,69] resulting in high aspect ratios. In addition, Consonni et al. proposed a high nucleation energy of 5.44 eV compared to a desorption energy of 2.75 eV prevents GaN nucleation on the NW sidewalls [69]. Successful growth of GaN NWs was carried out in a large range of III/V ratios, reaching from 1/3 [37] down to 1/125 [5]. At constant BEP_{Ga} , the effective III/V ratio decreases at the higher growth temperatures used for the fabrication of GaN NWs compared to GaN layers. Consequently, the three growth regimes are shifted to higher values of BEP_{Ga} . This is schematically shown in red in figure 4.1 ($T_2 > T_1$). An increase of the reactive nitrogen species (increasing forward power P_{N_2} and/or nitrogen flux Φ_{N_2}) also modifies the growth regimes [70,71]. In this case, the transition points are shifted to higher BEP_{Ga} and the maximum growth rate increases due to the absolute increase of available nitrogen (green in figure 4.1).

Self-assembled GaN NWs grow in the $[000\bar{1}]$ -direction of the wurtzite crystal lattice and the NW sidewalls are formed by $(10\bar{1}0)$ -planes due to minimization of the free-surface-energy [72]. Lateral growth is strongly suppressed and diffusion of Ga adatoms is reported to play a major role in sustaining such a low lateral growth rate during PAMBE growth [68]. Tchernycheva et al. reported the radial-to-axial growth rate ratio to be controllable in the range from 1 % to 10 % via the III/V ratio [73] while Furtmayr et al. found a value of 2 % for a III/V ratio of 1/3 [60]. However, while diffusion over the whole NW length on the scale of μm is reported [59,60], Lymperakis et al. theoretically predicted Ga diffusion along the c -direction on the NW sidewalls to be hindered [74]. The latter is in line with relatively low diffusion lengths of less than 100 nm reported by Debnath and Consonni et al. [68,69]. In addition, the possibility of stabilizing impinging reactive nitrogen species (N and N_2^*) plays an important role in defining the shape of GaN NWs. It is difficult to stabilize adsorbing nitrogen on the NW m -plane sidewalls [74] but stabilization is possible on the $(000\bar{1})$ growth front of the GaN NWs [75,76] promoting their axial growth. Further, the nucleation energy on the NW sidewalls is by a factor of two higher than the desorption energy of Ga adatoms [69]. Hence, Ga atoms either reach the NW tip through surface diffusion or desorb from the m -plane surface before they can contribute to a lateral growth of the NW. Readsorption by and subsequent desorption from neighboring NWs can transport Ga atoms to the NW tip where they can be efficiently incorporated into the crystal. In conclusion, the growth kinetics and columnar shape of GaN NWs depend on the interplay of adatom diffusion and desorption as well as nitrogen stabilization under the premiss of N-rich growth conditions. The possibility of N adatoms forming covalent bonds with surface N atoms of the GaN crystal which afterwards desorb as N_2 [74] even introduces the GaN decomposition

as a competing mechanism to the crystal formation. While thermally activated diffusion and desorption processes can be controlled via the substrate temperature, the composition of the arriving nitrogen species depends on the atom source operating parameters (cf. section 4.4.1). Together with the BEP_{Ga} , the latter also determine the overall III/V ratio, which in turn affects the growth regime. In the experimental section of this chapter the influence of the BEP_{Ga} and the composition of the nitrogen plasma on the structural and optical properties of GaN NWs is studied in detail.

4.2 Substrate preparation and GaN nanowire growth

Self-assembled growth of GaN NWs was performed on Si(111) substrates at temperatures of 790 °C to 800 °C [54]. The natural silicon oxide layer on the substrate was removed by HF dipping¹ prior to the deposition process. After heating the substrates to the growth temperature, the characteristic 7×7 reconstruction, an indication for a clean silicon surface, was observed by RHEED (cf. figure 4.2a)). Before the gallium shutter was opened, the

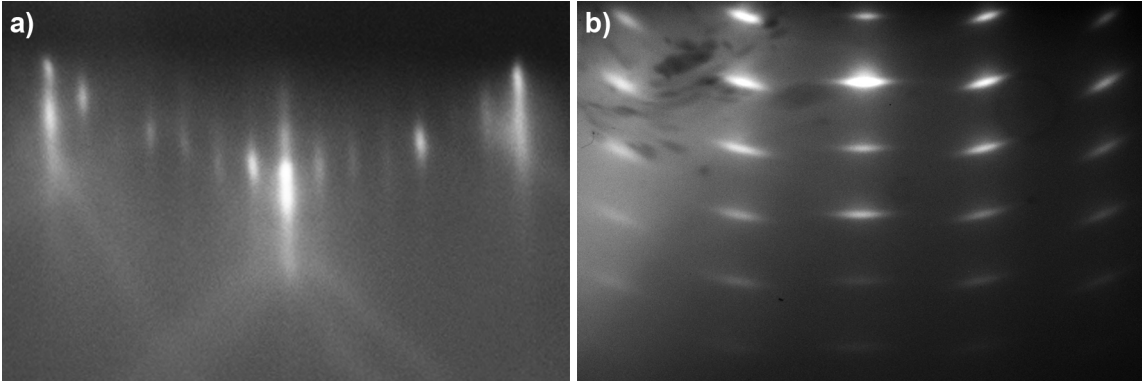


Figure 4.2: *The RHEED patterns of the 7×7 reconstruction of Si(111) and the three dimensional GaN NW growth are shown in a) and b), respectively.*

silicon surface was nitridated for 15 min by opening the shutter of the atom source which was operated at a forward power $P_{\text{N}_2} = 400 \text{ W}$ and a nitrogen flux $\Phi_{\text{N}_2} = 1 \text{ sccm}$. This nitridation step leads to the formation of an approximately 2 nm thick amorphous silicon nitride layer which is essential for the nucleation of the GaN NWs [60]. Furtmayr et al. assumed that local strain fields between the Si(111) substrate and the thin Si_xN_y layer lead to the formation of mobile Si interstitials within the substrate. This assumption was based on the observation of Si diffusion from substrate into the GaN NW base region [60]. All distinct RHEED reflexes vanish during the formation the amorphous Si_xN_y surface leaving a homogeneous fluorescence of the phosphorous screen. After nitridation, the shutter of

¹10%, Supplier: *AppliChem GmbH*

the nitrogen source was closed to adjust P_{N_2} and/or Φ_{N_2} according to the desired growth conditions of the GaN NWs. The substrate was exposed to the Ga and N fluxes by opening the respective shutters simultaneously in order to initialize the NW growth. When GaN NW nucleation occurs, the RHEED pattern depicted in figure 4.2b) begins to form. Instead of a streaky pattern which is observed for smooth layers, the occurrence of elongated dots indicates the three dimensional NW growth. After observing the first spots, the RHEED pattern evolves until the amount and intensity of the reflexes saturates, indicating a saturation of the NW density [77]. The time span between the opening of the shutters and the first NW nucleation is defined as the nucleation time (t_{nucl}) while the incubation time (t_{inc}) also includes the time needed to saturate the NW density. After t_{inc} , GaN NWs grow with a constant lateral and axial growth rate. The evolution of the NW length with growth time is presented in figure 4.3. All samples were grown with $BEP_{\text{Ga}} = 3 \times$

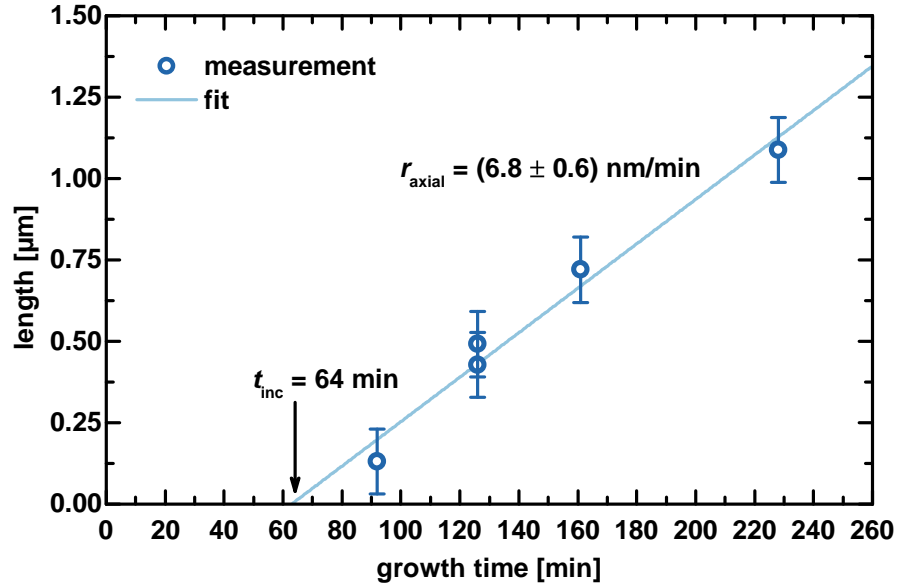


Figure 4.3: The length of the GaN NWs is plotted against the growth time after opening the Ga and N shutters. Symbols represent measurement data and a linear fit is represented by the solid line.

10^{-7} mbar, $P_{N_2} = 400$ W and $\Phi_{N_2} = 0.4$ sccm. An axial growth rate of (6.8 ± 0.8) nm/min is determined from a linear fit to the measurement data. In addition, the intercept of the fit and the abscissa gives an estimate for t_{inc} . In this case, t_{nucl} and t_{inc} were 40 min and 64 min, respectively. A list of the samples used for those experiments is given in appendix A.3. As mentioned before, lateral growth is strongly suppressed for the applied GaN NW growth conditions. However, the NW radius also increases linearly over time, but with

a comparably small growth rate which is two orders of magnitude lower than the axial growth rate. The lateral NW growth can lead to the coalescence of neighboring NWs which increases the total NW radius and facilitates the formation of structural defects in the coalescence region [78]. Hence, the III/V ratio should be optimized to minimize the occurrence of NW coalescence leading to thinner NWs with a lower density of structural defects. The investigation and discussion of the influence of the BEP_{Ga} , P_{N_2} and Φ_{N_2} on the structural and optical properties of GaN NWs is given in the following sections of this chapter.

4.3 Variation of the gallium flux

The total impinging Ga flux is directly proportional to the BEP_{Ga} . After adsorption, the Ga adatoms diffuse over the substrate and NW sidewalls to be incorporated into the (000 $\bar{1}$) tip surface or they can desorb. Diffusion and desorption are controlled by the substrate temperature and, therefore, the effective flux of Ga which is incorporated into the crystal at a given nitrogen concentration is defined by a combination of BEP_{Ga} and T_{subs} . All experiments that are presented in this section were performed at a constant T_{subs} and only the BEP_{Ga} was varied.

4.3.1 Morphology and growth rates

The dependence of the GaN NW diameter and the final NW density on BEP_{Ga} (figure 4.4a)) was evaluated. An approximately linear increase of the NW diameter, from $(29 \pm$

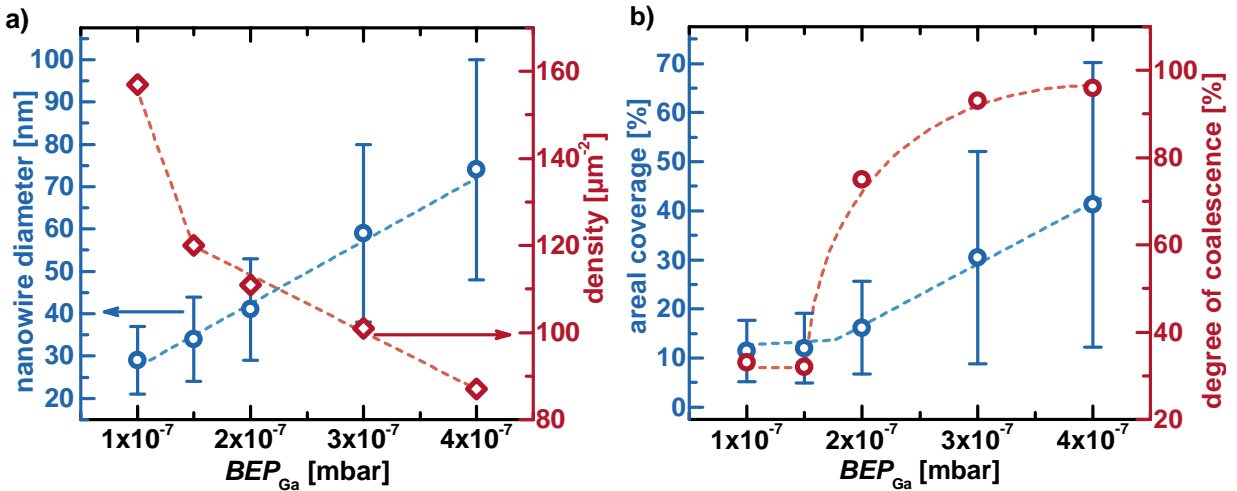


Figure 4.4: a) Evolution of the GaN NW diameter (left axis, blue symbols) and density (right axis, red symbols) with the BEP_{Ga} . b) Variation of the areal coverage (blue, left ordinate) and degree of coalescence (red, right ordinate) with BEP_{Ga} . Dashed lines were added to guide the eye.

8) nm for $BEP_{\text{Ga}} = 1 \times 10^{-7}$ mbar to (74 ± 26) nm for $BEP_{\text{Ga}} = 4 \times 10^{-7}$ mbar was observed. The final NW density decreases with increasing BEP_{Ga} from 157 to $87 \mu\text{m}^{-2}$. This final density, however, does not necessarily represent the initial NW nucleation density as many adjacent GaN nuclei can merge into one NW which is schematically shown for the yellow framed NW in figure 4.5b). Figure 4.5a) and figure 4.5b) show the top view SEM images of a

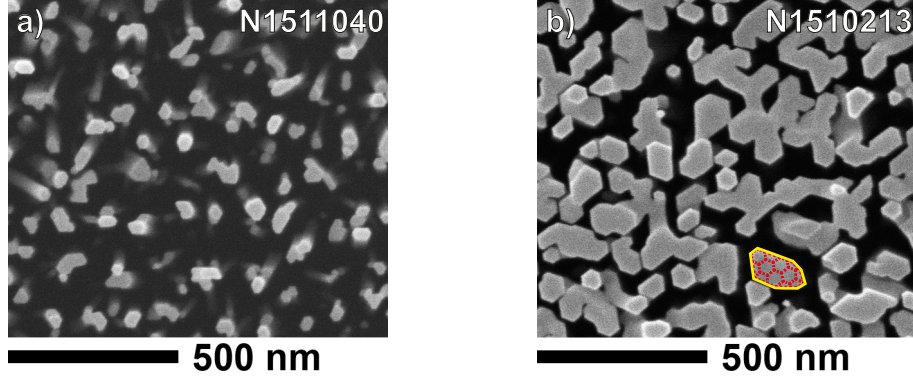


Figure 4.5: Top view SEM images of GaN NW samples grown with a) $BEP_{\text{Ga}} = 1.5 \times 10^{-7}$ mbar (N1511040) and b) $BEP_{\text{Ga}} = 4 \times 10^{-7}$ mbar (N1510213). The merging of several NW nuclei (red) into one final NW (yellow) is schematically shown for one of the NWs in b).

sample grown with $BEP_{\text{Ga}} = 1.5 \times 10^{-7}$ mbar and $BEP_{\text{Ga}} = 4 \times 10^{-7}$ mbar, respectively. An increase of the degree of coalescence with BEP_{Ga} is apparent from figure 4.5. The degree of coalescence was determined by dividing the number of visibly coalesced NWs by the total number of investigated NWs (figure 4.4b)) which yields values of 32% and 96% for the samples shown in figure 4.5a) and figure 4.5 b), respectively. However, to access information about the initial nucleation density, knowledge about the NW nucleation probability is required. With increasing BEP_{Ga} , t_{nucl} decreases (figure 4.6a)) and, therefore, the nucleation probability increases which should affect density of NW nuclei. In turn, a larger areal coverage by NWs is observed for increasing BEP_{Ga} (decreasing t_{nucl}) as demonstrated in figure 4.4b). The areal coverage was calculated by multiplying the mean NW area by the final NW density. Hence, the final NW density observed for increasing BEP_{Ga} is due to an increasing initial NW density (reduced inter NW distance) which leads to the early coalescence of adjacent NW nuclei yielding an increased areal coverage, NW diameter and degree of coalescence.

Additionally, the axial and lateral growth rates (r_{axial} and r_{lateral}) were determined by fixing the growth time and extracting r_{axial} and r_{lateral} with respect to t_{nucl} (figure 4.6b)). The axial growth rate increases from 3.3 to 9.3 nm/min, whereas the radial growth rate

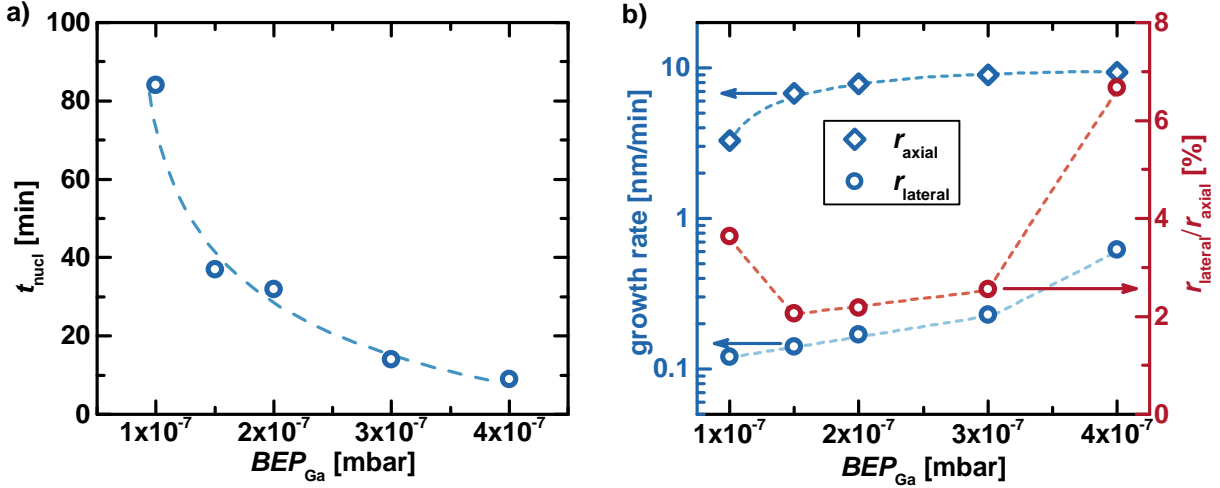


Figure 4.6: a) Dependence of t_{nucl} on BEP_{Ga} . b) Dependence of r_{axial} (left axis, blue diamonds) and $r_{lateral}$ (left axis, blue circles) as well as the ratio $r_{lateral}/r_{axial}$ (right axis, red symbols) on BEP_{Ga} . Dashed lines were added to guide the eye.

is increased from 0.12 to 0.62 nm/min when BEP_{Ga} is raised from 1×10^{-7} mbar to 4×10^{-7} mbar (figure 4.4b)). Between $BEP_{Ga} = 1.5 \times 10^{-7}$ and $BEP_{Ga} = 3 \times 10^{-7}$ mbar, the radial-to-axial growth rate ratio only slightly increases from 2 to 2.6 %. For the lowest and highest investigated BEP_{Ga} , 1×10^{-7} mbar and 4×10^{-7} mbar, respectively, this ratio is increased to 3.6 and 6.7 %. In the case of the former, this is due to a low axial growth rate of 3.3 nm/min which is an indication that Ga desorption starts to dominate the growth process. The strong increase of the radial growth rate in the case of the highest BEP_{Ga} also leads to an increase of $r_{lateral}/r_{axial}$. Therefore, growth should be carried out in the stable regime between $BEP_{Ga} = 1.5 \times 10^{-7}$ and 3×10^{-7} mbar, favoring lower values of BEP_{Ga} to keep the final degree of NW coalescence as well as the ratio $r_{lateral}/r_{axial}$ as low as possible.

4.3.2 Photoluminescence spectroscopy

Photoluminescence spectra of samples grown with a BEP_{Ga} of 2×10^{-7} mbar, 3×10^{-7} mbar and 4×10^{-7} mbar are shown in figure 4.7. Different linear scales were used for the abscissa, dividing the graph in subregions with an energy above and below 3.465 eV. A logarithmic scale was chosen for the intensity axis. The dominant emission in the GaN NW PL spectra stems from the neutral donor bound exciton at 3.472 eV ($D^0X_i^A$) due to the unintentional n-type doping of GaN, with silicon on a gallium site and/or oxygen on a nitrogen site. Due to a linewidth > 1 meV (4 meV for the red spectrum in figure 4.7) of the D^0X^A luminescence, the individual emissions related to O_N and Si_{Ga} donors ($\Delta E = 1$ meV [79,80]) cannot

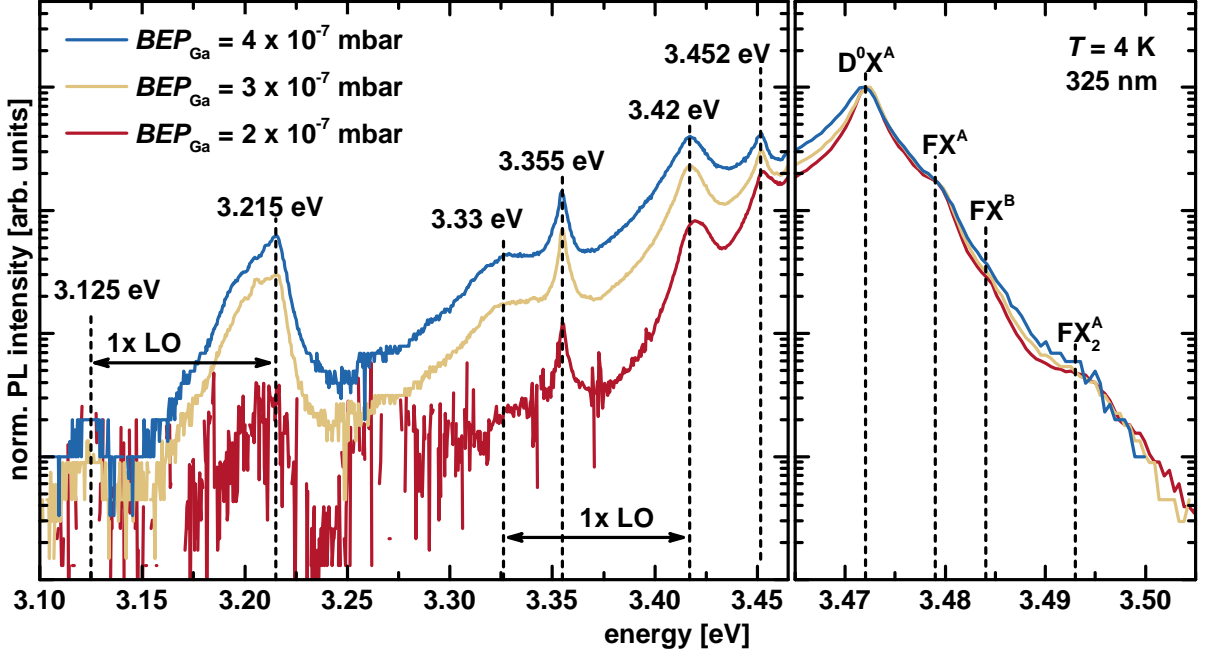


Figure 4.7: Low temperature PL spectra of three samples (N1510193, N1510203 and N1510213) grown with different BEP_{Ga} . The graph is divided in the section below the NBE regime with emission energies smaller than 3.465 eV on the left hand side as well as a detailed view of the NBE regime between 3.465 and 3.55 eV, on the right hand side. Note, that a finer energy scale of the NBE region as well as a logarithmic scale for the intensity axis were chosen to improve visibility. All spectra were normalized with respect to their emission maximum at 3.472 eV (D^0X^A). Assignments of individual emissions to the respective defects are given in the text.

be distinguished in the PL spectra in figure 4.7 ($\approx 10^6$ excited NWs). Both emissions can be observed separately in SNW PL experiments as demonstrated in figure 4.8 [54]. The $D^0X_{Si}^A$ emission is centered at 3.472 eV while the $D^0X_O^A$ gives rise to a signal at 3.471 eV, in good agreement with values reported for epitaxial GaN layers [79, 80] and GaN NWs [81]. Localisation energies of 6.5 and 7.5 meV are determined from figure 4.8 for the silicon and oxygen donor, respectively, using an emission energy of 3.4785 eV for the free exciton FX^A . Transitions of free excitons are observed at 3.479 (FX^A), 3.484 (FX^B) and 3.493 eV (excited state of the FX^A , the FX_2^A [82]) in the spectra shown in figure 4.7.

Apparent from figure 4.7 is the decreasing intensity of emission lines and signal background below the NBE regime (energy < 3.465 eV) of GaN with decreasing BEP_{Ga} . Especially, the intensity of the emission line at 3.215 eV (the longitudinal optical (LO) phonon replica is observed at 3.125 eV) is reduced by one order of magnitude when the BEP_{Ga} is decreased

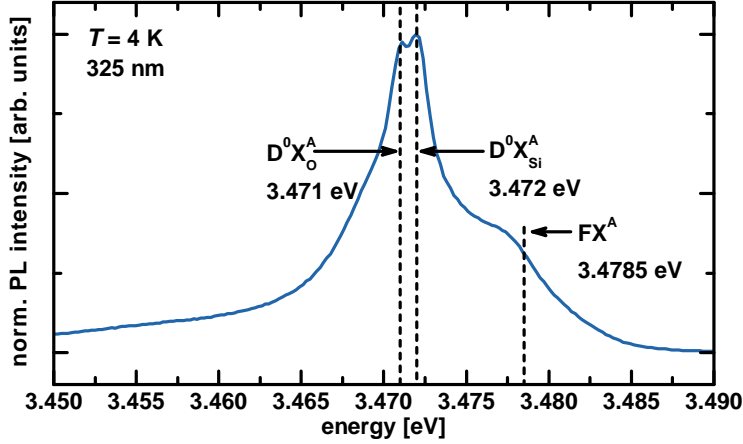


Figure 4.8: Low temperature PL spectrum of a single GaN NW (sample N1204270). Emission lines originating from excitons bound to neutral silicon and oxygen donors are labeled $D^0X_{Si}^A$ and $D^0X_O^A$, respectively. The data presented in this graph has already been published in Ref. [54].

from 3×10^{-7} to 2×10^{-7} mbar. As discussed in section 4.3.1, a stronger coalescence of neighboring GaN NWs occurs for higher values of BEP_{Ga} suggesting that this emission arises from structural defects introduced during NW coalescence as also stated in Ref. [37]. According to Reshchikov and Morçoç, the 3.215 eV emission arises from the recombination of an exciton which is bound to a point defect that is trapped by the stress field of a threading-edge dislocation [83]. The formation of dislocations at the coalescence region of GaN NWs was reported to be the main strain relieving mechanism [78] leaving dislocations to be the most probable candidate for the origin of the 3.215 eV emission line. At 3.33 eV, the LO replica of the 3.42 eV emission band is observed. The latter one has been previously assigned to a DAP transition [2] probably arising from structural defects at the substrate/NWs interface [4,37]. Finally, a sharp luminescence line was observed at 3.355 eV (cf. figure 4.7). Merely taking into account the energetic position, this could be the 1st order LO phonon line of the 3.452 eV emission which will be discussed in section 4.4.3. However, due to the small linewidth of this feature (full width at half maximum (FWHM) = 7 meV) in the present case, this assignment is not fully clear. A similar emission in the range of 3.35 eV to 3.6 eV was described in Ref. [83] and it was only observed in those N-face GaN layers which also exhibited the 3.21 eV emission band. Hence, this emission might also be assigned to excitons bound to point defects which are trapped by dislocations according to the studies of Reshchikov and Morçoç [83]. Compared to the 3.21 eV emission, those point defects contributing to the 3.355 eV line are located near the surface and, thus, the emission energy is increased. In addition, none of the investigated samples exhibited the

yellow emission band at 2.2 eV usually observed in GaN layers.

4.4 Impact of the atom source operating parameters

The presence of reactive nitrogen is necessary for the growth of group III-nitride NWs by PAMBE. However, little attention has been paid to the investigation of the atom source operating parameters and their effect on the growth of those NWs. Some reports exist, linking the measured N_2 flux [84], the optical output power [85] or the intensity of characteristic emission lines [86, 87] to the growth of GaN layers. The impact of the atom source operating parameters on GaN and $In_xGa_{1-x}N$ NWs, however, has only been discussed very briefly in literature [88–90]. The present work sheds some new light on this matter discussing the influence of the atom source operating parameters on the optical and morphological properties of GaN NWs (current section) and $In_xGa_{1-x}N/GaN$ NWHs (chapter 6, section 6.1) in detail.

4.4.1 Plasma diagnostics

A *HD25* RF atom source by *Oxford Applied Research* was used in the MBE growth experiments. In the present experiments, a nitrogen plasma is used to provide the activated nitrogen species that are necessary for the growth of group III-nitrides. Figure 4.9a) dis-

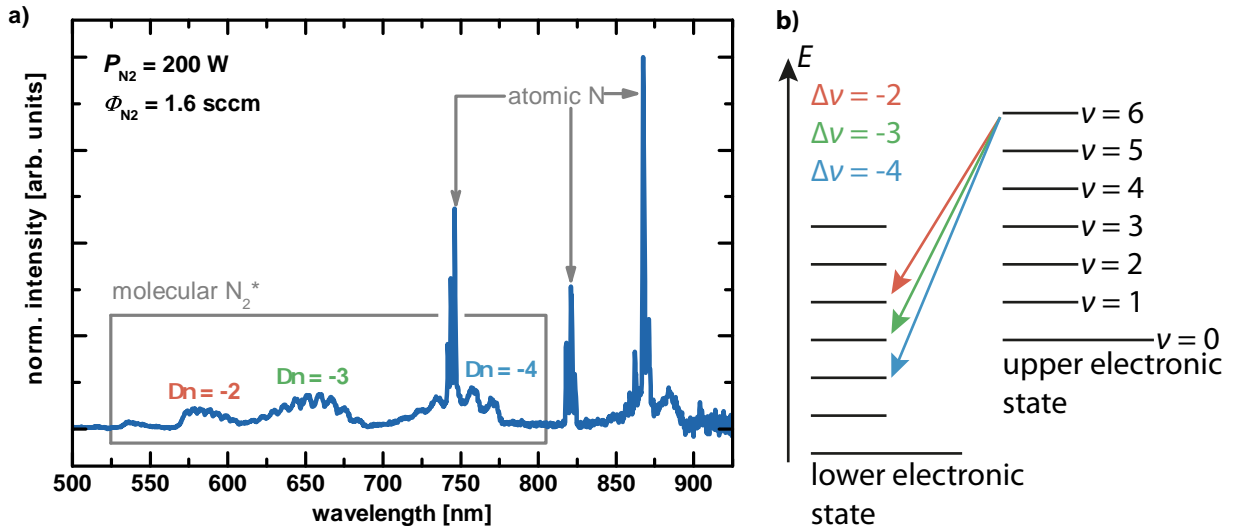


Figure 4.9: a) Spectrum of a RF nitrogen discharge for $P_{N_2} = 200 \text{ W}$ and $\Phi_{N_2} = 1.6 \text{ sccm}$. Molecular emission bands and atomic lines are highlighted. b) Schematic of the transition between two electronic states in excited molecular nitrogen with different $\Delta\nu$ of the vibrational level ν .

plays the emission spectrum of the nitrogen discharge in the investigated spectral range

from 500 nm to 900 nm². The electronic states of N₂ are split into vibrational sublevels ν (cf. figure 4.9b)) due to the additional degrees of freedom compared to atomic N. Transitions between two distinct electronic states of molecular N₂ are, therefore, observed as broad emission bands (cf. figure 4.9a)). Within each emission band, the change in the vibrational level $\Delta\nu$ stays constant. Transitions observed from 570 nm to 610 nm correspond to $\Delta\nu = -4$, those from 610 nm to 690 nm to $\Delta\nu = -3$ and $\Delta\nu = -2$ corresponds to the signals observed from 710 nm to 780 nm [87]. Emissions from multiplets of atomic N are detected at 746.1 nm, 812 nm and 867 nm. The intensity ratios of atomic emission lines to molecular emission bands are directly correlated to the density ratio $n(\text{N})/n(\text{N}_2^*)$. Therefore, all spectra were normalized to the dominant atomic line at 867 nm and the relative evolution of the N₂^{*} emission intensity was analyzed. Figure 4.10 depicts the evolution of the N₂^{*} emission band with $\Delta\nu = -3$ with P_{N_2} and Φ_{N_2} . Increasing P_{N_2} (Φ_{N_2}) leads to

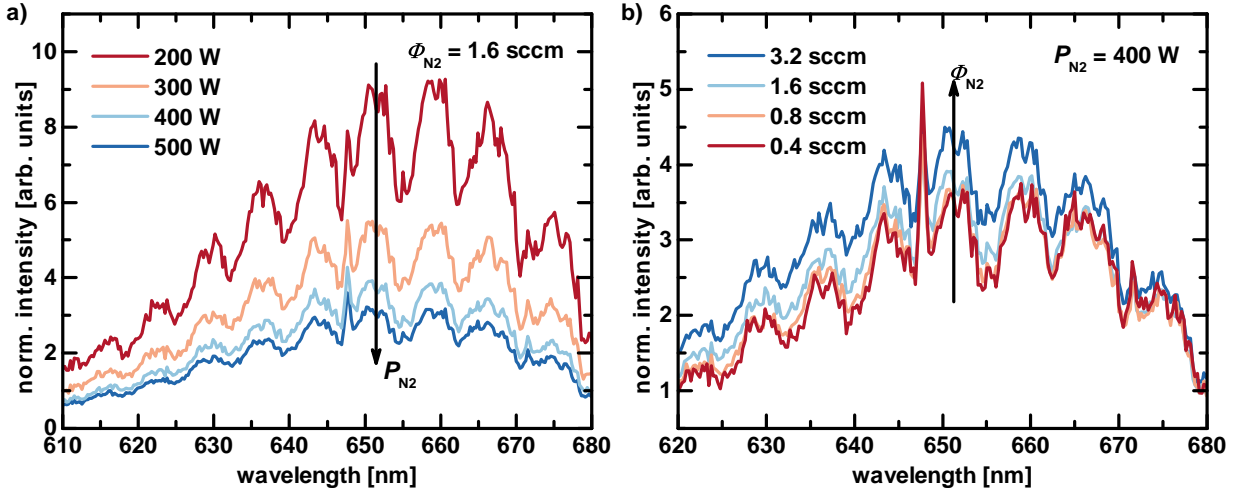


Figure 4.10: Evolution of the N₂^{*} emission intensity with respect to the dominant atomic emission line in dependence on a) P_{N_2} and b) Φ_{N_2} .

a relative decrease (increase) of the emission intensity in the investigated range. Consequently, $n(\text{N})/n(\text{N}_2^*)$ increases with P_{N_2} and decreases with Φ_{N_2} . The background pressure in the growth chamber p_{BG} increases linearly from 5×10^{-6} mbar to 3.8×10^{-5} mbar when Φ_{N_2} is increased from 0.4 sccm to 3.2 sccm (figure 4.11a)) and is not affected by P_{N_2} . At a fixed P_{N_2} the power-to-molecule ratio, therefore, decreases with increasing Φ_{N_2} which leads to the observed $n(\text{N})/n(\text{N}_2^*)$ decrease and also increases the amount of inert N₂ which can hinder the growth process. Both, increasing Φ_{N_2} or P_{N_2} leads to an overall increase of the integrated emission intensity as depicted in figure 4.11b) and figure 4.11c). The intensity

²An Ocean Optics HR4000CG-UV-NIR spectrometer attached to an optical fiber was used to record the spectra.

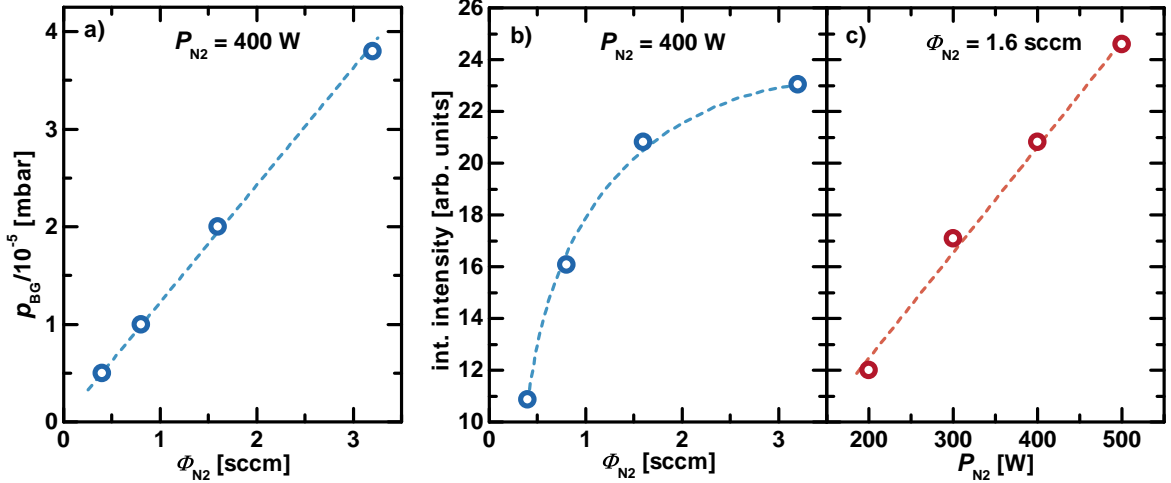


Figure 4.11: Evolution of a) p_{BG} with Φ_{N_2} and b) and c) the integrated intensity of the nitrogen discharge emission spectra with Φ_{N_2} and P_{N_2} .

increase with Φ_{N_2} follows a sublinear relationship while the emission intensity increases linearly with P_{N_2} . A change of the emission intensity by approximately 200 % is observed for P_{N_2} and Φ_{N_2} in either of the investigated ranges. This indicates that both parameters do not only change the plasma composition but also the absolute supply of reactive nitrogen species. However, the atomic nitrogen can also facilitate the decomposition reaction of the grown group III-N material as mentioned earlier. For increasing P_{N_2} , and thereby increasing $n(N)/n(N_2^*)$ ratio, this competing process to the GaN formation has to be kept in mind. Effectively, P_{N_2} mostly changes the composition of the plasma by favoring either excited molecular N_2^* (lower P_{N_2}) or atomic N (higher P_{N_2}).

Conclusively, the analysis of the emission spectra of the nitrogen discharge used to supply activated nitrogen species revealed that...

- P_{N_2} and Φ_{N_2} lead to an increase of activated nitrogen species that can contribute to the growth of GaN NWs.
- Increasing P_{N_2} increases density ratio $n(N)/n(N_2^*)$, additionally enhancing the GaN decomposition by atomic N. This reduces the effect of P_{N_2} on the amount of effectively incorporated N and might facilitate the incorporation of structural defects.
- Increasing Φ_{N_2} decreases the population density ratio $n(N)/n(N_2^*)$ reducing the N induced GaN decomposition rate. However, the additionally introduced inert N_2 due to an increase of p_{BG} with Φ_{N_2} might hinder the growth process.

4.4.2 Morphology and growth rates

The dependence of the GaN NW morphology and growth rates on Φ_{N_2} and P_{N_2} is investigated in the following.

Morphology

All samples that are subject to this section were grown for 180 min after nucleation was observed by RHEED. The substrate temperature was in the range of 795 °C to 800 °C while the BEP_{Ga} was set to 3.4×10^{-7} mbar. Both, P_{N_2} (200 W to 500 W) and Φ_{N_2} (0.6 sccm to 2.4 sccm) were systematically varied. A list of the investigated samples is given in appendix A.3. The top view SEM images of samples that were grown with different P_{N_2} ($\Phi_{N_2} = 1$ sccm) are presented in figure 4.12a) to figure 4.12c), whereas figure 4.12d) to figure

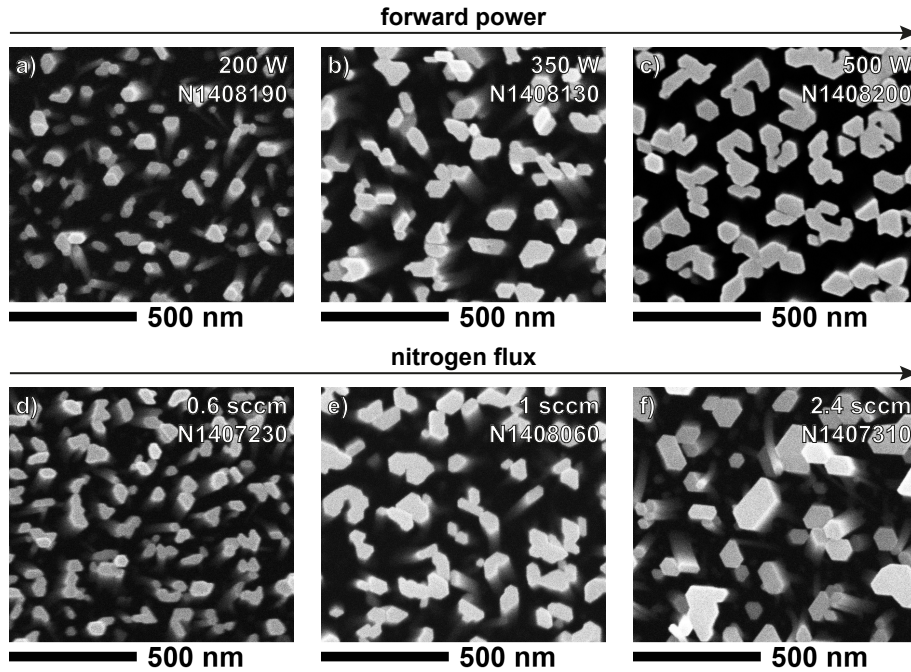


Figure 4.12: SEM top view images of samples grown with P_{N_2} of a) 200 W, b) 350 W and c) 500 W. The nitrogen flux was fixed at $\Phi_{N_2} = 1$ sccm. Also, the SEM top view images of samples grown with Φ_{N_2} set to d) 0.6 sccm, e) 1 sccm and f) 2.4 sccm are shown. For these samples, P_{N_2} was set to 400 W. Sample numbers are given in the respective images.

4.12f) show the images corresponding to samples where Φ_{N_2} was varied ($P_{N_2} = 400$ W). It is evident from figure 4.12 that an increase of either P_{N_2} or Φ_{N_2} leads to an increase of the NW diameter. Consequently, an apparent decrease of the final NW density due to an increased degree of coalescence is observed, similar to an increasing BEP_{Ga} at otherwise fixed growth parameters (cf. section 4.3.1). The quantitative analysis of the NW diameter

and final NW density in dependence on P_{N_2} and Φ_{N_2} is presented in figure 4.13. Increasing

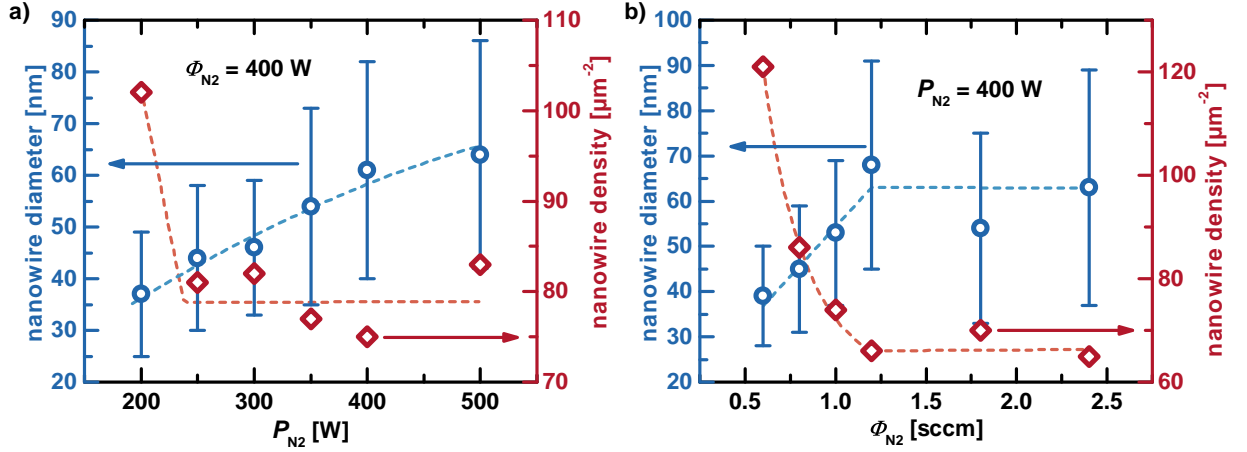


Figure 4.13: Evolution of the NW diameter and density with increasing a) P_{N_2} as well as b) Φ_{N_2} . Dashed lines were added to guide the eye.

P_{N_2} from 200 W to 500 W results in an increase of the NW diameter from (37 ± 12) nm to (64 ± 22) nm. An increase of Φ_{N_2} from 0.6 sccm to 2.4 sccm causes a diameter increase from (39 ± 11) nm to (63 ± 26) nm. However, while the NW diameter continuously grows when P_{N_2} is increased (figure 4.13a), it remains relatively constant for $\Phi_{N_2} \geq 1.2$ sccm. Both, increasing P_{N_2} and Φ_{N_2} leads to an increase of the standard deviation of the NW diameter (error bars in figure 4.13). This indicates an increasingly inhomogeneous radial growth. The decrease of the final NW density is more pronounced for an increase of Φ_{N_2} compared to P_{N_2} . A reduction of the NW density from $120 \mu\text{m}^{-2}$ to $65 \mu\text{m}^{-2}$ is observed when Φ_{N_2} is increased from 0.6 sccm to 2.4 sccm ($P_{N_2} = 400$ W). In contrast, a minimum NW density of $75 \mu\text{m}^{-2}$ is observed at $P_{N_2} = 400$ W ($\Phi_{N_2} = 1$ sccm) while a maximum density of $100 \mu\text{m}^{-2}$ was determined for $P_{N_2} = 200$ W ($\Phi_{N_2} = 1$ sccm). The final NW diameters and densities are the result of individual NW nuclei that coalesce into one NW during growth reducing the final NW density compared to its initial value. Information about the nucleation probability can be accessed by analyzing the dependence of t_{nucl} on P_{N_2} and Φ_{N_2} (figure 4.14). The nucleation time depends superlinearly on either of the investigated parameters. An increase of either P_{N_2} and Φ_{N_2} increases the absolute amount of activated nitrogen species (cf. section 4.4.1). The relative increase of the density of atomic nitrogen by an increase of P_{N_2} from 200 W to 500 W (at a fixed nitrogen supply of 1 sccm) causes a drastic reduction of the nucleation time from 68 min to 18 min. The relative increase of the density of N_2^* by raising Φ_{N_2} from 0.6 sccm to 2.4 sccm reduces t_{nucl} from 29 min to 8 min. Hence, all the nitrogen species that contribute to the growth of GaN [91] can also initiate

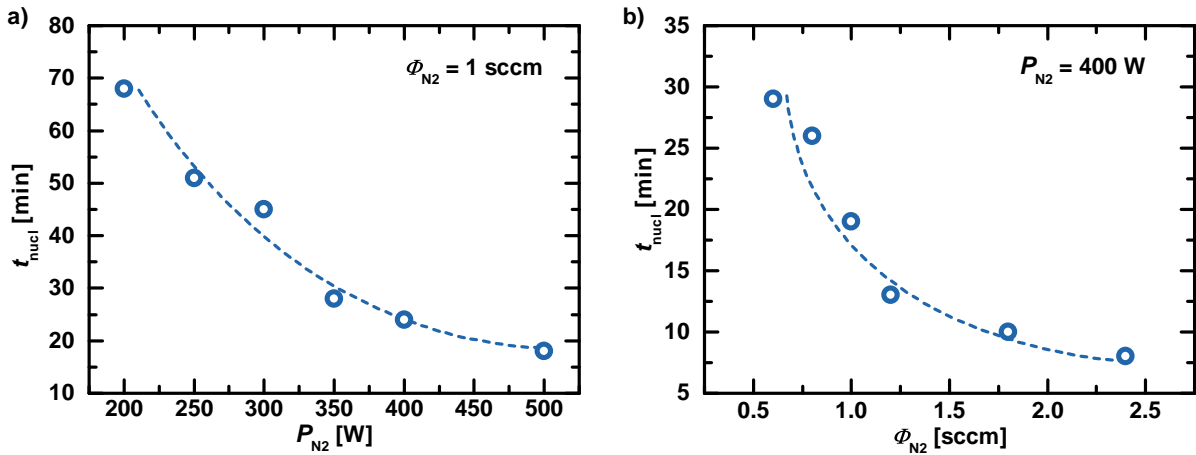


Figure 4.14: Dependence of the GaN NW nucleation time on a) the forward power and b) nitrogen flux.

the nucleation of GaN NWs. Consequently, the nucleation probability increases for higher values of P_{N_2} and Φ_{N_2} . Gallium nitride NW nuclei are, therefore, not only stabilized by Si diffusing through the amorphous Si_xN_y layer as proposed by Furtmayr et al. [60] but also by a sufficiently high concentration of reactive nitrogen species at the substrate surface. Figure 4.15a) and figure 4.15b) depict the dependence of the areal coverage and the degree of coalescence on P_{N_2} and Φ_{N_2} , respectively. Both parameters increase with increasing P_{N_2} . Together with the higher nucleation probability (lower t_{nucl}) at higher P_{N_2} , an increasing initial nucleation density is assumed. Accordingly, the same is inferred from the increase

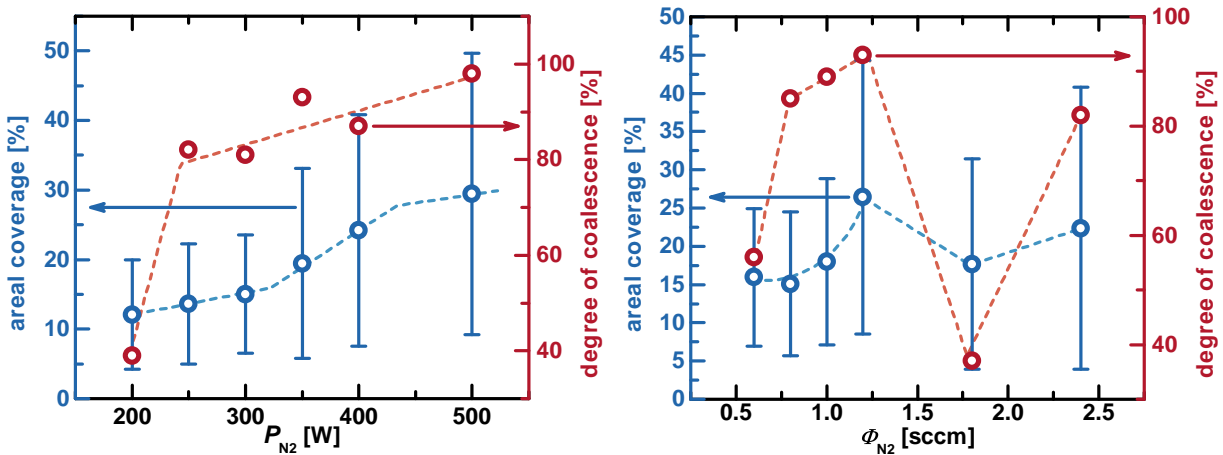


Figure 4.15: Dependence of the areal coverage and the degree of coalescence on a) the forward power and b) nitrogen flux.

of the degree of coalescence and areal coverage upon an increase of Φ_{N_2} up to 1.2 sccm.

A further increase of Φ_{N_2} leads to a decrease of both values, indicating a decrease of the initial nucleation site density in comparison to the sample grown with $\Phi_{N_2} = 1.2$ sccm. This observation seems to be in contradiction to the increase of the absolute amount of reactive nitrogen species and the increase in nucleation probability at higher Φ_{N_2} . However, the increase of p_{BG} with Φ_{N_2} additionally increases the total amount of nitrogen in the growth chamber. This raises the concentration of impinging inert N_2 (cf. section 4.4.1) that can inhibit NW nucleation which, in turn, reduces the initial NW nucleation density. Conclusively, the number of initial nucleation sites and the nucleation probability increase with P_{N_2} (200 W to 500 W) due to an increase of reactive nitrogen species which is also observed for an increase of Φ_{N_2} from 0.6 sccm to 1.2 sccm. However, increasing Φ_{N_2} also increases the nitrogen partial pressure in the growth chamber and the additional inert N_2 begins to significantly inhibit GaN nucleation on the substrate and Ga adatom diffusion at values > 1.2 sccm.

The influence of P_{N_2} and Φ_{N_2} on the axial growth of GaN NWs was studied based on cleaved edge SEM images of the individual samples (figure 4.16). The forward power

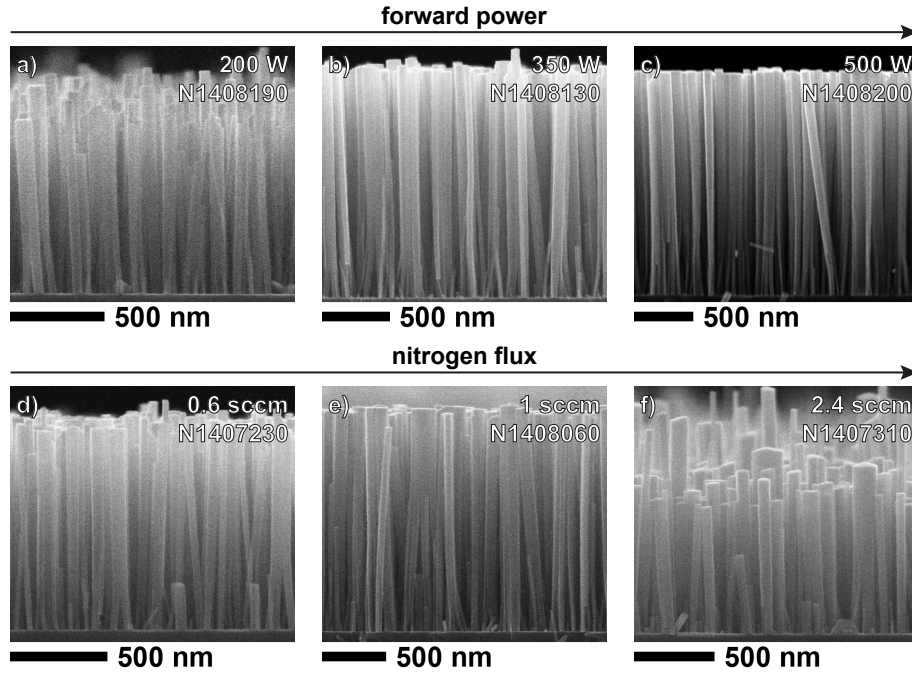


Figure 4.16: Cleaved edge SEM images of samples grown with P_{N_2} of a) 200 W, b) 350 W and c) 500 W. The nitrogen flux was fixed at $\Phi_{N_2} = 1$ sccm. Also, the SEM top view images of samples grown with $\Phi_{N_2} =$ d) 0.6 sccm, e) 1 sccm and f) 2.4 sccm are shown. For these samples, P_{N_2} was set to 400 W. Sample numbers are given in the respective images.

($\Phi_{N_2} = 1$ sccm) was varied corresponding to the images shown in figure 4.16a) to figure

4.16c), whereas the images in figure 4.16d) to figure 4.16f) represent samples which were grown with different nitrogen fluxes ($P_{N_2} = 400$ W). The length l of more than 100 NWs was measured and evaluated for each sample shown in figure 4.16. Errors correspond to the calculated standard deviation of the respective measurements. For increasing P_{N_2} from 200 W to 500 W, l increases from (967 ± 106) nm to (1864 ± 27) nm leading to a more homogeneous length profile of the GaN NWs with increasing P_{N_2} . This is the opposite behavior compared to the dependence of the NW diameter on P_{N_2} , where an increasing diameter inhomogeneity was observed for increasing P_{N_2} (cf. figure 4.13a)). In contrast, only an initial increase of the overall NW length from (1002 ± 54) nm to (1665 ± 38) nm is observed upon an increase of Φ_{N_2} from 0.6 sccm to 1 sccm. Raising Φ_{N_2} to 2.4 sccm reverses the trend, yielding a NW length of (1122 ± 217) nm. The large standard deviation of 217 nm reflects the inhomogeneous growth of the GaN NWs on this sample due to the hindered Ga diffusion for high Φ_{N_2} .

Growth rates

The axial and lateral growth rates of GaN NWs (r_{axial} and r_{lateral}) were analyzed based on the morphological characterization. In figure 4.17, the dependences of r_{axial} and r_{lateral} as

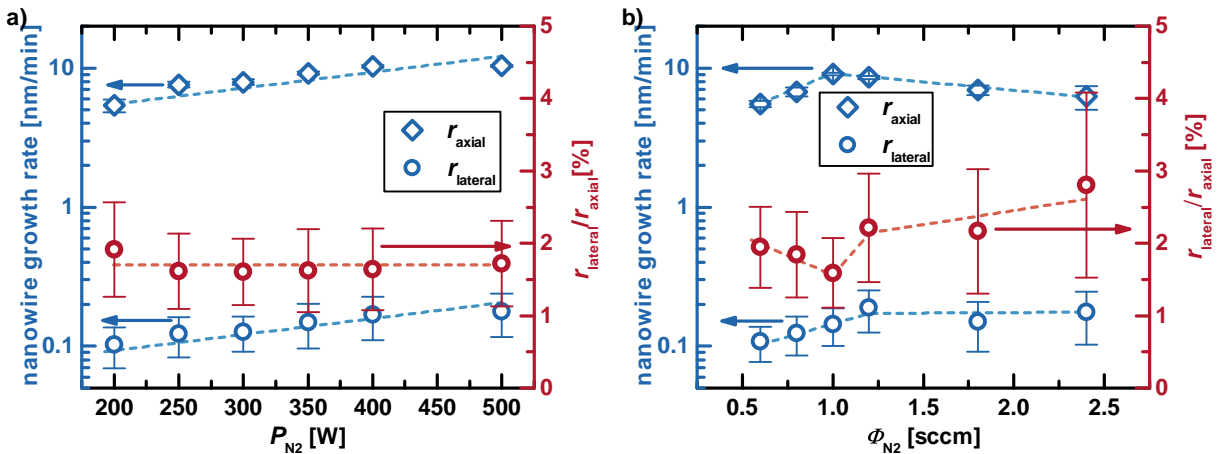


Figure 4.17: Dependence of the axial and radial GaN NW growth rate as well as the radial-to-axial growth rate ratio on a) P_{N_2} and b) Φ_{N_2} . A logarithmic scale was chosen for the left ordinate.

well as of the ratio $r_{\text{lateral}}/r_{\text{axial}}$ on the applied forward power and nitrogen flux are shown. An increase of the r_{axial} from (5.4 ± 0.6) nm/min to (10.4 ± 0.2) nm/min and an increase of r_{lateral} from (0.1 ± 0.03) nm/min to (0.18 ± 0.06) nm/min with increasing P_{N_2} is observed. The ratio $r_{\text{lateral}}/r_{\text{axial}}$ remains fairly constant around (1.7 ± 0.6) % over the whole range of applied forward powers. Therefore, the increase of the relative amount of atomic N accom-

panied by the total increase of reactive nitrogen species at a fixed nitrogen partial pressure enhances the nucleation of GaN NWs as well as their radial and axial growth without a clear preference of any growth direction. The possible damage which might be caused by an increased GaN dissociation rate at the NW surface, due to larger amounts of reactive atomic N, does not prevail even for the highest applied forward power $P_{N_2} = 500$ W.

An almost linear increase of r_{axial} from (5.5 ± 0.3) nm/min to (9 ± 0.2) nm/min and of r_{lateral} from (0.1 ± 0.03) nm/min to (0.14 ± 0.04) nm/min results from an increase of Φ_{N_2} from 0.6 sccm to 1 sccm (figure 4.17b)). The faster increase of r_{axial} compared to r_{lateral} leads to a decrease of $r_{\text{lateral}}/r_{\text{axial}}$ from (1.9 ± 0.6) % to (1.6 ± 0.5) %, up to a nitrogen flux of 1 sccm. At fluxes > 1 sccm, r_{axial} decreases linearly to (6.2 ± 1.2) nm/min at $\Phi_{N_2} = 2.4$ sccm. In contrast, r_{lateral} increases further until $\Phi_{N_2} = 1.2$ sccm is reached and remains almost constant up to the highest applied nitrogen flux of 2.4 sccm (cf. figure 4.17b)). Consequently, the ratio $r_{\text{lateral}}/r_{\text{axial}}$ increases for $\Phi_{N_2} > 1$ sccm and reaches a maximum value of (2.8 ± 1.3) % at $\Phi_{N_2} = 2.4$ sccm. The large error reflects the inhomogeneous growth of the GaN NWs at high nitrogen fluxes which was observed during the morphological investigations (figure 4.12f) and figure 4.16f)). Plasma diagnostic experiments (cf. section 4.4.1) revealed a relative increase of N_2^* in comparison to the higher energy atomic N with increasing Φ_{N_2} . In addition, the total nitrogen pressure within the MBE system increases with Φ_{N_2} . The increasing amount of N_2^* seems to facilitate the growth of GaN NWs similar to the growth of GaN layers. Up to $\Phi_{N_2} = 1$ sccm ($P_{N_2} = 400$ W), the axial growth is preferred over the radial growth of the NWs. Hence, the increasing amount of inert N_2 does not hinder the Ga adatom diffusion along the NW sidewalls and the lower reactivity of N_2^* compared to N results in a weaker increase of r_{lateral} compared to r_{axial} . The subsequent decrease of r_{axial} for $\Phi_{N_2} > 1$ sccm indicates an increasing restraint of the Ga diffusion towards the NW tip due to the increasing amount of inert N_2 . Gallium incorporation into the NW sidewalls is not affected by this increase of non-reactive nitrogen, indicated by the relatively constant lateral growth rate (figure 4.17b)).

Conclusively, the nitrogen flux can be used to minimize $r_{\text{lateral}}/r_{\text{axial}}$ at a fixed P_{N_2} which maximizes the aspect ratio of GaN NWs and also minimizes NW coalescence. The forward power does not seem to preferentially enhance either, lateral or axial GaN NW growth. Both, the radial and axial growth rates, however, increase with increasing P_{N_2} due to an increasing amount of reactive nitrogen species. The GaN decomposition reaction facilitated by the atomic nitrogen does not prevail for the investigated range of P_{N_2} as no decrease of the growth rate was observed for an increase of P_{N_2} .

4.4.3 Photoluminescence spectroscopy

The optical properties of GaN NWs were already discussed in section 4.3.2 based on low temperature (4 K) PL spectroscopy. The corresponding samples were fabricated using constant P_{N_2} and Φ_{N_2} . The current section is focused on the changes that are introduced to the PL spectra of GaN NWs by the variation of the atom source operating parameters. Figure 4.18 displays the low temperature PL spectra of GaN NW samples that were grown with different Φ_{N_2} ($P_{N_2} = 400$ W). All samples investigated exhibit their maximum emission

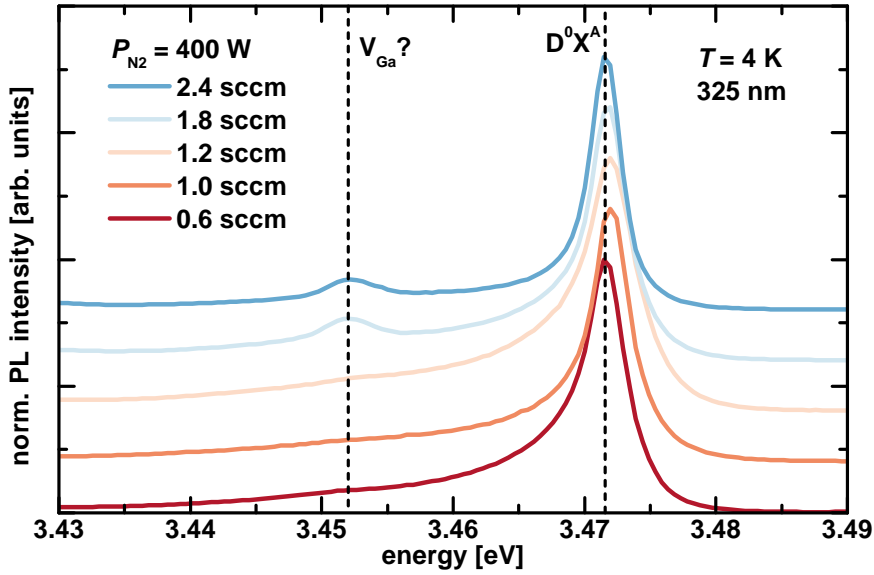


Figure 4.18: Low temperature PL spectra of GaN NWs grown with different nitrogen fluxes, keeping all other parameters constant. Emission lines of the donor bound exciton D^0X^A and the one possibly originating from V_{Ga} are marked by dashed lines. The spectra were recorded on samples N1407230A (0.6 sccm), N1408060A (1 sccm), N1407240B (1.2 sccm), N1407280A (1.8 sccm) and N1407310 (2.4 sccm).

intensity at the energy of the D^0X^A transition. The spectra are normalized to the emission maximum and were stacked along the ordinate. A luminescence line at 3.452 eV arises with increasing Φ_{N_2} from 0.6 sccm to 2.4 sccm ($P_{N_2} = 400$ W). This was already observed in similar samples which were presented in Ref. [54]. The 3.452 eV emission in GaN has so far been assigned to a two electron satellite (TES) [92] of the D^0X^A transition as well as excitons recombining at inversion domain boundaries [83, 93] and V_{Ga} at the NW surface [37, 54]. The interpretation that the 3.452 eV line stems from the recombination of a TES has been confuted by polarization-resolved and magneto-PL experiments by Sam-Giao and coworkers [94] while the assignment to V_{Ga} at the GaN NW surface is still in line with

the results of those experiments. The observation that the 3.452 eV emission increases in intensity with decreasing III/V ratio during growth also supports the assignment to V_{Ga} , not only because the relative amount of available Ga is reduced in comparison to N and N_2^* but also due to the hindered Ga adatom diffusion for higher Φ_{N_2} as discussed in section 4.4.2.

Figure 4.19 shows the low temperature PL spectra of samples grown with different values of the applied forward power ($\Phi_{\text{N}_2} = 1 \text{ sccm}$). All spectra were normalized to the D^0X^A

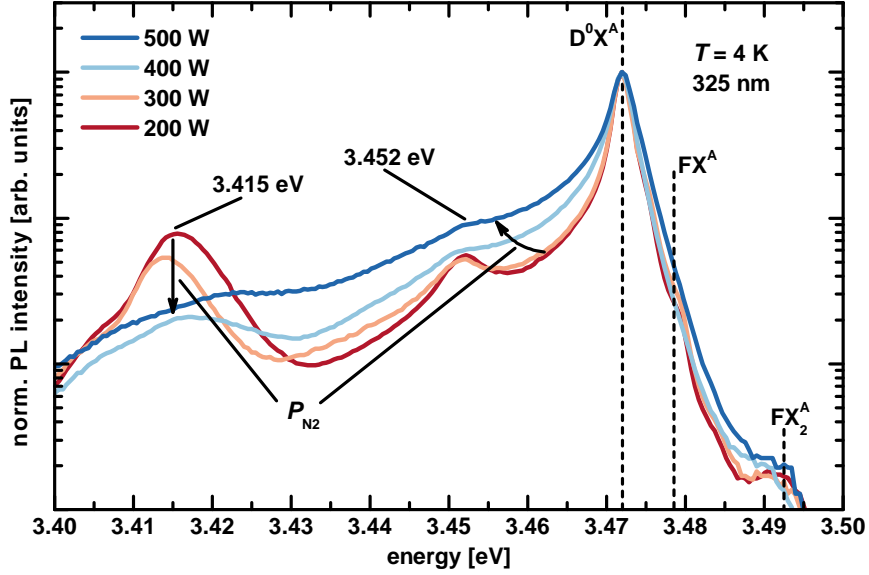


Figure 4.19: Low temperature PL spectra of GaN NWs grown with different P_{N_2} , keeping all other parameters constant. The characteristic D^0X^A and FX^A emissions of GaN is marked by dashed lines and the evolution of the spectra with increasing forward power is indicated by arrows. Spectra corresponding to $P_{\text{N}_2} = 200 \text{ W}$, 300 W , 400 W and 500 W correspond to the samples N1408190A, N1408150A, N1408120A and N1408200A, respectively.

emission line. The emission which corresponds to the FX^A is observed within the high energy shoulder for $P_{\text{N}_2} = 200 \text{ W}$ to 300 W but is not visible for higher values of P_{N_2} as the D^0X^A emission line is broadened from 2.6 meV (200 W) to 3.6 meV (500 W). All spectra exhibit the FX_2^A emission at 3.493 eV corresponding to the excited state of the free exciton. In addition, the intensity of the luminescence background at energies $< 3.472 \text{ eV}$ increases with increasing P_{N_2} . In contrast, the intensity of the 3.415 eV emission band is reduced for increasing P_{N_2} .

Conclusively, the higher Φ_{N_2} the more V_{Ga} are incorporated close to the NW surface which form acceptor-like states [95] and give rise to the emission at 3.452 eV [54]. Increasing the relative amount of atomic nitrogen by increasing P_{N_2} , leads to an increase of the FWHM

of the D^0X^A emission. The origin of this increase of the FWHM seems, therefore, to be correlated to the increasing decomposition rate of GaN by the reactive atomic N. In the decomposition reaction, impinging atomic N breaks the Ga-N bonds leading to the formation of N_2 that subsequently desorbs. Therefore, the formation of nitrogen vacancies V_N becomes more probable with increasing P_{N_2} . Nitrogen vacancies are the point defects with the lowest formation energy even under nitrogen-rich growth conditions [96]. Those V_N are predicted to form donor-like states in GaN which was corroborated by experiments performed by Look et al. [97]. They determined the activation energy of V_N in GaN to 70 meV and did not observe a PL line originating from these donor-like states. An unambiguous assignment of the increasing of FWHM of the D^0X^A line with increasing P_{N_2} to an increasing density of V_N is, however, not possible solely by the presented data. The increase in luminescence linewidth could also be the result of the increasing NW diameter inhomogeneity with increasing P_{N_2} (cf. section 4.4.2). Based on the experiments presented in this work, an in depth analysis of the PL of SNWs in dependence on P_{N_2} and the NW diameter yielding reliable statistics might enable to verify or falsify the assignment of the FWHM increase of the D^0X^A line to V_N .

The decrease of the intensity of the 3.415 eV emission band with increasing P_{N_2} is attributed to the increasing distance of the excited NW volume from the substrate because the NW length successively increases from $l = (967 \pm 106)$ nm to $l = (1864 \pm 27)$ nm when P_{N_2} is raised from 200 W to 500 W. This observation corroborates the assignment of this emission to interface defects and is in line with the experiments presented in Ref. [37]. Finally, the increasing degree of NW coalescence which is observed with increasing P_{N_2} (cf. figure 4.15a)) introduces additional structural defects in the coalescence regions [78]. Such an increase of structural defects most likely causes the observed increase of the luminescence background at lower energies ($E < 3.472$ eV).

4.4.4 Conclusion

In this section, the dependence of the GaN NW morphology, growth rates and PL on the plasma source operating parameters P_{N_2} and Φ_{N_2} was analyzed and correlated to the change of the plasma composition and absolute amount of nitrogen species in the growth chamber. Increasing either P_{N_2} or Φ_{N_2} leads to an increase of the absolute amount of reactive nitrogen while only Φ_{N_2} influences the overall amount of nitrogen (including inert N_2) in the growth chamber. An increase of the relative amount of atomic N (excited molecular N_2^*) is observed upon an increase of P_{N_2} (Φ_{N_2}).

The increase of reactive nitrogen species due to an increase of either P_{N_2} or Φ_{N_2} leads

to an increased GaN NW nucleation probability on the nitridated Si(111) substrates and facilitates lateral and axial NW growth. No influence of the GaN decomposition by atomic N on the NW morphology was observed in the investigated range of P_{N_2} . Radial growth of the NWs becomes more inhomogeneous with increasing amount of reactive nitrogen species independent on the composition ratio $n(N)/n(N_2^*)$. However, hindered adatom diffusion due to the increasing amount of inert N_2 reduces the initial NW nucleation density for $\Phi_{N_2} > 1.2$ sccm and also leads to an inhomogeneous axial NW growth. In addition, a luminescence line at 3.452 eV is observed for $\Phi_{N_2} > 1.2$ sccm probably due to enhanced formation of V_{Ga} at the applied growth conditions. The lowest linewidth of the D^0X^A emission (2.5 meV) was observed for the sample grown with and $P_{N_2} = 300$ W and $\Phi_{N_2} = 1$ sccm.

5 Analysis of internal electric fields in AlN/GaN nanowire heterostructures

The growth of GaN NDs embedded in $\text{Al}_x\text{Ga}_{1-x}\text{N}$ barriers enables the study of confinement effects in NWHs. Compositional fluctuations for $x < 1$ [98, 99] are avoided by using AlN as the barrier material. Due to the large lattice mismatch between GaN and AlN (2.5%), the resulting NDs and barriers are significantly strained despite the strain relaxation introduced by the NW geometry [100, 101]. The modification of the carrier confinement by the resulting strain field is the consequence [10, 102]. In addition, the PL emission from the GaN NDs embedded in AlN is shifted below the GaN bandgap if the NDs exceed a certain layer thickness [9, 103]. This behavior originates from the QCSE due to the strong polarization-induced internal electric fields (cf. chapter 2). The QCSE does not only influence the emission energy, the reduction of the electron and hole wavefunction overlap also significantly alters the carrier lifetimes. Therefore, a controlled manipulation of the internal electric fields in AlN/GaN NDSLs facilitates the optimization of the performance of (nano)-opto-electronic devices.

In this work, two approaches are used to alter the internal electric fields in 40x AlN/GaN NDSLs. First, Ge-doping of the GaN NDs is applied to electrostatically screen the internal electric fields by doping induced free carriers as presented in section 5.1. Secondly, the thickness of the AlN barriers is varied to influence the strength of the internal electric fields in the AlN/GaN NDSLs which will be discussed in section 5.2.

5.1 Doping-induced screening of internal electric fields

It has been shown that Si doping of GaN leads to the deterioration of the crystal quality at high Si concentrations [104] and induces strong tapering in the case of GaN:Si NWs [60]. Screening of internal electric fields by free carriers was not observed in Si doped GaN QDs, embedded in AlN barriers [105]. However, theory predicts electrostatic screening in $\text{Al}_x\text{Ga}_{1-x}\text{N}/\text{GaN}$ QWs for sufficiently high doping concentrations ($n > 10^{19} \text{ cm}^{-3}$) [106]. Germanium was found to be an excellent alternative to Si as an n-type dopant in GaN layers [107, 108] and recently also in GaN NWs [54]. In the case of NWs, Ge was incorporated in concentrations above 10^{20} cm^{-3} [54] which resulted in free carrier concentrations well above 10^{19} cm^{-3} [109]. Even at those Ge-concentrations, no structural degradation was observed. Single NW μ -PL measurements conducted on a n.i.d. and two Ge-doped ($[\text{Ge}] = 2.8 \times 10^{18}$ and $1 \times 10^{20} \text{ cm}^{-3}$) GaN NWs are presented in figure 5.1. Positions of the emissions from the FX^{A} , $\text{D}^0\text{X}_{\text{Si}}^{\text{A}}$ and $\text{D}^0\text{X}_{\text{O}}^{\text{A}}$ are marked by color coded dashed lines in figure 5.1. The emission at 3.468(5) eV which is labeled $\text{D}^0\text{X}_{\text{Ge}}^{\text{A}}$ in figure 5.1 was proposed to originate from

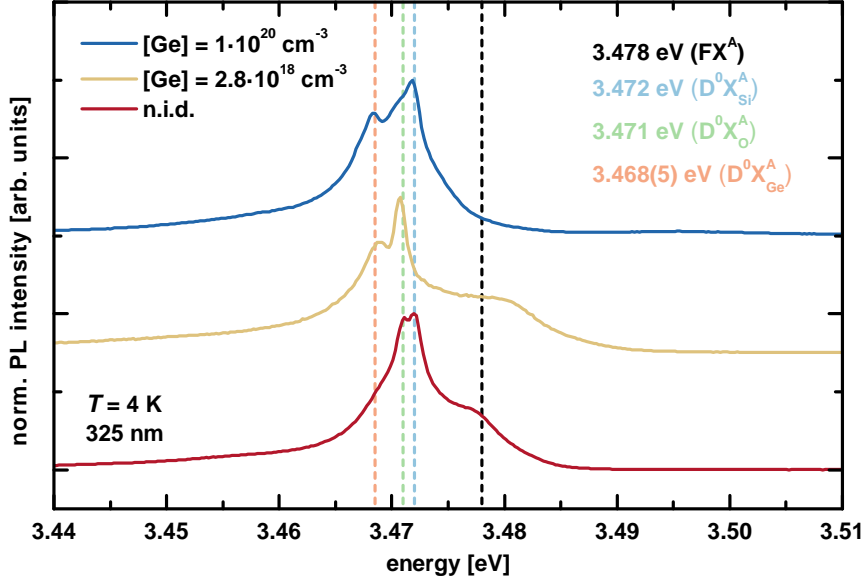


Figure 5.1: Single NW μ -PL spectra of sample N1204270 (*n.i.d.*), sample N1204250 ($[Ge] = 2.8 \times 10^{18} \text{ cm}^{-3}$) and sample N1204260 ($[Ge] = 1 \times 10^{20} \text{ cm}^{-3}$). Emissions of the FX^A (black), $D^0X_{Si}^A$ (light blue), $D^0X_O^A$ (light green) and $D^0X_{Ge}^A$ (light red) are marked by dashed lines. The data used for this figure has been previously published in Ref. [54].

excitons bound to neutral germanium donors due to its intensity increase with increasing Ge-concentration [54]. Doping induced band gap renormalization can be ruled out as the origin of this emission since neither the $D^0X_{Si}^A$ nor the $D^0X_O^A$ emission change in energy upon Ge-doping. Hence, a localization energy $E_{loc,Ge}$ of 9.5 meV is found for the excitation localization at neutral germanium donor sites. An emission energy of 3.478 eV was assumed for the FX^A [110] transition to calculate $E_{loc,Ge}$. This corroborates the prediction that Ge forms shallow donor states in GaN [111].

Germanium doping of GaN NDs is employed in the following to achieve screening of the internal electric fields. Fortyfold AlN/GaN NDSLs were grown with $BEP_{Ga} = 3 \times 10^{-7}$ mbar and $BEP_{Al} = 8 \times 10^{-8}$ mbar. The BEP_{Ge} was varied between 5×10^{-10} mbar and 3×10^{-9} mbar suggesting a range of donor concentrations from $9 \times 10^{19} \text{ cm}^{-3}$ to $6.2 \times 10^{20} \text{ cm}^{-3}$ according to Ref. [54]. However, the BEP_{Ge} is used in the following to describe the doping level of the GaN NDs because the doping efficiency for thin GaN NDs (on the order of a few nm) can differ from that observed for the homogeneously doped NWs as it was presented in Ref. [54].

5.1.1 Structural analysis

The structural properties of single 40x AlN/GaN(:Ge) NDSLs were studied by STEM analysis¹. Figure 5.2 displays HAADF images of two GaN NDSL structures, samples N1308210 (figure 5.2a) to figure 5.2c)) and N1308220 (figure 5.2d) to figure 5.2f)), respectively. The

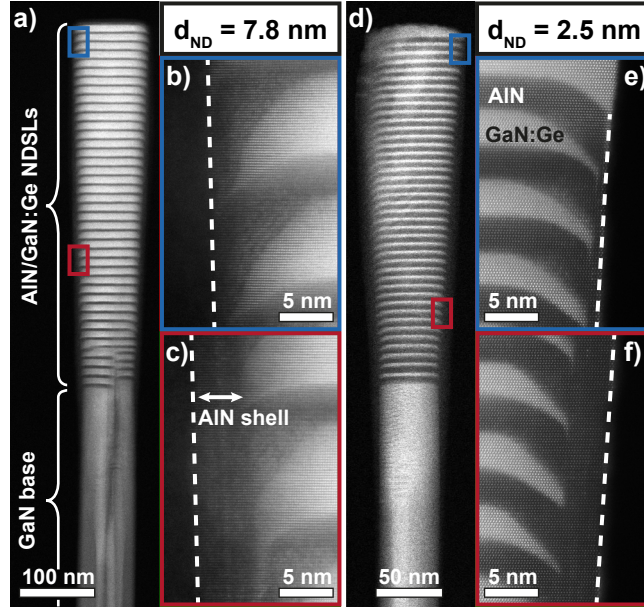


Figure 5.2: *a) to c) TEM images of sample N1308210 ($d_{ND} = 7.9$ nm). d) to f) TEM images of sample N1308220 ($d_{ND} = 2.5$ nm). While a) and d) show the whole NDSL structures, enlarged images of the marked areas (blue and red) are displayed in b), c), e) and f), respectively. The data used for this figure has been previously published in Ref. [112].*

AlN appears in darker contrast compared to the GaN. In sample N1308210, the ND thickness d_{ND} was determined to be (7.8 ± 1.1) nm, while $d_{ND} = (2.5 \pm 0.4)$ nm was measured for sample N1308220. In addition, a third sample (N1308020) investigated by STEM exhibited a d_{ND} of (3.8 ± 0.8) nm. For samples N1308020 and N1308210, a barrier thickness d_{barrier} of (4.2 ± 0.6) nm was extracted. Magnifications of the blue (red) framed regions in figure 5.2a) and figure 5.2d) are shown in figure 5.2b) and figure 5.2e) (figure 5.2c) and figure 5.2f)). An AlN shell is clearly visible from those images and accentuated by the white dashed lines. This shell is smaller at the NW tip (around 1 nm) and reaches a value of approximately 10 nm at the NW base. Figure 5.3a) shows the BF-high resolution transmission electron microscope (HRTEM) image of a NW from sample N1308210 ($d_{ND} = (7.8 \pm 1.1)$ nm). Magnifications that correspond to the regions framed in blue and green in figure 5.3a) are

¹TEM experiments were conducted by Prof. Jordi Arbiol at ICREA and Institut de Ciència de Materials de Barcelona, CSIC, Campus de la UAB, 08193 Bellaterra, CAT, Spain.

displayed in figure 5.3c) and figure 5.3e). Red arrows denote the growth direction of the NW. Gallium nitride NDs appear in dark contrast, whereas the AlN barriers and shell are

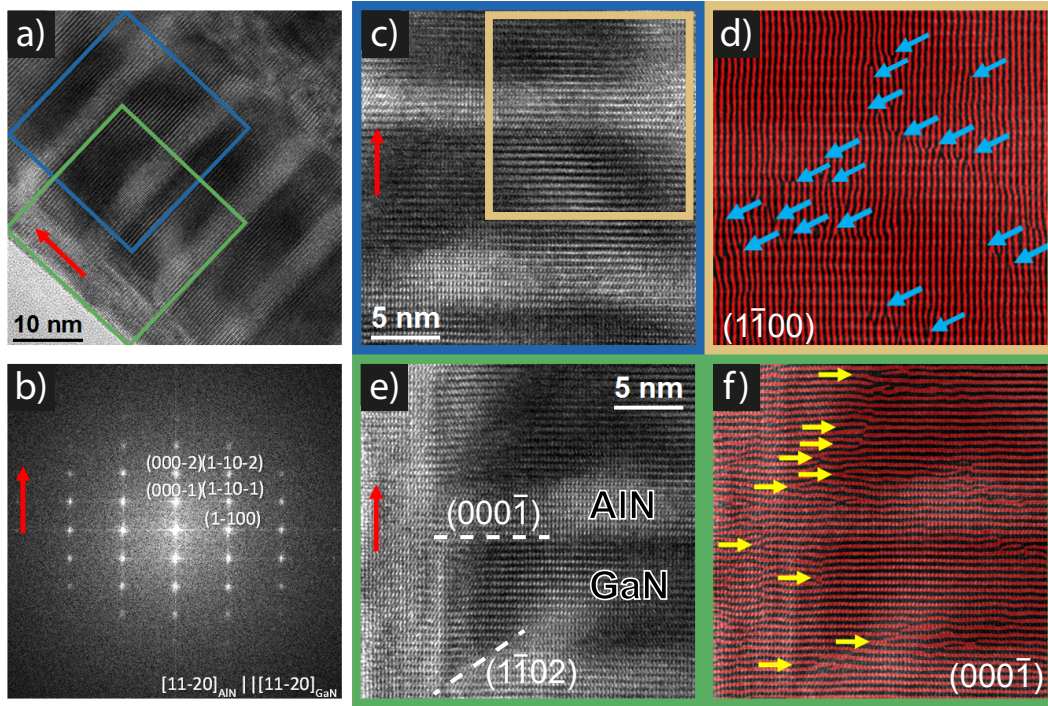


Figure 5.3: A HRTEM image of sample N1308210 ($d_{ND} = 7.8$ nm) is displayed in a). Magnified images of area marked by a blue (green) rectangle are shown in c) (e). The power spectrum of the green region is shown in b). Red arrows indicate the growth direction. The $(1\bar{1}00)$ and $(000\bar{1})$ lattice planes were filtered from the micrographs in c) and e), respectively. These filtered planes are shown in d) (f)) as an overlay to the framed region marked in c) (image e)). Arrows in d) and f) highlight the position of some misfit dislocations.

represented by the brighter areas of the micrographs. The power spectrum of figure 5.3e) which is displayed in figure 5.3b) reveals the epitaxial relationship between the AlN and GaN segments that both grow along the $(000\bar{1})$ direction. The morphology of the GaN NDs and AlN barriers is clearly visible from figure 5.3e). Semipolar $(1\bar{1}02)$ facets are introduced by the AlN barriers while GaN NDs finish with a flat $(000\bar{1})$ plane. The latter indicates a significantly faster growth rate of GaN on $\{1\bar{1}02\}$ surfaces. The magnified HRTEM images presented in figure 5.3c) and figure 5.3e) were filtered to extract the $(1\bar{1}00)$ and $(000\bar{1})$ planes, respectively. The filtered lattice planes are shown in figure 5.3d) as a red overlay to the yellow framed region in figure 5.3c) as well as an overlay to the whole image of figure 5.3e) in figure 5.3f). Blue (yellow) arrows highlight the position of misfit dislocations in figure 5.3 d) (figure 5.3 f)). No evidence of plastic strain relaxation was, however, found for the sample with a small d_{ND} of (2.5 ± 0.4) nm indicating pseudomorphic growth

of the GaN NDs in that case. Hence, the critical nanodisc thickness needed to accumulate enough strain energy for plastic strain relaxation seems to be in the range of $d_{\text{ND}} = 2.5$ nm to 7.8 nm, in the case of the presented AlN/GaN NDSLs ($d_{\text{barrier}} = 4.2$ nm). Furtmayr et al. already observed the formation of misfit dislocation in samples with $d_{\text{ND}} = 2.5$ nm [9]. In those experiments, the GaN NDs were, however, embedded in barriers of 7 nm AlN [9] which enhances the compressive strain in the ND compared to the experiments presented in the current work probably leading to a lower critical d_{ND} .

Fortyfold AlN/GaN NDSL ensembles were also analyzed by HRXRD to access information about the superlattice parameters on an ensemble scale. For this purpose, symmetrical ω - 2θ -scans were performed. Figure 5.4 shows the diffractogram of sample N1307290 in red and a corresponding simulation in blue. Satellite peaks (SL_{*i*}) that correspond to reflec-

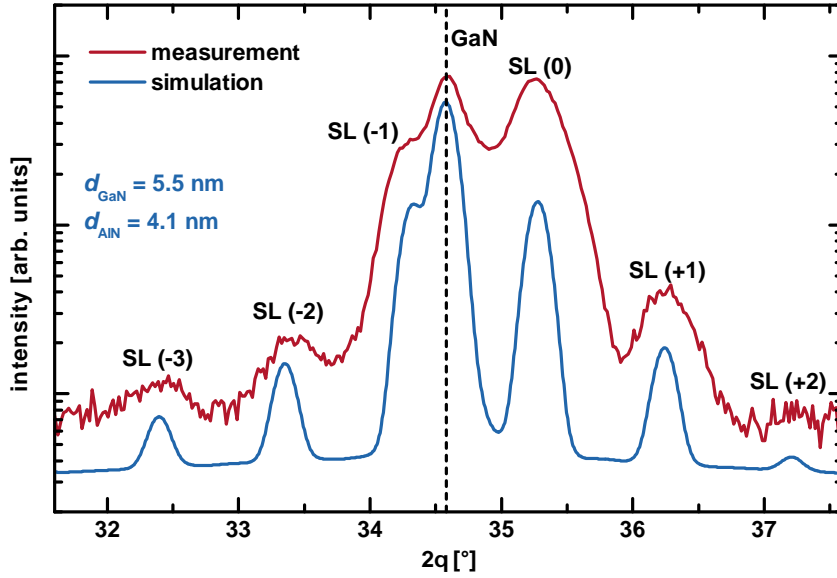


Figure 5.4: ω - 2θ diffractogram of sample N1307290 (red) and a corresponding simulation (blue). Superlattice peaks are labeled, the order of the respective reflections are given in brackets. The vertical dashed line highlights the position of the GaN reflex.

tions from the AlN/GaN NDSL are clearly visible up to the third order, in addition to the GaN reflex at $2\theta = 34.58^\circ$. This reveals a homogeneous layer periodicity on the ensemble scale. The *X'Pert Epitaxy* software package by *PANalytical* enables the simulation of the ω - 2θ diffractograms, based on dynamical diffraction theory. Results obtained by TEM ($d_{\text{barrier}} = 4.2$ nm) were used to calibrate the simulation input parameters, since the XRD data only reveals reliable information on the superlattice periodicity. A ND (barrier) thickness of 5.5 nm (4.1 nm) was used for the simulation shown in figure 5.4. Table 5.1 lists all

the acquired ND and barrier thicknesses. The thickness of the AlN barriers remains nominally the same for all samples listed in table 5.1. Therefore, d_{ND} can be reliably calculated

Probe	BEP_{Ge} [mbar]	$d_{\text{ND,XRD}}$ [nm]	$d_{\text{barrier,XRD}}$	$d_{\text{ND,TEM}}$ [nm]	$d_{\text{barrier,TEM}}$ [nm]
N1303043	n.i.d.	3.6^2	4.2^2	—	—
N1303063	5×10^{-10}	3.5^2	4.2^2	—	—
N1303073	1×10^{-9}	3.2^2	4.2^2	—	—
N1303083	1.5×10^{-9}	3.5^2	4.2^2	—	—
N1307263	n.i.d.	3.7	4.2^2	—	—
N1307290	n.i.d.	5.5	4.1	—	—
N1307303	n.i.d.	6.1^2	4.2^2	—	—
N1307313	n.i.d.	4.4^2	4.2^2	—	—
N1308013	n.i.d.	6.4^2	4.2^2	—	—
N1308020	8.7×10^{-10}	3.7^2	4.2^2	3.8 ± 0.8	4.2 ± 0.6
N1308023	8.7×10^{-10}	3.7^2	4.2^2	—	—
N1308053	8.7×10^{-10}	5.1^2	4.2^2	—	—
N1308063	8.7×10^{-10}	6.6^2	4.2^2	—	—
N1308160	n.i.d.	1.9	3.7	—	—
N1308210	8.7×10^{-10}	8^2	4.2^2	7.8 ± 1.1	4.2 ± 0.6
N1308213	8.7×10^{-10}	7.9^2	4.2^2	—	—
N1308220	8.7×10^{-10}	2.3^2	4.2^2	2.5 ± 0.4	—
N1308223	8.7×10^{-10}	2.7	4	—	—
N1312113	n.i.d.	2	4.1	—	—
N1312123	n.i.d.	3.2	4.2	—	—
N1312130	3×10^{-9}	3.4	3.8	—	—

Table 5.1: Summary of the structural parameters of the investigated 40x AlN/GaN(:Ge) NDSLs. The barrier thicknesses were extracted from XRD $d_{i,\text{XRD}}$ and TEM $d_{i,\text{TEM}}$ measurements, respectively.

taking the AlN barrier thickness determined by TEM into account. All further mentioned values of d_{ND} and d_{barrier} are based on the data obtained by HRXRD analysis.

5.1.2 Optical analysis

The optical properties of the 40x AlN/GaN NDSLs were analyzed by PL spectroscopy. Both, CW- and TR-PL measurements were performed. *Setup A* (cf. section 3.4) was used for the CW-PL analysis. Figure 5.5 displays the low temperature (4K) PL spectra of undoped (figure 5.5a)) and Ge-doped (figure 5.5b)) GaN NDs embedded in AlN barriers.

²Calculated from layer periodicity assuming $d_{\text{barrier}} = 4.2$ nm which was measured by TEM analysis on samples N1308020 and N1308210.

Nominally, d_{barrier} was kept constant at 4 nm (measured values are listed in table 5.1) and d_{ND} was varied. In the case of Ge-doping, d_{ND} was kept constant at nominally 4 nm and the BEP_{Ge} was varied. It is evident that the introduction of the GaN ND stack significantly broadens and blue shifts (≈ 4 meV) the D^0X^A emission of the GaN base compared to the PL spectrum of a n.i.d. GaN NW ensemble due to compressive strain exerted by the AlN shell (yellow in figure 5.5a)). The ND transition energy is smaller than the GaN NBE emission

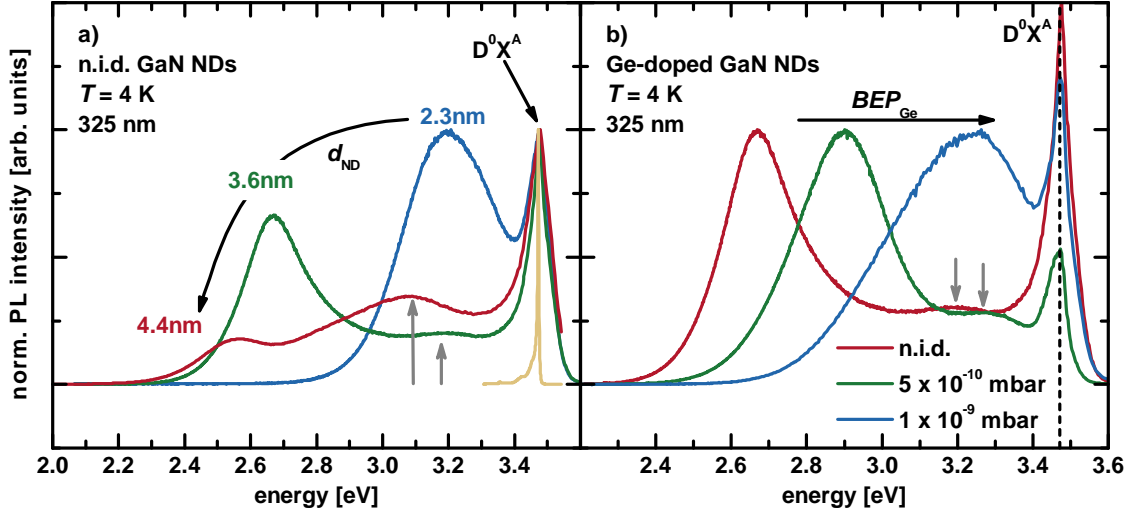


Figure 5.5: PL spectra of the undoped GaN ND samples N1312113 ($d_{\text{ND}} = 2.3$ nm, blue), N1303043 ($d_{\text{ND}} = 3.6$ nm, green) and N1307313 ($d_{\text{ND}} = 4.4$ nm, red) are shown in a). Also, the ensemble spectrum of a n.i.d. GaN NW sample (N140820) was added for comparison. The spectra of the Ge-doped samples N1303043 (n.i.d., $d_{\text{ND}} = 3.6$ nm, red), N1303063 ($BEP_{\text{Ge}} = 5 \times 10^{-10}$ mbar, $d_{\text{ND}} = 3.5$ nm, green) and N1303073 ($BEP_{\text{Ge}} = 1 \times 10^{-9}$ mbar, $d_{\text{ND}} = 3.2$ nm, blue) are displayed in b). All spectra in b) were normalized to the ND emission. Data used for b) has previously been published in Ref. [112].

energy, demonstrating the influence of the QCSE (cf. chapter 2) in the 40x AlN/GaN NDSLs. For samples with $d_{\text{ND}} > 2.3$ nm and $BEP_{\text{Ge}} < 1 \times 10^{-9}$ mbar, an additional broad transition band in the range of 3.1 eV to 3.3 eV is visible in the spectra shown in figure 5.5 (gray arrows). In GaN NWs which are not surrounded by an AlN shell, an emission band at 3.215 eV was assigned to recombinations of excitons trapped by dislocations in the coalescence region of neighboring NWs (cf. chapter 4, section 4.3.2). Due to its energetic position at 3.1 eV to 3.3 eV, the transition band observed in the ND samples might be due to excitons trapped at dislocations at the interface between the GaN base and the AlN shell. A successive red shift of the ND emission is observed with increasing d_{ND} which amounts to 640 meV when d_{ND} is changed from 2.3 nm to 4.4 nm. In addition, the strong red shift is accompanied by a decrease of the ND PL intensity with respect to the GaN base

emission (figure 5.5a)). An enhanced QCSE for larger values of d_{ND} is the origin of this observation. The PL signal of the NDs, however, significantly blue shifts with increasing BEP_{Ge} (constant d_{ND}) as demonstrated by the PL spectra in figure 5.5b). The evolution of the peak energy with BEP_{Ge} is shown in figure 5.6a). Error bars in the latter represent the FWHM of the respective emission. The emission energy of the GaN NDs is blue shifted

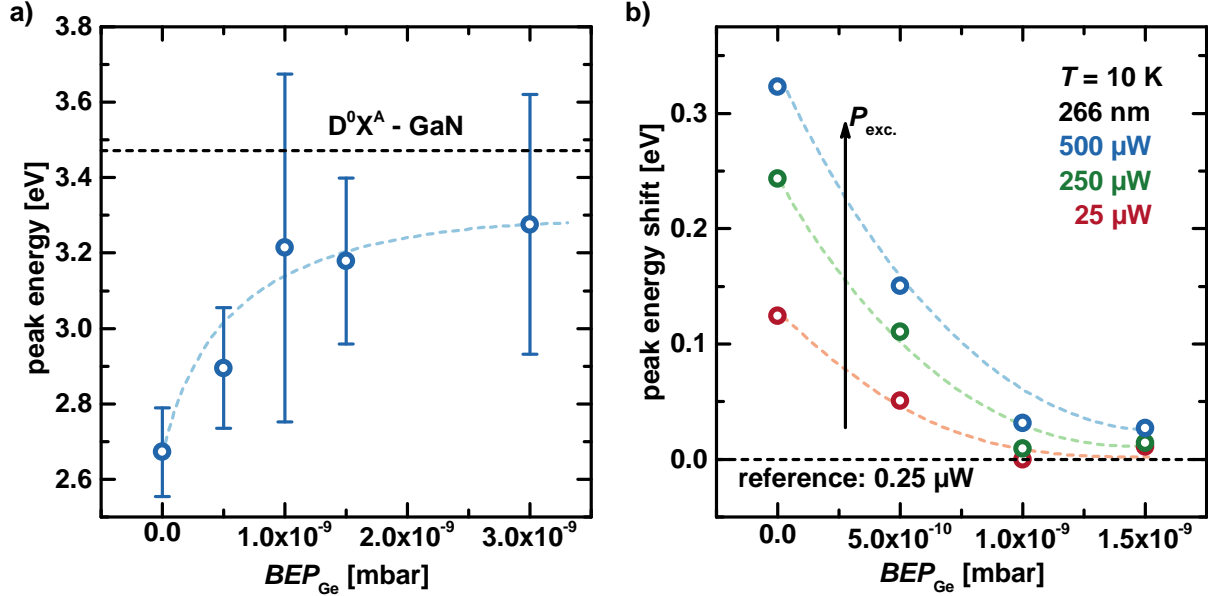


Figure 5.6: The evolution of the ND PL emission with increasing BEP_{Ge} is depicted in a). Error bars represent the FWHM of the respective luminescence signals. The shift of the ND emission, relative to its position for an excitation power of $0.25 \mu\text{W}$, is displayed for excitation powers of $25 \mu\text{W}$ (red), $250 \mu\text{W}$ (green) and $500 \mu\text{W}$ (blue) in dependence on BEP_{Ge} , in b). Dashed colored lines were added in both graphics to serve as a guide to the eye and a dashed horizontal line is given at the energy of the D^0X^A emission in GaN (3.472 eV). The data that was used in a) and b) has been published in Ref. [112].

from 2.67 eV (n.i.d.) to 3.3 eV ($BEP_{\text{Ge}} = 3 \times 10^{-9} \text{ mbar}$) upon Ge-doping, however, it remains below the D^0X^A energy (dashed line in figure 5.6a)). A saturation of the blue shift is observed above $BEP_{\text{Ge}} = 1 \times 10^{-9} \text{ mbar}$ which corresponds to a dopant concentration of $2 \times 10^{20} \text{ cm}^{-3}$, according to Ref. [54]. These results already imply significant screening of the internal electric fields by Ge-doping of the GaN NDs. Band gap renormalization [113] effects were not observed by Schäfer et al. in homogeneously Ge-doped GaN NWs up to free carrier concentrations of $5 \times 10^{19} \text{ cm}^{-3}$ [109]. However, a superposition of band gap renormalization and the Burstein-Moss shift might also lead to the observed behavior of the ND emission energy. In the present case, a comparison of the measurements and calculations of the transition energies of the GaN:Ge NDs suggest carrier concentrations

above 10^{20} cm^{-3} [114]. Hence, exchange interaction of carriers probably plays a dominant role in attenuation of the doping-induced blue shift of the ND PL emission. Furthermore, the free carrier concentration might still not suffice to fully screen the internal electric fields. Electrostatic screening of the polarization-induced fields in the GaN NDs should also be observed when the optical power for the PL excitation is increased. The shift of the ND emission due to screening by photo-excited carriers ($\lambda_{\text{exc.}} = 266 \text{ nm}$) as a function of the BEP_{Ge} is depicted in figure 5.6b)³. The reference value was obtained at an optical pumping power of $0.25 \mu\text{W}$ and the excitation power was increased up to $500 \mu\text{W}$. All samples exhibit an increasing blue shift of the ND PL with increasing excitation power. Therefore, full screening of the internal electric fields is not achieved, even for the highest doping concentrations. However, the relative shift of the PL signal due to the presence of photo-excited carriers is reduced for increasing BEP_{Ge} which implies that a higher concentration of free carriers is already present at high dopant concentrations. In addition, the effect of Ge-doping on the dependence of the ND luminescence energy on d_{ND} was analyzed. A nominal barrier thickness of 4 nm was used. The results are summarized in figure 5.7. The emission energy of the n.i.d. GaN NDs is shifted above the GaN bandgap for $d_{\text{ND}} < 2 \text{ nm}$. Larger values of d_{ND} lead to the aforementioned strong decrease of the luminescence energy, significantly below the GaN NBE regime (dashed horizontal line in figure 5.7). This red shift is much more pronounced for undoped samples (blue and yellow symbols) than for those containing Ge-doped GaN NDs ($BEP_{\text{Ge}} = 8.7 \times 10^{-10} \text{ mbar}$), confirming the screening of internal electric fields by free carriers in the doped samples. However, further proof is required to unambiguously assign the observed behavior of the ND PL to the electrostatic screening of the internal electric fields. The observed blue shift of the PL peak energy upon Ge-doping is expected to be accompanied by an increase of the oscillator strength when the QCSE is attenuated. TR-PL measurements were performed to assess this relation. Figure 5.8 presents the temperature dependence of the luminescence decay times in the GaN NDs⁴. A n.i.d. sample as well as samples doped with $BEP_{\text{Ge}} = 5 \times 10^{-10} \text{ mbar}$ to $1.5 \times 10^{-9} \text{ mbar}$ were used. Data of a n.i.d. QW was added for comparison. Detailed information about the measurement setup is given in Ref. [115]. At $T = 4 \text{ K}$, the PL decay time of n.i.d. GaN NDs is found to be one order of magnitude higher ($\tau = 4 \mu\text{s}$) than that of n.i.d. QWs ($\tau = 0.3 \mu\text{s}$). The high temperature stability of the PL decay times of the ND samples ($\Delta\tau = \pm 10\%$) compared to the QW sample demonstrates excellent 3D confinement in the NDs with a negligible influence of non-radiative recombination. An

³Measurements were performed by Dr. Nils Rosemann and Prof. Dr. Sangam Chatterjee.

⁴Measurements were performed by Dr. Mark Beeler, Dr. Joel Bleuse, Caroline Lim and Dr. Eva Monroy at the *CEA Grenoble (INAC/SP2M)*.

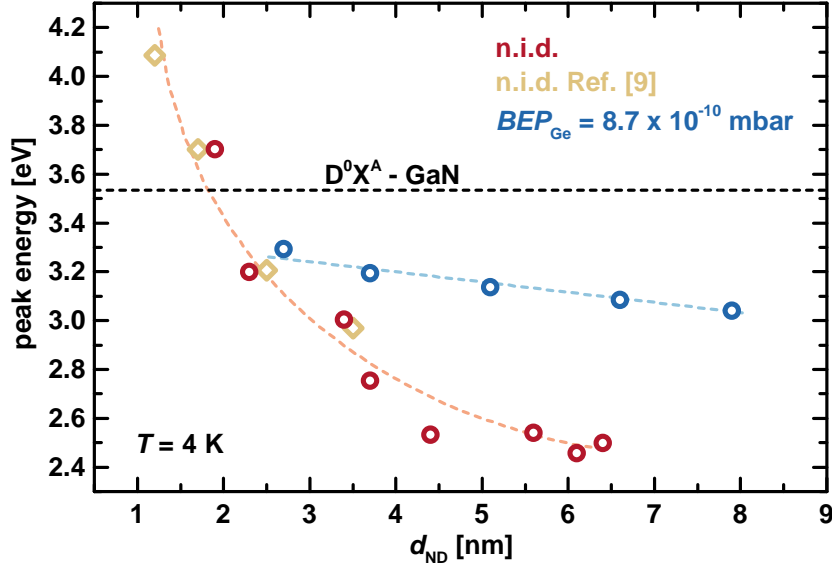


Figure 5.7: The dependence of the ND PL peak energy on d_{ND} is shown. Red circles represent data obtained on n.i.d. NDs while blue circles correspond to samples in which the NDs were doped with $BEP_{Ge} = 8.7 \times 10^{-10}$ mbar. The yellow diamonds are datapoints taken from Ref. [9] which were measured on 9x GaN NDs embedded in AlN barriers. Dashed colored lines were added to serve as a guide to the eye and a black dashed horizontal line is drawn at the energy of the D^0X^A emission of GaN (3.472 eV). The data used for this figure was already published in Ref. [112].

increase of BEP_{Ge} to 1×10^{-9} mbar leads to a reduction of the observed decay time from $4 \mu\text{s}$ to 57 ns. This is also the range where the largest doping-induced blue shift of the ND emission ($\Delta E = 530$ meV) was observed (cf. figure 5.6a)). Further increase of BEP_{Ge} to 1.5×10^{-9} mbar only slightly reduces the carrier lifetime to 40 ns. Together with the observed blue shift of the PL emission peak, the strong decrease of the carrier lifetime with increasing Ge concentration clearly demonstrates the electrostatic screening of the internal electric fields in 40x AlN/GaN(:Ge) NDSLs which leads to an attenuation of the QCSE in these structures.

The origin of the unusually large luminescence decay times of the NDSLs in the μs range originate from radial carrier separation due to the existence of lateral electric fields in the GaN NDs which further reduce the oscillator strength in those structures. An in depth discussion based on *nextnano*³ simulations is presented in Ref. [115]. Some examples of band profiles calculated with *nextnano*³ are shown in section 5.3.

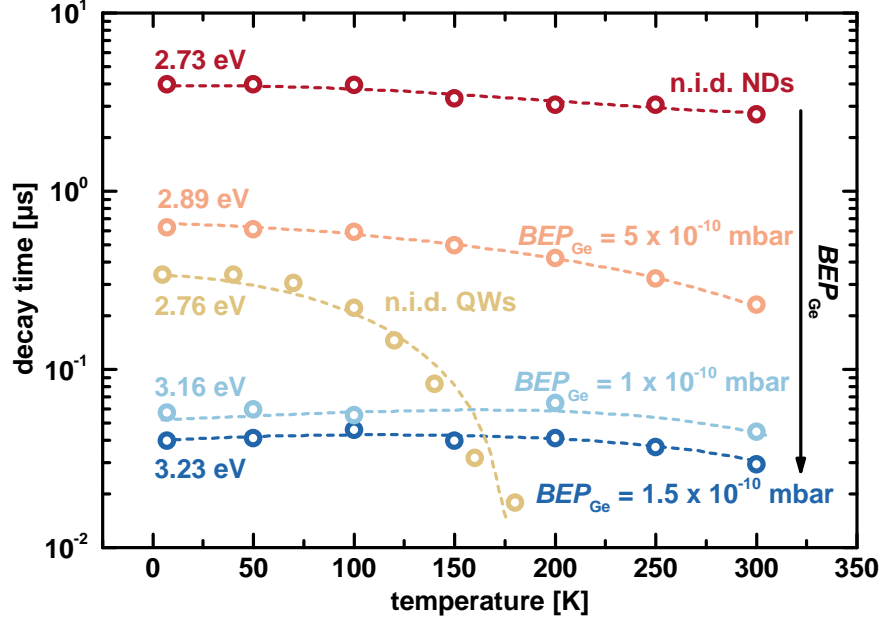


Figure 5.8: Temperature dependence of the PL decay times of samples N1303040 (n.i.d., dark red), N1303060 ($BEP_{Ge} = 5 \times 10^{-10}$ mbar, light red), N1303070 ($BEP_{Ge} = 1 \times 10^{-9}$ mbar, light blue) and N1303080 ($BEP_{Ge} = 1.5 \times 10^{-9}$ mbar, dark blue). Decay times measured on a n.i.d. QW (yellow) emitting at a similar energy as the n.i.d. AlN/GaN NDSL was added for comparison. The color coded emission energies correspond to the ND luminescence of the respective samples. Dashed colored lines were added as a guide to the eyes. The used data has been previously published in Ref. [115].

5.2 Influence of the AlN barrier thickness on internal electric fields

Another approach to reduce the internal electric fields in polar AlN/GaN NWHs is the introduction of the recently suggested Internal Field Guarded Active Region Design (IFGARD) [35]. Within the IFGARD model, the drop of the electrostatic potential which is usually observed in the active GaN region is shifted to the barrier material. This is achieved by reducing the thickness of the barrier material, thus bringing the oppositely charged barrier interfaces closer together. Hence, the electric field strength and thereby the QCSE are reduced in, *exempli gratia*, a GaN QW while the internal electric field strength is increased in the AlN barriers.

A series of samples with varying AlN barrier thickness ($d_{ND} = 4$ nm) was grown to experimentally assess the effect of IFGARD on 40x AlN/GaN NDSLs. A summary of the structural parameters of the investigated NWHs is given in table 5.2. Barrier and ND thicknesses d_i were determined by simulating the XRD ω - 2θ -scans using the *X'Pert Expi-taxy* software by PANalytical. As in section 5.1.1, TEM analysis was used to calibrate the

Probe	$d_{ND,XRD}$ [nm]	$d_{barrier,XRD}$	barrier relaxation [%]
N1603020	4.8	0.85	0
N1602250	4.2	1.7	20
N1602150	4.2	4.1	90
N1602290	4.1	5.8	100

Table 5.2: *Summary of the structural parameters of the 40x AlN/GaN NDSLs for IFGARD experiments.*

initial simulation parameters. One of the simulation parameters is the relaxation degree of the individual layers in the simulated superlattice. Assuming nominally relaxed NDs, the relaxation of the AlN barriers increases from 0 to 100 % when $d_{barrier}$ is increased from 0.85 nm to 5.8 nm. However, an error of several percent has to be assumed for those simulations due to simplifications made by the software. For example, the lateral AlN shell and strain relaxation at the NW sidewalls cannot be included in the *X'Pert Expitaxy* software which has a significant effect on the strain distribution in the ND stack [9]. Hence, the actual strain in the GaN NDs will be larger compared to the simulations, whereas the AlN barriers are probably less strained due to elastic strain relaxation at the NW sidewalls. The simulations, therefore, only reveal the trend of the strain evolution in the NDSL with $d_{barrier}$ and do not give reliable values for the actual strain in the system.

Optical investigation of the 40x AlN/GaN NDSLs were conducted by low temperature PL spectroscopy. Figure 5.9a) displays the low temperature PL spectra of the 40x AlN/GaN NDSLs with varying $d_{barrier}$ ⁵. All spectra were normalized to the ND emission intensity to highlight the effect of $d_{barrier}$. A strong blue shift of the ND emission energy from 2.75 eV ($d_{barrier} = 5.58$ nm) to 3.34 eV ($d_{barrier} = 0.85$ nm) is observed. This blue shift is accompanied by the successive reduction of the FWHM of the ND luminescence from 680 meV ($d_{barrier} = 5.58$ nm) to 77 meV ($d_{barrier} = 0.85$ nm). The values of the FWHM were obtained by fitting a single Voigt function to the emission maximum of the spectrum. Hence, the FWHM determined for sample N1602290 ($d_{barrier} = 5.58$ nm) is presumably underestimated as a second emission is visible in the high energy shoulder of the respective spectrum. The blue shift of the ND luminescence energy with decreasing $d_{barrier}$ is a clear indication for the reduction of the internal electric fields.

Again, an unambiguous assignment of the PL energy blue shift with decreasing $d_{barrier}$ to a

⁵All PL experiments that are presented in this section were conducted by Sarah Kristina Schlichting and Dr. Gordon Callsen in the group of Prof. Axel Hoffmann at the Institut für Festkörperphysik of the Technische Universität Berlin.

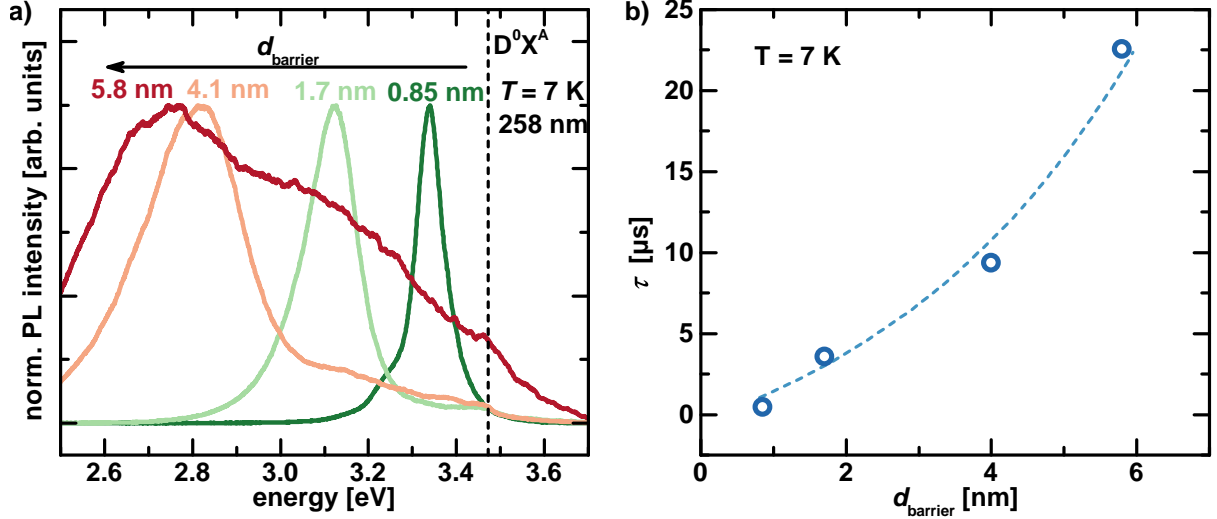


Figure 5.9: Low temperature PL spectra of 40x AlN/GaN NDSLs with varying d_{barrier} are displayed in a). The spectra were recorded on samples N1602290 ($d_{\text{barrier}} = 5.8$ nm), N1602150 ($d_{\text{barrier}} = 4.1$ nm), N1602250 ($d_{\text{barrier}} = 1.7$ nm) and N1603020 ($d_{\text{barrier}} = 0.85$ nm). All data was normalized to the ND emission. Figure b) depicts the dependence of τ on d_{barrier} . Luminescence decay times were measured at the peak energies of the spectra shown in a).

reduction of the internal electric field strength requires the demonstration of an accompanying increase of the oscillator strength. Therefore, TR-PL experiments were carried out to measure the variation of the luminescence lifetime τ with d_{barrier} . Figure 5.9b) depicts the dependence of τ on d_{barrier} for the samples corresponding to the spectra shown in figure 5.9a). A decrease of τ s is observed with decreasing d_{barrier} which confirms the reduction of the internal electric fields by the application of IFGARD [35] to AlN/GaN NDSLs.

5.3 Comparison

In this section, the screening of internal electric fields by Ge-doping of the GaN NDs (cf. section 5.1) and the application of IFGARD to NDSLs (cf. section 5.2) are compared. All data used in this section corresponds to samples presented in table 5.1 and table 5.2 and is based on the data shown in figure 5.6a), figure 5.8 and figure 5.9. Figure 5.10a) depicts the shift of the PL peak energy ΔE_{PL} as a function of d_{barrier} and BEP_{Ge} relative to the samples with a nominal barrier thickness of 4 nm (N1602150) and $BEP_{\text{Ge}} = 0$ mbar (N1303043). Similar slopes of ΔE_{PL} are observed in the ranges of $d_{\text{barrier}} = 0.85$ nm to 4 nm and $BEP_{\text{Ge}} = 0$ mbar to 1×10^{-9} mbar. Higher values of BEP_{Ge} and d_{barrier} lead to shallower slopes of ΔE_{PL} . Figure 5.10b) shows the dependence of the normalized luminescence decay time τ on the parameters BEP_{Ge} and d_{barrier} . Again, decreasing d_{barrier} and increasing BEP_{Ge} significantly reduces the luminescence decay time up to 5% and 1%

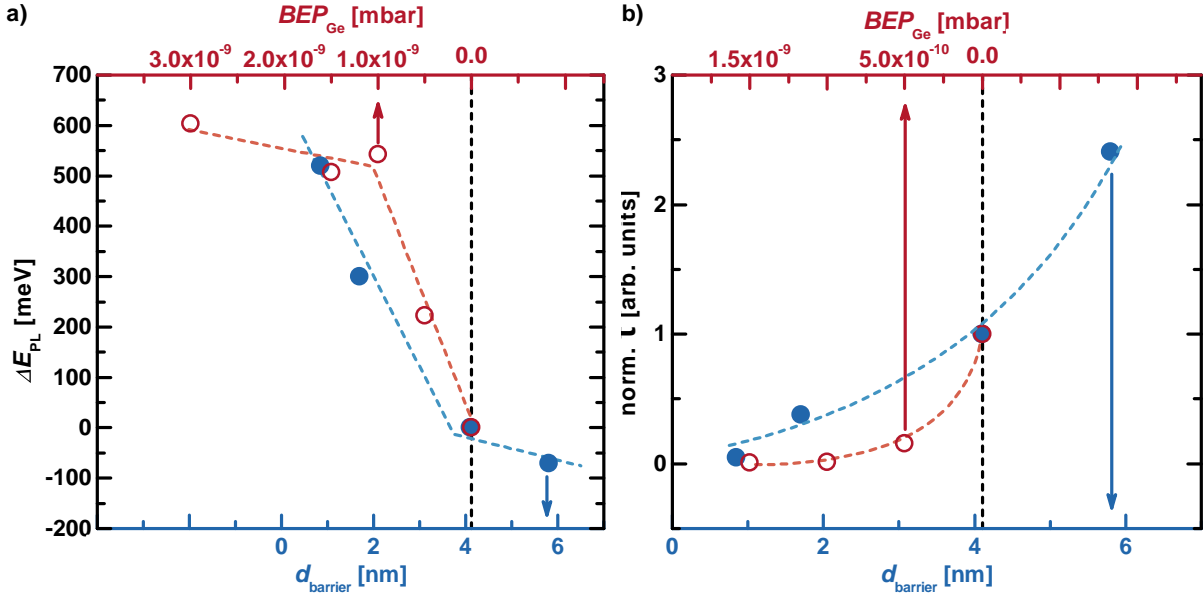


Figure 5.10: a) Relative shift of the ND PL energy ΔE_{PL} in dependence of $d_{barrier}$ (blue symbols, bottom abscissa) and BEP_{Ge} (red symbols, top abscissa). b) Normalized luminescence decay time τ as a function of $d_{barrier}$ (blue symbols, bottom abscissa) and BEP_{Ge} (red symbols, top abscissa). Values of the n.i.d. GaN NDs with $d_{barrier} = 4$ nm were used as reference data in figures a) and b). Dashed lines were added to guide the eye.

of the value observed for the samples grown with a nominal barrier thickness of 4 nm and $BEP_{Ge} = 0$ mbar. The luminescence decay time also decreases more rapidly with increasing BEP_{Ge} compared to a decrease of $d_{barrier}$. Hence, despite the apparent attenuation of the internal electric fields by either doping-induced free carriers or the application of IFGARD, both approaches have different effects on the optical properties. To illustrate, the difference between those two approaches, *nextnano*³ simulations are used. The results from the calculations published in Ref. [115] are used to describe the effect of free-carrier screening on the internal electric fields⁶ and will be qualitatively compared to simulations that were performed to understand the effect of IFGARD on AlN/GaN NDs⁷. Schematics of the input structures used in the calculations are presented in figure 5.11. The simulation parameters corresponding to simulations based on *Input A* and *Input B* are listed in appendix A.4. A lateral AlN shell was taken into account in all simulations, however, a constant shell thickness of 5 nm was used for *Input A* (constant $d_{barrier}$) while $r_{lateral}/r_{axial} = 5\%$ has been used in simulations according to *Input B* (variation of $d_{barrier}$), in agreement with the STEM investigations presented in section 5.1. The growth of the AlN shell leads to

⁶Simulation results by courtesy of Dr. Eva Monroy.

⁷Simulation results by courtesy of Jan Müßener.

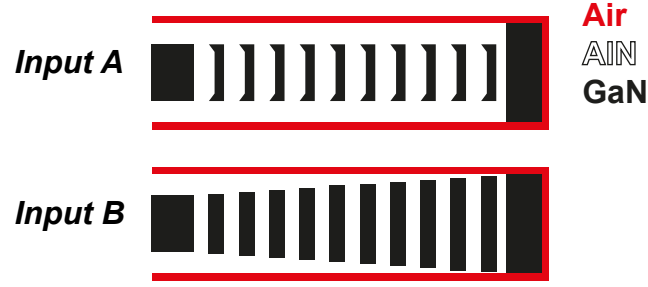


Figure 5.11: *Input A*: Schematic of the input structure used for the calculations of the doping-induced screening. *Input B*: Schematic of the input structure used for the calculations illustrating the effect of IFGARD. GaN is shown in black, AlN in white and the surrounding air volume in red.

an inhomogeneous radial and axial strain distribution in the GaN NDs which gives rise to non-zero shear strain components ϵ_{xz} and ϵ_{zx} resulting in the radial separation of electrons and holes by a radial electric field. For extensive studies on the effect of strain on the radial carrier confinement in polar GaN ND, the reader is referred to Refs. [7,9–11]. Truncation of the AlN barriers accounted for using *Input A* has a negligible effect on the radial position of electrons and holes [115]. A ND thickness of 4 nm was used in all simulations and d_{barrier} was kept constant at 4 nm for simulations according to *Input A* while it was varied for the simulations according to *Input B*. Figure 5.12a) and figure 5.12b) depict the axial CB and valence band (VB) profiles for a ND in the center of the stack for different free carrier concentrations n and different values of d_{barrier} , respectively. A carrier concentration of $1.7 \times 10^{20} \text{ cm}^{-3}$ transforms the sawtooth band profile (homogeneous electric field) into a s-shaped profile (inhomogeneous electric field). Electron and hole wavefunctions are, however, still located at the bottom and top interfaces, respectively [115]. In comparison, decreasing d_{barrier} does not modify the shape of the band profiles (only homogeneous electric fields). A reduction of the slope of the band edges with decreasing d_{barrier} is observed due to a reduction of the internal electric field strength. Figure 5.13a) and figure 5.13b) depict the lateral band profiles of a n.i.d. ND with $d_{\text{barrier}} = 4 \text{ nm}$ calculated according to *Input A* and *Input B*, respectively. Both simulations show the lateral separation of electrons and holes due to radial electric fields (arrows in figure 5.13). However, this effect is more pronounced in the case of simulation according to *Input A* due to radial electric fields in the range of several hundred meV compared to a field strength of only several ten meV when using *Input B*. The different radial electric field strengths are due to the different input parameters used in these calculations (cf. appendix A.4). Close to the ND/shell interface, the strain-induced band gap increase inside the ND additionally separates the

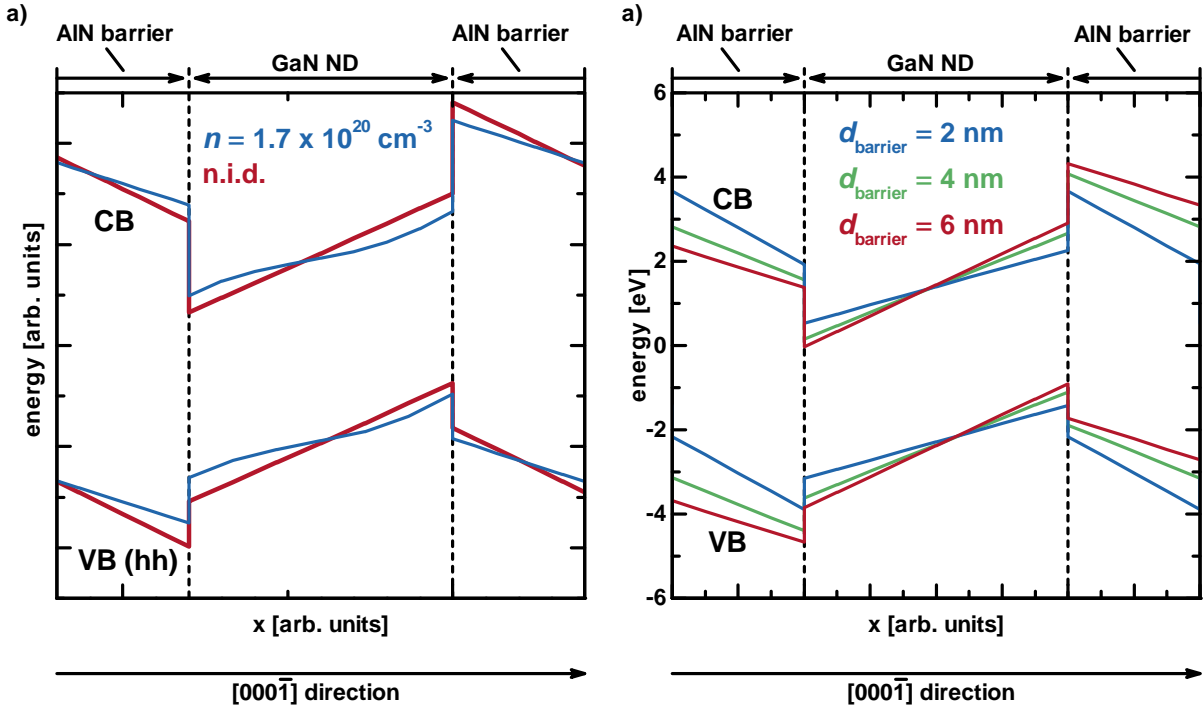


Figure 5.12: a) Axial CB and VB profiles for a n.i.d. GaN ND (red) and a ND with a free carrier concentration of $1.7 \times 10^{20} \text{ cm}^{-3}$ (blue) according to Input A. b) Axial band profiles for simulations of ND embedded in AlN barriers with different d_{barrier} according to Input B. Data used in a) was previously published in Ref. [115].

holes from this interface. Upon doping, the radial electric fields are efficiently screened and the holes are located in the ND center, radially aligning electrons and holes (figure 5.13c)). However, no qualitative change is observed upon a decrease of d_{barrier} to 2 nm in a n.i.d. GaN ND (figure 5.13d)). The holes move even closer to the lateral ND/shell interface for lower values of d_{barrier} indicating a weaker effect of strain-confinement due to a thinner AlN shell.

Based on the results of the simulations, the observed blue shift of the ND PL emission (cf. figure 5.10a)) is assigned to a reduction of the internal electric fields in axial direction. For high doping levels ($BEP_{\text{Ge}} > 1 \times 10^{-9} \text{ mbar}$), effects due to high n (*exempli gratia* band gap renormalization) seem to attenuate the blue shift of the emission energy (cf. figure 5.10a)). In contrast, the blue shift of the ND emission energy by IFGARD is only limited by the minimum of the experimentally accessible values of d_{barrier} . The significant reduction of the ND PL decay time in n.i.d. samples with decreasing d_{barrier} is also explained by the decrease of the axial electric field strength. However, only doping-induced screening allows to shield the lateral and axial electric fields simultaneously which explains the rapid reduction of

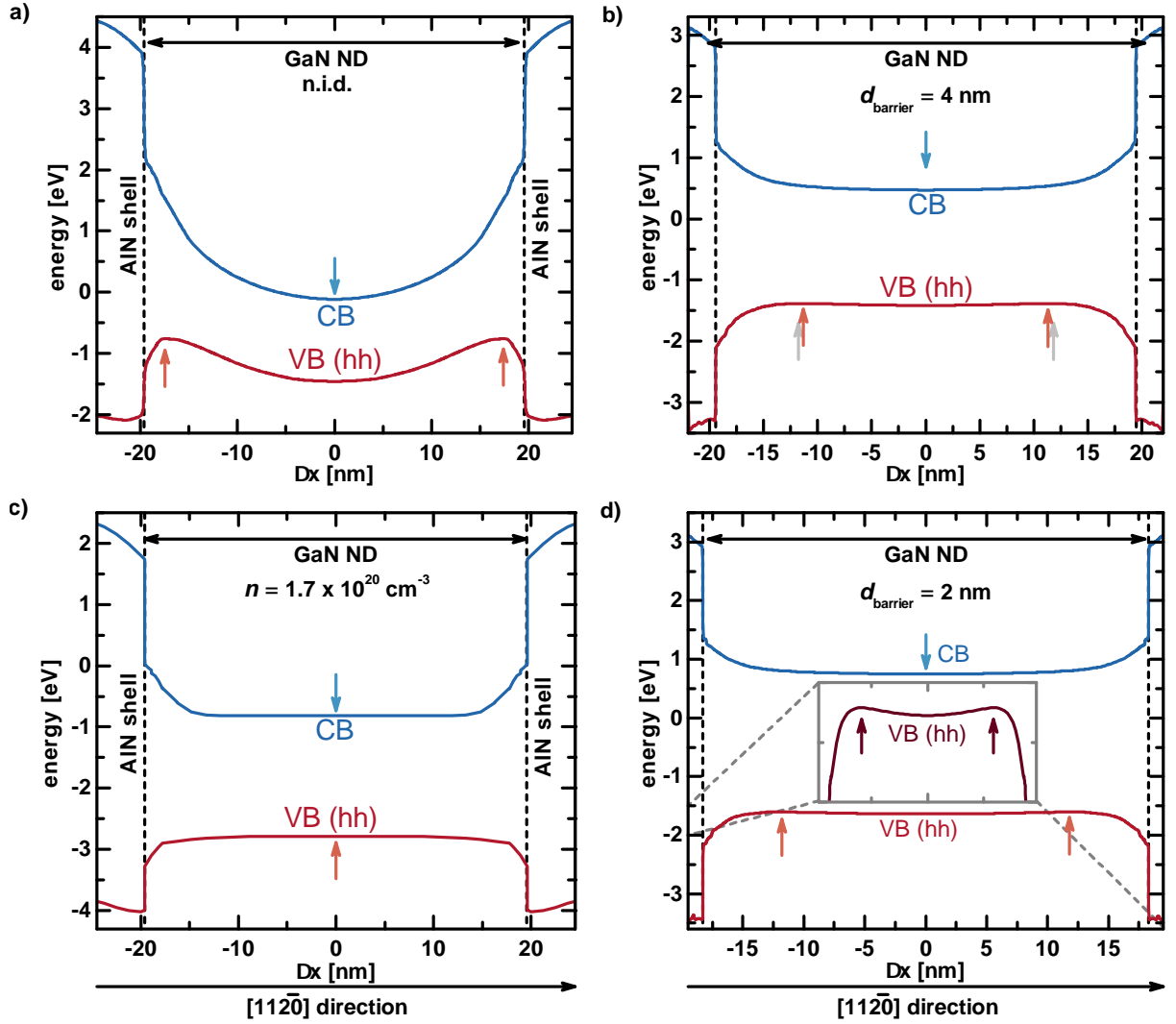


Figure 5.13: a) Lateral band profiles of a *n.i.d.* structure calculated according to Input A. b) Lateral band profiles of a ND with $d_{\text{barrier}} = 4 \text{ nm}$ calculated according to Input B. c) Lateral band profiles of a doped ND with $n = 1.7 \times 10^{20} \text{ cm}^{-3}$ calculated according to Input A. d) Lateral band profiles of a ND with $d_{\text{barrier}} = 2 \text{ nm}$ calculated according to Input B. The lateral position of electrons (blue) and holes (red) are highlighted by arrows and the lateral ND/shell interface is marked by vertical dashed lines. In addition, the lateral position of the holes for $d_{\text{barrier}} = 2 \text{ nm}$ is indicated by gray arrows in b). A magnification of the VB edge is shown as an insert in d). Data used in a) and c) was previously published in Ref. [115].

the luminescence decay time with BEP_{Ge} compared to the samples grown according to the IFGARD approach (cf. figure 5.10b)). Consequently, a combination of both sample designs is expected to further improve the efficiency of optical devices based on AlN/GaN NDSLs. Doping concentrations in the range of $n \approx 10^{19} \text{ cm}^{-3}$ are needed to fully screen the radial electric fields [115] which are probably achieved at $BEP_{\text{Ge}} = 1 \times 10^{-9} \text{ mbar}$ [109]. To

maximize the electron and hole recombination probability, d_{barrier} should then be chosen as low as possible.

5.4 Conclusion

Germanium doping of GaN NDs is suitable to achieve significant electrostatic screening of internal electric fields in polar 40x AlN/GaN NDSLs, as it allows the realization of high free carrier concentrations ($n > 10^{19} \text{ cm}^{-3}$). In n.i.d. GaN NDs, the lateral separation of photo-excited carriers in addition to the axial QCSE leads to an increase of the carrier lifetimes by more than one order of magnitude in comparison to n.i.d. 2D QWs. Furthermore, the decay times are rather constant up to room temperature which is due to efficient 3D carrier confinement by the inhomogeneous radial strain distribution in the NDs. For structural analysis, the high homogeneity of the superlattice periodicity in the analyzed samples enabled the determination of d_{ND} and d_{barrier} by XRD analysis.

Structures with constant d_{ND} and different d_{barrier} were fabricated to study the effect of the IFGARD on the PL properties of 40x AlN/GaN NDSLs. A strong influence of d_{barrier} on the ND emission energy and linewidth was observed. A blue shift and decreasing lifetime of the ND luminescence with decreasing d_{barrier} was attributed to the accompanying reduction of the axial internal electric field strength. In contrast to the doping-induced screening, the lateral electric fields are not reduced in the IFGARD samples.

6 $\text{In}_x\text{Ga}_{1-x}\text{N}/\text{GaN}$ nanowire heterostructures

The most prominent application of $\text{In}_x\text{Ga}_{1-x}\text{N}$ is in the field of solid state lighting which has also been acknowledged by awarding the Nobel Prize in Physics 2014 to Isamu Akasaki, Hiroshi Amano and Shuji Nakamura *"for the invention of efficient blue light-emitting diodes which has enabled bright and energy-saving white light sources"*¹. Besides the development of nano-LEDs [116], the possibility of tuning the band gap of $\text{In}_x\text{Ga}_{1-x}\text{N}$ from the UV (350 nm; $x = 0$) to the IR (1600 nm; $x = 1$) motivated the development of various NW-based device prototypes. The solar-to-hydrogen conversion by $\text{In}_x\text{Ga}_{1-x}\text{N}/\text{GaN}$ NWHs has been demonstrated [117, 118]. Also, the PL response of the latter to changes of the pH in liquid solutions [23] as well as the presence of H_2 , hydrocarbons [24] and oxidizing gases [25] was studied. The operation temperature of such devices is often above 100 °C to enhance the desorption of water and other adsorbates. Hence, an intense PL of the $\text{In}_x\text{Ga}_{1-x}\text{N}$ region is needed to ensure a sufficiently large signal-to-noise ratio at such high temperatures. The growth conditions of $\text{In}_x\text{Ga}_{1-x}\text{N}/\text{GaN}$ NWHs are discussed in this chapter focusing primarily on the influence of the atom source operating parameters on the structural and optical properties. Optimized growth parameters were used to fabricate 10x $\text{In}_x\text{Ga}_{1-x}\text{N}/\text{GaN}$ NDs.

6.1 Influence of the atom source operating parameters

Growth of high quality, high In content $\text{In}_x\text{Ga}_{1-x}\text{N}$ is challenged by the relatively low decomposition temperature of InN (565 °C [26]) and the presence of compositional fluctuations in the material [119]. The latter arises from spinodal decomposition of $\text{In}_x\text{Ga}_{1-x}\text{N}$ [120–122] due to its large miscibility gap [27], the strain-induced lattice pulling effect [89, 123–125] and facet-dependent In incorporation [126–128]. Increasing Φ_{N_2} during the PAMBE growth of $\text{In}_x\text{Ga}_{1-x}\text{N}$ has been predicted to have a stabilizing effect on the In-N bonds [129]. The model of Turski et al. was in line with the experimentally observed In content of $\text{In}_x\text{Ga}_{1-x}\text{N}$ layers ($x < 0.2$) [129]. However, the main parameters that have been used to adjust the In concentration in $\text{In}_x\text{Ga}_{1-x}\text{N}$ NWs are the substrate temperature [119, 124, 130] and the In/Ga flux ratio [120, 124, 131, 132]. Reports about the effect of the atom source operating parameters on the structural and optical properties of $\text{In}_x\text{Ga}_{1-x}\text{N}$ NWs grown by PAMBE are scarce. Recently, Albert et al. investigated the influence of Φ_{N_2} on the growth of $\text{In}_x\text{Ga}_{1-x}\text{N}/\text{GaN}$ NWHs [89]. A model explaining the morphological evolution of $\text{In}_x\text{Ga}_{1-x}\text{N}$ NWHs with Φ_{N_2} was proposed. The latter was based on the assumption that the NW diameter adjusts during growth to achieve local stoichiometric conditions at the growth front [89]. Also, Albert and coworkers observed a red shift of the $\text{In}_x\text{Ga}_{1-x}\text{N}$ photo-

¹https://www.nobelprize.org/nobel_prizes/physics/laureates/2014/, last visited Jan. 30th 2017.

luminescence with increasing Φ_{N_2} which is in line with the model of Turski et al. mentioned earlier [129]. As discussed in chapter 4, atomic nitrogen can also drive the decomposition of the growing III-nitride material [74]. This effect is expected to be even more pronounced in the case of $\text{In}_x\text{Ga}_{1-x}\text{N}$ compared to GaN which is due to the smaller InN binding energy (1.98 eV [36]) compared to the one of GaN (2.2 eV [36]).

Therefore, an in-depth analysis of the influence of the atom source operating parameter on the structural and optical properties of $\text{In}_x\text{Ga}_{1-x}\text{N}$ grown on GaN NW templates is presented in this section. The analysis of the plasma composition by studying the emission spectra of the nitrogen discharge in the atom source was already presented in chapter 4, section 4.4.1. It will also be used for the discussion of the results which are presented in this section.

6.1.1 Growth and structural analysis

Table 6.1 summarizes the $\text{In}_x\text{Ga}_{1-x}\text{N}$ growth parameters of the studied samples. The

sample	P_{N_2} [W]	Φ_{N_2} [sccm]	T_{heater} [°C]
N1404250	400	0.4	500
N1404251	400	0.4	500
N1502201	400	0.4	486
N1405050	400	0.8	498
N1405082	400	1.6	496
N1405120	400	3.2	498
N1405121	400	3.2	498
N1405232	200	1.6	496
N1405193	300	1.6	501
N1405163	500	1.6	495

Table 6.1: Growth parameters of the $\text{In}_x\text{Ga}_{1-x}\text{N}$ region of the $\text{In}_x\text{Ga}_{1-x}\text{N}/\text{GaN}$ NWHs studied in this section.

samples were grown with different Φ_{N_2} at constant P_{N_2} , and *vice versa*. In table 6.1, the varied parameter is printed in bold letters. Nominally, 350 nm of $\text{In}_x\text{Ga}_{1-x}\text{N}$ was grown on top of GaN NWs with a nominal length of 300 nm. The $\text{In}_x\text{Ga}_{1-x}\text{N}$ was grown with a constant In/Ga ratio ($\text{BEP}_{\text{Ga}} = 1.4 \times 10^{-7}$ mbar, $\text{BEP}_{\text{In}} = 1.3 \times 10^{-7}$ mbar). Different values of Φ_{N_2} (0.4 sccm to 3.2 sccm) and P_{N_2} (200 W to 500 W) were used for the growth of the $\text{In}_x\text{Ga}_{1-x}\text{N}$ segment. The nominal growth temperature measured with a pyrometer was 650 °C. The corresponding heater temperature T_{heater} is also given in table 6.1. Structural analysis of the samples was carried out by SEM, TEM and XRD

analysis.

Figure 6.1 depicts the top and side view SEM images of samples grown with different Φ_{N_2} . An increase of Φ_{N_2} from 0.4 sccm to 0.8 sccm ($P_{N_2} = 400$ W) leads to a change in

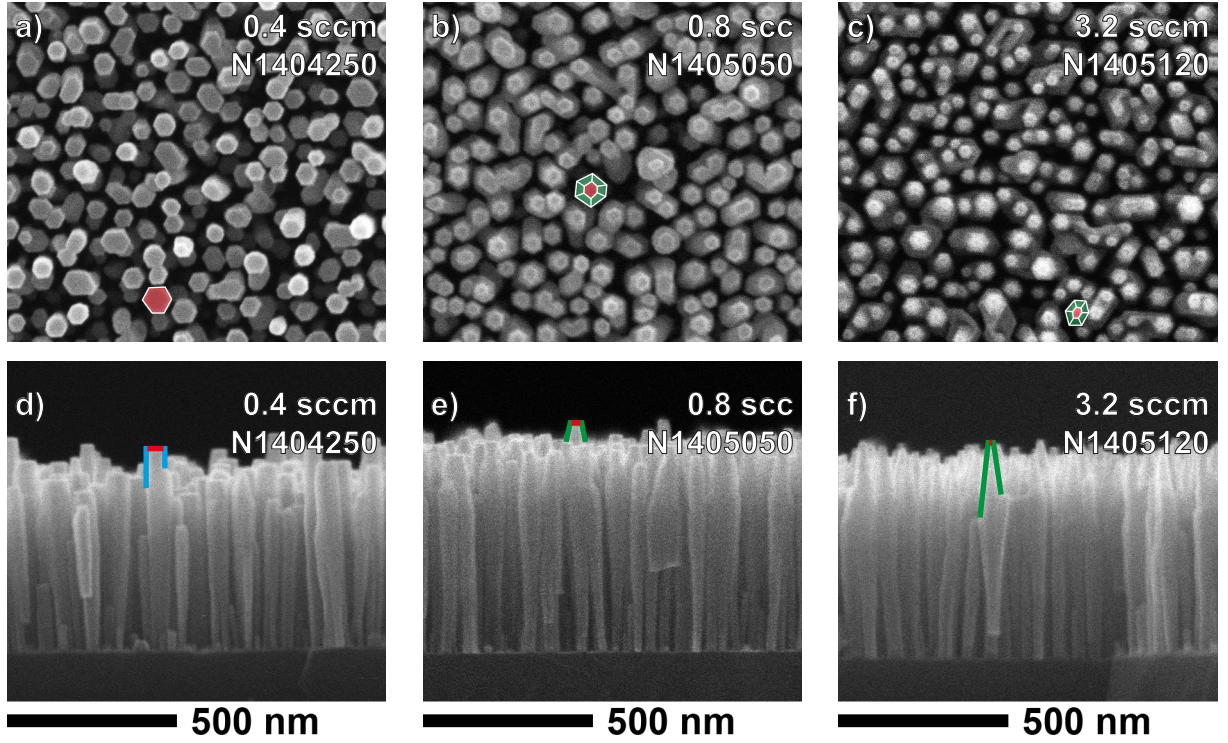


Figure 6.1: SEM top view images of samples grown with a) $\Phi_{N_2} = 0.4$ sccm, b) $\Phi_{N_2} = 0.8$ sccm and c) $\Phi_{N_2} = 3.2$ sccm are shown. Corresponding side view images are depicted in d), e) and f). All samples were grown with $P_{N_2} = 400$ W. Polar $(000\bar{1})$ surfaces are highlighted in red, semi-polar $(10\bar{1}\bar{l})$ surfaces in green and non-polar $(10\bar{1}0)$ planes in blue. The sample numbers are given in the respective images.

morphology of the NW tip. Prismatic shaped NWs with flat $(000\bar{1})$ surfaces (highlighted red) and straight m-plane side facets (highlighted blue) are obtained for $\Phi_{N_2} = 0.4$ sccm (figure 6.1a) and figure 6.1d)), while semi-polar $(10\bar{1}\bar{l})$ facets are introduced at the NW tip for $\Phi_{N_2} = 0.8$ sccm (green in figure 6.1b)) and in figure 6.1e). A similar morphology is observed for a further increase of Φ_{N_2} to 3.2 sccm, with the inclination starting earlier during the growth with a steeper angle compared to $\Phi_{N_2} = 0.8$ sccm. The latter leads to a reduced diameter of the $(000\bar{1})$ planes at the NW tip (cf. figure 6.1c)). These observations are in line with the model proposed by Albert et al. [89]. According to this model, the decrease of the NW tip radius increases the effective metal flux by diffusion of adatoms from the sidewalls to the growth front to keep a constant III/V ratio. An increase of the $\text{In}_x\text{Ga}_{1-x}\text{N}$ growth rate from 4.2 nm/min to 6.5 nm/min is observed upon an increase of Φ_{N_2}

from 0.4 sccm to 1.6 sccm, assuming a 300 nm GaN NW base for all investigated samples. Further increase of Φ_{N_2} to 3.2 sccm leads to a decrease of the growth rate to 4.9 nm/min similar to the GaN NW samples grown at high nitrogen fluxes which was assigned to hindered adatom diffusion by an increasing amount of inert N_2 (cf. section 4.4.2).

A variation of P_{N_2} did not systematically influence NW morphology or the growth rate. Single NWs of samples N1404251 ($P_{\text{N}_2} = 400 \text{ W}$, $\Phi_{\text{N}_2} = 0.4 \text{ sccm}$; figure 6.2a) and figure 6.2b)) and N1405193 ($P_{\text{N}_2} = 300 \text{ W}$, $\Phi_{\text{N}_2} = 1.6 \text{ sccm}$; figure 6.2c) and figure 6.2d)) were

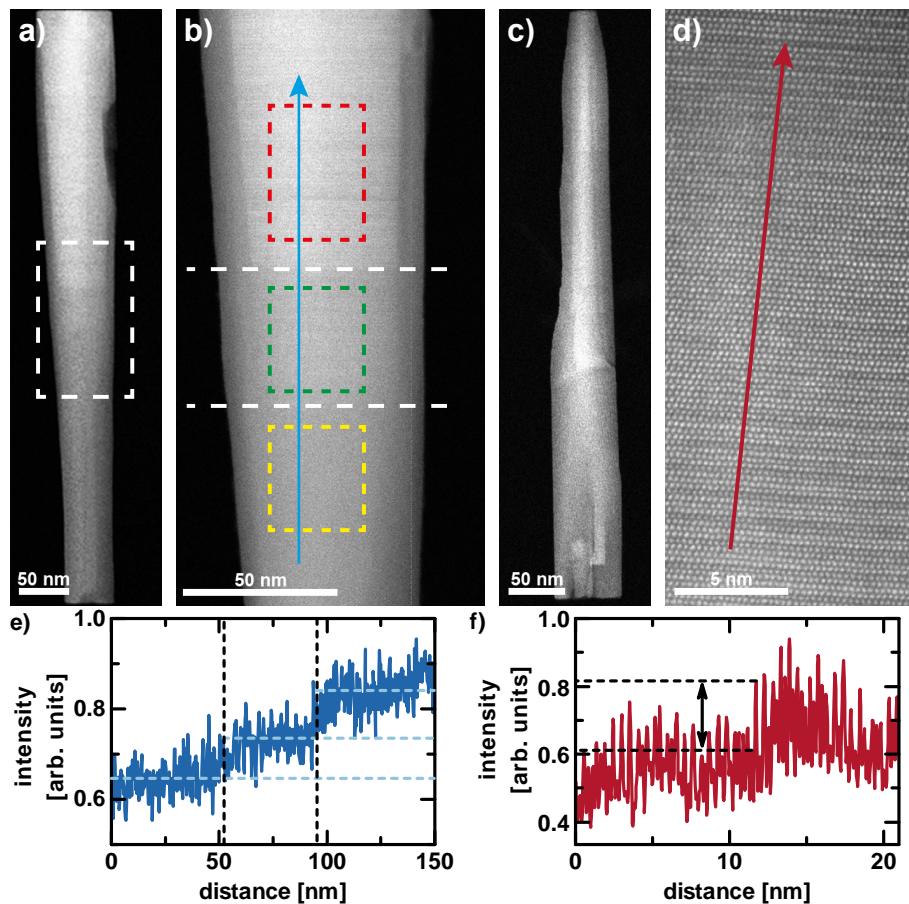


Figure 6.2: HAADF Z-contrast TEM images of SNWs from sample N1404251 ($\Phi_{\text{N}_2} = 0.4 \text{ sccm}$, $P_{\text{N}_2} = 400 \text{ W}$) in a) and b) as well as sample N1405193 ($\Phi_{\text{N}_2} = 1.6 \text{ sccm}$, $P_{\text{N}_2} = 300 \text{ W}$) in c) and d), are depicted. A magnification of the framed region in a) is shown in b). Horizontal lines indicate the interface between regions of different mean In concentrations which were determined for the colored framed details. An intensity linescan along the blue arrow in b) is displayed in e). The interfaces are marked by vertical dashed lines. Atomic resolution is achieved for the image in d) which corresponds to the tip region of a NW from sample N1405193. An intensity linescan was taken along the direction of the red arrow and is displayed in f). The arrow highlights the intensity change of two neighboring $\text{In}_x\text{Ga}_{1-x}\text{N}$ bilayers.

additionally analyzed by HAADF Z-contrast imaging². The TEM images of the entire NWs, which are shown in figure 6.2a) and figure 6.2c), exhibit a clear contrast difference between the GaN NW base (dark) and $\text{In}_x\text{Ga}_{1-x}\text{N}$ top part (bright). Tourbot et al. reported the observation of In-enriched cores in similar $\text{In}_x\text{Ga}_{1-x}\text{N}/\text{GaN}$ NW structures analysed by electron tomography [125]. This was also found in EDX analysis of the present samples (figure 6.3a)) and in Refs. [117, 122, 124, 133]. Most of the NWs dispersed on the TEM

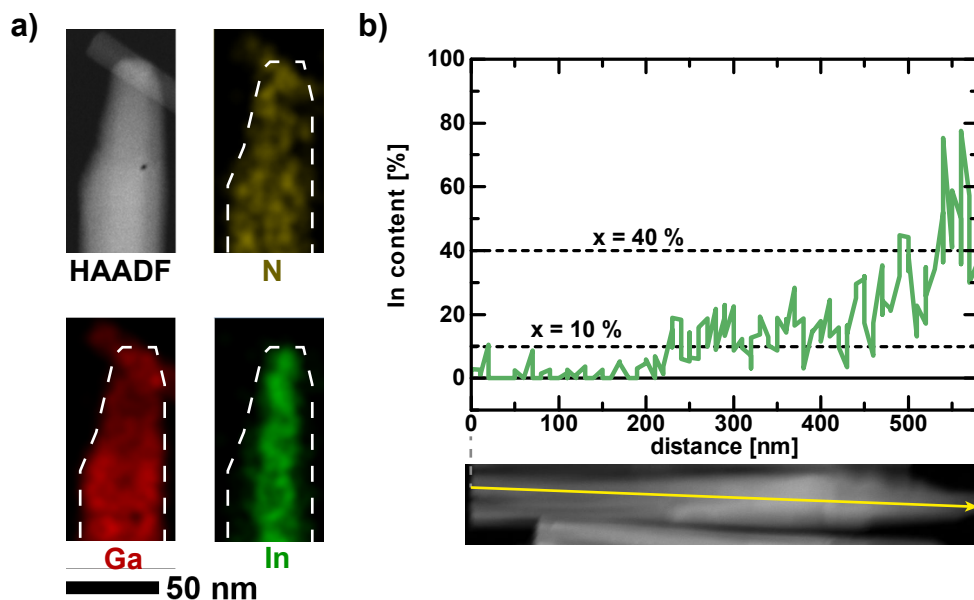


Figure 6.3: Figure a) displays the HAADF image of the tip of a NW from sample N1405193 together with the EDX mappings of nitrogen (yellow), gallium (red) and indium (green). The dashed line in the latter three images highlights the outline of the NW shown in the HAADF image. Another HAADF image of a NW from sample N1405193 is displayed below the graph in b). The graph presents the EDX determined In content that was measured along the yellow arrow overlaid to the TEM image.

grid did, however, exhibit a weaker contrast difference between the GaN base and the $\text{In}_x\text{Ga}_{1-x}\text{N}$ top. This indicates a rather low In concentration throughout the whole NW despite of In being present during the growth. An exemplary linescan of the In content (determined by EDX) in one of these NWs is depicted in figure 6.3b). The linescan was obtained along the growth direction (yellow arrow) overlaid to the HAADF TEM image shown below the graph. According to this measurement, the analyzed NW consists of a GaN base with a length of 225 nm which is covered by 350 nm $\text{In}_{0.1}\text{Ga}_{0.9}\text{N}$ followed by a gradual increase of the In content to a value around 40 % within the top 50 nm of the NW.

²TEM analysis and intensity calculations were performed by Dr. Katharina Gries in the group of Prof. Kerstin Volz at the Faculty of Physics and Materials Science Center of the Philipps-Universität Marburg.

This observation can be explained by the lattice pulling effect mentioned before and was, *exempli gratia*, also observed by Tabata and coworkers [124]. They also found a relatively low In concentration of 10 % along the NW growth axis and observed a strong increase of [In] up to 40 % in the last 100 nm of the NW [124].

Figure 6.2b) and figure 6.2d) depict the magnification of the framed region in figure 6.2a) and the tip of a NW from sample N1405193 ($P_{\text{N}_2} = 300 \text{ W}$; $\Phi_{\text{N}_2} = 1.6 \text{ sccm}$), respectively. An intensity linescan along the blue arrow in figure 6.2b) is shown in figure 6.2e). Three regions of different intensity (In content) can be identified from the linescan which are separated by horizontal dashed lines in figure 6.2b). The bottom region corresponds to the GaN NW base whereas the upper two regions correspond to $\text{In}_x\text{Ga}_{1-x}\text{N}$ segments with different mean In concentrations despite of nominally identical growth conditions. Higher intensities in the HAADF TEM images indicate a higher In content. Especially, the upper part of the NW displayed in figure 6.15b) shows an inhomogeneous intensity distribution (cf. figure 6.15e)) which indicates fluctuations of the In content. This is also evident from figure 6.2d), where the bilayers of the $\text{In}_x\text{Ga}_{1-x}\text{N}$ crystal are well resolved. The intensity linescan shown in figure 6.2f) was taken along the direction of the arrow in figure 6.2d). It visualizes the intensity fluctuations up several 10 % (arrow in figure 6.2f)) from one bilayer to the next. This is a clear indication of InN/GaN phase separation due to the aforementioned spinodal decomposition of the crystal [122].

A model developed by Rosenauer and Schowalter was used to assess the mean In concentrations in the framed regions of figure 6.2b) [52]. The HAADF TEM signal intensity which depends on the NW thickness and the mass of the elements in the analyzed sample region was calculated according to this model. Figure 6.4 depicts the results of simulations for hexagonal $\text{In}_x\text{Ga}_{1-x}\text{N}$ taking values up to $x = 0.5$ into account². The calculations were performed for the electron beam being parallel to the $(\bar{1}100)$ and $(11\bar{2}0)$ zone axis of the wurtzite lattice. Only the latter is displayed exemplary in figure 6.4. The simulations were compared to the measured intensities of several NWs that showed a clear intensity contrast between the GaN NW base and the $\text{In}_x\text{Ga}_{1-x}\text{N}$ capping. The former was used as an intensity reference for $x = 0$ (yellow frame in figure 6.2b)). For the NW depicted in figure 6.2b), a comparison to the calculations yielded In concentrations of 10% (green frame) and 30 % (red frame), respectively. A slight tapering of the NW in figure 6.2b) is visible. The variation of the NW diameter by 5 nm (cf. horizontal line in figure 6.4) already leads to a decrease of the determined In content by 10 %. Therefore, this method rather yields a rough estimate of the real In content in the $\text{In}_x\text{Ga}_{1-x}\text{N}$ NWs. The NWs also tend

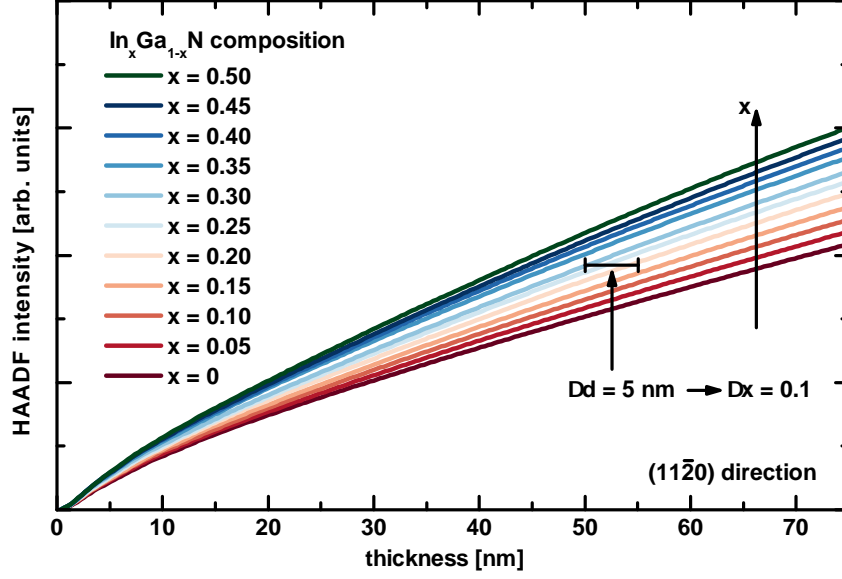


Figure 6.4: Calculations of the HAADF intensity in $[11\bar{2}0]$ direction in dependence on the sample thickness. The simulations were performed for different In contents x . The horizontal line indicates a sample thickness variation of 5 nm.

to agglomerate during the sample preparation³ and the coalescence of neighboring NWs is significantly enhanced due to the low substrate temperatures (cf. SEM top view images in figure 6.1). In addition, one of the zone axis' of the NWs ($(\bar{1}100)$ or $(11\bar{2}0)$) has to be precisely aligned with the electron beam for the model to be applicable. Hence, only a few NWs could be analyzed which prevented a systematic evaluation of the dependence of the In content on P_{N_2} and Φ_{N_2} . Nevertheless, Indium concentrations up to 50 % were measured in individual NWs. This is in contrast to the NWs exhibiting In contents of 10 % for the most part of their $In_xGa_{1-x}N$ segment.

Conclusively, the significant HAADF intensity fluctuations in the $In_xGa_{1-x}N$ part of individual NWs demonstrate strong variations of the In content down to the nm scale in SNWs. Additionally, the In content fluctuates from NW to NW and many NWs exhibit a segment of low In content ($x \approx 10\%$) with a length of several 100 nm while only the NW tip (< 100 nm) shows $x > 30\%$.

HRXRD reciprocal space maps (RSMs) were used to analyze the structural properties of $In_xGa_{1-x}N/GaN$ NW ensembles. Figure 6.5a) and figure 6.5b) show the RSMs of samples N1502201 ($P_{N_2} = 400$ W, $\Phi_{N_2} = 0.4$ sccm) and N1405121 ($P_{N_2} = 400$ W, $\Phi_{N_2} = 3.2$ sccm), respectively. To directly access the lattice parameters, the RSMs were converted to real

³NWs were either first suspended in isopropylalcohol or directly scratched onto a carbon grid for TEM analysis.

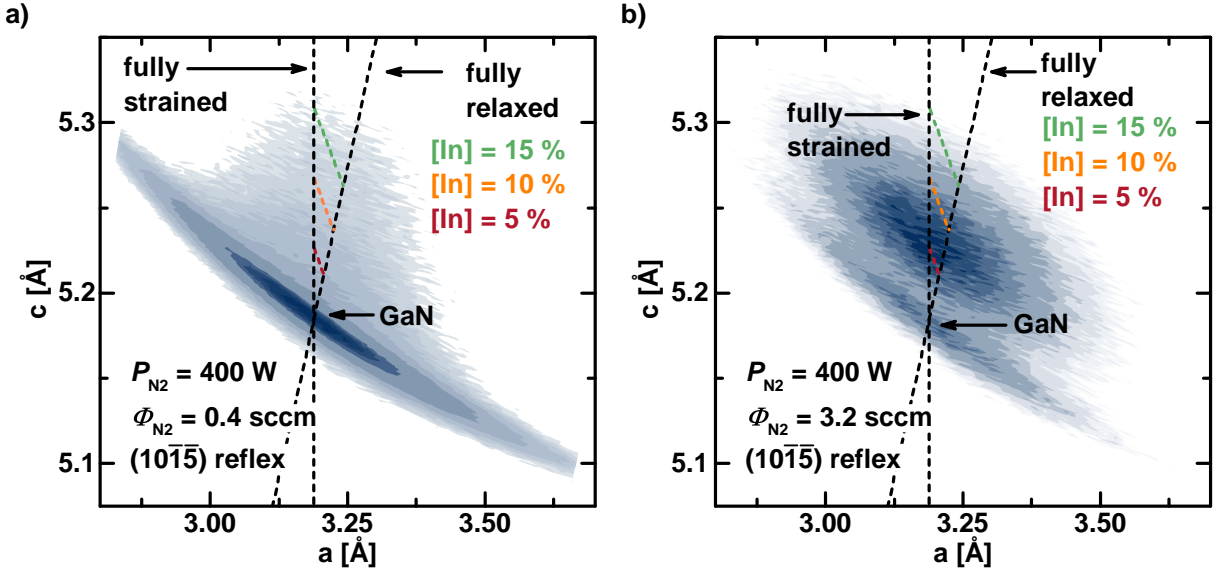


Figure 6.5: RSMs of the asymmetric $(10\bar{1}\bar{5})$ reflex are depicted after the conversion to real space units. The in plane (out of plane) lattice parameter is given on the abscissa (ordinate). Data shown in a) was obtained on sample N1502201 ($P_{N_2} = 400$ W, $\Phi_{N_2} = 0.4$ sccm) whereas the measurements for b) were performed on sample N1405121 ($P_{N_2} = 400$ W, $\Phi_{N_2} = 3.2$ sccm). Black dashed lines indicate the limits of fully strained (vertical line) and fully relaxed (tilted line) $\text{In}_x\text{Ga}_{1-x}\text{N}$. The two lines cross at the reflex of the GaN NW base. Additionally, isoconcentration lines were added to the graphics for $x = 5\%$ (red), 10% (orange) and 15% (green).

space. The abscissa gives the in-plane lattice parameter while the out of plane lattice parameter is plotted on the ordinate. Both RSMs exhibit a GaN reflex which is broadened due to the NW morphology. The NWs do not grow perfectly perpendicular to the surface normal of the Si(111) substrate, probably due to the amorphous Si_xN_y layer which forms before GaN NW nucleation [60]. No distinct $\text{In}_x\text{Ga}_{1-x}\text{N}$ related peak was observed for the sample grown with $\Phi_{N_2} = 0.4$ sccm (figure 6.5a)). However, significant intensity towards low In concentrations was detected in the shoulder of the GaN reflection. In contrast, raising Φ_{N_2} to 3.2 sccm gives rise to a signal with an intensity maximum indicating $x = 5\%$ to 10% (figure 6.5b)). No systematic deviation from the latter measurement is found for samples grown within the parameter ranges of $\Phi_{N_2} = 0.8$ sccm to 3.2 sccm ($P_{N_2} = 400$ W) and $P_{N_2} = 200$ W to 500 W ($\Phi_{N_2} = 1.6$ sccm). An unambiguous conclusion concerning the strain state of the $\text{In}_x\text{Ga}_{1-x}\text{N}$ top segment cannot be drawn as the peak is very broad, crossing both reference lines (fully strained and fully relaxed) in figure 6.5b).

The morphological and structural analysis of $\text{In}_x\text{Ga}_{1-x}\text{N}/\text{GaN}$ NWs grown under different

atom source operating parameters (Φ_{N_2} and P_{N_2}) are shortly summarized in the following:

- An increase of Φ_{N_2} leads to the formation of semi-polar facets at the NW tip.
- Long segments (several 100 nm) of low In content ($x \leq 10\%$) were observed in the NWs by EDX analysis, in agreement with the conducted XRD experiments. The In content increases to more than 30 % in the top 50 nm to 100 nm of the NWs.
- TEM analysis revealed an inhomogeneous In distribution in SNWs and In content fluctuations from NW to NW.

6.1.2 Photoluminescence spectroscopy

The optical properties of the $\text{In}_x\text{Ga}_{1-x}\text{N}/\text{GaN}$ NWHs (cf. table 6.1) were investigated on an ensemble (CW- and TR-PL) and SNW level (CW-PL).

Figure 6.6a) shows the low temperature PL spectra of the samples grown at different Φ_{N_2} ($P_{\text{N}_2} = 400$ W) and the spectra of SNWs from sample N1605083 ($\Phi_{\text{N}_2} = 1.6$ sccm) are depicted in figure 6.6b). Increasing Φ_{N_2} and thereby increasing the nitrogen partial pressure $p(\text{N}_2)$ and decreasing $n(\text{N})/n(\text{N}_2^*)$ (cf. chapter 4, section 4.4.1) successively red shifts the emission maximum from 2.48 eV ($\Phi_{\text{N}_2} = 0.4$ sccm) to 2.1 eV ($\Phi_{\text{N}_2} = 3.2$ sccm), corresponding to a change of the local In content from 27.8 % to 39.4 %, respectively. Calculations of the In content were based on the assumption that the emission energy represents the local band gap energy which allows the application of equation 2.1 using the parameters listed in Ref. [18]. The deviation of the PL data from the XRD results is in line with the assumption of potential fluctuations due to local In accumulation acting as radiative recombination centers. In the following, the In concentration x will be given according to the value calculated for the PL emission maxima. The systematic increase of the local In concentration with increasing nitrogen partial pressure is in accordance with previous reports [89]. Between 3.3 eV ($x = 5\%$) and 2.9 eV ($x = 15\%$), the PL emission expected for the In concentration extracted from XRD measurements is found. The related emission intensity is more than one order of magnitude lower than the emission from the In-rich regions in the NW, demonstrating efficient collection of photo-excited carriers by the potential minima in the $\text{In}_x\text{Ga}_{1-x}\text{N}$. A change of the spectral shape of the PL spectra is observed in addition to the red shift with increasing Φ_{N_2} . A single emission peak is recorded for sample N1404252 ($\Phi_{\text{N}_2} = 0.4$ sccm) while the spectra of the other samples ($\Phi_{\text{N}_2} > 0.4$ sccm) exhibit an additional emission in the high energy shoulder of the respective emission maximum. Therefore, SNW PL analysis was performed to elucidate the origin of this change in spectral shape. Figure 6.6 b) displays the spectrum of the

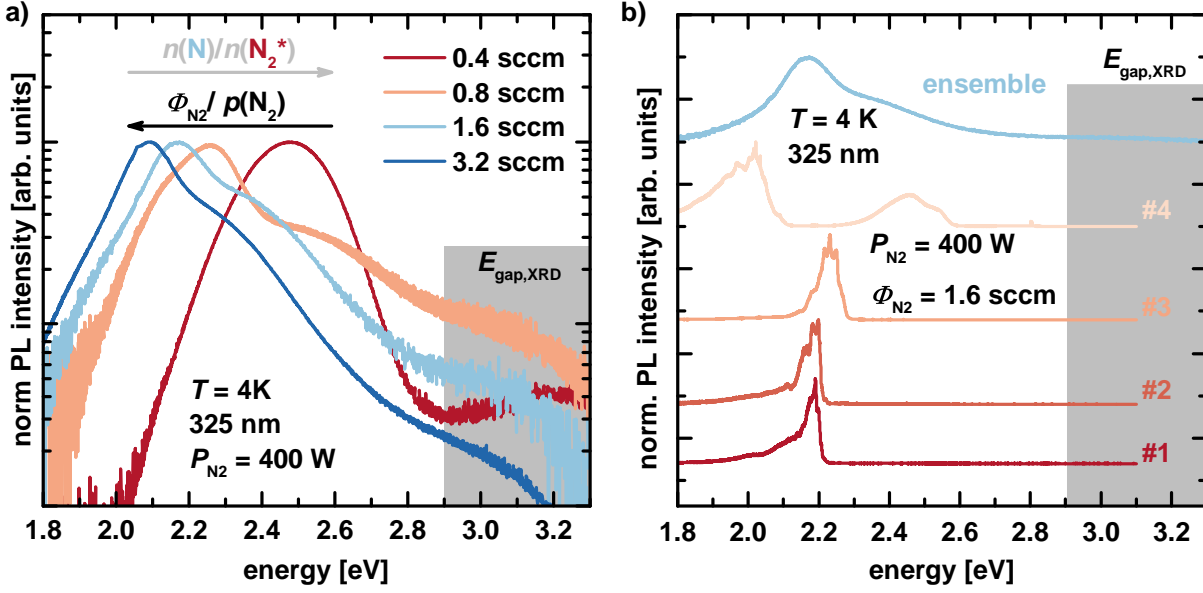


Figure 6.6: a) Low temperature PL spectra of samples N1404252 ($\Phi_{\text{N}_2} = 0.4\text{ sccm}$), N1405053 ($\Phi_{\text{N}_2} = 0.8\text{ sccm}$), N1405083 ($\Phi_{\text{N}_2} = 1.6\text{ sccm}$) and N1405121 ($\Phi_{\text{N}_2} = 3.2\text{ sccm}$). All samples were grown with $P_{\text{N}_2} = 400\text{ W}$. b) The SNW PL spectra of four NWs from sample N1405083 ($P_{\text{N}_2} = 400\text{ W}$, $\Phi_{\text{N}_2} = 1.6\text{ sccm}$) are compared to the ensemble spectrum (blue). All spectra were normalized to the emission maximum and a logarithmic scale was chosen for the ordinate in a). In the latter, arrows indicate the increase of Φ_{N_2} (black) and the nitrogen partial pressure (P_{N_2}) as well as the respective ratio of activated nitrogen species (gray). The spectral range of the PL expected from the results of the XRD analysis is marked by the gray area.

ensemble measurement performed on sample N1405083 ($\Phi_{\text{N}_2} = 1.6\text{ sccm}$) and the SNW PL spectra of four NWs from the same sample. All SNW spectra exhibit several sharp emission lines ($\text{FWHM} \leq 10\text{ meV}$) corroborating the assignment of the PL emission to local In-rich regions. In addition, NW #4 features two emission bands which are separated by more than 100 meV due to the significant fluctuations of the In content within one NW. However, none of the SNW spectra resembles the shape of the spectrum which was recorded on the NW ensemble. Conclusively, the ensemble's spectral shape is due to the strong fluctuations of the In content from NW to NW and the existence of two or more regions with different In concentrations in one NW.

Figure 6.7 depicts the low temperature ensemble PL spectra of the samples grown with different P_{N_2} at constant $\Phi_{\text{N}_2} = 1.6\text{ sccm}$. No systematic dependence of the emission energy on P_{N_2} is detected. A significant decrease of the emission intensity over the whole $\text{In}_x\text{Ga}_{1-x}\text{N}$ emission range is observed upon an increase of P_{N_2} . Therefore, an increase of $n(\text{N})/n(\text{N}_2^*)$ does not seem to affect the In incorporation but increases the non-radiative

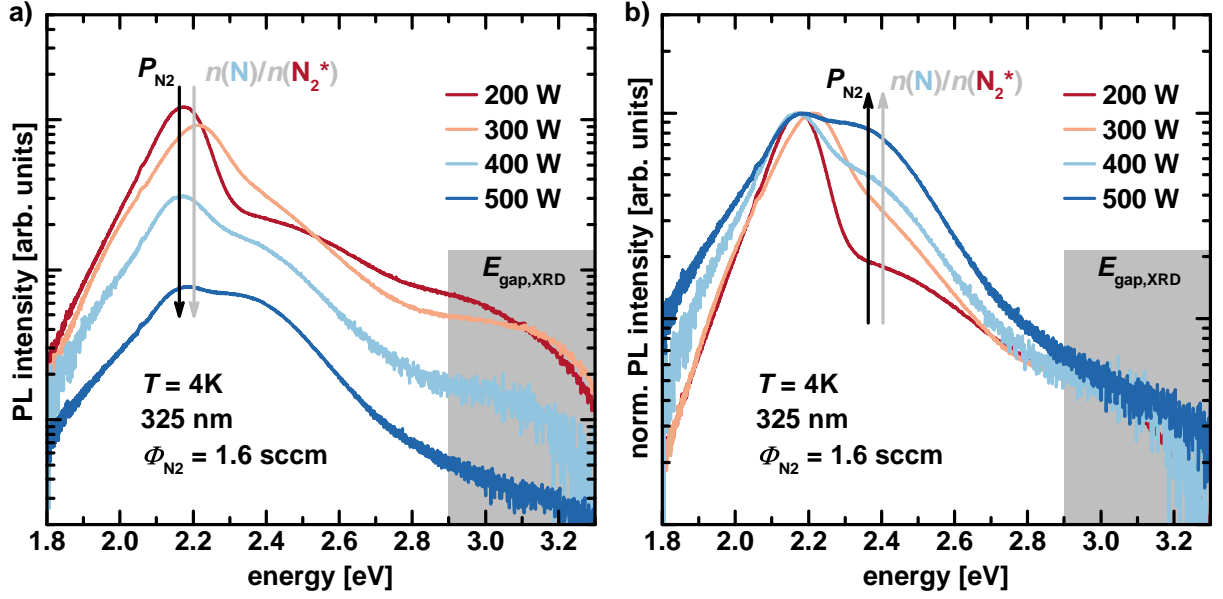


Figure 6.7: Low temperature PL spectra of samples N1405230 ($P_{N_2} = 200$ W), N1405193 ($P_{N_2} = 300$ W), N1405083 ($P_{N_2} = 400$ W) and N1405160 ($P_{N_2} = 500$ W). All samples were grown with $\Phi_{N_2} = 1.6$ sccm. The measured intensity is plotted in a) while all spectra shown in b) were normalized to the respective emission maxima to highlight the influence of P_{N_2} on the high energy emission shoulder. Arrows indicate the increase of P_{N_2} (black) as well as the respective ratio of activated nitrogen species (gray). The spectral range of the PL emission expected from the results of the XRD analysis is marked by the gray area.

recombination rate in $\text{In}_x\text{Ga}_{1-x}\text{N}/\text{GaN}$ NWs. The relative intensity decrease of the main emission and of the luminescence marked by $E_{\text{gap,XRD}}$ with increasing P_{N_2} is the same as evident from the normalized spectra shown in figure 6.7b). However, the relative emission intensity of the high energy shoulder in the main emission peak increases with increasing P_{N_2} . This indicates that the density of non-radiative defects increases faster with increasing $n(\text{N})/n(\text{N}_2^*)$ in those NWs that exhibit larger local In contents contributing to the main emission peak compared to those NWs with lower local In contents that contribute to the high energy shoulder of the ensemble spectrum.

Temperature dependent photoluminescence

Temperature dependent PL measurements were performed to gain insight into thermally activated mechanisms like carrier delocalization from potential fluctuations and thermally activated quenching of the PL. In addition, the internal quantum efficiency (*IQE*) can be estimated by comparison of integrated intensities at different temperatures. Figure 6.8a) depicts the PL spectra recorded on sample N1405230 ($P_{N_2} = 200$ W, $\Phi_{N_2} = 1.6$ sccm) in the temperature range from 4 K to 300 K. The main luminescence peak quenches relatively fast

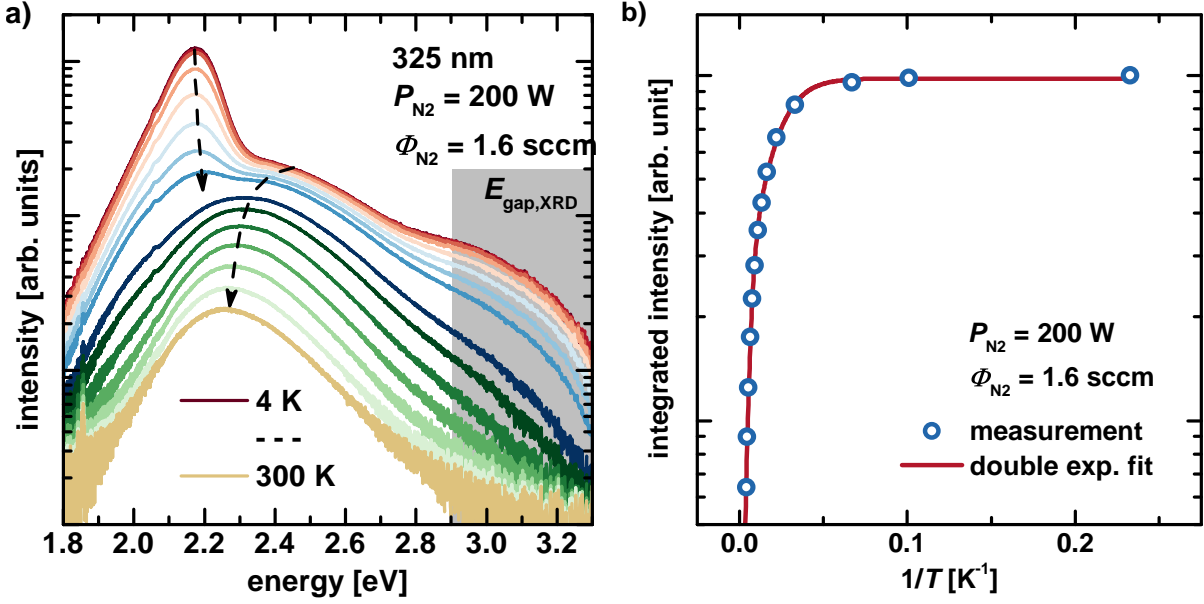


Figure 6.8: a) PL spectra recorded on sample N1405230 ($P_{N_2} = 200 \text{ W}$, $\Phi_{N_2} = 1.6 \text{ sccm}$) at temperatures ranging from 4 K to 300 K. Arrows indicate the evolution of the contributing emissions with increasing temperature. b) Corresponding Arrhenius plot of the integrated PL intensity of the measurements shown in a). Measured data is represented by symbols and a fit to those data points is shown in red.

in comparison to the emission at slightly higher energies. The latter dominates the spectrum at temperatures above 130 K. This is in line with the previous assumption of a higher density of non-radiative defects in vicinity of regions with higher local In content. The evolution of the PL spectra with temperature is qualitatively the same for all investigated samples. However, reliable deconvolution of the spectra was not possible over the whole temperature range due to the overlap of the high and low energy emissions at temperatures $> 130 \text{ K}$. and is therefore omitted. An Arrhenius plot of the integrated PL intensity of the spectra shown in figure 6.8a) is depicted in figure 6.8b). The data points were fitted with a double exponential function according to

$$I(T) = \frac{A}{1 + B \exp \frac{E_{\text{loc}}}{k_b T} + C \exp \frac{E_{\text{quench}}}{k_b T}} \quad (6.1)$$

The activation energies for delocalization of photo-excited carriers from potential fluctuations (E_{loc}) as well as the energy necessary for thermal quenching of the PL (E_{quench}) are obtained from the fit [134]. No physical meaning is extracted from the parameters A , B and C . Since the low energy emission dominates the spectra at lower energies, E_{loc} is mainly associated to the quenching of the PL emission from regions of high local In content. Above

100 K, the emission around 2.5 eV (at $T = 4$ K) dominates the spectra and, therefore, the E_{quench} is mainly determined by the quenching of this emission. Redistribution of carriers from regions of high local In content (low emission energy) to regions of low local In content (high emission energy) was observed in temperature dependent PL measurements performed on SNWs (figure 6.9). One NW exhibiting its emission band at the energy of

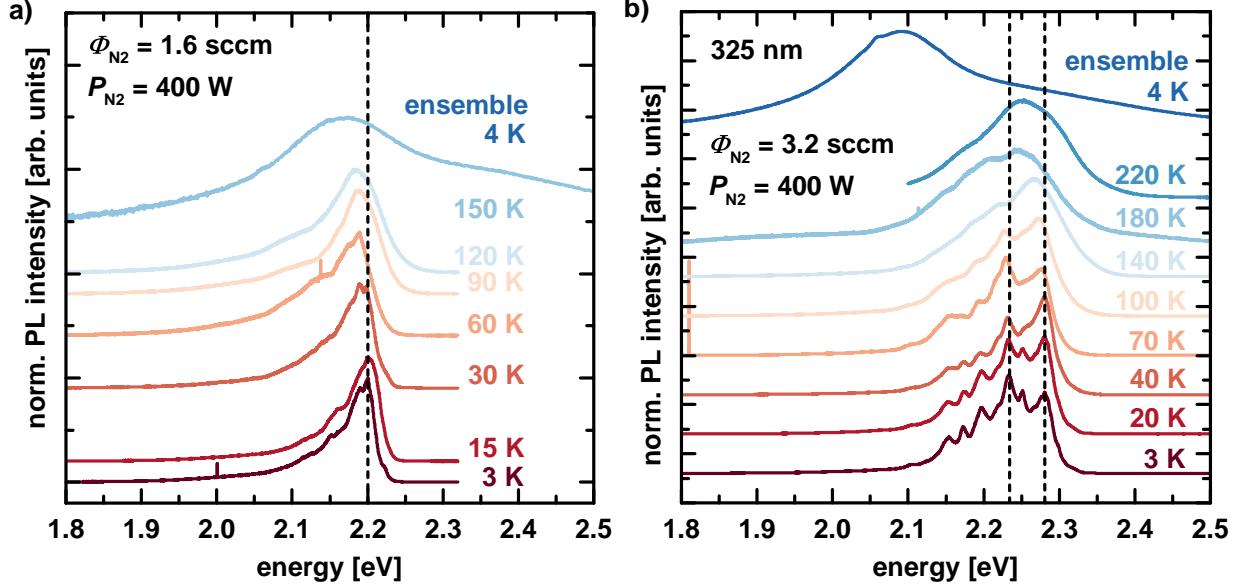


Figure 6.9: Temperature dependent PL measurements performed on a single NW of sample a) N1405083 ($P_{N_2} = 400$ W, $\Phi_{N_2} = 1.6$ sccm) and b) N1405120 ($P_{N_2} = 400$ W, $\Phi_{N_2} = 3.2$ sccm). A spectrum recorded at 4 K on the respective NW ensembles was added for comparison.

the main emission (high energy emission) was chosen for figure 6.9a) (figure 6.9b)). The energetic position of the emission bands remain relatively constant over the investigated temperature ranges. However, sharp emission features disappear with increasing temperature due to the additional thermal energy of the carriers and the formation of a broad emission band with a single peak is observed in figure 6.9a) and figure 6.9b). Hence, the observed temperature dependence of the PL of the NW ensemble is due to the different quenching behavior of the PL of SNWs emitting at different energies. Based on the measurements performed on NW ensembles, figure 6.10a) and figure 6.10b) depict the IQE and both activation energies as a function of Φ_{N_2} ($P_{N_2} = 400$ W) and P_{N_2} ($\Phi_{N_2} = 1.6$ sccm), respectively. The IQE was estimated according to

$$IQE = \frac{I_{300\text{K}}}{I_{4\text{K}}} \quad (6.2)$$

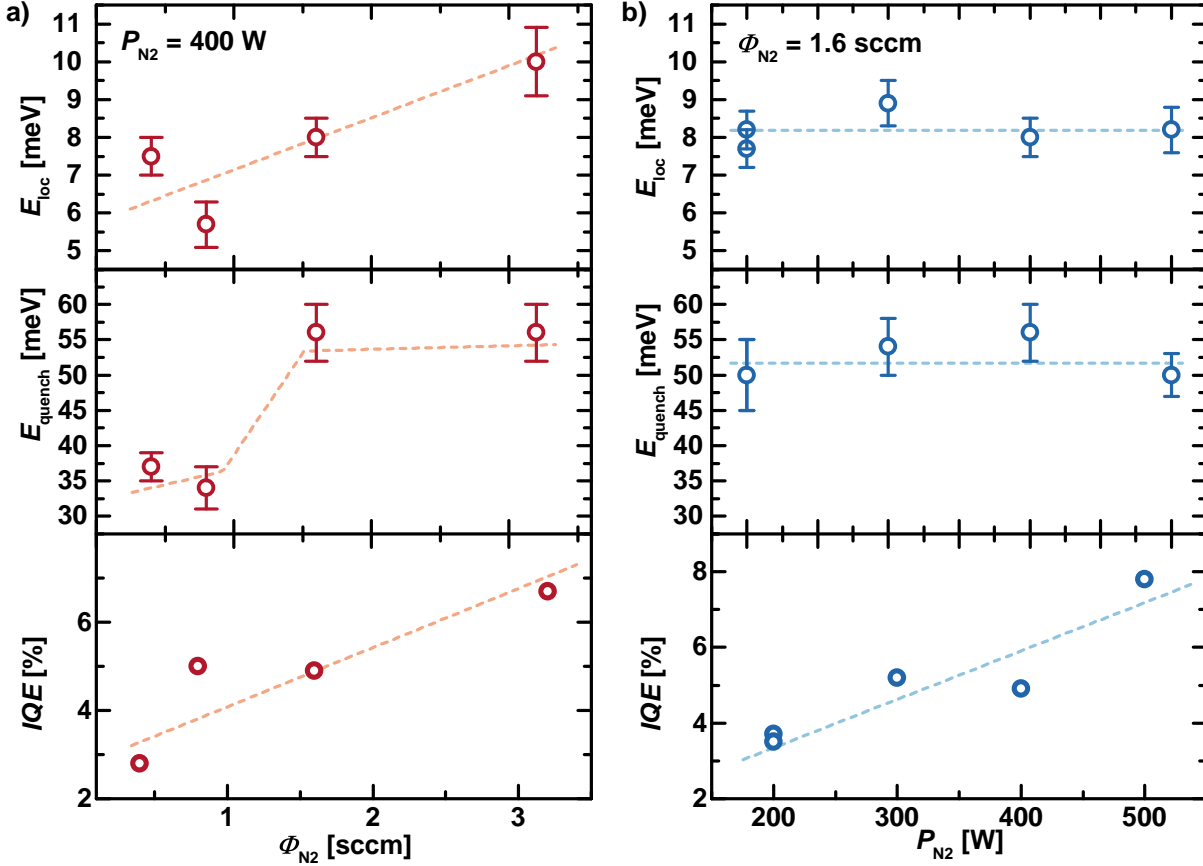


Figure 6.10: Activation energies E_{loc} , E_{quench} and IQE in dependence on a) Φ_{N_2} ($P_{N_2} = 400 \text{ W}$) and b) P_{N_2} ($\Phi_{N_2} = 1.6 \text{ sccm}$). Dashed lines were added as guides to the eye.

In equation 6.2, $I_{300\text{K}}$ corresponds to the integrated PL intensity at 300 K and $I_{4\text{K}}$ to its value obtained at 4 K. Increasing Φ_{N_2} during the $\text{In}_x\text{Ga}_{1-x}\text{N}$ growth leads to an increase of E_{loc} and E_{quench} . The increasing local In content due to the increase of the nitrogen partial pressure, hence, leads to an enhanced carrier localization. It also enlarges the energy barrier for photo-excited carriers to reach non-radiative recombination centers. Consequently, the IQE successively rises with an increase of Φ_{N_2} from 2.8 % at $\Phi_{N_2} = 0.4 \text{ sccm}$ to 6.7 % at $\Phi_{N_2} = 3.2 \text{ sccm}$ in agreement with previous reports on $\text{In}_x\text{Ga}_{1-x}\text{N}/\text{GaN}$ NWHs [29, 135]. In contrast to a variation of Φ_{N_2} , E_{loc} and E_{quench} remain constant (figure 6.10b)) when only P_{N_2} is changed despite of the significant reduction of the PL intensity with increasing P_{N_2} . The carrier localization does not change because the In content is not affected since the peak energy does not change with a variation of P_{N_2} . In addition, the type of non-radiative defects that are responsible for the quenching of the PL does not change over the investigated range of P_{N_2} because of the relatively unaffected E_{quench} in the range from 50 meV to 56 meV. However, the IQE increases with P_{N_2} from 3.5 % at $P_{N_2} = 200 \text{ W}$

to 7.8 % at $P_{N_2} = 500$ W despite of the significant decrease of the PL intensity that was observed for the same increase of P_{N_2} (figure 6.7a)). The explanation is given by the relative intensity increase of the PL peak in the high energy shoulder of the main emission with increasing P_{N_2} (figure 6.7b)). This emission is much more temperature stable as evident from the measurements presented in figure 6.8a). Hence, the increasing contribution of the emission around 2.5 eV to the overall spectrum leads to an increase of the *IQE* with increasing P_{N_2} . Samples grown at lower P_{N_2} , however, still have a significantly higher overall intensity at 300 K in direct comparison to those grown at higher P_{N_2} which is favorable for the device fabrication.

Time resolved photoluminescence

The CW-PL experiments suggest that the density of non-radiative defects is increased with increasing P_{N_2} (increasing amount of atomic nitrogen, cf. chapter 4, section 4.4.1). Time resolved PL spectroscopy was carried out to further assess this assumption⁴. Figure 6.11a) shows the low temperature PL spectrum of sample N1405053 ($P_{N_2} = 400$ W, $\Phi_{N_2} = 0.8$ sccm). Transients of the PL intensity recorded at the colored energy ranges are depicted in figure 6.11b). The carrier lifetimes decrease with increasing emission energy

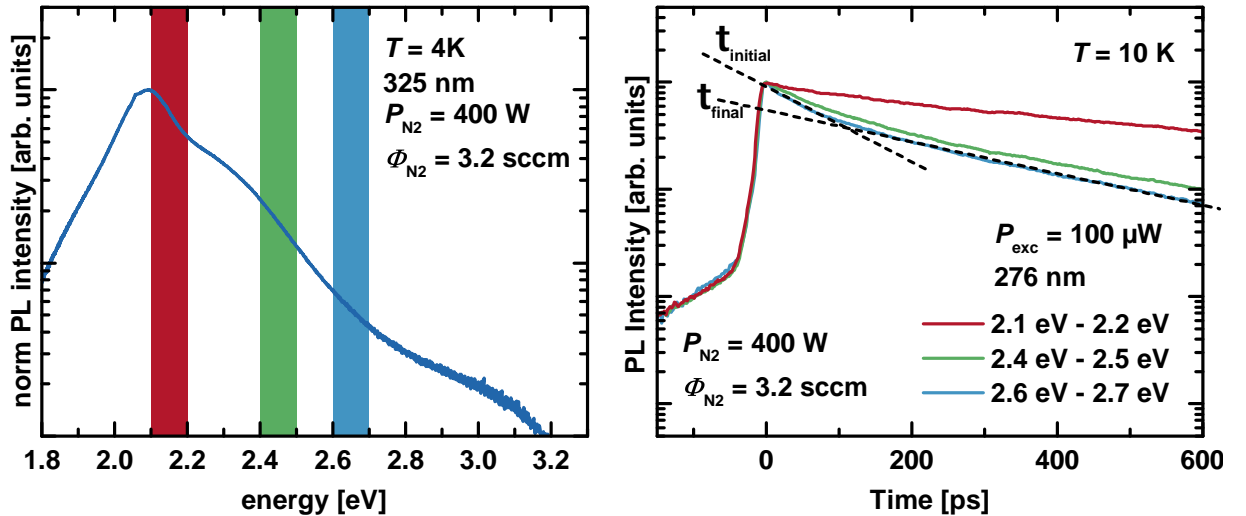


Figure 6.11: The low temperature PL spectrum of sample N1405053 is depicted in a). Graph b) displays the PL intensity transients recorded in the energy ranges that are highlighted by the corresponding colors in a). Dashed lines indicate the contributions of the two luminescence decay times described in the text.

⁴The TR-PL experiments were carried out by Dr. Nils Rosemann and Vanessa Dahmen in the group of Prof. Dr. Sangam Chatterjee at the Faculty of Physics and Materials Science Center of the Philipps-Universität Marburg.

which is a common observation in $\text{In}_x\text{Ga}_{1-x}\text{N}$ NWs due to exciton localization at local In accumulations [136]. This demonstrates that photo-excited carriers exhibit diffusion lengths that are large enough to reach regions of high local In contents in the NWs. A double exponential model was used to fit the transient data that was measured on the $\text{In}_x\text{Ga}_{1-x}\text{N}/\text{GaN}$ NWs yielding a fast (τ_{initial}) and slow (τ_{final}) time constant. Figure 6.12 illustrates the recombination dynamics for times t shortly after the excitation pulse and after the carrier relaxation process finished. The shorter τ_{initial} (cf. figure 6.11b)) reveals

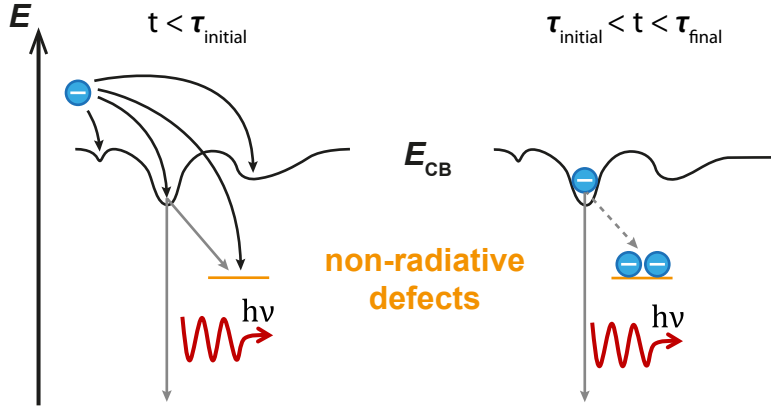


Figure 6.12: Schematic of the recombination dynamics shortly after the excitation pulse $t < \tau_{\text{initial}}$ and after the carrier relaxation process $\tau_{\text{initial}} < t < \tau_{\text{final}}$. The conduction band edge of $\text{In}_x\text{Ga}_{1-x}\text{N}$ is sketched together with energy levels of deep non-radiative recombination centers (orange). Fluctuations of the band gap due to an inhomogeneous In distribution were taken into account.

information about the relaxation of the carriers after photo-excitation where all recombination centers are available to the excited carriers leading to a rapid decrease of the PL intensity. Non-radiative recombination centers are quickly saturated ($\tau_{\text{initial}} < t < \tau_{\text{final}}$ in figure 6.12) and radiative recombination becomes the dominant process which is characterized by the larger time constant τ_{final} (figure 6.11b)). However, both carrier lifetimes are affected when the density of non-radiative defects increases due to a non-zero transition probability of relaxed carriers to non-radiative defects (dashed arrow in figure 6.12). Figure 6.13a) displays the normalized low temperature PL spectra of the samples that contain $\text{In}_x\text{Ga}_{1-x}\text{N}$ grown at different nitrogen fluxes. The PL decay times of the emission maxima were analysed in the marked energy ranges in dependence on the excitation power. Those results are depicted in figure 6.13b). Individually, a decrease of the carrier lifetimes is observed for high excitation powers ($P_{\text{exc}} > 1000 \mu\text{W}$) which is due to an enhanced carrier-carrier scattering. The shorter lifetime τ_{initial} is on the order of several 10 to 100 ps while the slower τ_{final} is in the range of 0.8 to 1 ns ($P_{\text{exc}} = 20 \text{ W}$). These values are in the same

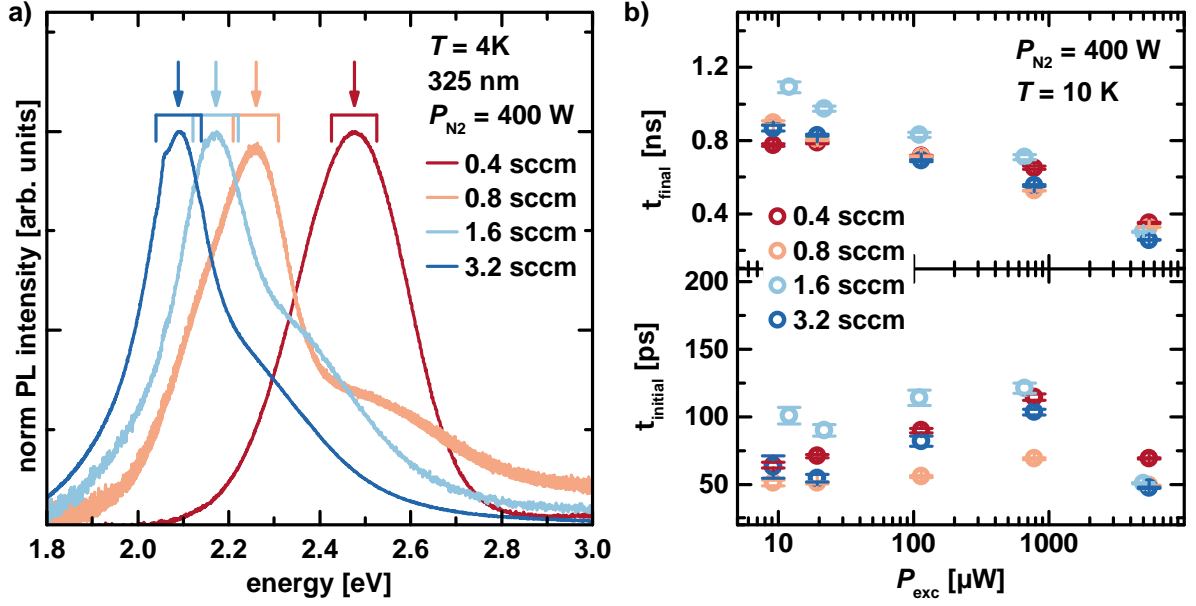


Figure 6.13: a) Low temperature PL spectra of the samples grown with different nitrogen fluxes. The investigated spectral ranges are marked by brackets. In b), the corresponding decay times τ_{final} and τ_{initial} are depicted as a function of the optical pumping power P_{exc} .

order of magnitude but by approximately a factor of five lower than those reported for other $\text{In}_x\text{Ga}_{1-x}\text{N}$ NWs [136, 137]. Neither τ_{initial} nor τ_{final} show a clear trend concerning Φ_{N_2} similar to the results obtained for the PL intensity. Hence, an increase of the local In content by stabilization of the In-N bonds due to an increase of the nitrogen partial pressure does not systematically introduce non-radiative defects.

The PL lifetimes measured for samples grown with different forward powers P_{N_2} are shown as a function of the optical pumping power P_{exc} in figure 6.14. All samples were grown with $\Phi_{\text{N}_2} = 1.6 \text{ sccm}$. A decrease of τ_{final} with increasing P_{N_2} is observed over the whole range of investigated excitation powers. At $P_{\text{exc}} = 100 \text{ W}$, values of $\tau_{\text{final}} = 1.26 \text{ ns}$ and 0.72 ns were obtained for samples N1405232 ($P_{\text{N}_2} = 200 \text{ W}$) and N1405160 ($P_{\text{N}_2} = 500 \text{ W}$), respectively. For an increase of P_{exc} to $660 \mu\text{W}$, τ_{initial} increases while it drops below 100 ps for all samples upon a further increase of P_{exc} . Assuming τ_{initial} to be correlated to the process of carrier relaxation directly links it to the exciton diffusion time τ_{diff} in the semiconductor. The diffusion length is calculated according to equation 6.3.

$$L_{\text{diff}} = \sqrt{D \cdot \tau_{\text{diff}}} \quad (6.3)$$

Increasing τ_{initial} consequently results in the increase of the diffusion length assuming a constant diffusion coefficient D . Therefore, the increase of τ_{initial} with an increase of the

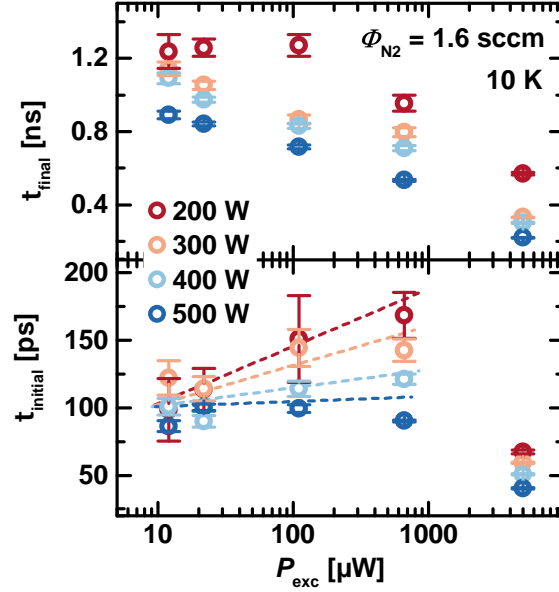


Figure 6.14: Decay times of the main $\text{In}_x\text{Ga}_{1-x}\text{N}$ luminescence of samples grown with different P_{N_2} (Φ_{N_2}).

excitation power indicates a saturation of radiative recombination centers as carriers have to be transported over larger distances to be localized at potential minima. The increase of τ_{initial} (L_{diff}) is more pronounced for samples grown with lower P_{N_2} as indicated by colored dashed lines in figure 6.14. This points to a decrease of the density of available recombination centers with decreasing P_{N_2} .

Conclusively, the reduction of the luminescence decay times and diffusion lengths, together, with the decrease of the PL intensity by more than one order of magnitude (cf. figure 6.7a)) demonstrates the significant increase of the density of non-radiative recombination centers when the relative amount of atomic N (P_{N_2}) is increased for the growth of $\text{In}_x\text{Ga}_{1-x}\text{N}$ NWs. Hence, damage induced by atomic N introduces additional non-radiative recombination centers in the $\text{In}_x\text{Ga}_{1-x}\text{N}$ segment of the NWs. This is due to the high reactivity of atomic N compared to excited molecular N_2 and the metastable growth conditions of $\text{In}_x\text{Ga}_{1-x}\text{N}$ during PAMBE [91]. The atomic N does not only drive the formation reaction of Ga-/In-N bonds but also facilitates the decomposition reaction which has already been observed in GaN growth experiments [138]. This is probably due to the large difference in binding energies of GaN (2.2 eV) and InN (1.98 eV) [36] compared to the strong triple bond of N_2 (9.81 eV) [139]. Ptak. et al. observed a significant decrease (increase) of the carrier mobility (concentration) for layers grown with a high amount of atomic nitrogen which was associated to the enhanced formation of point defects. Van de Walle et al. performed first

principle calculations of the formation energies of point defects in GaN [96]. They found similar formation energies of the investigated defects independent of the growth conditions being Ga- or N-rich. Results for InN are qualitatively comparable to those obtained for GaN [140]. The lowest formation energy was found for the V_N [96] which has been ascribed to the afore mentioned high binding energy of the N_2 molecule [140]. The decrease of luminescence decay times and emission intensity in the present $In_xGa_{1-x}N/GaN$ NWs is, therefore, assigned to non-radiative recombination channels introduced by V_N at higher fluxes of atomic N. This is in line with electrical and optical characterization of electron irradiated GaN layers published by Look et al. [97]. They found a donor with an activation energy of 70 meV which does not show a PL line and assigned it to V_N [97].

6.2 $\text{In}_x\text{Ga}_{1-x}\text{N}/\text{GaN}$ nanodisc superlattices

Tenfold $\text{In}_x\text{Ga}_{1-x}\text{N}$ NDs embedded in GaN barriers were grown to study carrier confinement in the active $\text{In}_x\text{Ga}_{1-x}\text{N}$ material. The NWHs were grown using the optimized growth process described in the previous section. A nominal substrate temperature of 630 °C was used for the growth of the NDSL that was placed on top of a 700 nm GaN NW template. The atom source operating parameters were set to $P_{\text{N}_2} = 300$ W and $\Phi_{\text{N}_2} = 1.6$ sccm and a BEP_{Ga} (BEP_{In}) of 1.4×10^{-7} mbar (1.3×10^{-7} mbar) was used. Only the growth time of the NDs (t_{ND}) was varied to study the effect of the ND thickness (d_{ND}) on the carrier confinement. The growth of the superlattice stack commenced with a GaN barrier after the substrate temperature was reduced to the $\text{In}_x\text{Ga}_{1-x}\text{N}$ growth temperature. Structural characterization of the samples was performed by BF TEM and HAADF STEM analysis while the optical properties have been assessed by PL spectroscopy. A list of the samples is given in table 6.2.

sample	t_{ND}	d_{ND} [nm]	d_{barrier} [nm]
N1503050	0.65	4	9
N1605090	0.2	1.7	8.2
N1605230	0.3	1.9 ⁵	
N1605060	0.4	3	8.1
N1605050	0.6	3.7 ⁵	
N1605040	0.8	4.4	9

Table 6.2: Growth parameters of the 10x $\text{In}_x\text{Ga}_{1-x}\text{N}/\text{GaN}$ ND structures studied in this section.

6.2.1 Electron microscopy

Three samples (N1605040, $t_{\text{ND}} = 0.8$ min; N1605060, $t_{\text{ND}} = 0.4$ min and N1605090, $t_{\text{ND}} = 0.2$ min) were analyzed by BF TEM to assess information about the structural properties of the NDSLs. Figure 6.15a) and figure 6.15b) display TEM images of sample N1605040, figure 6.15c) and figure 6.15d) depict images of sample N1605090. The thickness of the NDs (d_{ND}) was measured in the ND center and a growth rate of (6.2 ± 0.8) nm/min was determined for the $\text{In}_x\text{Ga}_{1-x}\text{N}$ NDs (figure 6.16). This growth rate was used to calculate d_{ND} of the samples that have not been investigated by TEM (cf. table 6.2). A truncation of the GaN (bright contrast) barriers introducing semipolar side facets is observed in both

⁵Calculated from growth rate obtained from TEM measurements on samples N1605040, N1605060 and N1605090.

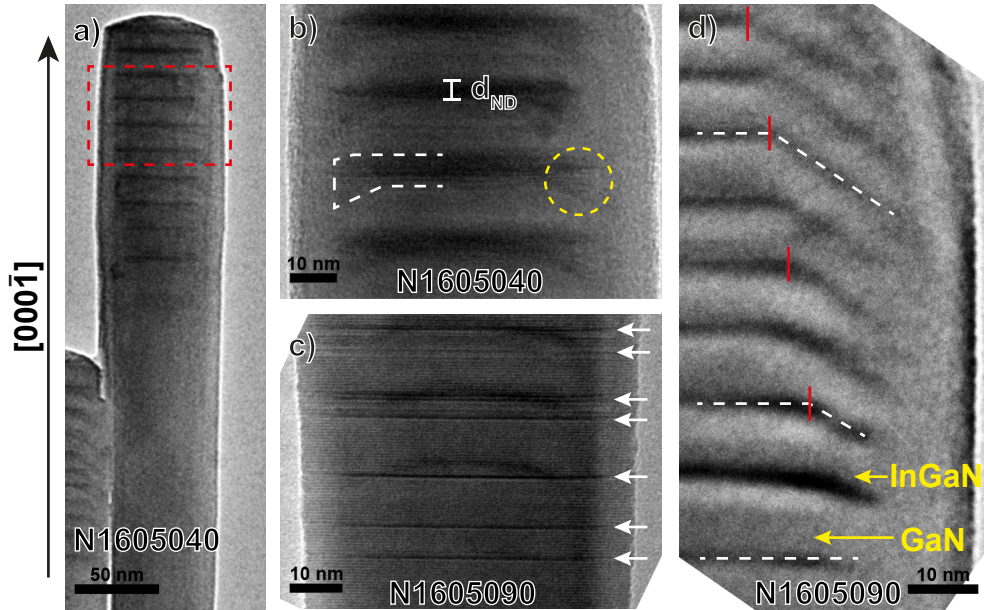


Figure 6.15: TEM images of samples N1605040 are shown in a) and b) while c) and d) were taken on NWs from sample N1605090. The magnification of the framed region in a) is shown in b). ND thicknesses (d_{ND}) were measured in the center of the NDs as indicated in b). A yellow circle highlights the region of a splitted ND. In c), the position of some stacking faults are marked by arrows. A NW without stacking faults is shown in d). The outer facets of the NDs are highlighted by dashed lines. Vertical lines mark the lateral position of the transition from the $-c$ -planes to the semipolar facets of the NDs.

samples, similar to the growth of the AlN barriers in the AlN/GaN NDSLs discussed in chapter 5. This faceting is partially compensated during the growth of the $\text{In}_x\text{Ga}_{1-x}\text{N}$ leading to a nearly pure $(000\bar{1})$ top interfaces of the NDs for $d_{ND} = 4.4$ nm indicating faster growth on the semipolar sidefacets compared to the polar surface (cf. framed region in figure 6.15b)). Theoretical investigations have shown that In prefers low coordination sites available on the semipolar facets which might explain the observed faster growth on these planes [141] corroborated by the results of Kehagias et al. who observed a similar ND morphology with higher In contents on the semipolar sidefacets [127]. In addition, the NDSLs were grown by switching the beam of In atoms on and off for the growth of the NDs and barriers, respectively, keeping the Ga flux constant. Hence, the metal flux decreased during the growth of the barrier material which results in a lower III/V ratio that can lead to a decrease of the NW tip radius (cf. section 6.1).

In samples with $d_{ND} = 1.7$ nm, the NDs adopt the morphology of the barriers exhibiting a homogeneous $\text{In}_x\text{Ga}_{1-x}\text{N}$ thickness over the entire ND radius (figure 6.15d)). As a consequence, the NW tip radius decreases from the first to the last ND. Hence, the first ND

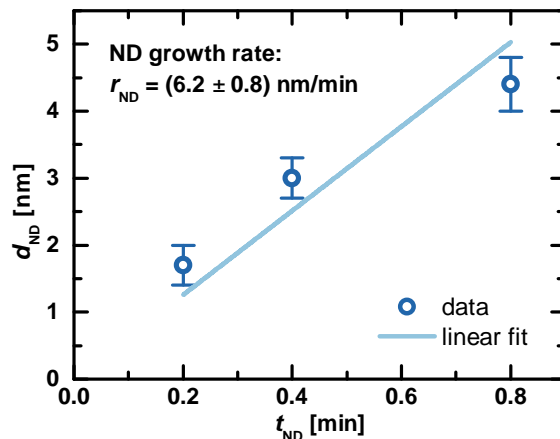


Figure 6.16: The mean measured d_{ND} (symbols) as a function of the ND growth time. Error bars amount to the maximum total deviation of measurements from the mean values. A linear regression was performed which revealed the ND growth rate.

in the stack exhibits a perfectly flat $(000\bar{1})$ orientation over the whole ND diameter and the inclination angle of the semipolar sidefacets increases for later grown NDs. In addition, the lateral extension of the $(000\bar{1})$ segment decreases for consecutively grown NDs as indicated by the vertical lines in figure 6.15d). This has also been observed during TEM investigations that were performed on similar samples by Kehagias et al. [127].

Due to the low growth temperature required for the In incorporation basal plane stacking faults (BSFs) are formed in the GaN barriers and $\text{In}_x\text{Ga}_{1-x}\text{N}$ NDs (arrows in figure 6.15c)). However, these BSFs were only found in some of the $\text{In}_x\text{Ga}_{1-x}\text{N}/\text{GaN}$ ND structures.

False conclusions are easily drawn from TEM images like those presented. These images are the result of a projection of the whole NW structure and do not necessarily represent a thin slice (< 1 nm) through the middle of a NW. The visualization of the latter is, however, possible by HAADF STEM tomography⁶. A single NW of sample N1503050 was attached to a tungsten tip allowing a 360° view of the sample [142]. Figure 6.17a) depicts the SEM image of a NW that has been attached to a W tip. Practically, the sample was tilted from -90° to 82° which enabled a detailed reconstruction of the whole hexagonal NW structure presented in figure 6.17b). An in depth description of the sample preparation and the applied tomography method is given in Ref. [142]. The same basic ND morphology as in the projected BF TEM images (figure 6.15) is observed when a 0.37 nm thin slice of the reconstructed NW is analyzed (figure 6.17c)). An increasing inclination of the outer $(10\bar{1}\bar{l})$

⁶Measurements and evaluation of the following data on HAADF STEM tomography of sample N1503050 were performed by Julian Schlechtweg and Dr. Katharina Gries in the group of Prof. Kerstin Volz at the Faculty of Physics and Materials Science Center of the Philipps-Universität Marburg.

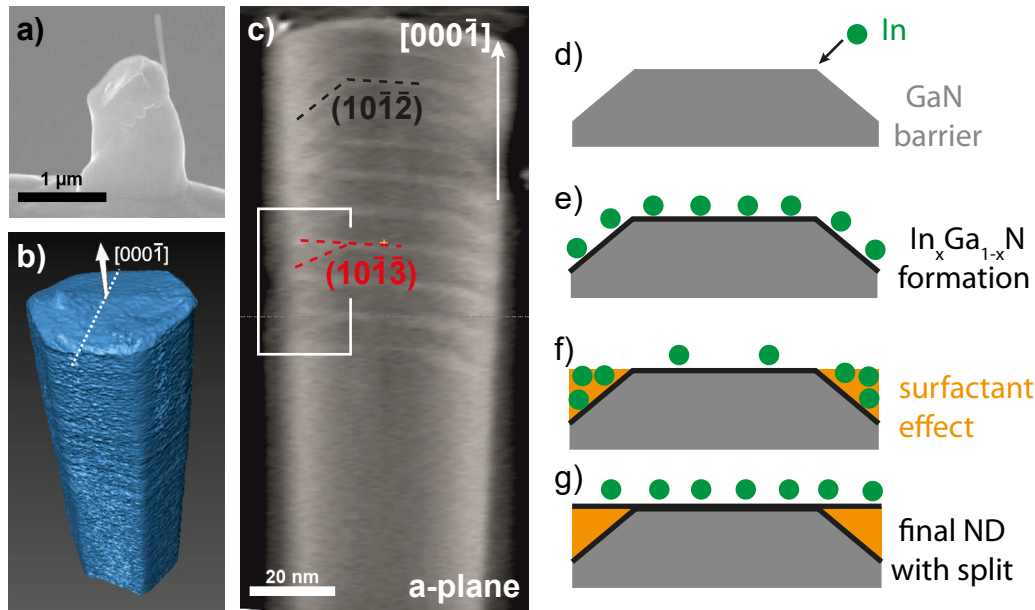


Figure 6.17: a) SEM image of a NW of sample N1503050 attached to a W tip. Image b) displays the reconstructed NW and c) shows a thin slice (0.37 nm) through the middle section of the NW. The latter was taken along an a -plane perpendicular to the NW sidewalls as indicated by the dashed line in b). Semipolar $(10\bar{1}\bar{l})$ sidefacets are marked by dashed lines and the rectangle highlights the split of the NDs. Data presented in a) to c) has already been submitted for publication in Ref. [142]. d) to f) Schematic of the formation of a ND exhibiting a split into a semipolar sidefacet and a polar $-c$ -plane.

facets of the $\text{In}_x\text{Ga}_{1-x}\text{N}$ NDs is observed as indicated by dashed lines in figure 6.17c). The fourth ND of the investigated NW exhibits a $(10\bar{1}\bar{3})$ facet (inclination angle of 32.04°) while the second to last ND has a steeper $(10\bar{1}\bar{2})$ facet (inclination angle of 43.19°). In addition, some NDs exhibit a split into a semipolar sidefacet (lower barrier/ND interface) and the continuation of the center $(000\bar{1})$ plane (upper ND/barrier interface). This has already been observed in projected TEM images, *exempli gratia*, in figure 6.15b) (yellow circle) and in Ref. [127] but projection errors can now be excluded due to the tomographic reconstruction of the NW. However, not all of the NDs show this split which suggests that the origin of this structural anomaly is localized. In addition, the split was only observed in the samples with a ND thickness of at least 4 nm. Indium incorporation is favorable on the semipolar sidefacets due to a low N coordination [141] and the resulting minimum in accumulated strain energy [143]. However, under N-rich conditions In is either incorporated into the crystal (lower III/V ratio) or acts as a surfactant (higher III/V ratio) depending on the actual III/V ratio during growth [141]. After the formation of a nucleation layer (figure 6.17e)) In accumulation at the semipolar sidefacets might reduce the III/V ratio until the

surfactant behavior prevails leading to the formation of a low In content interlayer (orange in figure 6.17f)). At some point of the ND growth, a polar $(000\bar{1})$ surface is established over the entire ND due to the higher growth rate on the semipolar facets and the In is distributed more evenly over the surface. This results in a decrease of the local III/V ratio favoring In incorporation again which might yield the observed split of the NDs (figure 6.17g)).

6.2.2 Photoluminescence spectroscopy

The optical properties of the $\text{In}_x\text{Ga}_{1-x}\text{N}/\text{GaN}$ ND samples were investigated by CW- and TR-PL spectroscopy. Figure 6.18a) depicts the low temperature PL spectra of a 370 nm $\text{In}_x\text{Ga}_{1-x}\text{N}$ reference (black line) and those of 10x $\text{In}_x\text{Ga}_{1-x}\text{N}/\text{GaN}$ NDSLs that were grown with different d_{ND} . The spectra were recorded using *Setup B* (cf. chapter 1,

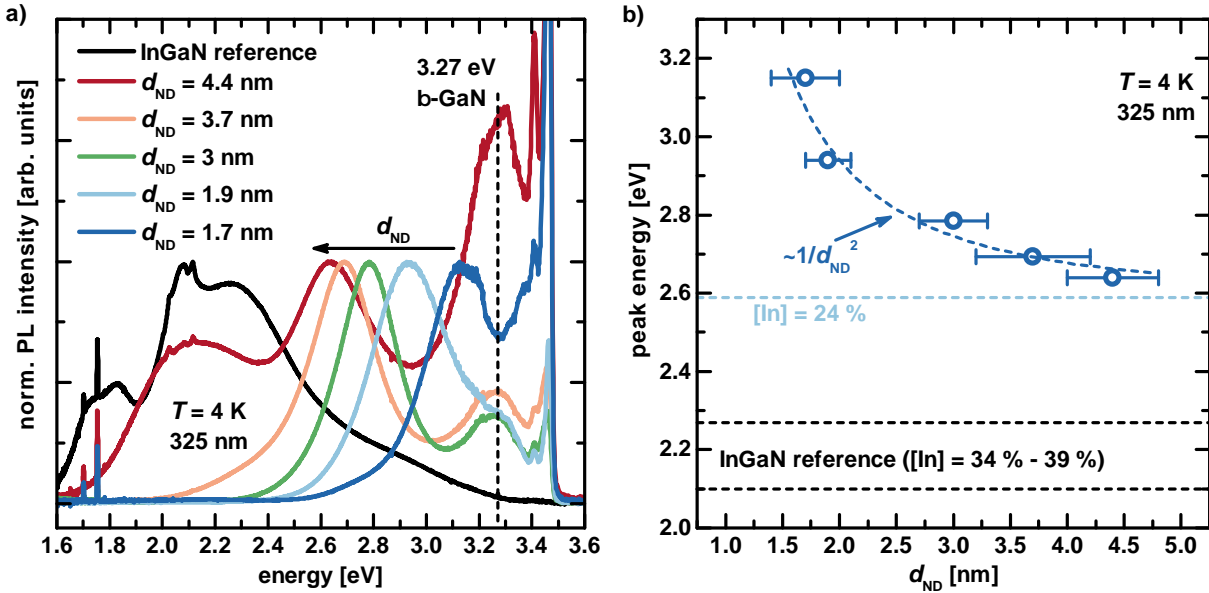


Figure 6.18: Low temperature PL spectra of a 370 nm $\text{In}_x\text{Ga}_{1-x}\text{N}$ reference (N160429, black line) and five 10x $\text{In}_x\text{Ga}_{1-x}\text{N}/\text{GaN}$ ND samples (N1605040, $d_{\text{ND}} = 4.4 \text{ nm}$; N1605050, $d_{\text{ND}} = 3.7 \text{ nm}$; N1605060, $d_{\text{ND}} = 3 \text{ nm}$; N1605230, $d_{\text{ND}} = 1.9 \text{ nm}$; N1605090, $d_{\text{ND}} = 1.7 \text{ nm}$) are shown in a). The band gap of cubic GaN is marked by a dashed line [144]. All spectra were normalized to the $\text{In}_x\text{Ga}_{1-x}\text{N}$ emission. The dependence of the ND PL peak position on d_{ND} is displayed in b) and the dark blue dashed line represents a function $\propto 1/d_{\text{ND}}^2$ that converges to 2.59 eV (light blue line).

section 3.4). Luminescence from the GaN NW base is observed at high energies ($> 3.4 \text{ eV}$) and the $\text{In}_x\text{Ga}_{1-x}\text{N}$ reference exhibits main emission peaks at 2.1 eV ([In]=39 %) and 2.27 eV ([In]=34 %), respectively. Additionally, weaker emissions at 1.7 eV and 1.8 eV are observed due to fluctuations of the In content. The emission energy increases upon the

introduction of NDs and successively further increases when d_{ND} is decreased from 4.4 nm (2.64 eV) to 1.7 nm (3.15 eV). Figure 6.18b depicts the dependence of the ND PL peak energy on d_{ND} . A good agreement to a $1/d_{\text{ND}}^2$ function converging to 2.59 eV is observed. This behavior indicates the successful formation of confined states in the $\text{In}_x\text{Ga}_{1-x}\text{N}$ NDs as well as a lower mean In content of 24% in the NDs compared to $[\text{In}] > 30\%$ in the reference sample.

Sample N1605040 ($d_{\text{ND}} = 4.4$ nm) also shows significant emission in the energy range of the reference sample at 2.09 eV. A combination of carrier localization at potential fluctuations due to an inhomogeneous In distribution and the confinement of carriers in ND states might be the explanation for this observation as illustrated in figure 6.19. In those NDs not

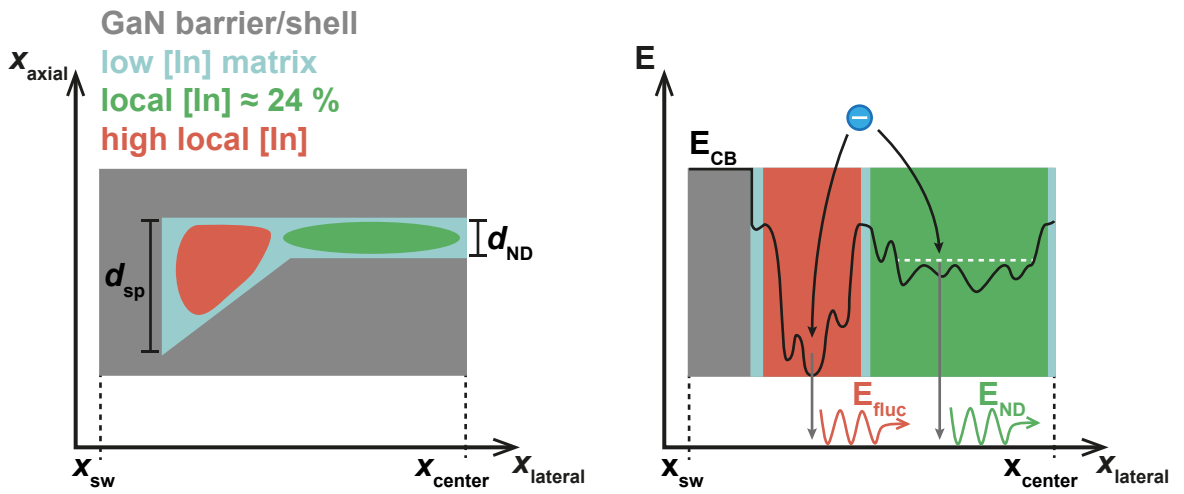


Figure 6.19: a) Schematic of the In distribution in an $\text{In}_x\text{Ga}_{1-x}\text{N}$ ND (light blue) embedded in GaN (gray). Laterally, the ND is sketched from the NW center x_{center} to one of the NW sidewalls x_{sw} . The thicknesses in the center of the ND d_{ND} and at the lateral ND/shell interface d_{sp} are labeled together with color coded regions of different In content. b) CB edge for the ND depicted in a). A confined state is represented by the white dashed line. Arrows indicate the carrier relaxation to available radiative recombination channels.

showing the discussed split morphology (cf. section 6.2.1), truncation of the NDs introduced by the GaN barriers is compensated for $d_{\text{ND}} \geq 4$ nm due to faster growth on the semipolar facets. The ND thickness at the ND/shell interface d_{sp} is, therefore, larger than d_{ND} in the ND center (figure 6.19a)). Since the supplied In favors the low coordination sites on the semipolar sidefacets, the formation of In-rich regions is expected to occur near the lateral ND/shell interface at a critical value $d_{\text{sp}} = d_{\text{crit}} > d_{\text{ND}}$. Accordingly, the luminescence of the ND ($E_{\text{ND}} = 2.64$ eV) in sample N1605040 ($d_{\text{ND}} = 4.4$ nm, red spectrum in figure 6.18) is assigned to quantum confined states in the center of the ND (figure 6.19b)). Consequently,

the low energy emission at $E_{\text{fluc}} = 2.09 \text{ eV}$ is attributed to highly localized carriers in potential fluctuations close to the lateral ND/shell interface (figure 6.19b)).

A third emission around the band gap energy of cubic GaN (3.27 eV [144]) was observed in the spectra shown in figure 6.18a). Only the reference sample did not show this emission. The significant overlap with the ND luminescence in sample N1605090 ($d_{\text{ND}} = 1.7 \text{ nm}$) prevents an unambiguous identification of the 3.27 eV band in this sample. Kehagias et al. previously assigned an emission at 3.15 eV to cubic inclusions of $\text{In}_x\text{Ga}_{1-x}\text{N}$ alloys. These are formed by the presence of BSFs at and In diffusion into the $\text{In}_x\text{Ga}_{1-x}/\text{GaN}$ interface regions which reduces the band gap energy of cubic GaN [127]. This assignment was based on HRTEM as well as temperature and time dependent PL analysis of 9x $\text{In}_x\text{Ga}_{1-x}\text{N}/\text{GaN}$ NDs. Therefore, temperature dependent PL measurements were conducted to study the evolution of the ND and 3.27 eV peaks.

Temperature dependent photoluminescence

Figure 6.20 depicts the spectra of a PL temperature series of sample N1605040 ($d_{\text{ND}} = 4.4 \text{ nm}$). The data is plotted on a semilogarithmic scale. Sample N1605040 exhibits the largest d_{ND}

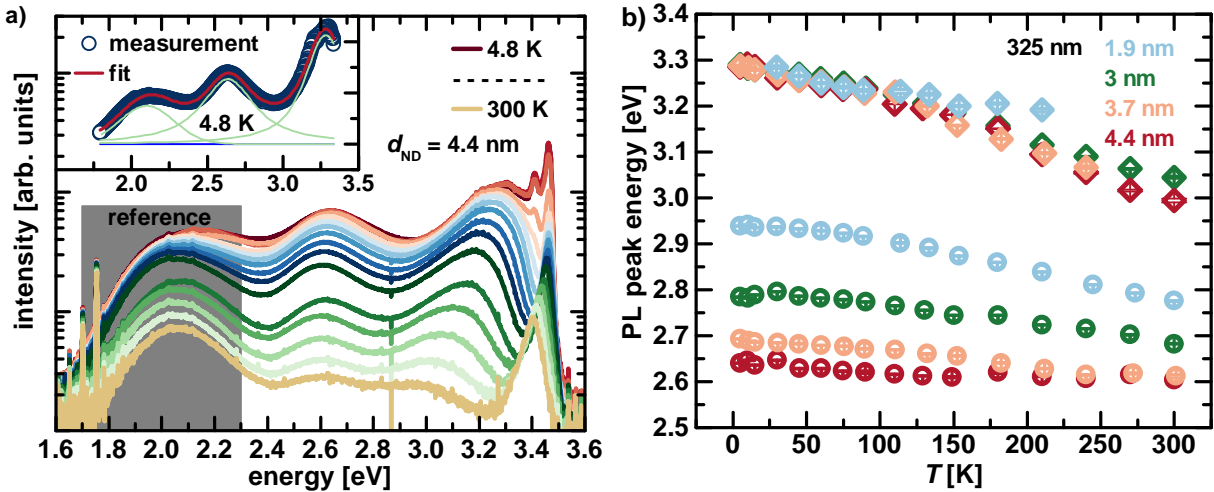


Figure 6.20: a) Spectra of a PL temperature series of sample N1605040 ($d_{\text{ND}} = 4.4 \text{ nm}$). The gray area highlights the emission range of the $\text{In}_x\text{Ga}_{1-x}\text{N}/\text{GaN}$ reference and the insert shows the fit (red line) to the measurement data (blue symbols) performed by three voigt functions (green). In b), the evolution of the ND peak energy and the 3.27 eV emission with temperature is shown for different d_{ND} .

of 4.4 nm and is the only sample that also shows a pronounced peak in the range of the reference sample. Similar measurements were performed for samples with smaller d_{ND} . The identified emissions below the GaN NBE regime were fitted by voigt functions (insert in

figure 6.20a)) which revealed the peak position and the integrated intensity (area of the fit). However, deconvolution of the ND emission and the 3.27 eV peak was not possible for sample N1605090 ($d_{\text{ND}} = 1.7$ nm) due to a strong overlap of these two emissions. The evolution of the ND PL peak and the 3.27 eV emission with the temperature is shown in figure 6.20b). Fitting of the 3.27 eV emission in samples N1605050 ($d_{\text{ND}} = 3.7$ nm) and N1605230 ($d_{\text{ND}} = 1.9$ nm) was not possible for temperatures higher than 240 K and 210 K, respectively. The ND emission below 3 eV is more stable for increasing d_{ND} exhibiting a red shift of $\Delta E = 40$ meV in the case of $d_{\text{ND}} = 4.4$ nm compared to a four times larger red shift of 160 meV for the sample with $d_{\text{ND}} = 1.9$ nm. Assuming an average In content of 24 % in the NDs, a temperature-induced shift of the band gap by $\Delta E = 61$ meV is expected in the investigated temperature range. As illustrated in figure 6.21a), temperature-induced carrier loss to potential fluctuations can lead to the larger shift of the emission energy ΔE for larger ND transition energies $E(d_{\text{ND}})$ at lower d_{ND} . All measured ND-related peak

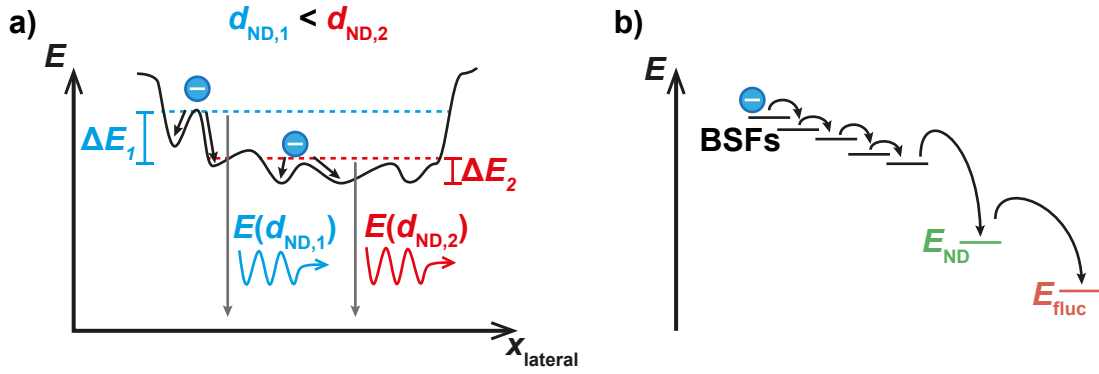


Figure 6.21: a) Schematic of lateral CB edge of a ND including confined states due to the axial ND dimension (blue and red dashed lines). The transition energies $E(d_{\text{ND},1})$ and $E(d_{\text{ND},2})$ are indicated by gray arrows for $d_{\text{ND},1} < d_{\text{ND},2}$. Temperature-induced carrier loss contributing to ΔE is indicated by arrows. b) Schematic of the temperature-induced feeding mechanisms observed in the $\text{In}_x\text{Ga}_{1-x}\text{N}/\text{GaN}$ ND samples.

energies and the corresponding ΔE at 300 K are listed in table 6.3. Table 6.4 lists the corresponding values for the 2.09 eV emission observed in sample N1605040. Similar shifts of the fluctuation-induced emission ($\Delta E_{\text{fluc}} = 32$ meV) and the ND emission ($\Delta E_{\text{ND}} = 40$ meV) are observed corroborating the assumption of a stronger influence of In fluctuations on the ND PL with increasing d_{ND} . The emission at 3.27 eV (4 K) evolves very similar over the whole range of investigated d_{ND} (figure 6.20b)). Hence, it is not directly correlated to confinement effects due to the ND. In addition, a red shift of this emission by 290 meV ($d_{\text{ND}} = 4.4$ nm) is observed. This is significantly larger than the 70 meV decrease of the band gap energy of cubic GaN in the same temperature range. Diffusion of In into the

sample	d_{ND} [nm]	E_{ND} [eV]	ΔE_{ND} [meV]	E_{loc} [meV]	E_{quench} [meV]	$\text{IQE}_{300\text{ K}}$ [%]
N1605230	1.9	2.94	160	14 ± 1	81 ± 3	3
N1605060	3	2.78	100	26 ± 4	161 ± 25	3
N1605050	3.7	2.69	80	13 ± 4	82 ± 15	5
N1605040	4.4	2.64	40	32 ± 9	148 ± 76	3

Table 6.3: List of the ND peak energy E_{ND} at 4 K as well as the emission red shift ΔE_{ND} observed when the sample temperature is increased to 300 K. Furthermore, the activation energies (E_{loc} and E_{quench}) obtained by fitting an Arrhenius function to the integrated PL data are listed together with the estimated IQE of the ND emission.

sample	d_{ND} [nm]	E_{fluc} [eV]	ΔE_{fluc} [meV]	E_{loc} [meV]	E_{quench} [meV]	$\text{IQE}_{300\text{ K}}$ [%]
N1605040	4.4	2.09	32	1 ± 0.5	57 ± 6	17

Table 6.4: List of E_{fluc} at 4 K as well as the emission red shift ΔE_{fluc} observed when the temperature is increased to 300 K. In addition, the activation energies (E_{loc} and E_{quench}) obtained by fitting an Arrhenius function to the integrated PL data are listed together with the estimated IQE of the ND emission.

GaN barriers in combination with BSFs was proposed to be the origin of a similar emission at 3.15 eV in Ref. [127]. This interpretation also fits to the present experiments because BSFs were found at the respective $\text{In}_x\text{Ga}_{1-x}\text{N}/\text{GaN}$ interfaces in the analyzed samples (cf. figure 6.15c)). The In diffusion process can lead to a graded In composition and carriers trapped at BSFs of lower In content are thermally activated to reach sites of slightly higher In content with increasing temperature. This is further supported by a relative decrease of the luminescence intensity of the 3.27 eV emission with benefit of the ND PL indicating an efficient feeding mechanism of the ND luminescence by carriers trapped by BSFs at ND/interface (figure 6.21b)). Such a feeding mechanism has also been observed for the fluctuation-induced emission in sample N1605040 (cf. figure 6.20a)). This results in an increase of the IQE (at 300 K) of this emission from 5 to 17% compared to an $\text{In}_x\text{Ga}_{1-x}\text{N}$ reference sample without NDs. Figure 6.22 exemplary displays the Arrhenius plot of the fit area of the ND luminescence of sample N1605040 ($d_{\text{ND}} = 4.4$ nm). The insert shows the Arrhenius plot obtained for the fluctuation-induced emission observed at 2.09 eV. The latter exhibits $E_{\text{quench}} = 57 \pm 6$ meV which is in agreement to the values obtained for the reference samples discussed in the section 6.1. No systematic dependence of E_{quench} and E_{loc} on d_{ND} was found (table 6.3). Both activation energies are, however, significantly larger

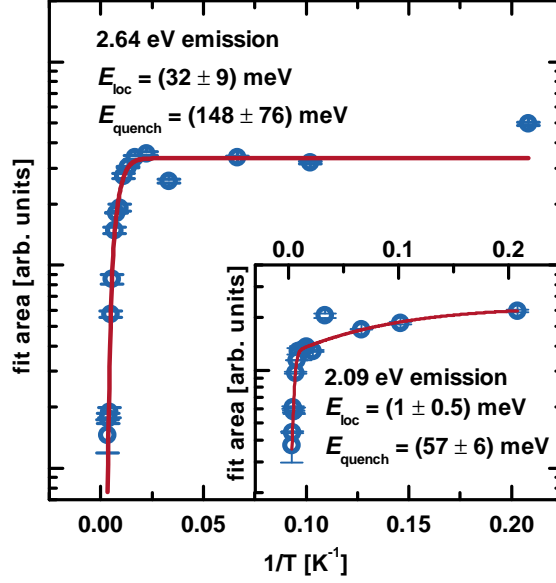


Figure 6.22: Arrhenius plot of the fit area of the ND PL of sample N1605040 ($d_{\text{ND}} = 4.4$ nm). Data obtained by fitting of the individual PL spectra is represented by blue symbols and a fit according to equation 6.1 is displayed as a red line. The insert shows the Arrhenius plot and fit corresponding to the fluctuation-induced emission observed in this sample.

than the maximum values obtained for the $\text{In}_x\text{Ga}_{1-x}\text{N}$ samples discussed earlier. For the ND emission, values ranging from (81 ± 3) meV to (161 ± 25) meV were found for E_{quench} , whereas E_{loc} was found to be in the range of (13 ± 4) meV to (32 ± 9) meV (table 6.3). The increasing activation energies compared to $\text{In}_x\text{Ga}_{1-x}\text{N}$ NW reference samples further substantiate the assumption of the formation of confined states in the NDs. The large non-systematic scattering of the activation energies also corroborates the hypothesis of an inhomogeneous In incorporation in the ND as sketched in figure 6.19 and figure 6.21a). A list of the obtained activation energies and IQE s is given in table 6.3. The IQE of the ND samples is similar to the values obtained for $\text{In}_x\text{Ga}_{1-x}\text{N}/\text{GaN}$ NW references (cf. section 6.1, figure 6.10). This rather low IQE (3 % to 5 %) is explained by the enhanced formation of non-radiative recombination at structural defects (point defects and/or BSFs) at the ND/barrier interfaces which counteract the benefit of quantum confined states in the NDs.

Time resolved photoluminescence

Time resolved PL was conducted at a temperature of 70 K on a GaN and $\text{In}_x\text{Ga}_{1-x}\text{N}$ reference as well as the 10x $\text{In}_x\text{Ga}_{1-x}\text{N}/\text{GaN}$ NDSL samples⁷. The GaN reference consisted of a

⁷All TR-PL experiments presented in this section were performed by Dr. Nils Rosemann in the group of Prof. Dr. Sangam Chatterjee at the Faculty of Physics and Materials Science Center of the Philipps-

GaN segment grown on a standard GaN NW template at the $\text{In}_x\text{Ga}_{1-x}\text{N}$ growth temperature. Figure 6.23a) displays the dependence of the fast (τ_{initial}) and slow component (τ_{final}) of the PL transients recorded on the 10x $\text{In}_x\text{Ga}_{1-x}\text{N}/\text{GaN}$ NDSLs. As mentioned in sec-

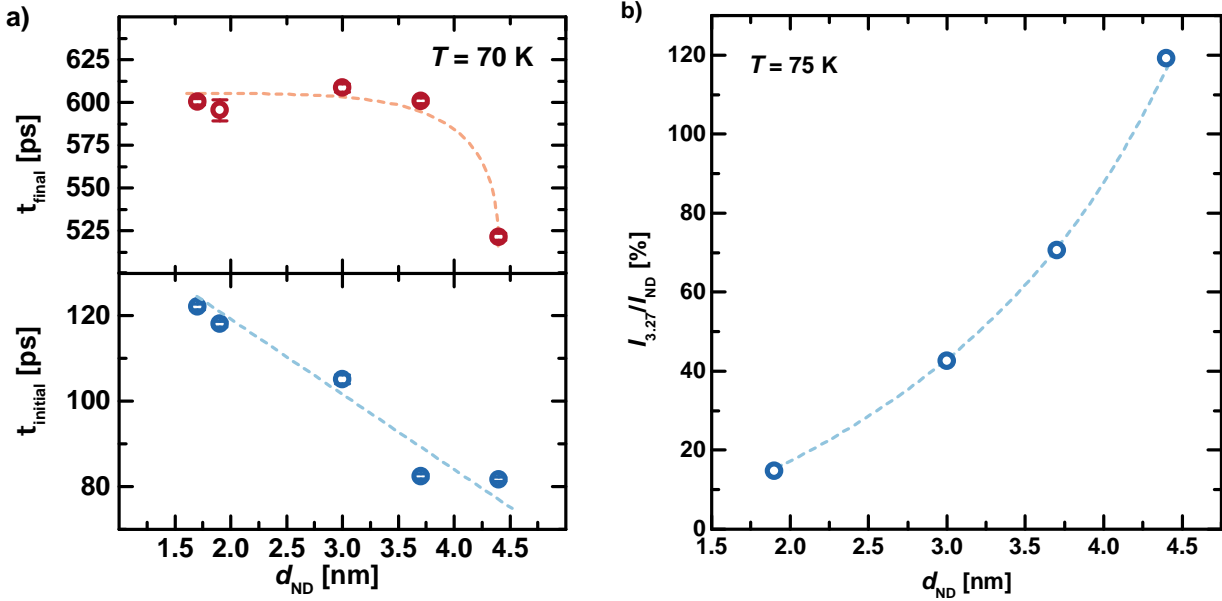


Figure 6.23: a) Decay times τ_{initial} and τ_{final} that were obtained by fitting of PL intensity transients plotted versus the ND thickness. In b), the relative intensity of the 3.27 eV emission of the ND samples (at 75 K) compared to the ND emission is plotted against d_{ND} . Dashed lines were added as guides to the eye.

tion 6.1.2, τ_{initial} reveals information about the relaxation process of the excited carriers and τ_{final} characterizes the following recombination process. Figure 6.24a) illustrates the carrier relaxation (black arrows) and recombination (gray arrows) in NDs that do not exhibit E_{fluc} at 2.09 eV ($d_{\text{ND}} < 4.4$ nm in the present experiments) while the fluctuation-induced emission is observed for those NDs schematically shown in figure 6.24b) ($d_{\text{ND}} = 4.4$ nm in the present experiments). In all cases, a higher In content is assumed to be present on the semipolar sidefacets as explained in section 6.2.1. However, for $d_{\text{ND}} < 4.4$ nm homogeneous carrier confinement over the whole ND is assumed as only one ND related emission E_{ND} is observed in the spectra (cf. figure 6.18a)). With increasing d_{ND} , τ_{final} remains fairly constant at around 600 ps and drops slightly to 521 ps for $d_{\text{ND}} = 4.4$ nm. This decrease of τ_{final} is explained by the additional contribution of the E_{fluc} recombination paths to the spectrum (figure 6.24b)). The fast component of the PL decay, on the other hand, decreases significantly from (122.1 ± 0.7) ps to (81.7 ± 0.6) ps with an increase of d_{ND} from

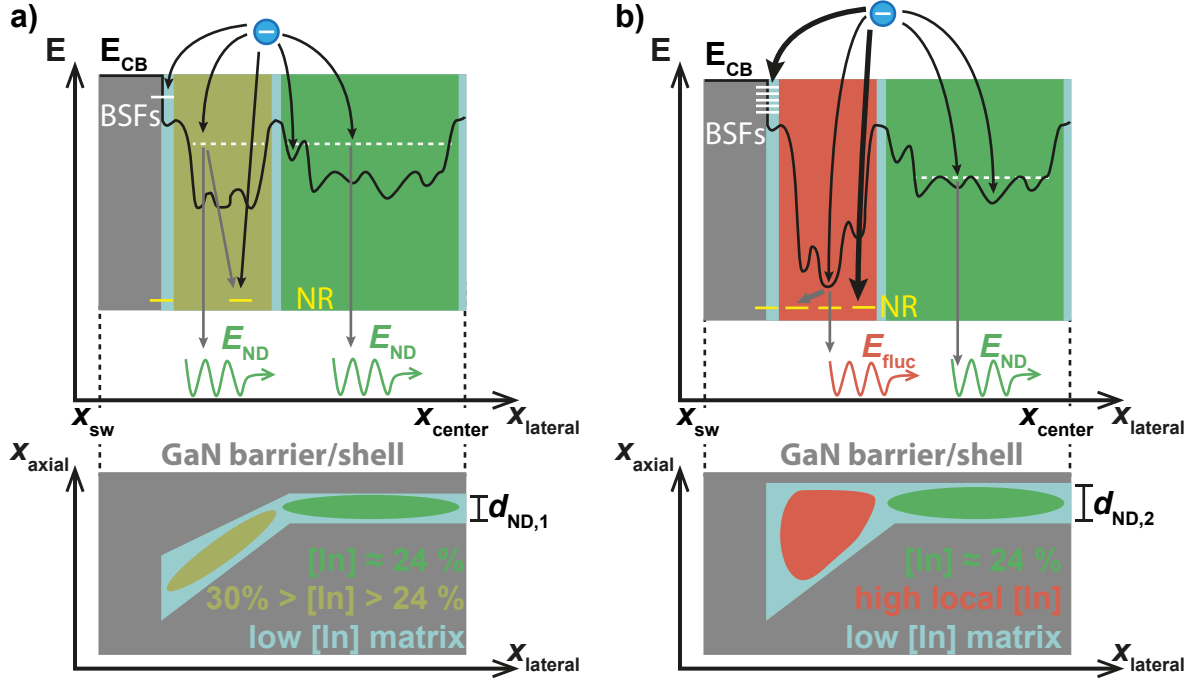


Figure 6.24: Schematic of the relaxation (black arrows) and recombination (gray arrows) processes of excited carriers in a ND. a) Example of a ND with small $d_{ND,1}$, not showing E_{fluc} . b) Example of a ND with large $d_{ND,2}$, exhibiting E_{fluc} . In the upper part, the CB edges are shown for the NDs sketched in the lower part of the figure. The energetic position of confined states (white dashed lines), non-radiative recombination centers (NR, yellow) and BSFs at the ND shell interface (white) are drawn. Comparing a) and b), an increasing linewidth of the arrows indicates an increasing probability for the respective relaxation/recombination process.

1.7 nm to 4.4 nm. This is mainly attributed to the higher density of structural defects (BSFs and point defects) with increasing d_{ND} (figure 6.24) which is corroborated by the relative intensity increase of the 3.27 eV emission with increasing d_{ND} as demonstrated in figure 6.23b). An overview on the decay times including a GaN and an $\text{In}_x\text{Ga}_{1-x}\text{N}/\text{GaN}$ NW reference is given in table 6.5. Both time constants (τ_{initial} and τ_{final}) are longer for the $\text{In}_x\text{Ga}_{1-x}\text{N}/\text{GaN}$ reference compared to the ND samples. This observation is attributed to the presence of a significant amount of BSFs in the ND samples which were not found in the $\text{In}_x\text{Ga}_{1-x}\text{N}/\text{GaN}$ references. The decay times of the GaN reference sample are significantly shorter than those of the $\text{In}_x\text{Ga}_{1-x}\text{N}$ NDs as well as the corresponding reference sample. Hauswald et al. [145] identified point defects in the GaN NWs to be the dominant non-radiative recombination channel over, *exempli gratia*, surface recombination. Consequently, the PL decay in the GaN NWs is faster compared to the $\text{In}_x\text{Ga}_{1-x}\text{N}$ samples where carriers are efficiently trapped in potential fluctuations as well as the ND confinement po-

Probe	d_{ND} [nm]	τ_{initial} [ps]	τ_{final} [ps]
N1606230	GaN ref.	25.3 ± 0.4	275 ± 7
N1605090	1.7	122.1 ± 0.7	600 ± 2
N1605230	1.9	118 ± 0.7	595 ± 6
N1605060	3	105 ± 1	608 ± 3
N1605050	3.7	82.4 ± 0.6	601 ± 2
N1605040	4.4	81.7 ± 0.6	521 ± 2
N1604290	$\text{In}_x\text{Ga}_{1-x}\text{N}$ ref.	138.7 ± 0.9	860 ± 3

Table 6.5: List of the fast (τ_{initial}) and slow (τ_{final}) component of the PL decay obtained by a double exponential fit to the PL transients (70 K).

tential. No indication was found for the influence of internal electric fields on the emission properties of the 10x ND samples as the PL transients do not change with the excitation power. Even, if the latter is varied over four orders of magnitude. The influence of internal electric fields on the optical properties of $\text{In}_x\text{Ga}_{1-x}\text{N}$ NDs, QWs and QDs is still under debate. Cardin et al. did not observe internal electric fields in $\text{In}_x\text{Ga}_{1-x}\text{N}$ NDs ($d_{\text{ND}} = 3 \text{ nm}$ to 8 nm) while Lähnemann et al. observed a strong influence of the QCSE in stacks of $\text{In}_x\text{Ga}_{1-x}\text{N}$ NDs with $d_{\text{ND}} = 11 \text{ nm}$ [146]. Carrier localization at In rich clusters was, however, assumed to be the origin of the PL observed in the latter case. Morel et al. also assumed the interaction between polarization fields and localization of electrons and holes at potential fluctuations to be the main mechanisms defining the PL in 1.5 nm to 6 nm thick $\text{In}_x\text{Ga}_{1-x}\text{N}$ QWs/QDs [147]. The attenuation of the internal electric field in $\text{In}_x\text{Ga}_{1-x}\text{N}$ NDs was ascribed to the diffusion of In into the GaN barrier in Ref. [127]. The latter is also likely to be the origin of the negligible polarization fields in the present samples. This is corroborated by the large temperature-induced red shift of the 3.27 eV emission which was assigned to a graded In content in combination with BSFs located at the ND/barrier interfaces.

6.3 Conclusion

Structural and optical properties of $\text{In}_x\text{Ga}_{1-x}\text{N}/\text{GaN}$ NWHs were investigated. The focus was set on the influence of the atom source operating parameters during growth as well as on carrier confinement effects in $\text{In}_x\text{Ga}_{1-x}\text{N}/\text{GaN}$ NDSLs. All investigated samples exhibited strong PL signals that originated from the inhomogeneous incorporation of In and the localization of carriers at the resulting potential fluctuations. An increasing Φ_{N_2} enhances local In accumulation due to an increase of the overall nitrogen partial pressure.

The increasing decomposition rate with increasing P_{N_2} due to a relative increase of atomic nitrogen was found to introduce a significant amount of additional non-radiative recombination centers. These were assigned to an increasing amount of V_N which are the intrinsic point defect with the lowest formation energy under the applied growth conditions.

It was demonstrated that the luminescence properties of $\text{In}_x\text{Ga}_{1-x}\text{N}$ NDs embedded in GaN barriers show complex behavior. Luminescence from confined states in the ND was observed in all investigated samples. The ND thickness was varied in the range of 1.7 nm to 4.4 nm which lead to PL emission from 3.15 eV to 2.64 eV. A strong interaction between carrier localization at potential fluctuations (probably close to the lateral ND/shell interface) and the additional axial confinement in the ND center due to the low axial ND dimension was observed for $d_{\text{ND}} > 4$ nm. This resulted in an additional PL band at 2.09 eV. A further signal observed in all $\text{In}_x\text{Ga}_{1-x}\text{N}$ ND samples at 3.27 eV was assigned to the presence of BSFs at ND/barrier interfaces and In diffusion into those defects. The TR-PL experiments performed on the present samples suggest negligible influence of internal electric fields on the optical properties of $\text{In}_x\text{Ga}_{1-x}\text{N}$ NDs.

7 Position-controlled growth of group III-nitride nanowires

Using metal-organic chemical vapor deposition (MOCVD) or metal-organic chemical vapor phase epitaxy (MOVPE), the growth of high quality, well-oriented GaN NWs is only feasible by PCG [148–152]. In contrast, the self-assembled growth has so far been widely used to grow group III-nitride NWs by MBE (cf. chapters 4, 5 and 6). Decent MBE-based PCG processes for the growth of GaN NWs on various substrates were only recently developed [28–34, 153, 154]. The major advantages of PCG over the self-assembled growth of GaN NWs are the control over the NW diameter and density as well as the suppression of NW coalescence. In this section, the development of a PCG process is described, including morphological and optical analysis of NW samples grown with a controlled morphology. The thickness of the used Ti mask and the growth conditions are optimized to achieve selectivity towards the NW growth in the nanoholes.

7.1 Growth mechanism and mask preparation

Figure 7.1 depicts the schematic of the PCG of GaN NWs using a nanohole mask that defines the NW diameter and density. At the applied growth conditions, PCG of GaN

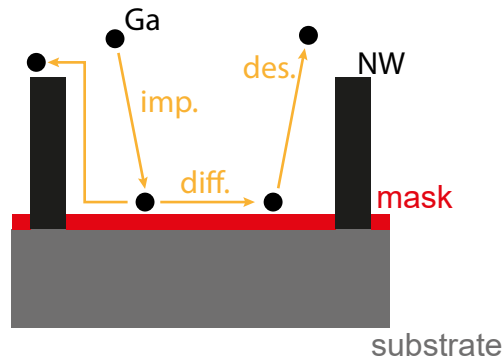


Figure 7.1: *Schematic of NW growth using PCG.*

NWs requires a lower sticking coefficient on the mask material compared to the substrate in order to suppress nucleation on the growth mask. Hence, impinging adatoms either diffuse towards the NWs growing in the mask openings, where they can contribute to the growth, or they desorb from the mask. Typical diffusion length in MBE-based PCG processes are in the range of several hundred nm [32, 33].

The quality of the used nanohole mask is most important for the successful PCG of GaN NWs. Various mask materials have been used over the years, including Si [32], Si_xN_y [30, 155], SiO_2 [153], molybdenum [34] and titanium [28, 33, 72, 154, 156]. A patterned Ti mask was used in this work to achieve selective growth on Si(111) substrates. Patterning

was carried out by electron beam lithography (EBL) using a negative resist. This resist is exposed to the electron beam (20 kV acceleration voltage) in the first step of the mask preparation (figure 7.2a)) using a writing dose of $200 \mu\text{C}/\text{cm}^2$. The exposed areas remain

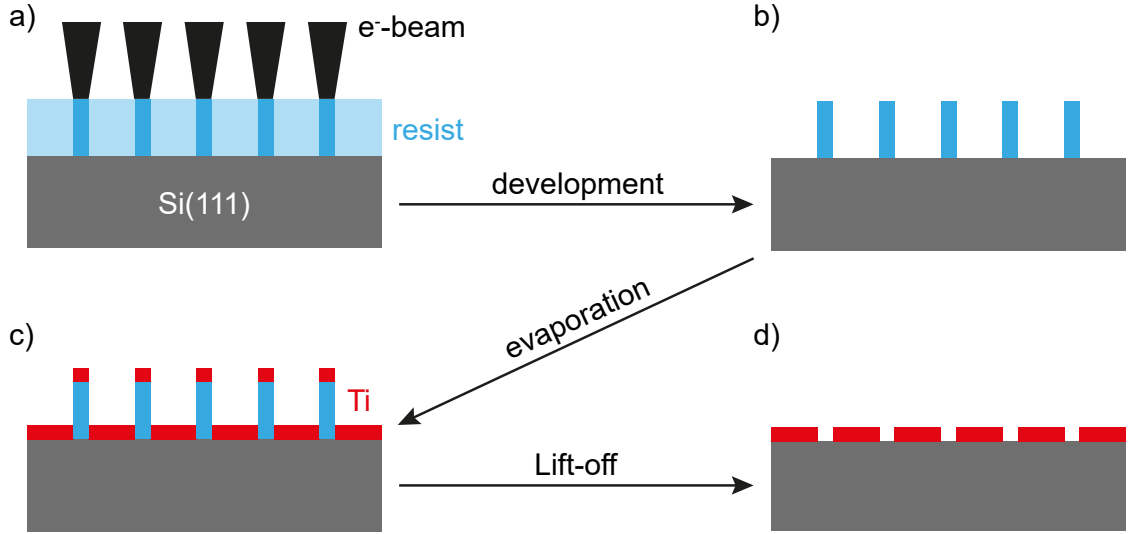


Figure 7.2: Schematic of the mask patterning process. a) A negative resist is exposed to an electron beam. Image b) displays the patterned resist after the development process and c) depicts the substrate after evaporation of Ti. The desired mask layout, shown in d), is realized after the Lift-off.

on the substrate after development (18 s) of the resist (figure 7.2b)) before the Ti mask material (2 nm to 14 nm) is evaporated (figure 7.2c)). The remaining resist is removed in acetone by an ultrasonication assisted lift-off (figure 7.2d)) leaving the desired mask. Detailed information on the process of the mask fabrication is given in appendix A.2. All masks exhibited a hexagonal nanohole array with a nominal hole diameter $d_{\text{hole}} = 50 \text{ nm}$ and variable pitch sizes $p = 350 \text{ nm} - 10 \mu\text{m}$. Figure 7.3a) shows the schematic of the nanohole mask with the relevant parameters p and d_{hole} . The SEM image of a finished growth mask is depicted in figure 7.3b). A nanohole diameter of $\approx 70 \text{ nm}$ (nominally 50 nm) was realized in a growth field with $p = 500 \text{ nm}$.

The Ti mask was nitrated in a two step process to form TiN prior to the PCG of GaN NWs. This process is in analogy to the one reported by Schuster et al. [33]. The initial nitridation ($P_{\text{N}_2} = 400 \text{ W}$, $\Phi_{\text{N}_2} = 1 \text{ sccm}$) of the substrate was carried out for 10 min at a heater temperature of 230°C . If this initial nitridation is omitted, the mask is unstable against the high substrate temperatures $> 750^\circ\text{C}$ used for the growth. A second nitridation of 5 min is carried out at the growth temperature to ensure complete nitridation of the Ti and to form the Si_xN_y nucleation layer in the mask openings.

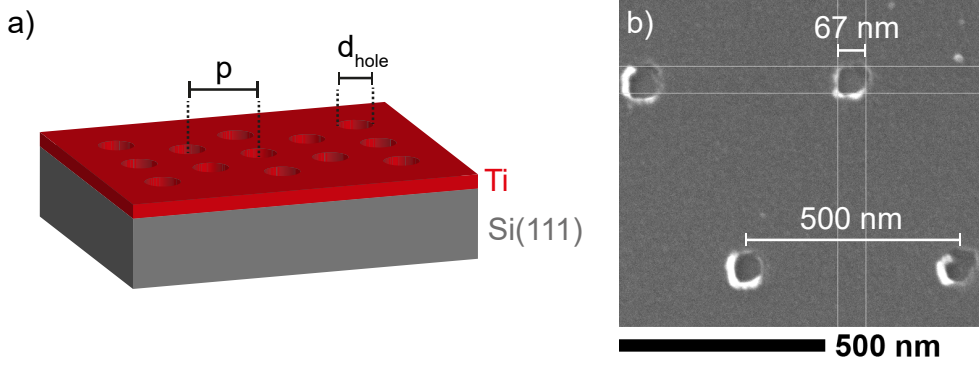


Figure 7.3: The schematic of a patterned Ti nanohole mask on a Si(111) substrate is shown in a). Nanoholes are arranged in a hexagonal array and the pitch p as well as the nanohole diameter d_{hole} are labeled. In b), the SEM image of substrate SiMat03-057 is displayed.

7.2 Position-controlled growth of GaN nanowires

The position-controlled growth of GaN NWs is discussed in this section. Influences of the mask thickness (d_{mask}), nitrogen flux (Φ_{N_2}) and growth time (t_{growth}) on the structural and optical properties of PCG NWs are evaluated using SEM and PL spectroscopy.

7.2.1 Influence of the mask thickness on the growth selectivity

The thickness of the growth mask was varied from $d_{\text{mask}} = 4 \text{ nm}$ to 14 nm to study its influence on the selectivity of the growth process. An effusion coefficient of $\epsilon = 0.75$ was used for the temperature measurements which yields reasonable temperatures for the used Si(111) substrates when a clean viewport is mounted. Figure 7.4a) depicts the temperatures of the Si(111) and TiN mask on the left ordinate measured with a pyrometer. The heater temperature was set to 735°C for all samples. A large mask opening was left on the substrate as schematically depicted in blue in the inset of figure 7.4a). This enabled the measurement of the surface temperatures of the TiN mask and the underlying Si(111) substrate individually. The latter is used as an estimate of the surface temperature of the nanoholes. Due to largely different geometries of the large mask opening and the nanoholes, the error of the measurements is assumed to be at least in the range of 5°C to 10°C . An increase of the Si(111) temperature is observed when increasing d_{mask} from 4 nm to 14 nm . On the other hand, the temperature of the TiN surface decreases with increasing d_{mask} . Consequently, the difference between the Si and TiN temperature $\Delta T_{\text{Si(111)-mask}}$ almost increases linearly as a function of d_{mask} as evident from figure 7.4a) (right ordinate).

The origin of this relative behavior is most likely due to increasing reflection of thermal radiation back into the substrate with increasing d_{mask} . Reflectance measurements per-

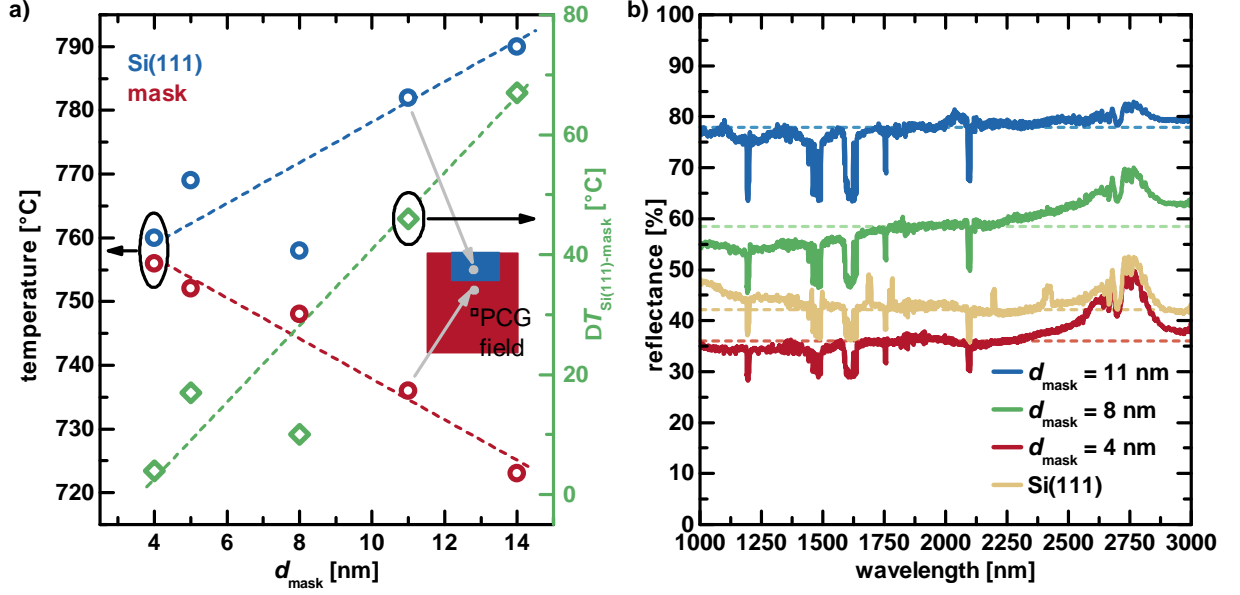


Figure 7.4: a) Measured temperatures of the Si(111) and TiN mask as a function of d_{mask} (left ordinate). The temperature difference between the mask and the Si surface $\Delta T_{\text{Si}(111)\text{-mask}}$ is given on the right ordinate. A schematic of the substrate with a large mask opening (blue region) is shown in the inset. The temperatures of the Si(111) and TiN were measured at the position of the gray dots. b) Reflectance measurements performed on empty substrate areas of samples N1602240 ($d_{\text{mask}} = 4$ nm), N1601280 ($d_{\text{mask}} = 8$ nm) and N1601070 ($d_{\text{mask}} = 11$ nm). The spectrum of a clean Si(111) substrate was added as a reference.

formed on empty areas of samples with different d_{mask} (after nitridation and growth) are presented in figure 7.4b), together, with a measurement conducted on an uncoated Si(111) reference¹. Sharp dips and peaks in the spectrum are due to the setup. The reflectance increases from around 36 % to 78 % when d_{mask} is increased from 4 nm to 11 nm. The initial decrease of the reflectance by 6 % for the sample with $d_{\text{mask}} = 4$ nm compared to the Si(111) reference is most likely associated to the rougher surface (0.56 nm compared to 0.21 nm) of the nitridated Ti layer.

Selectivity of the GaN NW growth is, hence, only achieved for the thinnest masks used here ($d_{\text{mask}} = 4$ nm and 5 nm) as demonstrated by the SEM images displayed in figure 7.5a) and figure 7.5b). The growth was carried out for 120 min with $BEP_{\text{Ga}} = 2.5 \times 10^{-7}$ mbar, $P_{\text{N}_2} = 400$ W and $\Phi_{\text{N}_2} = 1$ sccm. Mask openings of nominally $d_{\text{hole}} = 50$ nm were used with a pitch of $p = 750$ nm. Some residual growth is still observed on sample N1602040 ($d_{\text{mask}} = 5$ nm). However, no residual growth on the mask and only marginal growth of GaN

¹A L 900 from Perkin Elmer Ltd was used.

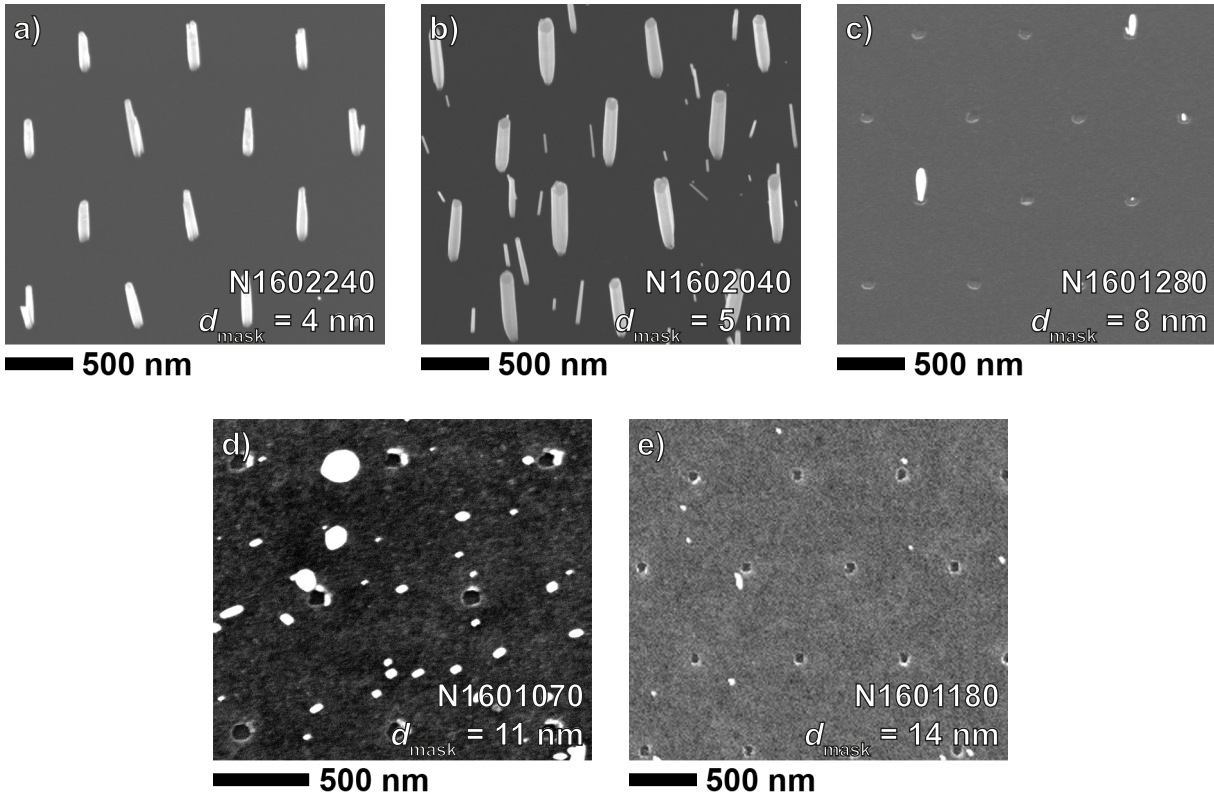


Figure 7.5: SEM images of samples grown on substrates with mask thicknesses of a) 4 nm, b) 5 nm, c) 8 nm, d) 11 nm and e) 14 nm, respectively. Images a) to c) were recorded under an angle of 25°C while d) and e) show top view micrographs of the samples. Sample numbers are given in the images.

NWs in the nanoholes is observed for a mask thickness of 8 nm. The residual growth on the former sample might be due to a lower actual growth temperature of several $^\circ \text{C}$ and/or due to an imperfect mask surface (roughening due to the nitridation or contamination of the TiN layer during Ti evaporation) offering some additional nucleation points. Selectivity towards GaN NW growth in the nanoholes is still observed for $d_{\text{mask}} = 8 \text{ nm}$, however, only very sparse growth is observed on the whole sample. Therefore, the critical substrate temperature for efficient nucleation on Si(111) is already exceeded for $d_{\text{mask}} = 8 \text{ nm}$. Further increase of the TiN mask thickness to 11 nm (figure 7.5d)) and 14 nm (figure 7.5e)) leads to an inverse selectivity of the growth: Nucleation is solely observed on the TiN mask and no NWs are found in the openings. This is explained by three effects that all facilitate this inverse selectivity. First of all, the temperature of the Si(111) increases to 782°C ($d_{\text{mask}} = 11 \text{ nm}$) and 790°C ($d_{\text{mask}} = 14 \text{ nm}$) enhancing Ga desorption which repulses adatoms out of the nanoholes. Secondly, the relative decrease of the TiN temperature (figure 7.4a)) leads to a decreasing diffusion length of the adsorbed Ga which increases the

nucleation probability on the mask. The increasing edge height of the nanoholes, finally, further increases the diffusion barrier towards the Si(111) surface.

Based on the presented observations, d_{mask} was limited to 4 nm for further experiments.

7.2.2 Influence of the nitrogen flux on the growth selectivity

The applied nitrogen flux has been reported to have significant influence on the selectivity of the growth process [33, 157]. However, Schuster et al. observed an improved selectivity with increasing Φ_{N_2} [33] while the opposite was reported by Bengoechea-Encabo et al. [157]. Hence, three samples were grown at $T_{\text{heater}} = 745^\circ \text{C}$ with $BEP_{\text{Ga}} = 2.5 \times 10^{-7} \text{mbar}$ and a growth time of two hours using $\Phi_{\text{N}_2} = 0.5 \text{sccm}$, 1sccm and 1.5sccm , respectively. Corresponding top and bird's-eye view images of those samples are shown in figure 7.6. Selectivity of the GaN NW growth was achieved for all applied nitrogen fluxes. The lowest

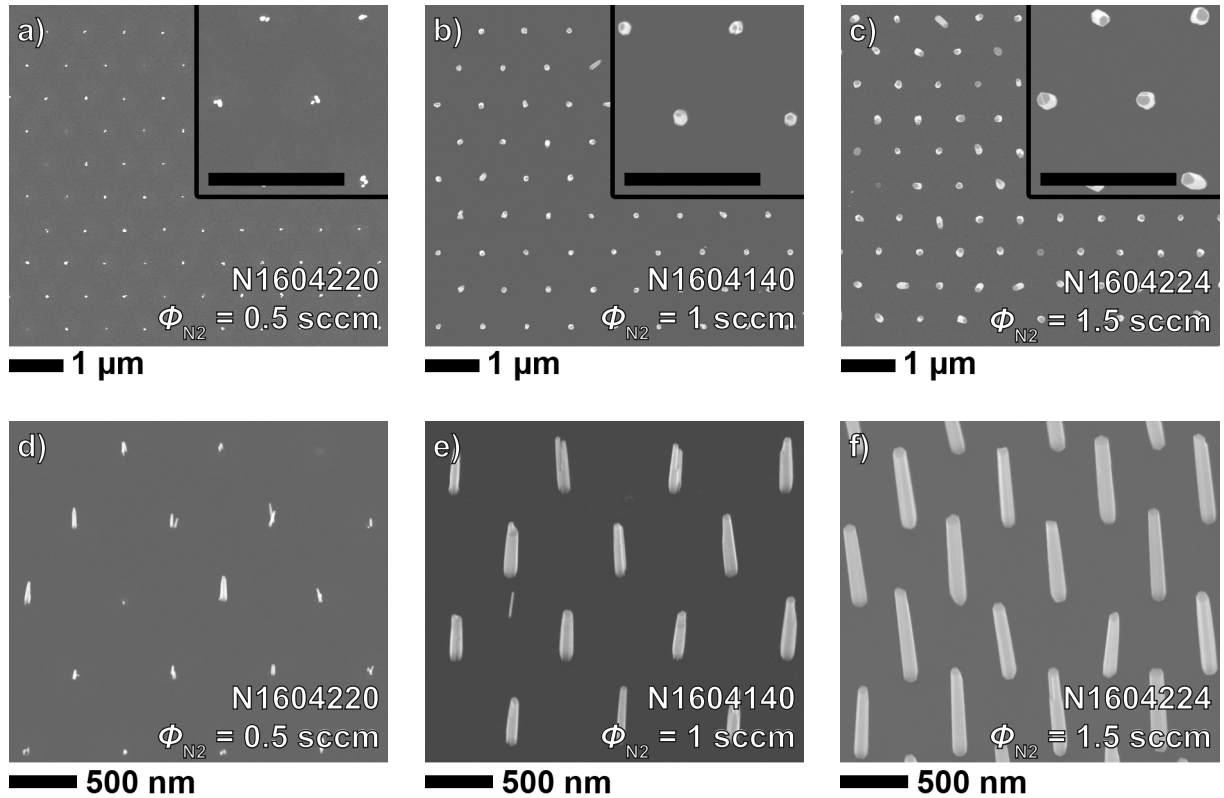


Figure 7.6: *SEM images of samples grown with $\Phi_{\text{N}_2} = 0.5 \text{sccm}$ (a) and d)), $\Phi_{\text{N}_2} = 1 \text{sccm}$ (b) and e)) as well as $\Phi_{\text{N}_2} = 1.5 \text{sccm}$ (c) and f)). The top row displays top view images while the bottom row depicts images taken under 25° tilt of the sample. Sample numbers are given in the images.*

nitrogen flux $\Phi_{\text{N}_2} = 0.5 \text{sccm}$ leads to an inhomogeneous occupation of the nanoholes with a NW diameter of $(30 \pm 14) \text{nm}$ and a NW length of $(170 \pm 105) \text{nm}$. This results in a radial

and axial growth rate of (0.13 ± 0.05) nm/min and (1.4 ± 0.9) nm/min, respectively. Also, multiple NWs nucleate in single nanoholes that afterwards coalesce to form a single NW which has also been observed by Gačević et al. [72]. Smaller nanoholes would, therefore, enable the growth of thinner PCG GaN NWs. The coalescence process is not completed on sample N1604220 ($\Phi_{N_2} = 0.5$ sccm). With an increase of Φ_{N_2} to 1 sccm (figure 7.6b)), all nanoholes are occupied by GaN NWs and the coalescence process of the NWs in individual holes is completed leading to one final NW per hole. The diameter of those NWs was measured to be (69 ± 21) nm at a NW length of (847 ± 96) nm. Consequently, the radial and axial growth rates increase with an increase of Φ_{N_2} from 0.5 sccm to 1 sccm and were measured to be (0.29 ± 0.09) nm/min and (7.1 ± 0.8) nm/min, respectively. A further increase of Φ_{N_2} to 1.5 sccm (figure 7.6) leads to an increase of the radial (axial) growth rate to (0.35 ± 0.05) nm/min ((11.4 ± 1.2) nm/min). A comparison of the self-assembled and position-controlled growth regarding the evolution of r_{axial} and $r_{lateral}/r_{axial}$ with Φ_{N_2} is depicted in figure 7.7a) and figure 7.7b), respectively. The ratio of the radial to the

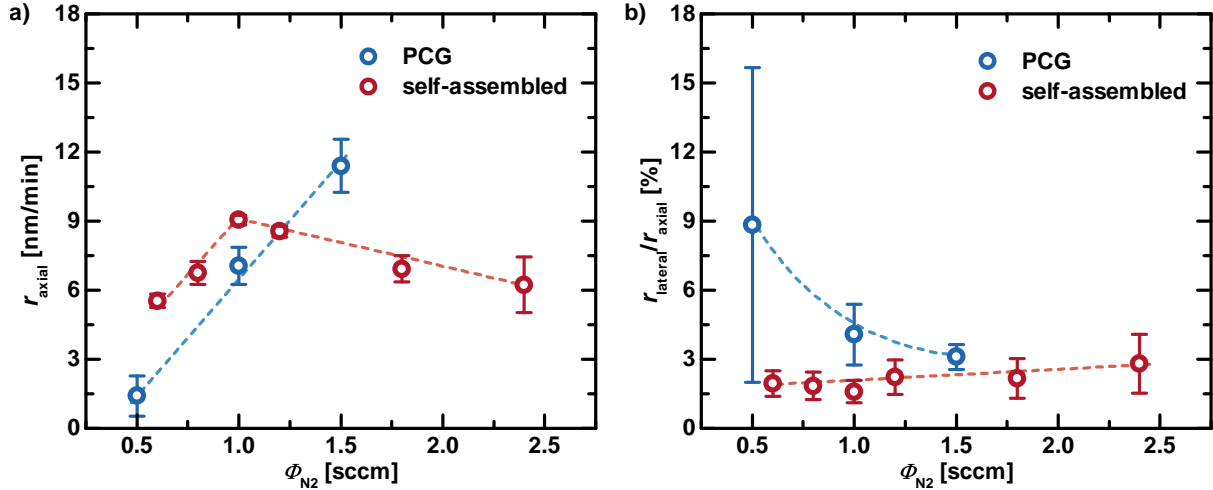


Figure 7.7: Comparison of the evolution of a) r_{axial} and b) $r_{lateral}/r_{axial}$ with Φ_{N_2} for the self-assembled growth and the PCG of GaN NWs.

axial growth rate decreases successively from 9% to 3% upon an increase of Φ_{N_2} from 0.5 sccm to 1.5 sccm. At low Φ_{N_2} , the NWs are still nucleating which leads to a high value of $r_{lateral}/r_{axial}$. The value at $\Phi_{N_2} = 1.5$ sccm is comparable to those obtained for the self-assembled growth of GaN NWs (figure 7.7b)). Comparing r_{axial} of both growth methods reveals a linear increase of r_{axial} over the whole range of analyzed Φ_{N_2} in the PCG approach, while r_{axial} already decreases for self-assembled grown GaN NWs at $\Phi_{N_2} > 1$ sccm due to hindered adatom diffusion at high background pressures (cf. chapter 4, section 4.4.2). A higher BEP_{Ga} of 3.4×10^{-7} mbar was used for the self-assembled grown NWs compared

to $BEP_{\text{Ga}} = 2.5 \times 10^{-7}$ mbar used for the PCG. Consequently, higher growth rates were observed in the case of the self-assembled growth for a given $\Phi_{\text{N}_2} \leq 1$ sccm. Hindered adatom diffusion expected for higher values of Φ_{N_2} does not seem to significantly influence the PCG, at least up to $\Phi_{\text{N}_2} = 1.5$ sccm.

Photoluminescence spectroscopy

The optical properties of the PCG GaN NWs were evaluated by μ -PL spectroscopy using *Setup C* (cf. chapter 3, section 3.4). Figure 7.8 depicts the low temperature (4K) μ -PL spectra of samples grown with different Φ_{N_2} , together, with a self-assembled grown GaN NW reference ($\Phi_{\text{N}_2} = 1$ sccm). The latter exhibits its emission maximum at 3.472 eV

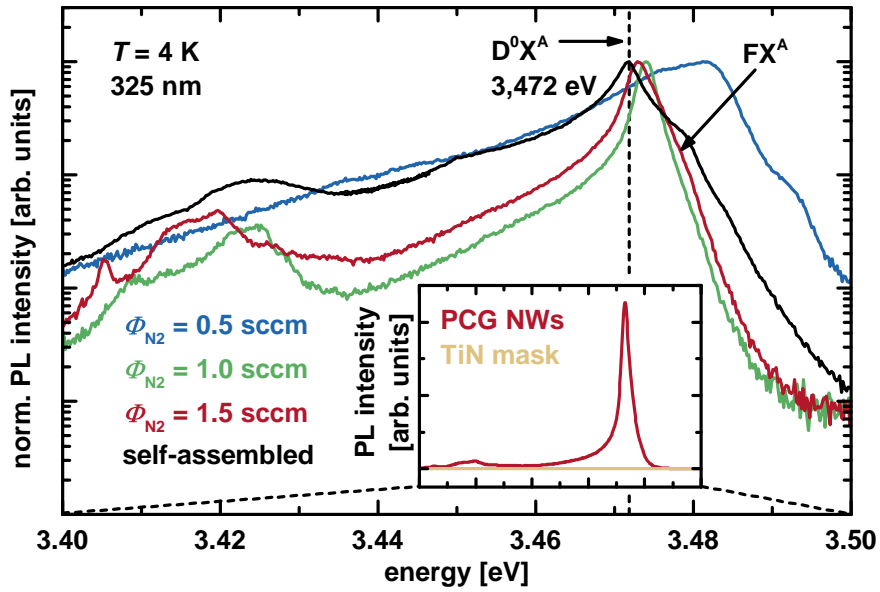


Figure 7.8: Low temperature μ -PL spectra of N1604220 ($\Phi_{\text{N}_2} = 0.5$ sccm), N1604140 ($\Phi_{\text{N}_2} = 1$ sccm), N1604224 ($\Phi_{\text{N}_2} = 1.5$ sccm) and the self-assembled GaN NW reference N1602080. All spectra were normalized to the emission maximum and a semilogarithmic scale was chosen. The insert depicts the spectrum of the sample grown with $\Phi_{\text{N}_2} = 1.5$ sccm in comparison to a spectrum recorded on the TiN mask (yellow).

(FWHM = 5.7 meV) corresponding to the $\text{D}^0\text{X}^{\text{A}}$ emission of relaxed GaN. The 3.45 eV emission related to V_{Ga} at the NW surface as well as the 3.42 eV emission band are also observed in this sample (cf. chapter 4, section 4.3.2). A broad emission centered at 3.481 eV (FWHM = 15.4 meV), similar to spectra recorded on highly Si-doped GaN NWs [37], is observed for the PCG sample grown with $\Phi_{\text{N}_2} = 0.5$ sccm. This is most likely due to a high background silicon concentration in these short (170 nm) NWs due to Si diffusion from the substrate that has also been observed in the case of self-assembled NW growth

on Si(111) [60]. An increase of Φ_{N_2} to 1 sccm and 1.5 sccm leads to a successive red shift of the $\text{D}^0\text{X}^{\text{A}}$ emission to 3.474 eV (FWHM = 2.9 meV) and 3.473 eV (FWHM = 4.2 meV). Both spectra, therefore, exhibit a smaller FWHM of the $\text{D}^0\text{X}^{\text{A}}$ than the reference, however, not showing the free exciton FX^{A} which is observed in the high energy shoulder of the self-assembled reference sample. The slight blue shift of the $\text{D}^0\text{X}^{\text{A}}$ might be due to compressively strained NWs in the case of the selectively grown samples. This however, is unlikely for NWs exhibiting a length > 847 nm due to the efficient strain relaxation at the lateral surfaces [3]. The emission of excitons recombining at neutral donors close to the NW surface is much more likely to be the origin for the slight blue shift of the $\text{D}^0\text{X}^{\text{A}}$ peak. Brandt et al. observed such a surface donor bound excitonic emission at 3.475 eV in SNW PL experiments performed on GaN NWs. A lower density of V_{Ga} at the NW surface might benefit exciton localization at donors close to the NW surface. This is corroborated by the absence of the, presumably, V_{Ga} related 3.45 eV emission in the PCG NWs. In addition, the intensity of the low energy tail of the $\text{D}^0\text{X}^{\text{A}}$ emission is significantly lower than in the case of the self-assembled GaN NWs indicating a lower density of structural defects, probably due to the suppression of NW coalescence during the later stages of growth. The emission band at 3.42 eV due to structural defects at the NW/substrate interface exhibits similar relative emission intensities comparing self-assembled and selectively grown NWs. Sharper features are, however, observed in this emission band in the case of the PCG GaN NWs, probably due to the lower NW density of $\approx 2 \mu\text{m}^{-2}$. Only 40 NWs are excited by the laserspot with a diameter of $5 \mu\text{m}$ compared to 1400 NWs in the case of the self-assembled GaN NWs with a density of 70 NWs/ μm^2 . Apparently, the TiN mask does not contribute to the PL in the investigated spectral range as demonstrated in the insert of figure 7.8.

The differences in the optical properties of the different PCG samples are the result of the different NW lengths due to different growth rates. Selectivity of the GaN NW growth combined with a high crystal quality (sharp $\text{D}^0\text{X}^{\text{A}}$ emission) and a high growth rate was found for a nitrogen flux of 1.5 sccm. The latter was, therefore, used for further growth experiments.

7.2.3 Influence of the growth time

Position-controlled growth of GaN NWs was performed at a heater temperature of 745°C and a $BE P_{\text{Ga}}$ of 2.5×10^{-7} mbar. The atom source was operated at $P_{\text{N}_2} = 400$ W and $\Phi_{\text{N}_2} = 1.5$ sccm. The growth time t_{growth} was varied from 15 min to 120 min to study the nucleation and coalescence process. Figure 7.9 depicts the SEM images recorded on samples grown for different t_{growth} . All large images were taken under an angle of 25° in

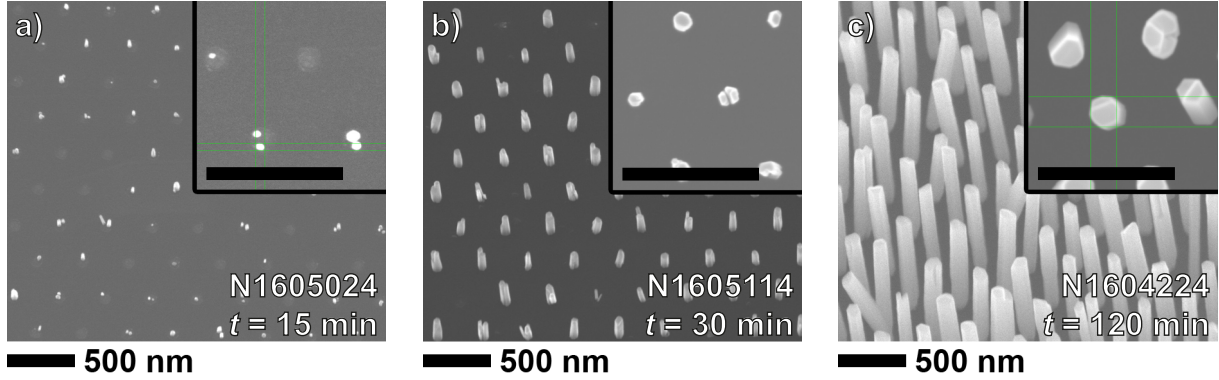


Figure 7.9: Bird's-eye view (25°) SEM images of samples grown for a) 15 min, b) 30 min and c) 120 min. The inserts are top view images and sample numbers are given in the images.

a field with a pitch of 350 nm while the magnified inserts display top view images. Only 60 % of the nanoholes are occupied after 15 min of NW growth which indicates that the nucleation process has not finished. Multiple NWs are found in individual holes and a NW length (diameter) of (80 ± 41) nm ((27 ± 9) nm) was determined. This yields an axial (radial) growth rate of (5.3 ± 2.7) nm/min ((0.9 ± 0.3) nm/min) with an radial to axial growth rate ratio of 15 %. For $t_{\text{growth}} = 30$ min, this ratio is reduced to 8 % due to an increased axial growth rate of (9.6 ± 1.9) nm/min while the radial growth rate remains constant. All nanoholes are occupied by NWs after 30 min of growth and almost complete coalescence of most of the NWs is observed (figure 7.9b)). The latter leads to an increase of the NW diameter to (48 ± 16) nm while the increased axial growth rate results in a NW length of (290 ± 57) nm. The growth field of sample N1604224 ($t_{\text{growth}} = 120$ min) with a nanohole pitch of 750 nm was already discussed earlier in this chapter (cf. section 7.2.2). Figure 7.9c) shows the SEM images of a growth field with a pitch of 350 nm. The NW length and diameter were determined to (1375 ± 118) nm and (975 ± 12) nm which gives radial and axial growth rates of (0.3 ± 0.1) nm/min and (12 ± 1) nm/min, respectively. These values are comparable to those determined for the growth field with $p = 750$ nm. A relative radial growth rate of 3 % compared to the axial growth rate is calculated.

Conclusively, the nucleation of the NWs including their full coalescence in the individual holes takes approximately 30 min after which all mask openings are occupied by GaN NWs which also show nearly full coalescence of the individual NW nuclei. Afterwards, the axial growth of the NWs dominates which results in a decrease of the relative radial growth rate by a factor of five after 120 min of growth.

Photoluminescence spectroscopy

Low temperature μ -PL spectroscopy was performed to study the optical properties of the PCG GaN NWs. Figure 7.10 depicts the spectra that were recorded on samples that were grown for different growth times in a growth field with a pitch of 750 nm. A broad

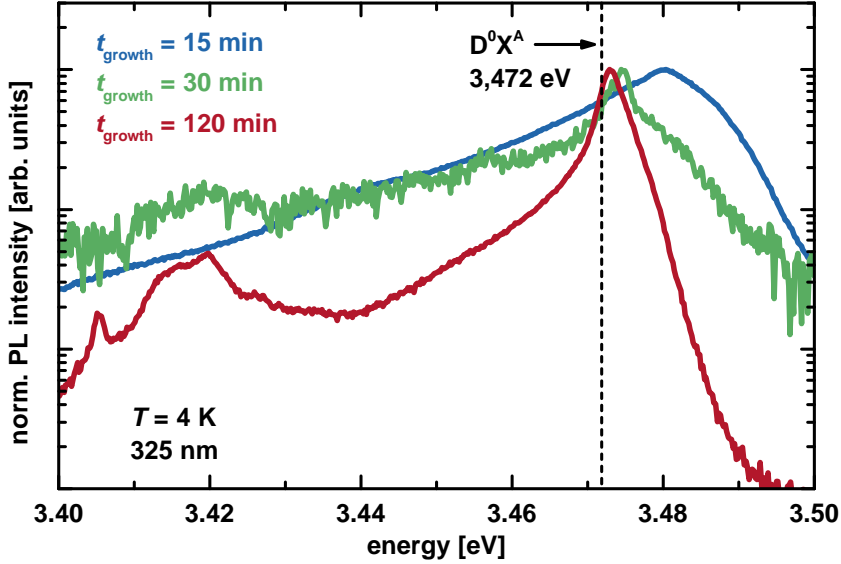


Figure 7.10: Low temperature μ -PL spectra of samples N1605024 ($t_{\text{growth}} = 15 \text{ min}$), N1605114 ($t_{\text{growth}} = 30 \text{ min}$) and N1604224 ($t_{\text{growth}} = 120 \text{ min}$). The position of the D^0X^A in unstrained GaN is marked in the figure.

and featureless peak was observed at 3.48 eV (FWHM = 19.4 meV) for the sample with the shortest NWs (growth time) of 80 nm (15 min). Again, this is attributed to the very short length (l_{NW}) of the NWs and the resulting high background doping concentration that leads to a band filling induced blue shift of the D^0X^A emission. A sharp (5.3 meV) donor bound excitonic emission becomes dominant at 3.474 eV for the GaN NWs grown for 30 min where the nucleation and coalescence process is almost finished (cf. figure 7.9b). The coalescence process is, however, still ongoing for some NWs of sample N1605114 ($l_{\text{NW}} = 290 \text{ nm}$) and the coalescence of neighbouring NWs leads to the formation of dislocations in the coalescence region [78]. These, dislocations introduce strain to the crystal in the coalescence region. Hence, the blue shift of the donor bound exciton emission by 1 meV in comparison to sample N1604224 ($l_{\text{NW}} = 1375 \text{ nm}$) might be due to a combination of compressive strain and neutral donor states at the NW surface. The latter sample exhibits the lower FWHM of the surface donor bound exciton emission (4.2 meV) and also the lowest background emission intensity on the lower energy tail of this emission. This demonstrates a lower defect density in the longer NWs.

7.2.4 Large nanohole pitches

The largest realized pitch of the nanoholes on sample N1604224 was $10\ \mu\text{m}$. The sample was grown for 120 min with $BEP_{\text{Ga}} = 2.5 \times 10^{-7}$ mbar, $P_{\text{N}_2} = 400$ W and $\Phi_{\text{N}_2} = 1.5$ sccm at a heater temperature of 745°C . An SEM image recorded under an incident angle of 25° is displayed in figure 7.11a). The upper part in the image corresponds to an unmasked

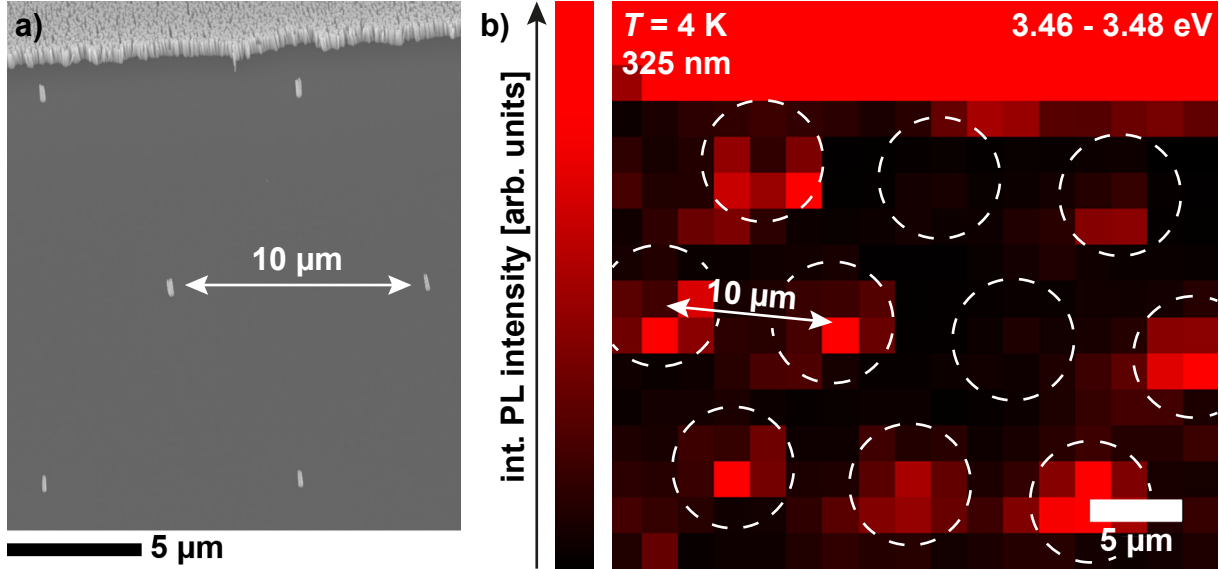


Figure 7.11: SEM image (25° bird's-eye view) of the $10\ \mu\text{m}$ pitch field of sample N1604224. A spatially resolved PL map recorded in same growth field of sample N1604224 is shown in b). The PL intensity recorded in the energy range of $3.46\ \text{eV}$ to $3.48\ \text{eV}$ is color coded.

marker region were self-assembled NW growth occurred. Selectivity of the NW growth was also achieved for this large pitch indicating that the surface temperature of the TiN mask is sufficiently high to inhibit nucleation of NWs on the mask. A μ -PL intensity map of a section of the field with $p = 10\ \mu\text{m}$ is depicted in figure 7.11b). The PL intensity integrated in the energy range of $3.46\ \text{eV}$ to $3.48\ \text{eV}$ is color coded. A bright PL was observed in the upper part of figure 7.11b), where the self-assembled growth of GaN NWs occurred. The laser spot had a diameter of $5\ \mu\text{m}$ and one pixel of the measurement has a length of $2\ \mu\text{m}$. The hexagonal grid of the nanohole mask is indicated by circles in figure 7.11b) and demonstrates that SNWs can be addressed individually by μ -PL using sufficiently large pitches. Additionally, the luminescence intensity of some NWs is comparatively low indicating strong non-radiative recombination in these NWs, most likely due to point defects and/or non-radiative surface states. Figure 7.12 displays the low temperature PL spectra recorded on a self-assembled reference and two SNWs grown in a $10\ \mu\text{m}$ pitch field. The luminescence of the donor bound exciton is blue shifted to $3.473\ \text{eV}$ in the case of the

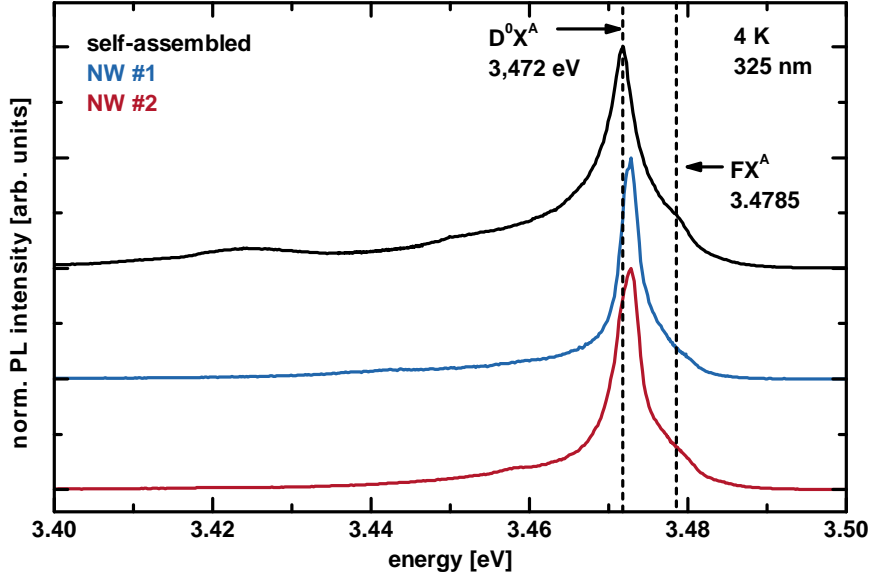


Figure 7.12: Low temperature PL spectra of a self-assembled GaN reference (N1602080) and two NWs in the $10\ \mu\text{m}$ pitch field of sample N1604224.

SNWs which was also observed for the PL recorded in the field with a pitch of 750 nm (cf. section 7.2.2). The FWHM of the D^0X^A emission was determined to 2.4 meV (NW #1), 4.1 meV (NW #2) and 5.6 meV (self-assembled reference), respectively. Lower linewidths were, therefore, measured for the selectively grown SNWs. However, the expected values of $\text{FWHM} < 1\ \text{meV}$ as observed in the SNW PL experiments shown in chapter 5, section 5.1 were not obtained. Reasons for this discrepancy might be the larger diameter ($d > 80\ \text{nm}$) of the PCG GaN NWs compared to the self-assembled grown samples ($d \leq 50\ \text{nm}$) and the possibility of the nucleation of multiple NWs in one nanohole. A significant contribution of the FX^A emission was observed in all spectra shown in figure 7.12.

Conclusively, the PCG of GaN NWs enables to grow NWs with pitches large enough to perform μ -PL experiments on a SNW basis on as grown samples. Conventionally, NWs are suspended in an organic solvent and dispersed on a substrate for μ -PL measurements on SNWs. The PCG, therefore, prevents contamination with solvent residues and adhesion-induced stress that can alter the emission spectrum [110]. Furthermore, after measuring the as grown NWs, they can still be detached from the substrate to measure the PL according to conventional SNW experiments which can be used to study the optical properties of the same NW under different excitation/collection geometries.

7.2.5 Conclusion

Nanohole masks with a nominal diameter of 50 nm were produced by EBL and a subsequent lift-off process. An actual nanohole diameter of approximately 70 nm was achieved. Thin (< 4 nm) Ti masks are required to achieve selectivity of the GaN NW growth. Multiple NWs nucleate in single nanoholes and form one NW after a growth time of approximately 30 min due to coalescence. If used as a template for the successive growth of NWHs, a growth time of at least 60 min is recommended to assure a defect-free growth surface enabling the growth of high quality heterostructure. The donor bound exciton emission observed in the selectively grown GaN NWs is blue shifted in the meV range compared to unstrained bulk GaN. This behavior was assigned to a stronger contribution of donor states close to the NW surface compared to the bulk-like emission of the self-assembled GaN NWs. Selectivity of the growth is also achieved for large NW pitches up to $10\ \mu\text{m}$ which enables the investigation of as grown SNWs by μ -PL.

7.3 Selective growth of $\text{In}_x\text{Ga}_{1-x}\text{N}/\text{GaN}$ nanowire heterostructures

The growth parameters for the position-controlled growth of $\text{In}_x\text{Ga}_{1-x}\text{N}$ on PCG GaN NW templates are discussed. The templates exhibited a NW length of approximately 400 nm ($BEP_{\text{Ga}} = 2 \times 10^{-7}$ mbar, $t_{\text{growth}} = 60$ min, $\Phi_{\text{N}_2} = 1.5$ sccm and $T_{\text{heater}} = 745^\circ\text{C}$). A list of the investigated samples and the applied growth conditions for the $\text{In}_x\text{Ga}_{1-x}\text{N}$ segment is given in table 7.1. The parameters T_{heater} , Φ_{N_2} and the In/Ga ratio were varied

Probe	$T_{\text{heater}} [^\circ\text{C}]$	$BEP_{\text{Ga}} [\text{mbar}]$	$BEP_{\text{In}} [\text{mbar}]$	In/Ga ratio	$\Phi_{\text{N}_2} [\text{sccm}]$
N1604270	510	1.4×10^{-7}	1.3×10^{-7}	0.93	1.6
N1606270	535	1.4×10^{-7}	1.3×10^{-7}	0.93	1.6
N1607020	560	1.4×10^{-7}	1.3×10^{-7}	0.93	1.6
N1607060	565	1.4×10^{-7}	1.3×10^{-7}	0.93	1.6
N1607040	585	1.4×10^{-7}	1.3×10^{-7}	0.93	1.6
N1607130	565	7×10^{-8}	2×10^{-7}	2.86	1
N1607120	565	7×10^{-8}	2×10^{-7}	2.86	1.6
N1607140	565	7×10^{-8}	2×10^{-7}	2.86	2.2
N1607150	565	5×10^{-8}	2×10^{-7}	4	2.2
N1607160	565	3.5×10^{-8}	2.4×10^{-7}	6.71	2.2

Table 7.1: Growth parameters of the $\text{In}_x\text{Ga}_{1-x}\text{N}$ region of the selectively grown $\text{In}_x\text{Ga}_{1-x}\text{N}/\text{GaN}$ NWHs studied in this section.

systematically (bold text in table 7.1). All $\text{In}_x\text{Ga}_{1-x}\text{N}$ segments were grown for 60 min with $P_{\text{N}_2} = 300$ W

7.3.1 Influence of the substrate temperature

Figure 7.13 depicts the SEM images of $\text{In}_x\text{Ga}_{1-x}\text{N}$ grown on top of PCG GaN NW templates. All images were recorded under an incident angle of 25° . Large (small) images were recorded in a growth field with a pitch of 350 nm (750 nm). The temperature was increased from 510°C (figure 7.13a)) to 585°C (figure 7.13e)) for the growth of the $\text{In}_x\text{Ga}_{1-x}\text{N}$. A nitrogen flux of 1.6 sccm as well as metal fluxes of $BEP_{\text{Ga}} = 1.4 \times 10^{-7}$ mbar and $BEP_{\text{In}} = 1.3 \times 10^{-7}$ mbar were used for all samples. Strong parasitic growth is observed on sample N1604270 ($T_{\text{heater}} = 510^\circ$, figure 7.13a)), independent of the nanohole pitch. The parasitic growth is driven by the low mobility and desorption rate of the Ga adatoms at the applied temperature. Increasing T_{heater} from 535°C (figure 7.13b)) to 565°C (figure 7.13d)) reduces parasitic growth significantly within the growth field with $p = 350$ nm. The effect on the parasitic growth in the field with a pitch of 750 nm, however, is not as pronounced. Finally, a heater temperature of 585°C (figure 7.13e)) leads to perfect selectivity

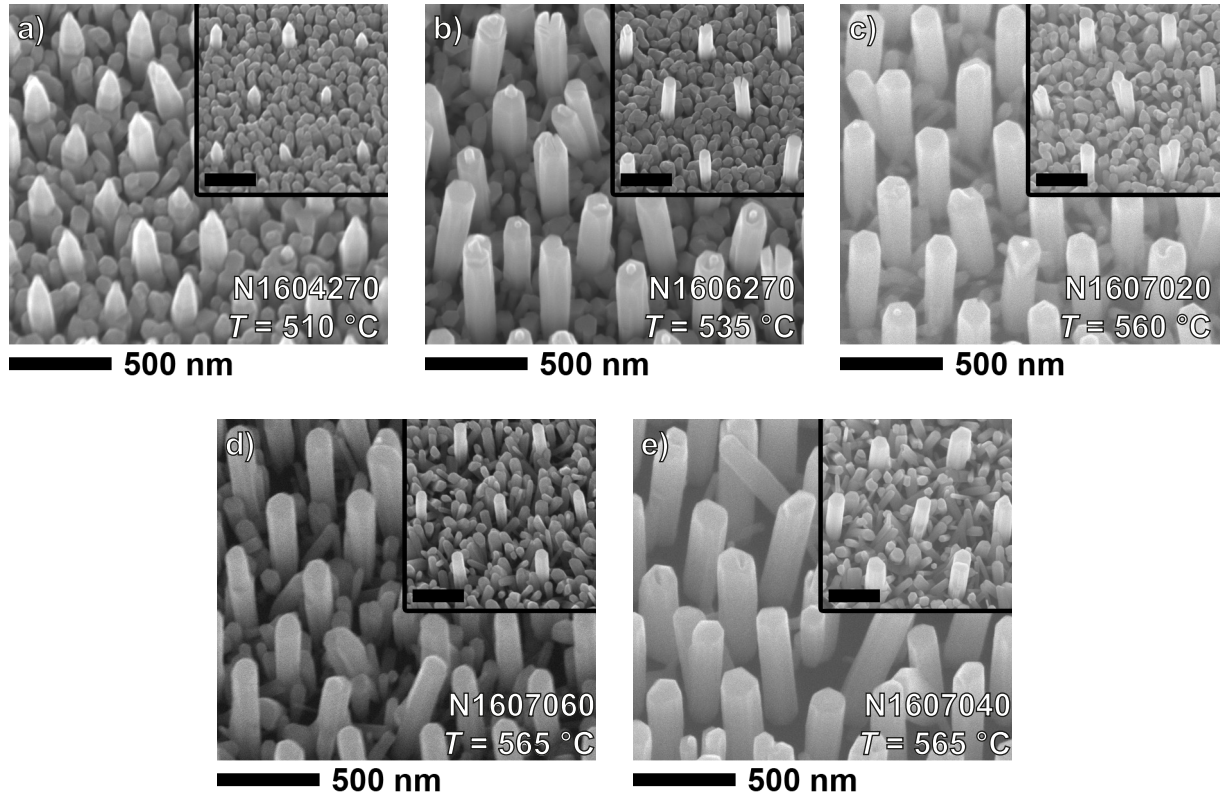


Figure 7.13: SEM images of samples grown with a) $T_{\text{heater}} = 510^\circ\text{C}$, b) $T_{\text{heater}} = 535^\circ\text{C}$, c) $T_{\text{heater}} = 560^\circ\text{C}$, d) $T_{\text{heater}} = 565^\circ\text{C}$ and e) $T_{\text{heater}} = 585^\circ\text{C}$. Large (small) images were recorded in a growth field with a pitch of 350 nm (750 nm). All images were recorded under an incident angle of 25° and sample numbers are given in the images.

for a nanohole pitch of 350 nm but still results in significant growth on the TiN mask for $p = 750$ nm. This indicates a diffusion length of the Ga adatoms below 375 nm on the TiN mask.

Photoluminescence spectroscopy

Figure 7.14a) depicts the μ -PL spectra (recorded with *Setup C* at 4K) of the five samples grown with different substrate temperatures. All spectra were recorded in the growth field with a pitch of 350 nm and the spectra were stacked along the ordinate. The corresponding growth temperature increases from the bottom to the top spectrum. Broad emission bands are observed in all of the spectra and only 180 NWs are excited simultaneously due to a laserspot diameter of $\approx 5\ \mu\text{m}$. The $\text{In}_x\text{Ga}_{1-x}\text{N}$ emission blue shifts from 2.3 eV ($T_{\text{heater}} = 510^\circ\text{C}$, $[\text{In}] = 33\%$) up to 2.6 eV ($T_{\text{heater}} = 565^\circ\text{C}$, $[\text{In}] = 24\%$) due to an increasing In desorption rate for higher temperatures. However, a broad PL band centered at 2.2 eV is observed upon a further increase of the substrate temperature to 585°C indicating a

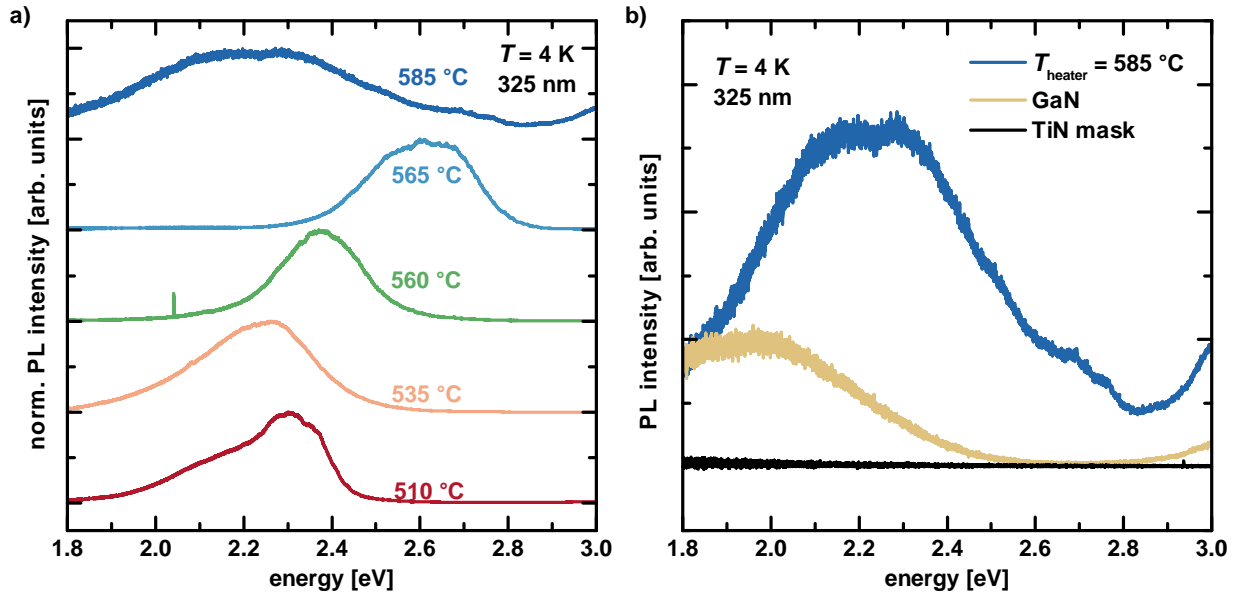


Figure 7.14: a) Micro-PL spectra recorded at 4 K on selectively grown $In_xGa_{1-x}N/GaN$ NWs. The spectra were normalized to the emission maximum and are stacked along the ordinate. All spectra are labeled according to the substrate temperature used during the $In_xGa_{1-x}N$ growth. Figure b) displays the PL spectrum recorded on the sample grown with $T_{heater} = 585^\circ C$ (blue), that of a GaN reference recorded in the 350 nm pitch field of sample N1604224 sample (red) and the spectrum recorded on a blank TiN mask (yellow).

higher In content in this particular sample. Therefore, the spectrum that was recorded on the sample grown with $T_{heater} = 585^\circ C$ is compared to the PL spectrum of a GaN reference sample and that of a blank TiN mask in figure 7.14b). In contrast to the self-assembled GaN NWs, the red luminescence at 1.9 eV due to structural defects in GaN is observed in PCG grown GaN NWs. In the studies of Reshchikov and Morkoç, this emission band was only observed in absence of the yellow luminescence (2.2 eV to 2.3 eV) and was assigned native defects or complex related defects acting as deep acceptors [83]. A GaN antisite defect was put forward as a likely candidate for the origin of the red luminescence in MBE grown samples [83]. Hence, the broad emission band of the $In_xGa_{1-x}N$ sample centered at 2.2 eV does not necessarily originate from regions of high local In content but might also be attributed to the yellow luminescence which originates from V_{Ga} complexes in defective GaN. The TiN mask does not show any distinct luminescence in the investigated spectral range (figure 7.14b)). Comparison of the PL spectra recorded on the samples grown at $T_{heater} = 565^\circ C$ and $T_{heater} = 585^\circ C$ further indicates the absence of In in the PCG NWs of the sample grown at the higher temperature (figure 7.15). A spectrum recorded on NWs grown on the TiN mask is shown for each sample in figure 7.15. This parasitic growth

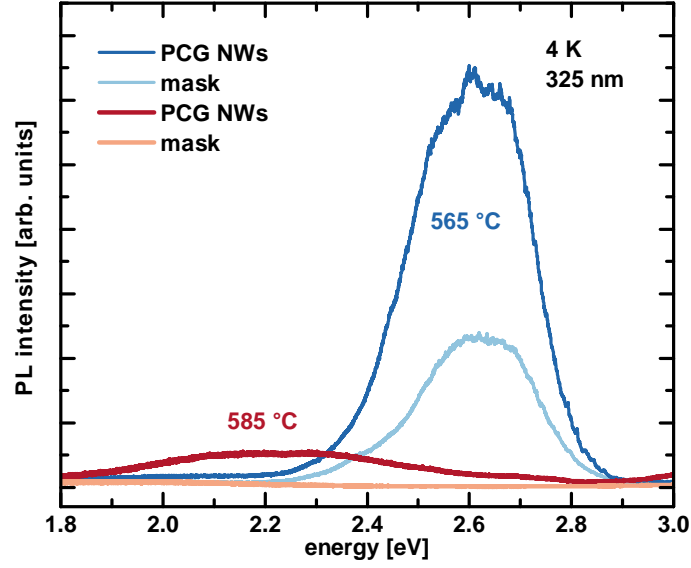


Figure 7.15: Low temperature PL recorded on NWs with 350 nm pitch grown with $T_{\text{heater}} = 565^\circ\text{C}$ (blue) and $T_{\text{heater}} = 585^\circ\text{C}$ (red) are shown together with spectra recorded on the NWs grown on the TiN mask outside of the growth field.

cannot be suppressed at the applied substrate temperatures. The PL intensity of the PCG NWs on the sample grown at a higher T_{heater} is by one order of magnitude lower than the intensity of the sample grown at a lower temperature. Additionally, the NWs grown on the TiN mask do not feature an $\text{In}_x\text{Ga}_{1-x}\text{N}$ related emission for $T_{\text{heater}} = 585^\circ\text{C}$ indicating complete desorption of arriving In atoms. In contrast, the parasitically grown NWs on the sample grown at a lower substrate temperature exhibit a significant $\text{In}_x\text{Ga}_{1-x}\text{N}$ related PL. However, the PL intensity of the NWs grown on the TiN mask is by more than a factor of two lower than the PL intensity of the PCG NWs. Due to the residual growth on the TiN mask, the diffusion of In towards the PCG NWs is unlikely and, therefore, the origin of the 2.2 eV emission band in the sample grown at 585°C is probably due to structural defects in the low temperature GaN grown on top of PCG GaN NW templates.

Consequently, a substrate temperature of 565°C was chosen for further experiments because an improved selectivity compared to lower growth temperatures was achieved while still exhibiting a significant $\text{In}_x\text{Ga}_{1-x}\text{N}$ luminescence.

7.3.2 Influence of the nitrogen flux

The growth temperature of the $\text{In}_x\text{Ga}_{1-x}\text{N}$ segment was fixed to 565°C and the metal fluxes were set to $\text{BEP}_{\text{Ga}} = 7 \times 10^{-8}$ mbar and $\text{BEP}_{\text{In}} = 2 \times 10^{-7}$ mbar. A lower Ga flux compared to the samples discussed in the previous section was used to prevent parasitic

NW growth on the TiN mask. The total incident metal flux was kept nominally constant, increasing the In/Ga ratio by a factor of three (cf. table 7.1). Figure 7.16 depicts the SEM bird's-eye view (25° tilt angle) images of samples grown with different Φ_{N_2} . The large

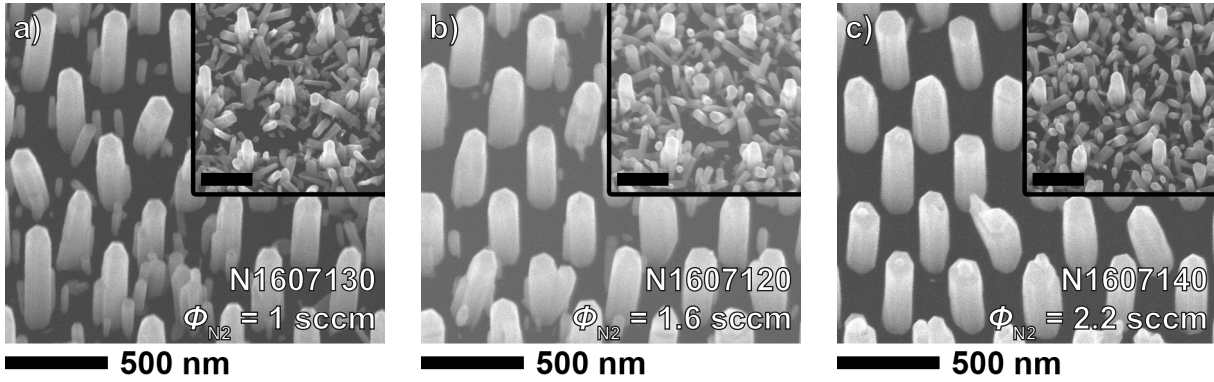


Figure 7.16: *Bird's-eye view (25° tilt angle) SEM images of samples grown with a) $\Phi_{N_2} = 1$ sccm, b) $\Phi_{N_2} = 1.6$ sccm and c) $\Phi_{N_2} = 2.2$ sccm. Large (small) images correspond to fields with $p = 350$ nm ($p = 750$ nm). Sample numbers are given in the images.*

images were taken in the 350 nm pitch field while the small images stem from the growth field with $p = 750$ nm. Selectivity was not achieved for a pitch of 750 nm but increasing Φ_{N_2} from 1 sccm to 2.2 sccm lead to a successive suppression of NW nucleation on the TiN mask for a pitch of 350 nm. Samples N1607120 (In/Ga = 2.86, figure 7.16b)) and N1607060 (In/Ga = 0.93, figure 7.13d), section 7.3.1) were grown under nominally identical growth conditions except the incident In/Ga flux ratio. While a constant overall metal flux was used, sample N1607120 was grown with only half of the BEP_{Ga} that was used for sample N1607060. The almost perfect selectivity achieved at $p = 350$ nm in the case of the smaller incident Ga flux illustrates the previous assumption that the adsorbed Ga is the origin of the NW nucleation on the TiN mask. The reduced adatom diffusion/desorption rate due to the low substrate temperatures has, therefore, to be compensated by lowering the incident Ga flux. Consequently, a systematic variation of the In/Ga flux ratio was performed and its influence on the PCG of the $In_xGa_{1-x}N/GaN$ NWHs is discussed in section 7.3.3

Photoluminescence spectroscopy

The μ -PL spectra (4K) recorded on samples grown with different Φ_{N_2} are depicted in figure 7.17a). Increasing Φ_{N_2} from 1 sccm to 2.2 sccm leads to the red shift of the $In_xGa_{1-x}N$ luminescence from 2.6 eV ([In] = 24 %) to 2.45 eV ([In] = 28 %). This is due to an enhanced In incorporation at higher Φ_{N_2} which was also discussed in chapter 6, section 6.1. Figure 7.17b) displays the dependence of the integrated PL intensity on Φ_{N_2} . The sample grown

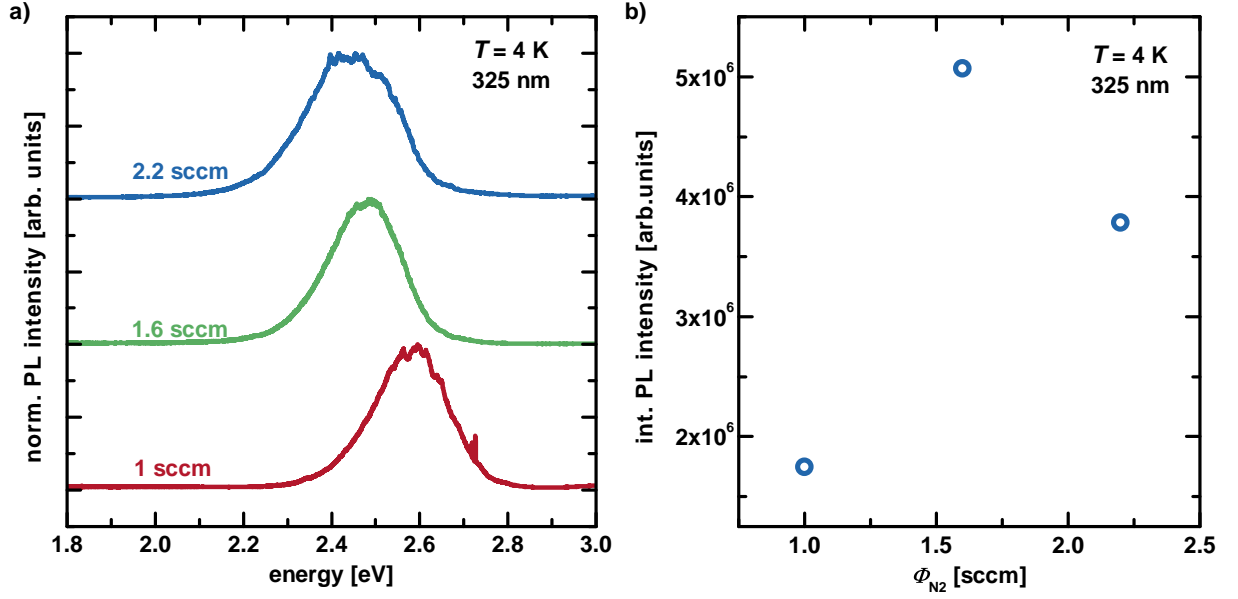


Figure 7.17: a) Micro-PL spectra recorded on samples N1607130 (red), N1607120 (green) and N1607140 (blue). The spectra were normalized to the respective emission maxima and are shifted along the ordinate. b) Integrated intensity of the non-normalized PL spectra recorded on samples grown with different Φ_{N_2} .

with $\Phi_{\text{N}_2} = 1$ sccm exhibits an emission intensity that is by a factor of 2 lower than that of the other two samples due to the low In incorporation efficiency at lower Φ_{N_2} .

A nitrogen flux of 2.2 sccm was, therefore, used for further growth experiments due to the improved selectivity achieved for the $\text{In}_x\text{Ga}_{1-x}\text{N}$ growth at a pitch of 350 nm.

7.3.3 Influence of the metal flux ratio

Three samples were grown at a fixed substrate temperature ($T_{\text{heater}} = 565^\circ\text{C}$) and nitrogen flux ($\Phi_{\text{N}_2} = 2.2$ sccm), only varying the incident metal fluxes. The In/Ga ratio was varied from 2.86 ($\text{BEP}_{\text{In}} = 2 \times 10^{-7}$ mbar, $\text{BEP}_{\text{Ga}} = 7 \times 10^{-8}$ mbar) to 6.86 ($\text{BEP}_{\text{In}} = 2.4 \times 10^{-7}$ mbar, $\text{BEP}_{\text{Ga}} = 3.5 \times 10^{-8}$ mbar). Figure 7.18 displays the bird's-eye view SEM images of the corresponding samples. Selectivity is achieved for all samples when a nanohole pitch of 350 nm is used. An improvement of the selectivity in the field with $p = 750$ nm was observed with an increase of the In/Ga ratio as demonstrated by the small images displayed in figure 7.18. Complete selectivity was, however, not achieved for a pitch of 750 nm at the low T_{heater} used for the growth of the $\text{In}_x\text{Ga}_{1-x}\text{N}$. The diameter of the NW tip of the samples shown in figure 7.18 decreases with decreasing BEP_{Ga} . For self-assembled samples presented in chapter 6, section 6.1, a similar trend was observed for increasingly N-rich growth conditions. Due to the low Ga desorption rate at the applied temperatures, the

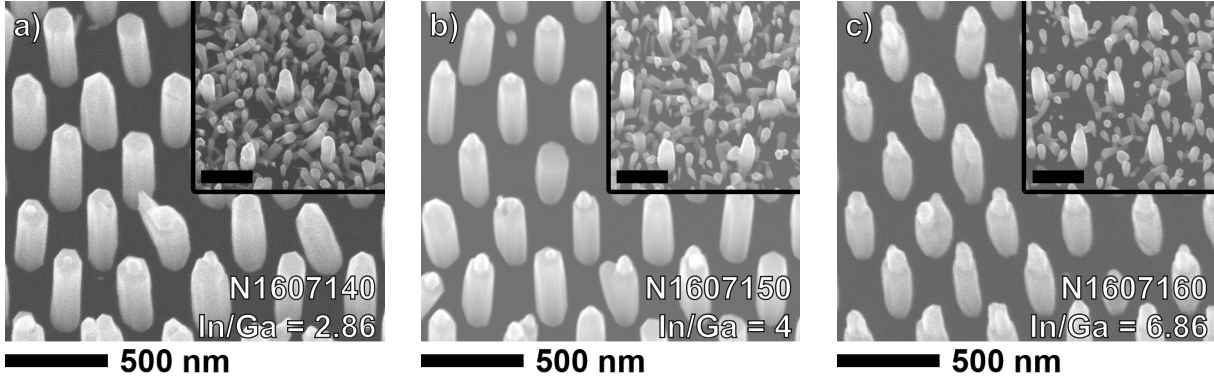


Figure 7.18: SEM images of samples grown with a) $In/Ga = 2.86$ ($BEP_{In} = 2 \times 10^{-7}$ mbar, $BEP_{Ga} = 7 \times 10^{-8}$ mbar), b) $In/Ga = 4$ ($BEP_{In} = 2 \times 10^{-7}$ mbar, $BEP_{Ga} = 5 \times 10^{-8}$ mbar) and c) $In/Ga = 6.86$ ($BEP_{In} = 2.4 \times 10^{-7}$ mbar, $BEP_{Ga} = 3.5 \times 10^{-8}$ mbar). Large (small) images were taken in a growth field with a pitch of 350 nm (750 nm). All images were taken under an incident angle of 25° and sample numbers are given in the images.

III/V ratio is mainly determined by the BEP_{Ga} and decreases with decreasing BEP_{Ga} which leads to the observed decrease of the diameter of the $In_xGa_{1-x}N$ NW tip.

Photoluminescence spectroscopy

The optical properties of the three samples displayed in figure 7.18 were investigated by μ -PL spectroscopy at a temperature of 4 K. Figure 7.19a) depicts the PL spectra recorded on the samples grown with different In/Ga ratios. A slight blue shift of the PL emission band from 2.45 eV ([In] = 28 %) to 2.51 eV ([In] = 27 %) is observed when the In/Ga ratio is increased from 2.86 to 4. Further increase of the In/Ga ratio to 6.86 is accompanied by a red shift of the luminescence peak to 2.34 eV ([In] = 32 %). Figure 7.19b) shows the evolution of the integrated PL intensity with increasing In/Ga flux ratio. An increase of In/Ga from 2.86 to 6.86 leads to a decrease of the luminescence intensity by one order of magnitude. Turski et al. reported that Ga and N_2 , both, have a stabilizing effect on the InN incorporated into the $In_xGa_{1-x}N$ [129]. Hence, the absolute amount of incorporated In is reduced with increasing In/Ga ratio when the total metal flux is kept constant leading to a strong reduction of the luminescence intensity. The maximum local In concentration, however, directly scales with the In/Ga ratio as an increase of the local In content from 28 % to 32 % was observed with increasing In/Ga.

Conclusively, a low In/Ga flux ratio should be chosen to maximize the luminescence intensity in PCG $In_xGa_{1-x}N$ NWs.

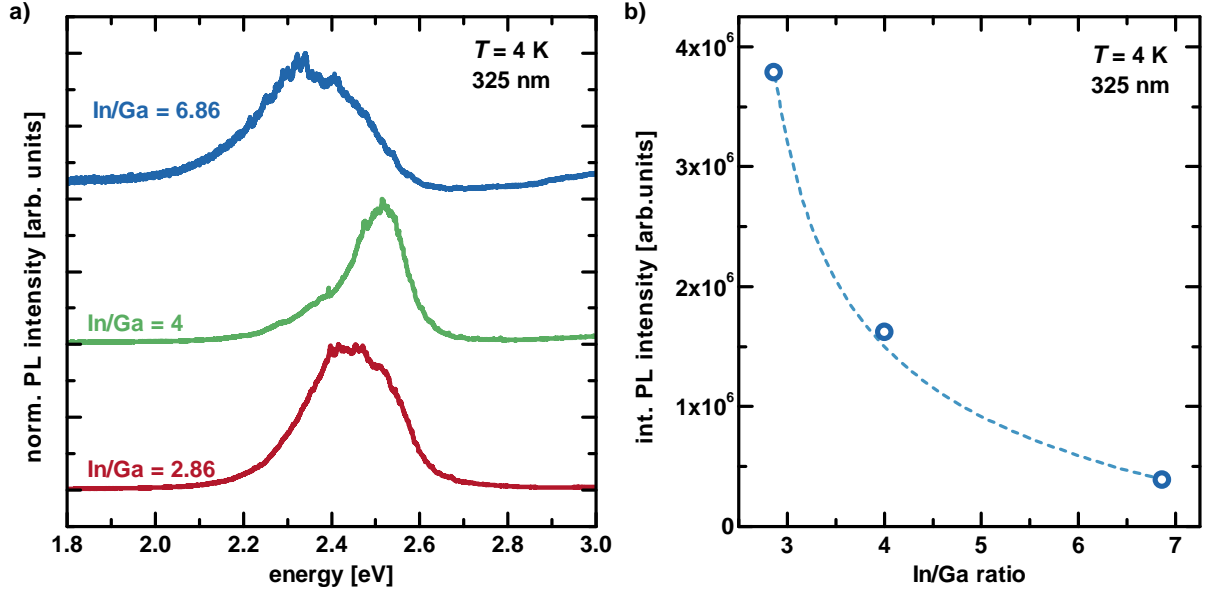


Figure 7.19: a) Micro-PL spectra of samples grown with a In/Ga ratio of 2.86 (red), 4 (green) and 6.86 (blue) are plotted and vertically shifted. Figure b) displays the dependence of the integrated PL intensity of the non-normalized spectra on the In/Ga ratio. A dashed line was added to b) to guide the eye.

7.3.4 Conclusion

The PCG of $\text{In}_x\text{Ga}_{1-x}\text{N}/\text{GaN}$ NWHs was demonstrated. The substrate temperature has only a limited influence on the selectivity of the growth process of the $\text{In}_x\text{Ga}_{1-x}\text{N}$ segment. Mainly the In desorption rate is influenced by T_{heater} while Ga adatom diffusion/desorption is not significantly affected within the $\text{In}_x\text{Ga}_{1-x}\text{N}$ growth window. Reducing the Ga flux and thereby increasing the In/Ga flux ratio leads to the desired selectivity of the $\text{In}_x\text{Ga}_{1-x}\text{N}$ growth on the selectively grown GaN NW templates. Additionally, the nitrogen flux has to be adjusted to further improve the selectivity. The results obtained here demonstrate that the constraint of a selective growth of $\text{In}_x\text{Ga}_{1-x}\text{N}/\text{GaN}$ NWHs poses new challenges to the applied PAMBE process. A major parameter dominating the properties of the selectively grown $\text{In}_x\text{Ga}_{1-x}\text{N}$ could not be identified. The complex interplay between substrate temperature, atom source operating parameters and metal fluxes suggests the systematic exploration of all these parameters resulting in a complex growth diagram.

8 Summary

Gallium nitride nanowires were grown in a self-assembled PAMBE process on Si(111) and have been used as templates for the subsequent growth of group III-nitride nanowire heterostructures. Additionally, the position-controlled growth of GaN nanowires was established using a titanium nanohole mask on Si(111), structured by electron beam lithography. These selectively grown GaN nanowires were used as templates for the growth of $\text{In}_x\text{Ga}_{1-x}\text{N}$.

Analysis of the influence of the atom source operating parameters on the structural and optical properties of self-assembled grown GaN and $\text{In}_x\text{Ga}_{1-x}\text{N}/\text{GaN}$ nanowire heterostructures was conducted. Evaluation of the emission spectra of the used nitrogen discharge revealed an increase (decrease) of the $n(N)/n(N_2)$ ratio with increasing forward power (nitrogen flux). The increase of both, the forward power and the nitrogen flux, leads to the stabilization of nanowire nuclei. Furthermore, the radial and axial growth rates increase with increasing forward power and nitrogen flux. However, inhomogeneous nanowire growth is observed for high nitrogen fluxes.

An increasing density of V_N was proposed to be the origin of the observed degradation of the optical properties with increasing forward power due to the ability of atomic nitrogen to dissociates Ga-N bonds. An increase of the nitrogen flux gave rise to an emission at 3.45 eV which substantiates the assignment of this emission to V_{Ga} at the NW surface.

Fortyfold AlN/GaN nanodisc superlattices were grown on self-assembled GaN NW templates. The recent discovery of the outstanding doping efficiency of Ge in GaN motivated the investigation of the doping-induced electrostatic screening of the internal electric fields in these nanodisc superlattices. Significant screening of these electric fields was achieved using Ge concentrations in the range of 10^{20} cm^{-3} , reducing the photoluminescence decay times by two orders of magnitude due to an increased electron and hole wavefunction overlap. In addition, the nanodisc emission energy was blue shifted by several hundred meV due to a reduced quantum-confined Stark effect.

A second approach to reduce the electric fields in undoped AlN/GaN nanodisc superlattices was followed by reducing the AlN barrier thickness. The latter brings the oppositely charged interfaces of the barrier closer together, shifting the potential drop more into the barriers. Consequently, a strong reduction (increase) of the luminescence decay time (emission energy) was observed for a decreasing barrier thickness at a constant ND thickness.

The influence of the atom source operating parameters on the structural and optical properties of $\text{In}_x\text{Ga}_{1-x}\text{N}/\text{GaN}$ nanowire heterostructures was also analyzed. All samples were subject to an inhomogeneous In incorporation due to the formation of In-rich regions.

Increasing the nitrogen flux leads to a stabilization of In-N bonds due to the increased nitrogen partial pressure, as theoretically predicted, which results in a significant increase of the local In content. An increase of the forward power, on the other hand, does not affect the In incorporation but significantly increases the density of non-radiative recombination centers in the $\text{In}_x\text{Ga}_{1-x}\text{N}$, reflected by a strong decrease of the photoluminescence intensity as well as the luminescence decay time. The increasing probability of the formation of V_N due to an enhanced decomposition reaction at higher densities of atomic nitrogen was proposed to be the origin of the increasing non-radiative recombination rate.

Tenfold $\text{In}_x\text{Ga}_{1-x}\text{N}/\text{GaN}$ nanodisc superlattices were fabricated to study quantum confinement effects in the $\text{In}_x\text{Ga}_{1-x}\text{N}$ nanodiscs. A strong interplay between the localized states due to compositional fluctuations and the quantum mechanical states due to the axial dimension of the nanodiscs was observed. Additionally, time-resolved photoluminescence revealed a negligible influence of internal electric fields on the luminescence properties of the present samples.

A position-controlled growth process for the selective growth of GaN nanowires was developed. Nanohole diameters down to 70 nm were realized by a process based on electron beam lithography transferring a hexagonal nanohole pattern to thin Ti layers. Selectivity of the growth was achieved for Ti mask thicknesses below 4 nm. Diameters below 100 nm were realized for nanowires up to a length of approximately $1.5\ \mu\text{m}$. Pitches up to $10\ \mu\text{m}$ were demonstrated enabling the $\mu\text{-PL}$ analysis of single as grown nanowires. The growth of $\text{In}_x\text{Ga}_{1-x}\text{N}$ on top of position-controlled growth GaN NW templates was studied as a function of the substrate temperature as well as in dependence of the metal and nitrogen fluxes. The strong interplay between those parameters was demonstrated and conditions for the selective growth of $\text{In}_x\text{Ga}_{1-x}\text{N}$ were established.

Finally, the presented results yield a comprehensive understanding of the PAMBE growth of self-assembled and position-controlled GaN nanowire templates and the subsequent fabrication of group III-nitride nanowire heterostructures. Hence, this work will help to improve the quality of nanowire based (nano)-opto-electronic devices based on the technological relevant group III-nitride material system.

Appendix

A.1 Effusion cell calibrations

Figure A.1 displays *BEP* calibration curves of all effusion cells used in the presented experiments.

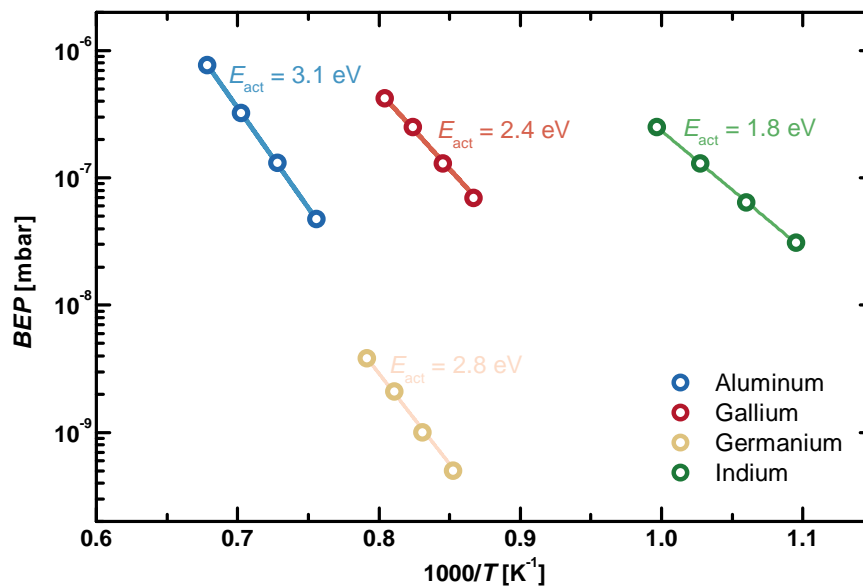


Figure A.1: *BEP* calibration curves of all cells that were used during the growth experiments.

Symbols represent measurement data and lines correspond to exponential fits. The resulting activation energies for the evaporation of the source material are given in the graph.

A.2 Patterning of Ti nanohole masks

The following recipe was used to fabricate Ti nanohole masks on Si(111)¹:

1. Ultrasonication assisted cleansing of the substrate in acetone² (60 s).
2. Rinsing of the substrate in 2-Propanol², dry blowing with nitrogen.
3. Etching in hydrofluoric acid (10 %)² and subsequent rinsing in *Millipore water*.
4. Coating of the substrate with the primer *HMDS*³ in a clean room environment *ISO class 6* within 15 min after etching.
 - The dehydration bake is omitted to prevent oxidation of the Si(111) surface.
 - Excess primer solution was removed after 30 s of reaction time by putting the substrate on a spin coater operated at 3000 rpm for 4 s.
5. Baking of the primer layer on a hot plate for 60 s at 100°C.
6. Spin coating of the primed substrate with the negative resist *ma-N 2401*³ for 40 s at 2000 rpm (nominal layer thickness of 110 nm).
7. Baking of the coated substrate on a hot plate for 90 s at 90°C.
8. Transfer of the sample into the SEM specimen chamber for the EBL process which was carried out using an acceleration voltage of 20 kV (15 kV for areas larger than $1 \times 1\text{mm}^2$), an exposure dose of $200 \mu\text{C}/\text{cm}^2$ and a beam current of 80 pA.
9. Development of the patterned resist in the developer solution *ma-D 331*³ for a time of 18 s.
10. Rinsing in demineralized water for 15 s and dry blowing with N₂.
11. The Ti layer was evaporated onto the patterned substrate using electron beam evaporation at a background pressure of 5×10^{-6} mbar. A slow deposition rate of 0.1 nm/s was used.
12. Finally, an ultrasonication assisted lift-off process in acetone was used to remove the remaining resist and finish the processing of the nanohole masks.

¹Supplier: *Silicon Materials Inc.*

²Supplier: *AppliChem GmbH*

³Supplier: *micro resist technology GmbH*

A.3 List of samples

Table A.1 lists all NW samples that were used/grown during this work. The sample name

Sample	Material	Sample	Material	Sample	Material
N1204250	GaN:Ge	N1404252	InGaN/GaN	N1602040	PCG GaN
N1204260	GaN:Ge	N1405050	InGaN/GaN	N1602080	PCG GaN
N1204270	GaN	N1405053	InGaN/GaN	N1602150	AlN/GaN NDs
N1303040	AlN/GaN NDs	N1405082	InGaN/GaN	N1602240	PCG GaN
N1303043	AlN/GaN NDs	N1405083	InGaN/GaN	N1602250	AlN/GaN NDs
N1303060	AlN/GaN:Ge NDs	N1405120	InGaN/GaN	N1602290	AlN/GaN NDs
N1303063	AlN/GaN:Ge NDs	N1405121	InGaN/GaN	N1603020	AlN/GaN NDs
N1303070	AlN/GaN:Ge NDs	N1405160	InGaN/GaN	N1603230	AlN/GaN NDs
N1303073	AlN/GaN:Ge NDs	N1405163	InGaN/GaN	N1604140	PCG GaN
N1303080	AlN/GaN:Ge NDs	N1405193	InGaN/GaN	N1604220	PCG GaN
N1303083	AlN/GaN:Ge NDs	N1405230	InGaN/GaN	N1604224	PCG GaN
N1303190	InGaN/GaN	N1405232	InGaN/GaN	N1604270	PCG GaN
N1304110	GaN	N1405233	InGaN/GaN	N1604290	InGaN/GaN
N1304120	GaN	N1407230	GaN	N1605024	PCG GaN
N1304150	GaN	N1407240	GaN	N1605040	InGaN/GaN NDs
N1304153	GaN	N1407280	GaN	N1605050	InGaN/GaN NDs
N1304160	GaN	N1407290	GaN	N1605060	InGaN/GaN NDs
N1307263	AlN/GaN NDs	N1407310	GaN	N1605090	InGaN/GaN NDs
N1307290	AlN/GaN NDs	N1408060	GaN	N1605114	PCG GaN
N1307303	AlN/GaN NDs	N1408120	GaN	N1605230	InGaN/GaN NDs
N1307313	AlN/GaN NDs	N1408130	GaN	N1606230	GaN
N1308013	AlN/GaN NDs	N1408150	GaN	N1606270	PCG InGaN/GaN
N1308020	AlN/GaN:Ge NDs	N1408180	GaN	N1607020	PCG InGaN/GaN
N1308023	AlN/GaN:Ge NDs	N1408190	GaN	N1607040	PCG InGaN/GaN
N1308053	AlN/GaN:Ge NDs	N1408200	GaN	N1607060	PCG InGaN/GaN
N1308063	AlN/GaN:Ge NDs	N1409120	InGaN/GaN	N1607080	AlN/GaN NDs
N1308160	AlN/GaN NDs	N1409123	InGaN/GaN	N1607120	PCG InGaN/GaN
N1308210	AlN/GaN:Ge NDs	N1502201	InGaN/GaN	N1607130	PCG InGaN/GaN
N1308213	AlN/GaN:Ge NDs	N1510193	GaN	N1607140	PCG InGaN/GaN
N1308220	AlN/GaN:Ge NDs	N1510203	GaN	N1607150	PCG InGaN/GaN
N1308223	AlN/GaN:Ge NDs	N1510213	GaN	N1607160	PCG InGaN/GaN
N1312113	AlN/GaN NDs	N1511030	GaN	N1607191	AlN/GaN NDs
N1312123	AlN/GaN NDs	N1511040	GaN	N1607200	PCG InGaN/GaN
N1312130	AlN/GaN:Ge NDs	N1601070	PCG GaN	N1607201	InGaN/GaN
N1404250	InGaN/GaN	N1601180	PCG GaN	N1607210	AlN/GaN NDs
N1404251	InGaN/GaN	N1601280	PCG GaN		

Table A.1: *List of all samples discussed in this work. The sample name is listed together with the material used for the NWs.*

containing the date of growth is given together with the material that was used. Table A.2 lists all substrates that were used for the PCG of $(\text{In}_x\text{Ga}_{1-x}\text{N})/\text{GaN}$.

PCG substrates					
SiMat03-057	SiMat03-073	SiMat03-102	SiMat03-111	SiMat03-119	SiMat03-129
SiMat03-067	SiMat03-075	SiMat03-103	SiMat03-118	SiMat03-123	SiMat03-130
SiMat03-070	SiMat03-083	SiMat03-108	SiMat03-121	SiMat03-124	SiMat03-136
SiMat03-061	SiMat03-099	SiMat03-109	SiMat03-122	SiMat03-128	

Table A.2: *List of the substrates that were used for the PCG growth of $(\text{In}_x\text{Ga}_{1-x}\text{N})/\text{GaN}$ NWs.*

A.4 Nextnano³ input parameters

The NWH simulated according to *Input A* (cf. chapter 5, section 5.3) consisted of a 50 nm GaN base (20 nm radius, 5 nm AlN shell) followed by nine GaN NDs (4 nm) embedded in AlN (4 nm) barriers. The whole structure was capped with 22 nm of GaN [115]. For *Input B* (cf. chapter 5, section 5.3), the AlN/GaN NWH is composed of a 20x AlN/GaN NDSLs with constant $d_{\text{ND}} = 4$ nm using different sets of d_{barrier} . The GaN base (17 nm radius) and the cap of the NDSL were simulated with a length of 15 nm, respectively. A lateral growth ($r_{\text{lateral}}/r_{\text{axial}}$) of 5% was assumed for the AlN shell leading to a diameter increase of consecutive NDs along the NDSL. *Input A* and *Input B* were surrounded by air to allow elastic deformation of the lateral surfaces or minimize strain. The nextnano³ input parameters used to calculate the bandprofiles shown in chapter 5, section 5.3 are listed in table A.3 (*Input A*) and table A.4 (*Input B*).

Parameters	GaN	AlN
Lattice parameters [Å]		
a	3.1892	3.112
c	5.185	4.982
Spontaneous polarization [C/m ²]	-0.029	-0.81
Piezoelectric polarization [C/m ²]		
e_{31}	-0.49	-0.6
e_{33}	0.73	1.46
Elastic constants [GPa]		
C_{11}	390	396
C_{12}	145	140
C_{13}	106	108
C_{33}	398	373
Deformation potentials [eV]		
a_1	-4.6	-4.5
a_2	-4.6	-4.5
D_1	-1.7	-2.89
D_2	6.3	4.89
D_3	8	7.78
D_4	-4	-3.89
D_5	-4	-3.34
D_6	-5.66	-3.94

Table A.3: Material parameters listed in [158] used to calculate the band profiles according to *Input A*.

Parameters	GaN	AlN
Lattice parameters [\AA]		
a	3.189	3.112
c	5.185	4.982
Spontaneous polarization [C/m^2]	-0.034	-0.09
Piezoelectric polarization [C/m^2]		
e_{31} [159]	-0.35	-0.5
e_{33} [159]	1.27	1.79
e_{15} [36]	-0.3	-0.48
Elastic constants [GPa]		
C_{11}	390	396
C_{12}	145	137
C_{13}	106	108
C_{33}	398	373
Deformation potentials [eV]		
a_1	-4.9	-3.4
a_2	-11.3	-11.8
D_1	-3.7	-17.1
D_2	4.5	7.9
D_3	8.2	8.8
D_4	-4.1	-3.9
D_5	-4	-3.4
D_6	-5.1	-3.4

Table A.4: *Material parameters used to calculate the band profiles according to Input B. If not otherwise noted, the parameters were taken from Ref. [18].*

A.5 List of publications

A list of articles published during this work is given in the following.

As first author

P. Hille, J. Müßener, P. Becker, M. de la Mata, N. Rosemann, C. Magén, J. Arbiol, J. Teubert, S. Chatterjee, J. Schörmann and M. Eickhoff *Screening of the quantum-confined Stark effect in AlN/GaN nanowire superlattices by germanium doping* Appl. Phys. Lett. **104** (2014), 102104

As co-author

J. M. Philipps, G. M. Müntze, P. Hille, J. Wallys, J. Schörmann, J. Teubert, D. M. Hofmann and M. Eickhoff *Radical formation at the gallium nitride nanowire–electrolyte interface by photoactivated charge transfer*, Nanotechnology **24** (2013), 325701

J. Schörmann, P. Hille, M. Schäfer, J. Müßener, P. Becker, P. J. Klar, M. Kleine-Boymann, M. Rohnke, M. de la Mata, J. Arbiol, D. M. Hofmann, J. Teubert, and M. Eickhoff *Germanium doping of self-assembled GaN nanowires grown by plasma-assisted molecular beam epitaxy*, J. Appl. Phys. **114** (2013), 103505

M. Beeler, P. Hille, J. Schörmann, J. Teubert, M. de la Mata, J. Arbiol, M. Eickhoff and E. Monroy *Intraband Absorption in Self-Assembled Ge-Doped GaN/AlN Nanowire Heterostructures*, Nano Lett. **14** (2014), 1665–1673

K. Maier, A. Helwig, G. Müller, P. Becker, P. Hille, J. Schörmann, J. Teubert and M. Eickhoff *Detection of oxidising gases using an optochemical sensor system based on GaN/InGaN nanowires*, Sensor. Actuat. B-Chem. **197** (2014), 87–94

J. Müßener, J. Teubert, P. Hille, M. Schäfer, J. Schörmann, M. de la Mata, J. Arbiol, and M. Eickhoff *Probing the Internal Electric Field in GaN/AlGaN Nanowire Heterostructures* Nano Lett. **14** (2014), 5118–5122

M. Beeler, C. B. Lim, P. Hille, J. Bleuse, J. Schörmann, M. de la Mata, J. Arbiol, M. Eickhoff and E. Monroy *Long-lived excitons in GaN/AlN nanowire heterostructures*, Phys. Rev. B **91** (2015), 205440

M. Schäfer, M. Günther, C. Länger, J. Müßener, M. Feneberg, P. Uredat, M. T. Elm, P. Hille, J. Schörmann, J. Teubert, T. Henning, P. J. Klar and M. Eickhoff *Electrical transport properties of Ge-doped GaN nanowires*, Nanotechnology **26** (2015), 135704

K. Maier, A. Helwig, G. Müller, P. Hille and M. Eickhoff *Effect of Water Vapor and Surface Morphology on the Low Temperature Response of Metal Oxide Semiconductor Gas Sensors*, *Materials* **8** (2015), 6570-6588

M. T. Elm, P. Uredat, J. Binder, L. Ostheim, M. Schäfer, P. Hille, J. Müßener, J. Schörmann, M. Eickhoff and P. J. Klar *Doping-Induced Universal Conductance Fluctuations in GaN Nanowires*, *Nano Lett.* **15** (2015), 7822–7828

J. Lähnemann, M. I. den Hertog, P. Hille, M. de la Mata, T. Fournier, J. Schörmann, J. Arbiol, M. Eickhoff and E. Monroy *UV Photosensing Characteristics of Nanowire Based GaN/AlN Superlattices*, *Nano Lett.* **16** (2016), 3260–3267

K. Maier, A. Helwig, G. Müller, P. Hille, J. Teubert, M. Eickhoff *Photoluminescence Probing of Complex H₂O Adsorption on InGaN/GaN Nanowires*, *Nano Lett.* **17** (2017), 615–621

M. Riedel, S. Hölzel, P. Hille, J. Schörmann, M. Eickhoff and F. Lisdat, *InGaN/GaN nanowires as a new platform for photoelectrochemical sensors – detection of NADH*, *Biosens. Bioelectron.* **94** (2017), 298–304

J. Müßener, P. Hille, T. Grieb, J. Schörmann, J. Teubert, E. Monroy, A. Rosenauer and M. Eickhoff *Bias-controlled Optical Transitions in GaN/AlN Nanowire Heterostructures*, *ACS Nano* **submitted** (2017)

K. I. Gries, J. Schlechtweg, P. Hille, J. Schörmann, M. Eickhoff and K. Volz, *Three dimensional reconstruction of InGaN nanodisks in GaN nanowires: improvement of the nanowire sample preparation to avoid missing wedge effects*, *Microsc. Microanal.* **submitted** (2017)

Acknowledgments/Danksagung

Abschließend möchte ich allen Personen danken, die mir bei dem erfolgreichen Abschluss meiner Promotion geholfen haben.

Prof. Dr. Martin Eickhoff danke ich für die Möglichkeit, diese Dissertation in seiner Arbeitsgruppe *Nanotechnologische Materialien* anzufertigen. Sein großes Interesse an meinem Dissertationsthema und die daraus resultierende intensive Betreuung haben mir während der Promotion sehr geholfen. Die Möglichkeit, darüberhinaus regelmäßig an internationalen Konferenzen teilzunehmen sowie mit internationalen Kooperationspartnern zusammenzuarbeiten, half mir, die nötige Motivation auch während längerer Stillstände der MBE nicht zu verlieren. Der freundliche Umgang und der gute Zusammenhalt, den er stets innerhalb der gesamten Arbeitsgruppe förderte, führte zu einer sehr produktiven Arbeitsatmosphäre.

Dr. Jörg Schörmann danke ich für die exzellente Zusammenarbeit und Betreuung, die bereits mit dem Beginn meiner Masterarbeit angingen. Ich konnte stets auf seine Unterstützung zählen, sei es bei Fragen rund um die MBE und das Wachstum, der Durchführung von XRD-Messungen, der Gesellschaft bei einer Tasse Kaffee oder aber wenn es darum ging, meine persönlichen Utensilien nach dem Kentern auf der Lahn wieder aus dem Wasser zu ziehen, Jörg war immer da! Vielen Dank!

Dr. Jörg Teubert danke ich für seine fachliche Beratung und die gute Gesellschaft bei zahlreichen außerfachlichen Abendveranstaltungen am I. Physikalischen Institut und auf Tagungen.

Max Kracht, Felix Walther, Christian Dern und Alexander Karg danke ich für die tolle Zusammenarbeit an der MBE. Max danke ich des Weiteren für die Hilfe bei den Reflexions- und AFM-Messungen.

Felix Walther und Christian Dern möchte ich für den wichtigen Beitrag zu meiner Arbeit danken, den Sie durch das Anfertigen ihrer Bachelor- und/oder Masterarbeiten geleistet haben.

Pascal Becker, Jan Müßener, Jan Philipps und Philip Klement danke ich für die zahlreichen PL-Messungen.

Prof. Dr. Slobodan Mitić und Julian Kaupe danke ich für die Hilfe bei der Untersuchung der Emissionsspektren des Stickstoffplasmas.

Außerdem danke ich **Prof. Dr. Detlev Hofmann** für die fachliche Unterstützung und die TEM-Untersuchungen vieler Nanodrähte. In diesem Zusammenhang möchte ich auch **Pascal Vöpel** danken, der die TEM-Untersuchungen in der letzten Zeit mit mir durchgeführt hat.

I sincerely thank **Dr. Eva Monroy** for the kind hospitality during my two weeks stay at the CEA-Grenoble and the intense scientific collaboration on the topic of the AlN/GaN NDSLs.

Many thanks to **Prof. Dr. Jordi Arbiol** for conducting the STEM analysis on the AlN/GaN NWHs.

Prof. Dr. Sangam Chatterjee, Dr. Nils Rosemann und Vanessa Dahmen gilt mein Dank für die Messung von zeitaufgelöster PL an den Nanodrahtheterostrukturen. Sangam Chatterjee danke ich außerdem für den fachlichen Austausch über zeitaufgelöste Photolumineszenzspektroskopie.

Dr. Gordon Callsen und Sarah Schlichting danke ich für das Messen zeitlich aufgelöster Photolumineszenz an den IFGARD-Strukturen und die Erlaubnis, meine Arbeit mit diesen Ergebnissen zu unterstützen.

Prof. Dr. Kerstin Volz und Dr. Katharina Gries danke ich für die TEM-Untersuchungen an den $\text{In}_x\text{Ga}_{1-x}\text{N}/\text{GaN}$ Nanodrahtheterostrukturen.

Allen nicht namentlich erwähnten Mitgliedern der Arbeitsgruppe *Nanotechnologische Materialien* sowie Mitarbeitern des *I. Physikalischen Instituts* danke ich für die harmonische Atmosphäre während und außerhalb der Arbeitszeit.

Meinen Freunden und meiner Familie, vor allem **Elena(!!!)**, danke ich für die umfangreiche Unterstützung während der Anfertigung dieser Arbeit.

Bibliography

- [1] M. Yoshizawa, A. Kikuchi, M. Mori, N. Fujita, and K. Kishino, *Growth of Self-Organized GaN Nanostructures on Al₂O₃(0001) by RF-Radical Source Molecular Beam Epitaxy*, Jpn. J. Appl. Phys. **36** (1997), L459–L462, <http://dx.doi.org/10.1143/JJAP.36.L459>.
- [2] F. Calle, F. J. Sánchez, J. M. G. Tijeroz, M. A. Sánchez-García, E. Calleja, and R. Beresford, *Exciton and donor-acceptor recombination in undoped GaN on Si(111)*, Semicond. Sci. Technol. **12** (1997), 1396–1403, <http://dx.doi.org/10.1088/0268-1242/12/11/011>.
- [3] F. Glas, *Critical dimensions for the plastic relaxation of strained axial heterostructures in free-standing nanowires*, Phys. Rev. B **74** (2006), <http://dx.doi.org/10.1103/PhysRevB.74.121302>.
- [4] E. Calleja, M. A. Sánchez-García, F. J. Sánchez, F. Calle, F. B. Naranjo, E. Muñoz, U. Jahn, and K. Ploog, *Luminescence properties and defects in GaN nanocolumns grown by molecular beam epitaxy*, Phys. Rev. B **62** (2000), 16826–16834, <http://dx.doi.org/10.1103/PhysRevB.62.16826>.
- [5] K. Bertness, A. Roshko, N. Sanford, J. Barker, and A. Davydov, *Spontaneously grown GaN and AlGa_xN nanowires*, J. Cryst. Growth **287** (2006), 522 – 527, <http://dx.doi.org/10.1016/j.jcrysgro.2005.11.079>.
- [6] J. Ristic, E. Calleja, M. A. Sánchez-García, J. M. Ulloa, J. Sánchez-Páramo, J. M. Calleja, U. Jahn, A. Trampert, and K. H. Ploog, *Characterization of GaN quantum discs embedded in Al_xGa_{1-x}N nanocolumns grown by molecular beam epitaxy*, Phys. Rev. B **68** (2003), 125305, <http://dx.doi.org/10.1103/PhysRevB.68.125305>.
- [7] J. Ristic, C. Rivera, E. Calleja, S. Fernández-Garrido, M. Povoloskyi, and A. Di Carlo, *Carrier-confinement effects in nanocolumnar GaN/Al_xGa_{1-x}N quantum disks grown by molecular-beam epitaxy*, Phys. Rev. B **72** (2005), 085330, <http://dx.doi.org/10.1103/PhysRevB.72.085330>.
- [8] T. Kouno, A. Kikuchi, and K. Kishino, *Growth of high-In-content InGa_xN multiple quantum disk nanocolumns on Si(111) by RF plasma-assisted molecular-beam epitaxy*, phys. stat. sol. (c) **243** (2006), 1481–1485, <http://dx.doi.org/10.1002/pssb.200565254>.

- [9] F. Furtmayr, J. Teubert, P. Becker, S. Conesa-Boj, J. R. Morante, A. Chernikov, S. Schäfer, S. Chatterjee, J. Arbiol, and M. Eickhoff, *Carrier confinement in GaN/Al_xGa_{1-x}N nanowire heterostructures (0 < x ≤ 1)*, Phys. Rev. B **84** (2011), 205303, <http://dx.doi.org/10.1103/PhysRevB.84.205303>.
- [10] C. Rivera, U. Jahn, T. Flissikowski, J. L. Pau, E. Muñoz, and H. T. Grahn, *Strain-confinement mechanism in mesoscopic quantum disks based on piezoelectric materials*, Phys. Rev. B **75** (2007), 045316, <http://dx.doi.org/10.1103/PhysRevB.75.045316>.
- [11] L. Rigutti, J. Teubert, G. Jacopin, F. Fortuna, M. Tchernycheva, A. De Luna Bugallo, F. H. Julien, F. Furtmayr, M. Stutzmann, and M. Eickhoff, *Origin of energy dispersion in Al_xGa_{1-x}N/GaN nanowire quantum discs with low Al content*, Phys. Rev. B **82** (2010), 235308, <http://dx.doi.org/10.1103/PhysRevB.82.235308>.
- [12] N. Grandjean, J. Massies, and M. Leroux, *Self-limitation of AlGa_xN/GaN quantum well energy by built-in polarization field*, Appl. Phys. Lett. **74** (1999), 2361–2363, <http://dx.doi.org/10.1063/1.123851>.
- [13] J. Müßener, J. Teubert, P. Hille, M. Schäfer, J. Schörmann, M. de la Mata, J. Arbiol, and M. Eickhoff, *Probing the Internal Electric Field in GaN/AlGa_xN Nanowire Heterostructures*, Nano Lett. **14** (2014), 5118–5122, <http://dx.doi.org/10.1021/nl501845m>.
- [14] S. Li and A. Waag, *GaN based nanorods for solid state lighting*, J. Appl. Phys. **111** (2012), 071101, <http://dx.doi.org/10.1063/1.3694674>.
- [15] M. Beeler, E. Trichas, and E. Monroy, *III-nitride semiconductors for intersubband optoelectronics: a review*, Semicond. Sci. Technol. **28** (2013), 074022, <http://dx.doi.org/10.1088/0268-1242/28/7/074022>.
- [16] D. Cociorva, W. G. Aulbur, and J. W. Wilkins, *Quasiparticle calculations of band offsets at AlN–GaN interfaces*, Solid State Commun. **124** (2002), 63–66, [http://dx.doi.org/10.1016/s0038-1098\(02\)00326-5](http://dx.doi.org/10.1016/s0038-1098(02)00326-5).
- [17] M. Tchernycheva, L. Nevou, L. Doyennette, F. H. Julien, E. Warde, F. Guillot, E. Monroy, E. Bellet-Amalric, T. Remmele, and M. Albrecht, *Systematic experimental and theoretical investigation of intersubband absorption in GaN–AlN quantum wells*, Phys. Rev. B **73** (2006), <http://dx.doi.org/10.1103/physrevb.73.125347>.

-
- [18] I. Vurgaftman and J. R. Meyer, *Band Parameters for Nitrogen-Containing Semiconductors*, J. Appl. Phys. **94** (2003), 3675–3696, <http://dx.doi.org/10.1063/1.1600519>.
- [19] V. Davydov, A. Klochikhin, V. Emtsev, D. Kurdyukov, S. Ivanov, V. Vekshin, F. Bechstedt, J. Furthmüller, J. Aderhold, J. Graul, A. V. Mudryi, H. Harima, A. Hashimoto, A. Yamamoto, , and E. E. Haller, *Band Gap of Hexagonal InN and InGaN Alloys*, phys. sta. sol. (b) **234** (2002), 787–795, [http://dx.doi.org/10.1002/1521-3951\(200212\)234:3<787::aid-pssb787>3.0.co;2-h](http://dx.doi.org/10.1002/1521-3951(200212)234:3<787::aid-pssb787>3.0.co;2-h).
- [20] H. Amano, M. Kito, K. Hiramatsu, and I. Akasaki, *P-Type Conduction in Mg-Doped GaN Treated with Low-Energy Electron Beam Irradiation (LEEBI)*, Jpn. J. Appl. Phys. **28** (1989), L2112–L2114, <http://dx.doi.org/10.1143/jjap.28.12112>.
- [21] S. Nakamura, T. Mukai, and M. Senoh, *High-Power GaN P-N Junction Blue-Light-Emitting Diodes*, Jpn. J. Appl. Phys. **30** (1991), L1998–L2001, <http://dx.doi.org/10.1143/jjap.30.11998>.
- [22] S. Nakamura, M. Senoh, and T. Mukai, *P-GaN/N-InGaN/N-GaN Double-Heterostructure Blue-Light-Emitting Diodes*, Jpn. J. Appl. Phys. **32** (1993), L8–L11, <http://dx.doi.org/10.1143/jjap.32.18>.
- [23] J. Wallys, J. Teubert, F. Furtmayr, D. M. Hofmann, and M. Eickhoff, *Bias-Enhanced Optical pH Response of Group III-Nitride Nanowires*, Nano Lett. **12** (2012), 6180–6186, <http://dx.doi.org/10.1021/nl303021v>.
- [24] S. Paul, A. Helwig, G. Müller, F. Furtmayr, J. Teubert, and M. Eickhoff, *Optochemical sensor system for the detection of H₂ and hydrocarbons based on InGaN/GaN nanowires*, Sensor. Actuat. B-Chem. **173** (2012), 120–126, <http://dx.doi.org/10.1016/j.snb.2012.06.022>.
- [25] K. Maier, A. Helwig, G. Müller, P. Becker, P. Hille, J. Schörmann, J.ermann, J. Teubert, and M. Eickhoff, *Detection of oxidising gases using an optochemical sensor system based on GaN/InGaN nanowires*, Sensor. Actuat. B-Chem. **197** (2014), 87–94, <http://dx.doi.org/10.1016/j.snb.2014.02.002>.
- [26] C. Adelman, R. Langer, G. Feuillet, , and B. Daudin, *Indium incorporation during the growth of InGaN by molecular-beam epitaxy studied by reflection high-energy electron diffraction intensity oscillations*, Appl. Phys. Lett. **75** (1999), 3518, <http://dx.doi.org/10.1063/1.125374>.
-

- [27] I.-h. Ho and G. B. Stringfellow, *Solid phase immiscibility in GaInN*, Appl. Phys. Lett. **69** (1996), 2701, <http://dx.doi.org/10.1063/1.117683>.
- [28] H. Sekiguchi, K. Kishino, and A. Kikuchi, *Ti-mask Selective-Area Growth of GaN by RF-Plasma-Assisted Molecular-Beam Epitaxy for Fabricating Regularly Arranged InGaN/GaN Nanocolumns*, APEX **1** (2008), 124002, <http://dx.doi.org/10.1143/apex.1.124002>.
- [29] S. Albert, A. Bengoechea-Encabo, M. A. Sánchez-García, X. Kong, A. Trampert, and E. Calleja, *Selective area growth of In(Ga)N/GaN nanocolumns by molecular beam epitaxy on GaN-buffered Si(111): from ultraviolet to infrared emission*, Nanotechnology **24** (2013), 175303, <http://dx.doi.org/10.1088/0957-4484/24/17/175303>.
- [30] M. D. Brubaker, S. M. Duff, T. E. Harvey, P. T. Blanchard, A. Roshko, A. W. Sanders, N. A. Sanford, and K. A. Bertness, *Polarity-Controlled GaN/AlN Nucleation Layers for Selective-Area Growth of GaN Nanowire Arrays on Si (111) Substrates by Molecular Beam Epitaxy*, Cryst. Growth Des. (2015), <http://dx.doi.org/10.1021/acs.cgd.5b00910>.
- [31] Z. Gačević, A. Bengoechea-Encabo, S. Albert, A. Torres-Pardo, J. M. González-Calbet, and E. Calleja, *Crystallographically uniform arrays of ordered (In)GaN nanocolumns*, J. Appl. Phys. **117** (2015), 035301, <http://dx.doi.org/10.1063/1.4905951>.
- [32] T. Gotschke, T. Schumann, F. Limbach, T. Stoica, and R. Calarco, *Influence of the adatom diffusion on selective growth of GaN nanowire regular arrays*, Appl. Phys. Lett. **98** (2011), 103102, <http://dx.doi.org/10.1063/1.3559618>.
- [33] F. Schuster, M. Hetzl, S. Weiszer, J. A. Garrido, M. de la Mata, C. Magen, J. Arbiol, and M. Stutzmann, *Position-Controlled Growth of GaN Nanowires and Nanotubes on Diamond by Molecular Beam Epitaxy*, Nano Lett. (2015), 150129093602003, <http://dx.doi.org/10.1021/nl504446r>.
- [34] A. Urban, M. Müller, C. Karbaum, G. Schmidt, P. Veit, J. Malindretos, F. Bertram, J. Christen, and A. Rizzi, *Optical emission of individual GaN nanocolumns analyzed with high spatial resolution*, Nano Lett. (2015), 150730135403006, <http://dx.doi.org/10.1021/acs.nanolett.5b01278>.

-
- [35] G. M. O. Hönig, S. Westerkamp, A. Hoffmann, and G. Callsen, *Shielding electrostatic fields in polar semiconductor nanostructures*, arXiv (2016), <http://dx.doi.org/10.1101/061111>.
- [36] O. Ambacher, *Growth and Applications of Group III Nitrides*, J. Phys. D: Appl. Phys. **31** (1998), 2653–2710, <http://dx.doi.org/10.1088/0022-3727/31/20/001>.
- [37] F. Furtmayr, M. Vilemeyer, M. Stutzmann, A. Laufer, B. K. Meyer, and M. Eickhoff, *Optical properties of Si- and Mg-doped gallium nitride nanowires grown by plasma-assisted molecular beam epitaxy*, J. Appl. Phys. **104** (2008), 074309, <http://dx.doi.org/10.1063/1.2980341>.
- [38] G. Jacopin, L. Rigutti, L. Largeau, F. Fortuna, F. Furtmayr, F. H. Julien, M. Eickhoff, and M. Tchernycheva, *Optical properties of wurtzite/zinc-blende heterostructures in GaN nanowires*, J. Appl. Phys. **110** (2011), 064313, <http://dx.doi.org/10.1063/1.3638698>.
- [39] L. Vegard, *Die Konstitution der Mischkristalle und die Raumfüllung der Atome*, Z. Physik **5** (1921), 17–26, <http://dx.doi.org/10.1007/bf01349680>.
- [40] O. Ambacher, J. Majewski, C. Miskys, A. Link, M. Hermann, M. Eickhoff, M. Stutzmann, F. Bernardini, V. Fiorentini, V. Tilak, and et al., *Pyroelectric properties of Al(In)Ga_N/Ga_N hetero- and quantum well structures*, Journal of Physics: Condensed Matter **14** (2002), 3399–3434, <http://dx.doi.org/10.1088/0953-8984/14/13/302>.
- [41] M. de la Mata, C. Magen, J. Gazquez, M. I. B. Utama, M. Heiss, S. Lopatin, F. Furtmayr, C. J. Fernández-Rojas, B. Peng, J. R. Morante, R. Rurali, M. Eickhoff, A. Fontcuberta i Morral, Q. Xiong, and J. Arbiol, *Polarity Assignment in ZnTe, GaAs, ZnO, and GaN-AlN Nanowires from Direct Dumbbell Analysis*, Nano Lett. **12** (2012), 2579–2586, <http://dx.doi.org/10.1021/nl300840q>.
- [42] A. Minj, A. Cros, N. Garro, J. Colchero, T. Auzelle, and B. Daudin, *Assessment of Polarity in GaN Self-Assembled Nanowires by Electrical Force Microscopy*, Nano Lett. **15** (2015), 6770–6776, <http://dx.doi.org/10.1021/acs.nanolett.5b02607>.
- [43] D. P. Williams, A. D. Andreev, E. P. O’Reilly, and D. A. Faux, *Derivation of built-in polarization potentials in nitride-based semiconductor quantum dots*, Phys. Rev. B **72** (2005), 235318, <http://dx.doi.org/10.1103/physrevb.72.235318>.
-

- [44] F. Bernardini, V. Fiorentini, and D. Vanderbilt, *Spontaneous polarization and piezoelectric constants of III-V nitrides*, Phys. Rev. B **56** (1997), R10024–R10027, <http://dx.doi.org/10.1103/physrevb.56.r10024>.
- [45] M. Knudsen, *Die Molekularströmung der Gase durch Öffnungen und die Effusion*, Ann. Phys. **333** (1909), 999–1016, <http://dx.doi.org/10.1002/andp.19093330505>.
- [46] M. Knudsen, *Experimentelle Bestimmung des Druckes gesättigter Quecksilberdämpfe bei 0° und höheren Temperaturen*, Ann. Phys. **334** (1909), 179–193, <http://dx.doi.org/10.1002/andp.19093340614>.
- [47] M. A. Herman, W. Richter, and H. Sitter, *Epitaxy: physical principles and technical implementation* (Springer, 2004).
- [48] L. Pauling, *Atomic Radii and Interatomic Distances in Metals*, J. Am. Chem. Soc. **69** (1947), 542–553, <http://dx.doi.org/10.1021/ja01195a024>.
- [49] T. Fließbach, *Statistische Physik* (Elsevier, 2007).
- [50] Y. Zhang, J. R. G. Evans, and S. Yang, *Corrected Values for Boiling Points and Enthalpies of Vaporization of Elements in Handbooks*, J. Chem. Eng. Data **56** (2011), 328–337, <http://dx.doi.org/10.1021/je1011086>.
- [51] N. D. Browning, E. M. James, K. Kishida, I. Arslan, J. P. Buban, J. A. Zaborac, S. J. Pennycook, Y. Xin, and G. Duscher, *SCANNING TRANSMISSION ELECTRON MICROSCOPY: AN EXPERIMENTAL TOOL FOR ATOMIC SCALE INTERFACE SCIENCE*, Rev. Adv. Mater. Sci. **1** (2000), 1–26, <http://dx.doi.org/666>.
- [52] A. Rosenauer and M. Schowalter, *STEMSIM-a New Software Tool for Simulation of STEM HAADF Z-Contrast Imaging*, Microscopy of Semiconducting Materials 2007 **120** (2008), 170–172, http://dx.doi.org/10.1007/978-1-4020-8615-1_36.
- [53] E. Okunishi, I. Ishikawa, H. Sawada, F. Hosokawa, M. Hori, and Y. Kondo, *Visualization of Light Elements at Ultrahigh Resolution by STEM Annular Bright Field Microscopy*, Microsc. Microanal. **15** (2009), 164–165, <http://dx.doi.org/10.1017/s1431927609093891>.
- [54] J. Schörmann, P. Hille, M. Schaefer, J. Musener, P. Becker, P. J. Klar, M. Klein-Boymann, M. Rohnke, M. de la Mata, J. Arbiol, D. M. Hofmann, J. Teubert, and

-
- M. Eickhoff, *Germanium doping of self-assembled GaN nanowires grown by plasma-assisted molecular beam epitaxy*, J. Appl. Phys. **114** (2013), 103505, <http://dx.doi.org/10.1063/1.4820264>.
- [55] L. Spieß, R. Schwarzer, H. Behnken, and G. Teichert, *Modernde Röntgenbeugung* (Teubner Verlag, 2005).
- [56] R. S. Wagner and W. C. Ellis, *Vapor-liquid-solid mechanism of single crystal growth*, Appl. Phys. Lett. **4** (1964), 89–90, <http://dx.doi.org/10.1063/1.1753975>.
- [57] A. Fontcuberta i Morral, C. Colombo, G. Abstreiter, J. Arbiol, and J. R. Morante, *Nucleation mechanism of gallium-assisted molecular beam epitaxy growth of gallium arsenide nanowires*, Appl. Phys. Lett. **92** (2008), 063112, <http://dx.doi.org/10.1063/1.2837191>.
- [58] F. Jabeen, V. Grillo, S. Rubini, and F. Martelli, *Self-catalyzed growth of GaAs nanowires on cleaved Si by molecular beam epitaxy*, Nanotechnology **19** (2008), 275711, <http://dx.doi.org/10.1088/0957-4484/19/27/275711>.
- [59] L. Geelhaar, C. Chèze, W. M. Weber, R. Averbeck, H. Riechert, T. Kehagias, P. Komninou, G. P. Dimitrakopoulos, and T. Karakostas, *Axial and radial growth of Ni-induced GaN nanowires*, Appl. Phys. Lett. **91** (2007), 093113, <http://dx.doi.org/10.1063/1.2776979>.
- [60] F. Furtmayr, M. Vielemeyer, M. Stutzmann, J. Arbiol, S. Estradé, F. Peirò, J. R. Morante, and M. Eickhoff, *Nucleation and growth of GaN nanorods on Si (111) surfaces by plasma-assisted molecular beam epitaxy - The influence of Si- and Mg-doping*, J. Appl. Phys. **104** (2008), 034309, <http://dx.doi.org/10.1063/1.2953087>.
- [61] V. Consonni, *Self-induced growth of GaN nanowires by molecular beam epitaxy: A critical review of the formation mechanisms*, physica status solidi (RRL) - Rapid Research Letters **7** (2013), 699–712, <http://dx.doi.org/10.1002/pssr.201307237>.
- [62] C. Chèze, L. Geelhaar, O. Brandt, W. Weber, H. Riechert, S. Münch, R. Rothe-mund, S. Reitzenstein, A. Forchel, T. Kehagias, P. Komninou, G. Dimitrakopoulos, and T. Karakostas, *Direct comparison of catalyst-free and catalyst-induced GaN nanowires*, Nano Res. **3** (2010), 528–536, <http://dx.doi.org/10.1007/s12274-010-0013-9>.
-

- [63] B. Daudin and F. Widmann, *Layer-by-layer growth of AlN and GaN by molecular beam epitaxy*, *J. Cryst. Growth* **182** (1997), 1–5, [http://dx.doi.org/10.1016/S0022-0248\(97\)00339-4](http://dx.doi.org/10.1016/S0022-0248(97)00339-4).
- [64] C. Adelman, J. Brault, D. Jalabert, P. Gentile, H. Mariette, G. Mula, and B. Daudin, *Dynamically stable gallium surface coverages during plasma-assisted molecular-beam epitaxy of (0001) GaN*, *J. Appl. Phys.* **91** (2002), 9638, <http://dx.doi.org/10.1063/1.1471923>.
- [65] B. Heying, R. Averbeck, L. F. Chen, E. Haus, H. Riechert, and J. S. Speck, *Control of GaN surface morphologies using plasma-assisted molecular beam epitaxy*, *J. Appl. Phys.* **88** (2000), 1855, <http://dx.doi.org/10.1063/1.1305830>.
- [66] E. J. Tarsa, B. Heying, X. H. Wu, P. Fini, S. P. DenBaars, and J. S. Speck, *Homoepitaxial growth of GaN under Ga-stable and N-stable conditions by plasma-assisted molecular beam epitaxy*, *J. Appl. Phys.* **82** (1997), 5472, <http://dx.doi.org/10.1063/1.365575>.
- [67] H. Okumura, K. Balakrishnan, H. Hamaguchi, T. Koizumi, S. Chichibu, H. Nakanishi, T. Nagatomo, and S. Yoshida, *Analysis of MBE growth mode for GaN epilayers by RHEED*, *J. Cryst. Growth* **189-190** (1998), 364–369, [http://dx.doi.org/10.1016/S0022-0248\(98\)00313-3](http://dx.doi.org/10.1016/S0022-0248(98)00313-3).
- [68] R. K. Debnath, R. Meijers, T. Richter, T. Stoica, R. Calarco, and H. Lüth, *Mechanism of molecular beam epitaxy growth of GaN nanowires on Si(111)*, *Appl. Phys. Lett.* **90** (2007), 123117, <http://dx.doi.org/10.1063/1.2715119>.
- [69] V. Consonni, V. G. Dubrovskii, A. Trampert, L. Geelhaar, and H. Riechert, *Quantitative description for the growth rate of self-induced GaN nanowires*, *Phys. Rev. B* **85** (2012), 155313, <http://dx.doi.org/10.1103/PhysRevB.85.155313>.
- [70] K. Wang, J. Singh, and D. Pavlidis, *Theoretical study of GaN growth: A Monte Carlo approach*, *J. Appl. Phys.* **76** (1994), 3502, <http://dx.doi.org/10.1063/1.357479>.
- [71] E. Calleja, M. A. Sánchez-García, E. Monroy, F. J. Sánchez, E. Muñoz, A. Sanz-Hervás, C. Villar, and M. Aguilar, *Growth kinetics and morphology of high quality AlN grown on Si(111) by plasma-assisted molecular beam epitaxy*, *J. Appl. Phys.* **82** (1997), 4681, <http://dx.doi.org/10.1063/1.366208>.

-
- [72] Z. Gačević, D. Gómez Sánchez, and E. Calleja, *Formation Mechanisms of GaN Nanowires Grown by Selective Area Growth Homoepitaxy*, Nano Lett. (2015), 150122142835006, <http://dx.doi.org/10.1021/nl504099s>.
- [73] M. Tchernycheva, C. Sartel, G. Cirlin, L. Travers, G. Patriarche, J.-C. Harmand, L. S. Dang, J. Renard, B. Gayral, L. Nevou, and F. Julien, *Growth of GaN free-standing nanowires by plasma-assisted molecular beam epitaxy structural and optical characterization*, Nanotechnology **18** (2007), 385306, <http://dx.doi.org/10.1088/0957-4484/18/38/385306>.
- [74] L. Lymperakis and J. Neugebauer, *Large anisotropic adatom kinetics on nonpolar GaN surfaces: Consequences for surface morphologies and nanowire growth*, Phys. Rev. B **79** (2009), 241308, <http://dx.doi.org/10.1103/PhysRevB.79.241308>.
- [75] T. Zywietz, J. Neugebauer, and M. Scheffler, *Adatom diffusion at GaN (0001) and (0001) surfaces*, Appl. Phys. Lett. **73** (1998), 487–489, <http://dx.doi.org/DOI:10.1063/1.121909>.
- [76] J. E. Northrup, J. Neugebauer, R. M. Feenstra, and A. R. Smith, *Structure of GaN(0001): The laterally contracted Ga bilayer model*, Phys. Rev. B **61** (2000), 9932–9935, <http://dx.doi.org/10.1103/PhysRevB.61.9932>.
- [77] V. Consonni, M. Hanke, M. Knelangen, L. Geelhaar, A. Trampert, and H. Riechert, *Nucleation mechanisms of self-induced GaN nanowires grown on an amorphous interlayer*, Phys. Rev. B **83** (2011), 035310, <http://dx.doi.org/10.1103/PhysRevB.83.035310>.
- [78] F. Furtmayr, *Nitride Nanowire Heterostructures*, Doktorarbeit, Technische Universität München (2013).
- [79] J. A. Freitas, W. J. Moore, B. V. Shanabrook, G. C. B. Braga, S. K. Lee, S. S. Park, and J. Y. Han, *Donor-related recombination processes in hydride-vapor-phase epitaxial GaN*, Phys. Rev. B **66** (2002), 233311, <http://dx.doi.org/10.1103/PhysRevB.66.233311>.
- [80] B. Monemar, P. P. Paskov, J. P. Bergman, G. Pozina, A. A. Toropov, T. V. Shubina, T. Malinauskas, and A. Usui, *Transient photoluminescence of shallow donor bound excitons in GaN*, Phys. Rev. B **82** (2010), 235202, <http://dx.doi.org/10.1103/PhysRevB.82.235202>.
-

- [81] P. Corfdir, J. K. Zettler, C. Hauswald, S. Fernández-Garrido, O. Brandt, and P. Lefebvre, *Sub-meV linewidth in GaN nanowire ensembles: Absence of surface excitons due to the field ionization of donors*, Phys. Rev. B **90** (2014), 205301, <http://dx.doi.org/10.1103/physrevb.90.205301>.
- [82] J. A. Freitas, *Optical studies of bulk and homoepitaxial films of III-V nitride semiconductors*, J. Cryst. Growth **281** (2005), 168–182, <http://dx.doi.org/10.1016/j.jcrysgro.2005.03.048>.
- [83] M. A. Reshchikov and H. Morkoç, *Luminescence properties of defects in GaN*, J. Appl. Phys. **97** (2005), 061301, <http://dx.doi.org/10.1063/1.1868059>.
- [84] J. Osaka, M. Senthil Kumar, H. Toyoda, T. Ishijima, H. Sugai, and T. Mizutani, *Role of atomic nitrogen during GaN growth by plasma-assisted molecular beam epitaxy revealed by appearance mass spectrometry*, Appl. Phys. Lett. **90** (2007), 172114, <http://dx.doi.org/10.1063/1.2734390>.
- [85] K. Klosek, M. Sobanska, G. Tchutchulashvili, Z. Zytkeiwicz, H. Teisseyre, and L. Klopotoski, *Optimization of nitrogen plasma source parameters by measurements of emitted light intensity for growth of GaN by molecular beam epitaxy*, Thin Solid Films **534** (2013), 107–110, <http://dx.doi.org/10.1016/j.tsf.2013.02.013>.
- [86] H. Carrère, A. Arnoult, A. Ricard, and E. Bedel-Pereira, *RF plasma investigations for plasma-assisted MBE growth of (Ga,In)(As,N) materials*, J. Cryst. Growth **243** (2002), 295–301, [http://dx.doi.org/10.1016/s0022-0248\(02\)01527-0](http://dx.doi.org/10.1016/s0022-0248(02)01527-0).
- [87] E. Iliopoulos, A. Adikimenakis, E. Dimakis, K. Tsagaraki, G. Konstantinidis, and A. Georgakilas, *Active nitrogen species dependence on radiofrequency plasma source operating parameters and their role in GaN growth*, J. Cryst. Growth **278** (2005), 426–430, <http://dx.doi.org/10.1016/j.jcrysgro.2005.01.013>.
- [88] K. Bertness, A. Roshko, L. Mansfield, T. Harvey, and N. Sanford, *Nucleation conditions for catalyst-free GaN nanowires*, J. Cryst. Growth **300** (2007), 94–99, <http://dx.doi.org/c>.
- [89] S. Albert, A. M. Bengoechea-Encabo, X. Kong, M. A. Sánchez-García, A. Trampert, and E. Calleja, *Correlation between growth conditions, morphology and optical properties of nanocolumnar InGaN/GaN heterostructures selectively grown by molecular*

-
- beam epitaxy*, Cryst. Growth Des. **15** (2015), 2661–2666, <http://dx.doi.org/10.1021/cg501798j>.
- [90] A. Debnath, J. S. Gandhi, M. Kesaria, R. Pillai, D. Starikov, and A. Bensaoula, *Effect of N_2^* and N on GaN nanocolumns grown on Si(111) by molecular beam epitaxy*, J. Appl. Phys. **119** (2016), 104302, <http://dx.doi.org/10.1063/1.4943179>.
- [91] N. Newman, *The energetics of the GaN MBE reaction: a case study of metastable growth*, J. Cryst. Growth **178** (1997), 102–112, [http://dx.doi.org/10.1016/S0022-0248\(97\)00083-3](http://dx.doi.org/10.1016/S0022-0248(97)00083-3).
- [92] P. Corfdir, P. Lefebvre, J. Ristić, P. Valvin, E. Calleja, A. Trampert, J.-D. Ganière, and B. Deveaud-Plédran, *Time-resolved spectroscopy on GaN nanocolumns grown by plasma assisted molecular beam epitaxy on Si substrates*, J. Appl. Phys. **105** (2009), 013113, <http://dx.doi.org/10.1063/1.3062742>.
- [93] T. Auzelle, B. Haas, M. Den Hertog, J.-L. Rouvière, B. Daudin, and B. Gayral, *Attribution of the 3.45 eV GaN nanowires luminescence to inversion domain boundaries*, Appl. Phys. Lett. **107** (2015), 051904, <http://dx.doi.org/10.1063/1.4927826>.
- [94] D. Sam-Giao, R. Mata, G. Tourbot, J. Renard, A. Wyszomolek, B. Daudin, and B. Gayral, *Fine optical spectroscopy of the 3.45 eV emission line in GaN nanowires*, J. Appl. Phys. **113** (2013), 043102, <http://dx.doi.org/10.1063/1.4775492>.
- [95] J. Neugebauer and C. G. Van de Walle, *Atomic geometry and electronic structure of native defects in GaN*, Phys. Rev. B **50** (1994), 8067–8070, <http://dx.doi.org/10.1103/PhysRevB.50.8067>.
- [96] C. G. V. de Walle, editor, *Effects on stoichiometry on point defects and impurities in gallium nitride*, Proceedings of the 4th Symposium on Non-Stoichiometric III-V Compounds (Friedrich-Alexander-Universität Erlangen, 2002), <http://dx.doi.org/10.1063/1.1623009>.
- [97] D. C. Look, G. C. Farlow, P. J. Drevinsky, D. F. Bliss, and J. R. Sizelove, *On the nitrogen vacancy in GaN*, Appl. Phys. Lett. **83** (2003), 3525, <http://dx.doi.org/10.1063/1.1623009>.
- [98] A. Pierret, C. Bougerol, B. Gayral, M. Kociak, and B. Daudin, *Probing alloy composition gradient and nanometer-scale carrier localization in single AlGaIn nanowires*
-

- by nanocathodoluminescence, *Nanotechnology* **24** (2013), 305703, <http://dx.doi.org/10.1088/0957-4484/24/30/305703>.
- [99] M. Belloeil, B. Gayral, and B. Daudin, *Quantum Dot-Like Behavior of Compositional Fluctuations in AlGaN Nanowires*, *Nano Lett.* (2016), <http://dx.doi.org/10.1021/acs.nanolett.5b03904>.
- [100] E. Calleja, M. A. Sánchez-García, F. Calle, F. B. Naranjo, E. Muñoz, U. Jahn, K. Ploog, J. Sánchez, J. M. Calleja, K. Saarinen, and P. Hautojärvi, *Molecular beam epitaxy growth and doping of III-nitrides on Si(1 1 1): layer morphology and doping efficiency*, *Mater. Sci. Eng. B-Adv.* **82** (2001), 2–8, [http://dx.doi.org/10.1016/S0921-5107\(00\)00721-2](http://dx.doi.org/10.1016/S0921-5107(00)00721-2).
- [101] L. Cerutti, J. Ristić, S. Fernández-Garrido, E. Calleja, A. Trampert, K. H. Ploog, S. Lazic, and J. M. Calleja, *Wurtzite GaN nanocolumns grown on Si(001) by molecular beam epitaxy*, *Appl. Phys. Lett.* **88** (2006), 213114, <http://dx.doi.org/10.1063/1.2204836>.
- [102] J. Ristic, E. Calleja, A. Trampert, S. Fernández-Garrido, C. Rivera, U. Jahn, and K. H. Ploog, *Columnar AlGaIn/GaN Nanocavities with AlN/GaN Bragg Reflectors Grown by Molecular Beam Epitaxy on Si(111)*, *Phys. Rev. Lett.* **94** (2005), 146102, <http://dx.doi.org/10.1103/PhysRevLett.94.146102>.
- [103] J. Renard, R. Songmuang, G. Tourbot, C. Bougerol, B. Daudin, and B. Gayral, *Evidence for quantum-confined Stark effect in GaN/AlN quantum dots in nanowires*, *Phys. Rev. B* **80** (2009), <http://dx.doi.org/10.1103/PhysRevB.80.121305>.
- [104] K. Forghani, L. Schade, U. T. Schwarz, F. Lipski, O. Klein, U. Kaiser, and F. Scholz, *Strain and defects in Si-doped (Al)GaIn epitaxial layers*, *J. Appl. Phys.* **112** (2012), 093102, <http://dx.doi.org/10.1063/1.4761815>.
- [105] F. Guillot, E. Bellet-Amalric, E. Monroy, M. Tchernycheva, L. Nevou, L. Doyennette, F. H. Julien, L. S. Dang, T. Remmele, M. Albrecht, T. Shibata, and M. Tanaka, *Si-doped GaN/AlN quantum dot superlattices for optoelectronics at telecommunication wavelengths*, *J. Appl. Phys.* **100** (2006), 044326, <http://dx.doi.org/10.1063/1.2335400>.
- [106] S. Riyopoulos, *Electrostatically Shielded Quantum Confined Stark Effect Inside Polar Nanostructures*, *Nanoscale Res. Lett.* **4** (2009), 993–1003, <http://dx.doi.org/10.1007/s11671-009-9347-1>.

-
- [107] P. Hageman, W. Schaff, J. Janinski, and Z. Liliental-Weber, *n-type doping of wurtzite GaN with germanium grown with plasma-assisted molecular beam epitaxy*, *J. Cryst. Growth* **267** (2004), 123 – 128, <http://dx.doi.org/10.1016/j.jcrysgro.2004.03.024>.
- [108] S. Fritze, A. Dadgar, H. Witte, M. Bügler, A. Rohrbeck, J. Bläsing, A. Hoffmann, and A. Krost, *High Si and Ge n-type doping of GaN doping - Limits and impact on stress*, *Appl. Phys. Lett.* **100** (2012), 122104, <http://dx.doi.org/10.1063/1.3695172>.
- [109] M. Schäfer, M. Günther, C. Länger, J. Müßener, M. Feneberg, P. Uredat, M. T. Elm, P. Hille, J. Schörmann, J. Teubert, T. Henning, P. J. Klar, and M. Eickhoff, *Electrical transport properties of Ge-doped GaN nanowires*, *Nanotechnology* **26** (2015), 135704, <http://dx.doi.org/10.1088/0957-4484/26/13/135704>.
- [110] O. Brandt, C. Pfüller, C. Chèze, L. Geelhaar, and H. Riechert, *Sub-meV linewidth of excitonic luminescence in single GaN nanowires: Direct evidence for surface excitons*, *Phys. Rev. B* **81** (2010), 045302, <http://dx.doi.org/10.1103/PhysRevB.81.045302>.
- [111] H. Wang and A.-B. Chen, *Calculation of shallow donor levels in GaN*, *J. Appl. Phys.* **87** (2000), 7859–7863, <http://dx.doi.org/10.1063/1.373467>.
- [112] P. Hille, J. Müßener, P. Becker, M. de la Mata, N. Rosemann, C. Magén, J. Arbiol, J. Teubert, S. Chatterjee, J. Schörmann, and et al., *Screening of the quantum-confined Stark effect in AlN/GaN nanowire superlattices by germanium doping*, *Appl. Phys. Lett.* **104** (2014), 102104, <http://dx.doi.org/10.1063/1.4868411>.
- [113] M. Feneberg, S. Osterburg, K. Lange, C. Lidig, B. Garke, R. Goldhahn, E. Richter, C. Netzel, M. D. Neumann, N. Esser, S. Fritze, H. Witte, J. Bläsing, A. Dadgar, and A. Krost, *Band gap renormalization and Burstein-Moss effect in silicon- and germanium-doped wurtzite GaN up to 10^{20}cm^{-3}* , *Phys. Rev. B* **90** (2014), <http://dx.doi.org/10.1103/physrevb.90.075203>.
- [114] M. Beeler, P. Hille, J. Schörmann, J. Teubert, M. de la Mata, J. Arbiol, M. Eickhoff, and E. Monroy, *Intraband Absorption in Self-Assembled Ge-Doped GaN/AlN Nanowire Heterostructures*, *Nano Lett.* **14** (2014), 1665–1673, <http://dx.doi.org/10.1021/nl5002247>.
-

- [115] M. Beeler, C. B. Lim, P. Hille, J. Bleuse, J. Schörmann, M. de la Mata, J. Arbiol, M. Eickhoff, and E. Monroy, *Long-lived excitons in GaN/AlN nanowire heterostructures*, Phys. Rev. B **91** (2015), 205440, <http://dx.doi.org/10.1103/physrevb.91.205440>.
- [116] K. Kishino, K. Nagashima, and K. Yamano, *Monolithic Integration of InGaN-Based Nanocolumn Light-Emitting Diodes with Different Emission Colors*, APEX **6** (2013), 012101, <http://dx.doi.org/10.7567/apex.6.012101>.
- [117] B. AlOtaibi, H. P. T. Nguyen, S. Zhao, M. G. Kibria, S. Fan, and Z. Mi, *Highly Stable Photoelectrochemical Water Splitting and Hydrogen Generation Using a Double-Band InGaN/GaN Core/Shell Nanowire Photoanode*, Nano Lett. **13** (2013), 4356–4361, <http://dx.doi.org/10.1021/nl402156e>.
- [118] J. Benton, J. Bai, and T. Wang, *Significantly enhanced performance of an InGaN/GaN nanostructure based photo-electrode for solar power hydrogen generation*, Appl. Phys. Lett. **103** (2013), 133904, <http://dx.doi.org/10.1063/1.4823550>.
- [119] K. D. Goodman, V. V. Protasenko, J. Verma, T. H. Kosel, H. G. Xing, and D. Jena, *Green luminescence of InGaN nanowires grown on silicon substrates by molecular beam epitaxy*, J. Appl. Phys. **109** (2011), 084336, <http://dx.doi.org/10.1063/1.3575323>.
- [120] Y.-L. Chang, J. L. Wang, F. Li, and Z. Mi, *High efficiency green, yellow, and amber emission from InGaN/GaN dot-in-a-wire heterostructures on Si(111)*, Appl. Phys. Lett. **96** (2010), 013106, <http://dx.doi.org/10.1063/1.3284660>.
- [121] C. Tessarek, S. Figge, T. Aschenbrenner, S. Bley, A. Rosenauer, M. Seyfried, J. Kalden, K. Sebald, J. Gutowski, and D. Hommel, *Strong phase separation of strained $In_xGa_{1-x}N$ layers due to spinodal and binodal decomposition: Formation of stable quantum dots*, Physical Review B **83** (2011), 115316, <http://dx.doi.org/10.1103/physrevb.83.115316>.
- [122] D. Cherns, R. F. Webster, S. V. Novikov, C. T. Foxon, A. M. Fischer, F. A. Ponce, and S. J. Haigh, *Compositional variations in $In_{0.5}Ga_{0.5}N$ nanorods grown by molecular beam epitaxy*, Nanotechnology **25** (2014), 215705, <http://dx.doi.org/10.1088/0957-4484/25/21/215705>.

-
- [123] T. Kehagias, *Nanoscale indium variation along InGaN nanopillars grown on (111) Si substrates*, Phys. E **42** (2010), 2197–2202, <http://dx.doi.org/10.1016/j.physe.2010.04.016>.
- [124] T. Tabata, J. Paek, Y. Honda, M. Yamaguchi, and H. Amano, *Growth of InGaN nanowires on a (111)Si substrate by RF-MBE*, phys. stat. sol. (c) **9** (2012), 646–649, <http://dx.doi.org/10.1002/pssc.201100446>.
- [125] G. Tourbot, C. Bougerol, F. Glas, L. F. Zagonel, Z. Mahfoud, S. Meuret, P. Gilet, M. Kociak, B. Gayral, and B. Daudin, *Growth mechanism and properties of InGaN insertions in GaN nanowires*, Nanotechnology **23** (2012), 135703, <http://dx.doi.org/10.1088/0957-4484/23/13/135703>.
- [126] A. Das, S. Magalhães, Y. Kotsar, P. K. Kandaswamy, B. Gayral, K. Lorenz, E. Alves, P. Ruterana, and E. Monroy, *Indium kinetics during the plasma-assisted molecular beam epitaxy of semipolar (11-22) InGaN layers*, Appl. Phys. Lett. **96** (2010), 181907, <http://dx.doi.org/10.1063/1.3427310>.
- [127] T. Kehagias, G. P. Dimitrakopoulos, P. Becker, J. Kioseoglou, F. Furtmayr, T. Koukoula, I. Häusler, A. Chernikov, S. Chatterjee, T. Karakostas, U. T. S. H-M Solowan, M. Eickhoff, and P. Komninou, *Nanostructure and strain in InGaN/GaN superlattices grown in GaN nanowires*, Nanotechnology **24** (2013), 435702, <http://dx.doi.org/10.1088/0957-4484/24/43/435702>.
- [128] Z. Gačević, N. Vukmirović, N. García-Lepetit, A. Torres-Pardo, M. Müller, S. Metzner, S. Albert, A. Bengoechea-Encabo, F. Bertram, P. Veit, J. Christen, J. M. González-Calbet, and E. Calleja, *Influence of composition, strain, and electric field anisotropy on different emission colors and recombination dynamics from InGaN nanodisks in pencil-like GaN nanowires*, Phys. Rev. B **93** (2016), <http://dx.doi.org/10.1103/physrevb.93.125436>.
- [129] H. Turski, M. Siekacz, Z. Wasilewski, M. Sawicka, S. Porowski, and C. Skierbiszewski, *Nonequivalent atomic step edges - Role of gallium and nitrogen atoms in the growth of InGaN layers*, J. Cryst. Growth **367** (2013), 115–121, <http://dx.doi.org/10.1016/j.jcrysgro.2012.12.026>.
- [130] R. Armitage and K. Tsubaki, *Multicolour luminescence from InGaN quantum wells grown over GaN nanowire arrays by molecular-beam epitaxy*, Nanotechnology **21** (2010), 195202, <http://dx.doi.org/10.1088/0957-4484/21/19/195202>.
-

- [131] G. Tourbot, C. Bougerol, A. Grenier, M. D. Hertog, D. Sam-Giao, D. Cooper, P. Gilet, B. Gayral, and B. Daudin, *Structural and optical properties of InGaN/GaN nanowire heterostructures grown by PA-MBE*, *Nanotechnology* **22** (2011), 075601, <http://dx.doi.org/10.1088/0957-4484/22/7/075601>.
- [132] S. M. Hamad, D. P. Norman, Q. Y. Chen, F. Keles, and H. W. Seo, *Competitive In and Ga incorporations for $In_xGa_{1-x}N$ ($0.29 < x < 0.36$) nanorods grown at a moderate temperature*, *AIP Adv.* **3** (2013), 072128, <http://dx.doi.org/10.1063/1.4816805>.
- [133] M. Gómez-Gómez, N. Garro, J. Segura-Ruiz, G. Martinez-Criado, A. Cantarero, H. T. Mengistu, A. García-Cristóbal, S. Murcia-Mascarós, C. Denker, J. Malindretos, and A. Rizzi, *Spontaneous core-shell elemental distribution in In-rich $In_xGa_{1-x}N$ nanowires grown by molecular beam epitaxy*, *Nanotechnology* **25** (2014), 075705, <http://dx.doi.org/10.1088/0957-4484/25/7/075705>.
- [134] E. Monroy, N. Gogneau, F. Enjalbert, F. Fossard, D. Jalabert, E. Bellet-Amalric, L. S. Dang, and B. Daudin, *Molecular-beam epitaxial growth and characterization of quaternary III-nitride compounds*, *J. Appl. Phys.* **94** (2003), 3121, <http://dx.doi.org/10.1063/1.1598633>.
- [135] H. Murotani, H. Andoh, T. Tsukamoto, T. Sugiura, Y. Yamada, T. Tabata, Y. Honda, M. Yamaguchi, and H. Amano, *Emission Wavelength Dependence of Internal Quantum Efficiency in InGaN Nanowires*, *Jpn. J. Appl. Phys.* **52** (2013), 08JE10, <http://dx.doi.org/10.7567/JJAP.52.08JE10>.
- [136] H. Murotani, Y. Yamada, T. Tabata, Y. Honda, M. Yamaguchi, and H. Amano, *Effects of exciton localization on internal quantum efficiency of InGaN nanowires*, *J. Appl. Phys.* **114** (2013), 153506, <http://dx.doi.org/10.1063/1.4825124>.
- [137] Y. Kawakami, S. Suzuki, A. Kaneta, M. Funato, A. Kikuchi, and K. Kishino, *Origin of high oscillator strength in green-emitting InGaN-GaN nanocolumns*, *Appl. Phys. Lett.* **89** (2006), 163124, <http://dx.doi.org/10.1063/1.2363958>.
- [138] A. J. Ptak, M. R. Millecchia, T. H. Myers, K. S. Ziemer, and C. D. Stinespring, *The relation of active nitrogen species to high-temperature limitations for (000 $\bar{1}$) GaN growth by radio-frequency-plasma-assisted molecular beam epitaxy*, *Appl. Phys. Lett.* **74** (1999), 3836, <http://dx.doi.org/10.1063/1.124196>.

-
- [139] L. I. Berger, A. K. Covington, R. B. Fox, H. P. R. Frederikse, J. Fuhr, R. N. Goldberg, K. A. Gschneidner, C. R. Hammond, R. F. Hampson, N. E. Holden, H. D. B. Jenkins, H. V. Kehiaian, J. A. Kerr, N. Kishore, R. Lennen, F. J. Lovas, W. C. Martin, J. S. Miller, T. M. Miller, J. Reader, L. E. Snyder, D. W. Stocker, B. N. Taylor, T. G. Trippe, P. Vany'sek, W. L. Wiese, E. S. Wilks, and C. Wohlfarth, *Handbook of Chemistry and Physics* (CRC Press, 2003), 84th edition.
- [140] C. G. Van de Walle and J. Neugebauer, *First-principles calculations for defects and impurities: Applications to III-nitrides*, J. Appl. Phys. **95** (2004), 3851, <http://dx.doi.org/10.1063/1.1682673>.
- [141] J. Neugebauer, *Surfactants and antisurfactants on group-III-nitride surfaces*, phys. stat. sol. (c) **0** (2003), 1651–1667, <http://dx.doi.org/10.1002/pssc.200303132>.
- [142] K. I. Gries, J. Schlechtweg, P. Hille, J. Schörmann, M. Eickhoff, and K. Volz, *Three dimensional reconstruction of InGaN nanodisks in GaN nanowires: improvement of the nanowire sample preparation to avoid missing wedge effects*, Microsc. Microanal. **submitted** (2017), <http://dx.doi.org/10.1002/pssa.201127278>.
- [143] M. V. Durnev, A. V. Omelchenko, E. V. Yakovlev, I. Y. Evstratov, and S. Y. Karpov, *Strain effects on indium incorporation and optical transitions in green-light InGaN heterostructures of different orientations*, Phys. Status Solidi A **208** (2011), 2671–2675, <http://dx.doi.org/10.1002/pssa.201127278>.
- [144] H. Okumura, K. Ohta, K. Ando, W. Rühle, T. Nagatomo, and S. Yoshida, *Bandgap energy of cubic GaN*, Solid-State Electron. **41** (1997), 201–204, [http://dx.doi.org/10.1016/s0038-1101\(96\)00166-9](http://dx.doi.org/10.1016/s0038-1101(96)00166-9).
- [145] C. Hauswald, P. Corfdir, J. K. Zettler, V. M. Kaganer, K. K. Sabelfeld, S. Fernández-Garrido, T. Flissikowski, V. Consonni, T. Gotschke, H. T. Grahn, L. Geelhaar, and O. Brandt, *Origin of the nonradiative decay of bound excitons in GaN nanowires*, Phys. Rev. B **90** (2014), 165304, <http://dx.doi.org/10.1103/physrevb.90.165304>.
- [146] J. Lähnemann, O. Brandt, C. Pfüller, T. Flissikowski, U. Jahn, E. Luna, M. Hanke, M. Knelangen, A. Trampert, and H. T. Grahn, *Coexistence of quantum-confined Stark effect and localized states in an (In,Ga)N/GaN nanowire heterostructure*, Phys. Rev. B **84** (2011), 155303, <http://dx.doi.org/10.1103/physrevb.84.155303>.
-

- [147] A. Morel, P. Lefebvre, S. Kalliakos, T. Taliercio, T. Bretagnon, and B. Gil, *Donor-acceptor-like behavior of electron-hole pair recombinations in low-dimensional (Ga,In)N/GaN systems*, Phys. Rev. B **68** (2003), 045331, <http://dx.doi.org/10.1103/physrevb.68.045331>.
- [148] W. Bergbauer, M. Strassburg, C. Kölper, N. Linder, C. Roder, J. Lähnemann, A. Trampert, S. Fündling, S. F. Li, H.-H. Wehmann, and et al., *Continuous-flux MOVPE growth of position-controlled N-face GaN nanorods and embedded InGaN quantum wells*, Nanotechnology **21** (2010), 305201, <http://dx.doi.org/10.1088/0957-4484/21/30/305201>.
- [149] Y.-T. Lin, T.-W. Yeh, and P. Daniel Dapkus, *Mechanism of selective area growth of GaN nanorods by pulsed mode metalorganic chemical vapor deposition*, Nanotechnology **23** (2012), 465601, <http://dx.doi.org/10.1088/0957-4484/23/46/465601>.
- [150] K. Choi, M. Arita, and Y. Arakawa, *Selective-area growth of thin GaN nanowires by MOCVD*, J. Cryst. Growth **357** (2012), 58–61, <http://dx.doi.org/10.1016/j.jcrysgro.2012.07.025>.
- [151] S. Sundaram, R. Puybaret, Y. El Gmili, X. Li, P. L. Bonanno, K. Pantzas, G. Orsal, D. Troadec, Z.-H. Cai, G. Patriarche, and et al., *Nanoscale selective area growth of thick, dense, uniform, In-rich, InGaN nanostructure arrays on GaN/sapphire template*, J. Appl. Phys. **116** (2014), 163105, <http://dx.doi.org/10.1063/1.4900531>.
- [152] X. Wang, J. Hartmann, M. Mandl, M. Sadat Mohajerani, H.-H. Wehmann, M. Strassburg, and A. Waag, *Growth kinetics and mass transport mechanisms of GaN columns by selective area metal organic vapor phase epitaxy*, J. Appl. Phys. **115** (2014), 163104, <http://dx.doi.org/10.1063/1.4871782>.
- [153] T. Schumann, T. Gotschke, F. Limbach, T. Stoica, and R. Calarco, *Selective-area catalyst-free MBE growth of GaN nanowires using a patterned oxide layer*, Nanotechnology **22** (2011), 095603, <http://dx.doi.org/10.1088/0957-4484/22/9/095603>.
- [154] S.-T. Lee, R. S. Kumar, S.-K. Jeon, M.-D. Kim, S.-G. Kim, and J.-E. Oh, *Influence of growth parameters on the optical properties of selective area grown GaN nanorods by plasma-assisted molecular beam epitaxy*, J. Lumin. **151** (2014), 188–192, <http://dx.doi.org/10.1016/j.jlumin.2014.02.026>.

-
- [155] K. A. Bertness, A. W. Sanders, D. M. Rourke, T. E. Harvey, A. Roshko, J. B. Schlager, and N. A. Sanford, *Controlled Nucleation of GaN Nanowires Grown with Molecular Beam Epitaxy*, *Adv. Funct. Mater.* **20** (2010), 2911–2915, <http://dx.doi.org/10.1002/adfm.201000381>.
- [156] K. Kishino, H. Sekiguchi, and A. Kikuchi, *Improved Ti-mask selective-area growth (SAG) by rf-plasma-assisted molecular beam epitaxy demonstrating extremely uniform GaN nanocolumn arrays*, *J. Cryst. Growth* **311** (2009), 2063–2068, <http://dx.doi.org/10.1016/j.jcrysgro.2008.11.056>.
- [157] A. Bengoechea-Encabo, F. Barbagini, S. Fernandez-Garrido, J. Grandal, J. Ristic, M. Sanchez-Garcia, E. Calleja, U. Jahn, E. Luna, and A. Trampert, *Understanding the selective area growth of GaN nanocolumns by MBE using Ti nanomasks*, *J. Cryst. Growth* **325** (2011), 89–92, <http://dx.doi.org/10.1016/j.jcrysgro.2011.04.035>.
- [158] M. Beeler, *Ingénierie quantique de nanostructures à base de semi-conducteurs III-Nitrures pour l'optoélectronique infrarouge*, Doktorarbeit, Université de Grenoble (2015).
- [159] I. Vurgaftman, J. R. Meyer, and L. R. Ram-Mohan, *Band parameters for III-V compound semiconductors and their alloys*, *J. Appl. Phys.* **89** (2001), 5815–5875, <http://dx.doi.org/10.1063/1.1368156>.

Versicherung

Ich erkläre:

Ich habe die vorgelegte Dissertation selbständig und ohne unerlaubte fremde Hilfe und nur mit den Hilfen angefertigt, die ich in der Dissertation angegeben habe. Alle Textstellen, die wörtlich oder sinngemäß aus veröffentlichten Schriften entnommen sind, und alle Angaben, die auf mündlichen Auskünften beruhen, sind als solche kenntlich gemacht. Bei den von mir durchgeführten und in der Dissertation erwähnten Untersuchungen habe ich die Grundsätze guter wissenschaftlicher Praxis, wie sie in der „Satzung der Justus-Liebig-Universität Gießen zur Sicherung guter wissenschaftlicher Praxis“ niedergelegt sind, eingehalten.

Gießen, den _____

Pascal Hille